

# Analysis of reflector antenna systems by means of new conical wave objects

---

Škokić, Siniša

Doctoral thesis / Disertacija

2010

*Degree Grantor / Ustanova koja je dodijelila akademski / stručni stupanj:* **University of Zagreb, Faculty of Electrical Engineering and Computing / Sveučilište u Zagrebu, Fakultet elektrotehnike i računarstva**

*Permanent link / Trajna poveznica:* <https://urn.nsk.hr/urn:nbn:hr:168:505709>

*Rights / Prava:* [In copyright](#)/[Zaštićeno autorskim pravom.](#)

*Download date / Datum preuzimanja:* **2024-07-13**



*Repository / Repozitorij:*

[FER Repository - University of Zagreb Faculty of Electrical Engineering and Computing repository](#)



UNIVERSITY OF ZAGREB  
FACULTY OF ELECTRICAL ENGINEERING AND COMPUTING  
SVEUČILIŠTE U ZAGREBU  
FAKULTET ELEKTROTEHNIKE I RAČUNARSTVA

SINIŠA ŠKOKIĆ

**ANALYSIS OF REFLECTOR  
ANTENNA SYSTEMS BY MEANS OF  
NEW CONICAL WAVE OBJECTS**

**ANALIZA REFLEKTORSKIH ANTENSKIH  
SUSTAVA POMOĆU NOVIH KONUSNIH  
VALNIH OBJEKATA**

DOCTORAL THESIS  
DOKTORSKA DISERTACIJA

ZAGREB, 2009.

This Thesis was made at:

**Department of Wireless Communications  
Faculty of Electrical Engineering and Computing  
University of Zagreb, Zagreb, Croatia**

and

**Department of Information Engineering  
Faculty of Engineering  
University of Siena, Siena, Italy.**

Advisor 1: **Prof. Zvonimir Šipuš, Ph.D.**, University of Zagreb

Advisor 2: **Prof. Stefano Maci**, University of Siena

Thesis has 155 pages.

Thesis No.:

**The dissertation evaluation committee:**

1. **Professor Juraj Bartolić**, Ph.D., Faculty of Electrical Engineering and Computing, University of Zagreb
2. **Professor Zvonimir Šipuš**, Ph.D., Faculty of Electrical Engineering and Computing, University of Zagreb
3. **Professor Stefano Maci**, Department of Information Engineering, University of Siena, Italy
4. **Professor Darko Žubrinić**, Ph.D., Faculty of Electrical Engineering and Computing, University of Zagreb
5. **Assistant Professor Radovan Zentner**, Ph.D., Faculty of Electrical Engineering and Computing, University of Zagreb

**The dissertation defense committee:**

1. **Professor Juraj Bartolić**, Ph.D., Faculty of Electrical Engineering and Computing, University of Zagreb
2. **Professor Zvonimir Šipuš**, Ph.D., Faculty of Electrical Engineering and Computing, University of Zagreb
3. **Professor Stefano Maci**, Department of Information Engineering, University of Siena, Italy
4. **Professor Darko Žubrinić**, Ph.D., Faculty of Electrical Engineering and Computing, University of Zagreb
5. **Assistant Professor Radovan Zentner**, Ph.D., Faculty of Electrical Engineering and Computing, University of Zagreb

Date of dissertation defense: **23<sup>rd</sup> April 2010**

## ACKNOWLEDGEMENTS

**Turns out, no matter how hard you try, you simply can't do everything just by yourself.**

Over the course of these four years, a number of people have endeavored me in one way or another. Some lent me a hand in a critical situation. Some gave me golden advice. Some others were simply there for me. This page I dedicate to them all.

Among the many, three clearly stand out. The first place on my “Thank you” list, without any doubt, goes to **Massimiliano Casaletti** of the University of Siena, Italy, who saved me and my whole Ph.D. TWICE. The first time, I had been stuck for months and was just about to miss all the deadlines and gloriously fail, due to one last error in my code that I was unable to locate. Fortunately, Massimiliano had the patience to rederive all my formulas and recode all my functions, and he managed to spot the darn error and eliminate it. The second time, I was stuck again, but the error had nothing to do with me or my functions. It was caused by a faulty GPOF function that we had inherited from others. However, at the time I never would have dared claim that the only function I hadn't written myself was faulty, especially since it was already used by so many other people. Fortunately for me, Massimiliano had the experience and the self-confidence to claim just that. Grazie mille Massimiliano, sei un grande!

The second most important “Thank you” I owe to **Stig Sørensen** of Ticra, Denmark. Towards the end of the Ph.D., when a hundred auxiliary problems had to be solved in order to put all the pieces of the puzzle together, my questions became too specific for both my advisors. I was more than lucky to have Stig on the same team, for he was the only person who could say “Been there, done that,” and provide me with a quick fix and a precise answer every time. And he never spared the time to do so. Dear Stig, your hand-written answers and comments were precious, but your kindness was priceless. Thank you for that.

Finally, the third big “Thank you” goes out to my colleague **Mario Muštra**, who selflessly lent me a hand in a time of crisis, only weeks from the thesis defense. It was at that very time that the infamous Murphy's Law reared its ugly head and my faithful laptop decided it was time it broke down. And so, as I was despairing over yet another lost week and trying to figure out where and how to continue with my simulations, in came Mario and reminded me of the super-computer that his group had bought some time ago. Hours later, I was back in the saddle. A friend in need is a friend indeed. Thanks, man!

Among other people, those who were there for me and who are still there for me, I would like to mention in particular my officemates and friends **Tomislav Debogović** and **Marko Bosiljevac**, who were almost always the first ones to hear out my Ph.D.-related frustrations. I have to say they did a tremendous job absorbing them, and I will make sure to return the favour, but hopefully in a lesser extent, for their sake! Naturally, after work I would go on complaining about my Ph.D. to people I know outside work, in particular my dearest friends **Lucky** and **Andrej**, and then **Slaven, Vuki, Céline, Marin, Ana** and **others**.

A very special “Thank you” is dedicated to **my family**. Firstly, for all the obvious reasons, and then for all non-obvious ones, such as all the discussions about the meaning of life, death, cars and Ph.D. that I shared with **my brother**, or all the times when **my parents** did all they could to not upset me or bother me in any way, because I was so busy (even if just the sight of them trying so hard not to bother me was already enough to upset me!).

Here I would also like to thank **Ticra and all the people who work or have worked there**, who not only developed one of the most powerful electromagnetic simulators out there (GRASP), but also made it probably the most transparent one. GRASP may well be the only commercial software where every single analysis method and every single model are explained in-depth and presented clearly, for everyone to understand. I ended up reaching for its Technical Description more often than any textbook on computational electromagnetics. Without it, I don’t know how I would have ever finished my thesis. Thank you guys for not keeping your knowledge to yourselves.

Finally, I would like to thank my two advisors, **Prof. Zvonimir Šipuš** and **Prof. Stefano Maci**, for all their help, advice and support over the years. I hope you won’t mind being put at the end of the “Thank you” queue. There is a reason for that, and it’s my mum. When I would come home from school with yet another good grade, she would say simply “It’s expected of you”. Zvonimir and Stefano, thank you for everything, I didn’t expect anything less from you!

\*\*\*

Special thanks to Steely Dan and the makers of Wódka Żołądkowa Gorzka for the inspiration.

# CONTENTS

<b>1. INTRODUCTION .....</b>	<b>1</b>
<b>2. ANALYSIS METHODS FOR REFLECTOR SYSTEMS .....</b>	<b>4</b>
2.1. Propagation via Radiation Integral.....	7
2.1.1. Radiation Integral in Spectral Domain.....	13
2.1.2. Radiation Integral and Dyadic Green's Functions.....	21
2.2. Propagation via Expansion into Wave Objects .....	23
2.2.1. Plane, Cylindrical and Spherical Waves .....	24
2.2.2. Fields from Sources Located in Complex Space .....	26
2.2.3. Gaussian Beams and Higher-order Gauss-Hermite Modes.....	29
2.3. Reflection from Metallic Objects .....	36
2.3.1. Reflection via Radiation Integral .....	36
2.3.2. Mode-matching Techniques.....	41
2.3.3. Simplified High-frequency Model: Ray and Beam Reflection .....	43
<b>3. COMPLEX CONICAL BEAMS .....</b>	<b>51</b>
3.1. Formulation – Scalar Case .....	51
3.1.1. Analytic Solution of Wave Objects in Space Domain .....	54
3.1.2. Numerical Considerations.....	58
3.1.3. Properties of the Wave Objects.....	63
3.2. Vectorisation of Conical Beams.....	65
3.2.1. Vectorisation Strategy 1: Fourier Transform Approach .....	65
3.2.2. Vectorisation Strategy 2: Auxiliary Vector Potentials Approach .....	66
3.2.3. Differentiation of Complex Conical Beams.....	67
<b>4. APPLICATION OF CONICAL BEAMS IN THE ANALYSIS OF REFLECTOR SYSTEMS.....</b>	<b>79</b>
4.1. Merging Physical Optics With Conical Beams – A-PO Approach.....	81
4.1.1. Obtaining Field Spectrum Directly from Field in the Focal Plane.....	82
4.1.2. Obtaining Field Spectrum from Far-field Radiation Pattern.....	88
4.2. Efficient Calculation of the PO Integral.....	93
4.3. Auxiliary Calculations.....	97
4.3.1. Coordinate System Transformations.....	98
4.3.2. Estimation of Position of the Reflected Beam's Waist.....	103
4.4. Description of the Developed Simulation Program .....	108
4.4.1. Algorithm Description .....	108
4.4.2. Program Optimization and Enhancements .....	110
<b>5. NUMERICAL VALIDATION.....</b>	<b>114</b>
5.1. Test Sources .....	114
5.1.1. Circular Waveguide Modes .....	115
5.1.2. Huygens Source in Complex Space .....	115
5.2. Verification: Scalar Beams (TM mode) .....	118
5.3. Verification: Vectorised Beams (TM mode).....	121
5.4. Analysis of a Single Reflector.....	123
5.5. Analysis of a Two-Reflector System (Huygens' Source).....	124
5.6. Discussion .....	130

<b>6. CONCLUSIONS .....</b>	<b>131</b>
<b>APPENDIX A: FUNCTION APPROXIMATION VIA THE GENERALIZED PENCIL-OF-FUNCTIONS METHOD.....</b>	<b>134</b>
<b>APPENDIX B: FOURIER TRANSFORM OF TM CIRCULAR WAVEGUIDE MODES.....</b>	<b>137</b>
B.1. 2-D Fourier Transform of a Vector Function in Polar Coordinates .....	137
B.2. Fourier Transform of TM Circular Waveguide Modes .....	138
<b>APPENDIX C: PSEUDO-POLAR FFT ALGORITHM .....</b>	<b>143</b>
<b>REFERENCES .....</b>	<b>149</b>
<b>INTERNET REFERENCES .....</b>	<b>153</b>
<b>LIST OF SYMBOLS .....</b>	<b>154</b>
<b>SAŽETAK .....</b>	<b>155</b>
<b>SUMMARY.....</b>	<b>156</b>
<b>KEYWORDS / KLJUČNE RIJEČI .....</b>	<b>157</b>
<b>BIOGRAPHY.....</b>	<b>158</b>
<b>ŽIVOTOPIS.....</b>	<b>159</b>



## 1. INTRODUCTION

The term quasi-optical region covers a range of frequencies spanning from the upper end of the microwave range and all the way up to terahertz frequencies. The main characteristic of this frequency range is that the devices interacting with the electromagnetic wave are much larger than a wavelength, but still not large enough as to be able to take full advantage of the simplifications that optical systems and devices benefit from. The term "simplifications" here refers not only to the analysis of such systems, but also to the electric and magnetic properties of matter. For example, at optical frequencies optical fibres are commonly used to conduct the electromagnetic signal with minimal losses to very long distances. This is feasible because at such high frequencies there is almost no interaction between the electromagnetic wave and the molecules of the fibre, due to the molecules being too heavy to be able to follow the rapid variations of the electric field and absorb the wave's energy. Similarly, at microwave frequencies, electromagnetic signals (waves) can be conducted with minimal losses using waveguides, because the surfaces of the metallic waveguide walls are large, resulting in low current density and therefore low losses.

In the quasi-optical region, on the other hand, neither of the two conditions is satisfied, and the losses in both metallic and dielectric guiding structures can be as high as 0.5 dB/cm [1]. Probably the only available medium with low losses in this frequency range is air, and the idea is to try and conduct the electromagnetic wave from the generator to the main radiating antenna through air, while trying to keep it as focused as possible so as to ensure minimal leakage of energy, i.e. minimal losses. The wave is directed in space and kept focused by a sequence of curved, shaped metallic reflectors called a beam waveguide, shown in Fig. 1.1. Such a solution for conducting the electromagnetic wave is clearly more complicated than the ones mentioned above, and presents significant challenges both from practical and analytical aspect. The analytical aspect of beam waveguides and other multi-reflector systems is the primary concern of this thesis.

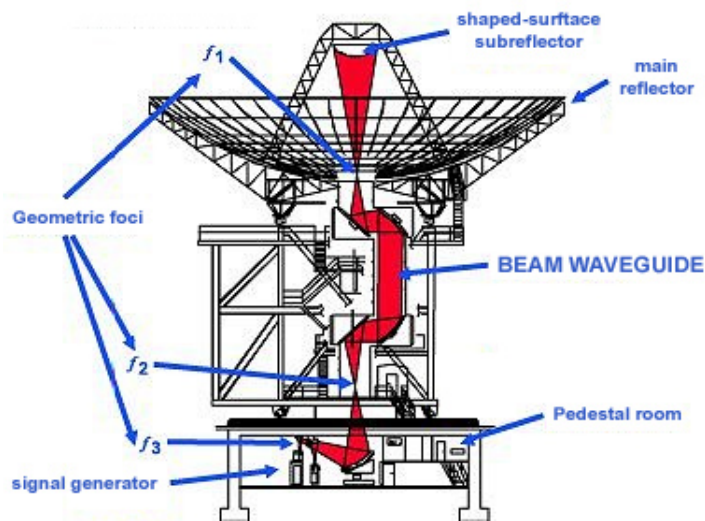


Figure 1.1. Beam Waveguide

The analysis of reflector antenna systems at millimetre-wave frequencies requires the development of new methods particularly suited for that frequency and size range. For example, a beam waveguide is composed of a sequence of reflectors, each of which can be a hundred wavelengths in diameter. Discretising the analysis domain with a resolution of  $\lambda/10$  in the fashion of classical numerical methods (e.g. Method of Moments or Finite Difference Time-Domain Method [14]-[17]) would lead to systems of equations with more than a million unknowns per one reflector, which would in return be prohibitively slow if not impossible to solve. Instead, in the quasi-optical region the analysis methods seek to express the radiated field in terms of a relatively low number of wave objects of higher complexity and in this way reduce the number of unknowns in the system. The aim is to develop a modular process, whereby the total reflected field from one reflector can be re-expanded into a new sum of wave objects of the same kind, and the whole procedure can be repeated in the same way for all subsequent reflectors.

A number of different objects have been introduced that are more or less suitable to the described approach, each with its own combination of complexity, accuracy and speed. These are the Gaussian Beams [2]-[3], higher-order Gauss-Laguerre and Gauss-Hermite modes [4], [5], Complex Source Points [6], [7], etc. This dissertation introduces a new kind of wave objects, with a formulation that has several advantages over other approaches, most important of which are that the new wave objects respect the wave equation in the region of interest, and that their generation is done in an efficient and natural way starting from the aperture field

spectrum. Also presented is their integration in the framework of reflector antenna systems analysis. The resulting method is shown to have the same level of accuracy as Physical Optics, which is considered to be the reference solution in the analysis of quasi-optical systems. Due to the modular approach, the simulation time increases linearly with the number of reflectors, proving this method to be especially advantageous for analysing a sequence of reflectors such as the beam waveguide.

The thesis is organized as follows. Chapter 2 explains the key steps in the analysis of reflector antenna systems and gives an overview of various existing methods for solving such electromagnetic problems. The emphasis is not so much on going into the specifics of each particular method, as much as it is on presenting them in the context of a range of possible approaches to the same basic problem. Chapter 3 gives a detailed account of the new wave objects, the so-called Complex Conical Beams (CCB's), which are the primary concern of this thesis. First the scalar formulation is presented, followed by the necessary mathematical derivations for extending the analysis to the realistic vector electromagnetic fields. The key intermediate step, the Generalized Pencil-of-Functions approximation (GPOF expansion), is also considered in some detail. Next, Chapter 4 describes the linking of this new propagation model to the Physical Optics reflection model in order to create a complete analysis method suitable for analysing a sequence of metallic reflectors. In order to be able to verify the mathematical model, the method has been translated into a computer programme, and its critical parts are also presented in this chapter, with a brief mention of various acceleration techniques applied for speeding up the analysis. The numerical tests and comparisons to other existing techniques, most notably Gaussian beam analysis and Physical Optics, follow in Chapter 5. Finally, the conclusions and pointers for future research are summarized in Chapter 6. Some of the lengthier intermediate mathematical derivations have been moved to the Appendix, in order to preserve the clarity and compactness of the text.

## 2. ANALYSIS METHODS FOR REFLECTOR SYSTEMS

The analysis of reflector antenna systems comes down to two things: the calculation of propagation of the wave between the reflectors (including the initial path from the source to the first reflector and the final path from the last reflector to the observation point, as shown in Fig. 2.1.), and the calculation of reflection from the surface of each reflector. Here, "reflection" is meant in the more general sense, and depending on the method of choice may also include the calculation of diffraction effects from the edges of a reflector.

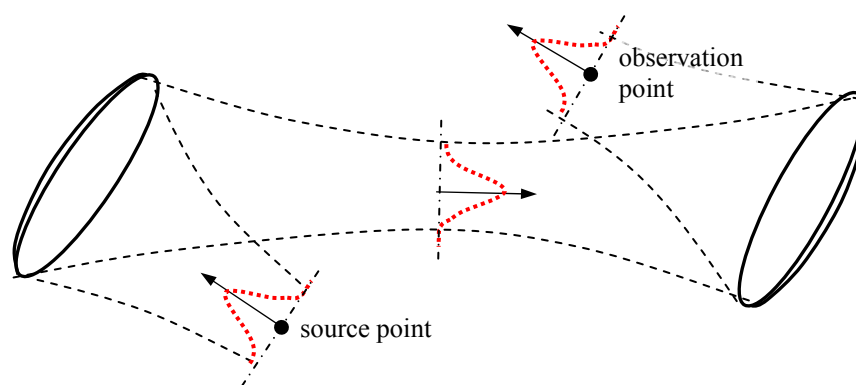


Figure 2.1. Propagation of a shaped wave in a multi-reflector system

There are different ways that one can go about solving this problem, each with its own compromise between accuracy and speed. A number of models that introduce the necessary mathematical formalism for the description of the chosen approach and a number of numerical methods for obtaining concrete results from a given model have been developed in the past. However, as textbooks more often focus on the numerical methods rather than the problems themselves [10], [14]-[16], it is rather hard to get a grasp of the "big picture". The idea of this introductory chapter is therefore to give a sketch of different approaches to the same problem of reflector antenna system analysis, and link each approach to a model and/or a numerical method that can be applied to obtain numerical results.

Considering reflection from metallic surfaces, three general approaches can be distinguished:

- 1) calculate reflection from scattering equations via the radiation integral
- 2) calculate reflection via mode-matching techniques
- 3) calculate reflection via simple geometrical models, with or without diffraction corrections

The first approach consists of calculating the currents on the reflector and then reusing them in the subsequent radiation integral. It is the most general of the approaches and is not concerned with the notion of the actual direction of propagation of the reflected wave: the procedure for computing the fields is the same for any point in space. The currents can be calculated via an exact (Method of Moments) or an approximate (Physical Optics) model, yielding different levels of speed and accuracy. The two models are the subject of Sec. 2.3.1.

The second approach is completely different from the first one, in that it neither calculates the surface currents nor employs the radiation integral to calculate the scattered fields. It consists of expanding both the incident (known) and the reflected (unknown) field in a set of *modes*, and of calculating the field that each of the two sets of modes produces on the surface of the reflector. This results in a set of linear equations with the unknowns containing the information on the amplitude and phase of each reflected wave's mode. When the unknown coefficients have been calculated, one can proceed and calculate the reflected field at the observation point by means of summation of field values of the reflected modes.

The third approach, typically used for the analysis of electrically very large reflectors, is the simplest of the three. In this approach, there is no system of equations whatsoever, resulting in the fastest possible analysis<sup>1</sup>. Instead, the incident wave is represented by means of *rays* or *beams* (in this sense a beam is a ray with an attached amplitude distribution, e.g. a simple Gaussian beam), and relations from classical geometry and optics are used to calculate the reflection of each ray or beam [1], [3]. This is naturally the least accurate method, and often has to be augmented by forced calculation of the diffraction effects (diffraction from edges, corners etc. [17]) in order to give satisfactory results.

Regarding wave propagation, the basic problem is to calculate the field at a given observation point if the field distribution is known at a previous point or set of points (e.g. a plane). To do this, essentially two approaches are possible, which are also often closely related to the chosen method for calculating reflection. One approach is to calculate the equivalent currents on a surface of choice, most often a plane, and sum up individual contributions from each

---

<sup>1</sup> The analysis is the fastest only when considering a single reflector. When considering multiple reflectors, the calculation of diffraction effects has a negative impact on the speed of the analysis, because an independent ray-tracing analysis has to be implemented in order to properly take into account higher-order diffraction effects (rays scattered by one reflector and then diffracted from another one).

equivalent source point. This in the limiting case leads to the same radiation integral as the one described in the context of propagation. In fact, the only difference between the two cases lies in the fact that in the latter case, the fields on the "source" surface are known, while in the former case, prior to determining the mere value of the integral, one also has to find the currents on the surface of the reflector.

The basic idea of the second approach to treating propagation is the expansion of the field in the source plane (physical or equivalent) into a series of wave objects or modes, for which it is possible to compute propagation analytically in a closed form. Each of these modes or general wave objects radiates a field with a certain more complex radiation pattern. The field at the observation point is obtained by summing up contributions of all the modes, thus avoiding the lengthy integration of the radiation integral. Notice that there is a significant difference between modes and wave objects. Modes refer to such mathematical objects that form a complete and orthogonal set and provide a general basis for expanding any function (in this case function = electric or magnetic field distribution), typically by means of Fourier-like expansions. Being orthogonal, it is clear that each mode itself has a different radiation pattern. Wave objects, on the other hand, are more general and do not necessarily have to satisfy the conditions of orthogonality and completeness, and the expansion need not be of the Fourier type. For example, in [11] the field at the reflector surface is represented by a summation of simple Gaussian beams, which all essentially produce the same field distribution. The expansion is achieved by pointing the Gaussian beams in different directions with different amplitudes and referent phases, which are determined by a least-squares matching procedure. Clearly, there is much more variety and freedom when looking at the problem from the more general wave-object perspective; however, an expansion procedure may be application-specific, meaning that the same algorithm may not work equally well for two different structures.

The following sections will briefly present the models used to treat propagation and reflection in reflector antenna systems, with regard to different approaches outlined here. The methods used later in this thesis will be explained in more detail, while for others only an overview will be given.

## 2.1. Propagation via Radiation Integral

The relationship between the electromagnetic fields and sources is governed by the Maxwell's equations. These, written in their most general form for time-harmonic fields, are [27]:

$$\nabla \times \vec{E} = -\vec{M} - j\omega\mu\vec{H}, \quad (2.1)$$

$$\nabla \times \vec{H} = \vec{J} + j\omega\varepsilon\vec{E}, \quad (2.2)$$

$$\nabla \cdot \vec{E} = \frac{q_e}{\varepsilon}, \quad (2.3)$$

$$\nabla \cdot \vec{H} = \frac{q_m}{\mu}, \quad (2.4)$$

where  $\vec{J}$  and  $\vec{M}$  denote the electric and magnetic current density, while  $q_e$  and  $q_m$  represent the electric and magnetic charge densities. The sources can be either real or equivalent, therefore both electric and magnetic sources are included in the relations, which helps enhance the symmetry and duality of the system and simplifies subsequent derivations.

The Maxwell's equations in their canonical form, as shown in the above expressions, are not always suitable for practical purposes due to each of the equations (2.1) and (2.2) containing both the electric and magnetic fields and only one kind of sources. In practice, one often wants to link only one of the two fields to all possible sources causing it, so as to be able to calculate the field when the sources are known. To achieve this, the curl of either (2.1) or (2.2) can be taken and inserted in the remaining of the two equations, yielding after some manipulations the following general relationships:

$$\nabla^2 \vec{E} + k^2 \vec{E} = \nabla \times \vec{M} + j\omega\mu\vec{J} + \frac{1}{\varepsilon} \nabla q_e; \quad (2.5)$$

$$\nabla^2 \vec{H} + k^2 \vec{H} = -\nabla \times \vec{J} + j\omega\varepsilon\vec{M} + \frac{1}{\mu} \nabla q_m. \quad (2.6)$$

However, now the relationship between the fields on the left-hand side of expressions (2.5) and (2.6), and the forcing function on the corresponding right-hand side involves curl and gradient operations, making the direct solution rather complicated. These difficulties can be circumvented by introducing the auxiliary vector potentials, which allows calculating the fields in a two-step procedure, whereby the auxiliary vector potentials are calculated first, and the fields are then obtained from the relationships linking the vector potentials to the fields. This standard procedure is widely documented in most all textbooks on electromagnetics [9],

[17], [27]. We define the magnetic vector potential  $\vec{A}$  and the electric vector potential  $\vec{F}$  in a region away from the sources as:

$$\vec{H}_A = \frac{1}{\mu} \nabla \times \vec{A}; \quad (2.7)$$

$$\vec{E}_F = -\frac{1}{\varepsilon} \nabla \times \vec{F}, \quad (2.8)$$

where the subscripts  $A$  and  $F$  indicate that the field is due to the auxiliary vector magnetic or auxiliary vector electric potential, respectively. Inserting (2.7) and (2.8) into (2.1) and (2.2), applying a few vector analysis identities and imposing the so-called Lorentz gauge, the corresponding electric or magnetic field due to the same potentials  $A$  and  $F$  can be found as

$$\vec{E}_A = \frac{1}{j\omega\varepsilon} \nabla \times \vec{H}_A = -j\omega\vec{A} - j\frac{1}{\omega\mu\varepsilon} \nabla(\nabla \cdot \vec{A}); \quad (2.9)$$

$$\vec{H}_F = -\frac{1}{j\omega\mu} \nabla \times \vec{E}_F = -j\omega\vec{F} - j\frac{1}{\omega\mu\varepsilon} \nabla(\nabla \cdot \vec{F}). \quad (2.10)$$

Skipping all intermediate steps, thoroughly elaborated in electromagnetics textbooks, one eventually obtains these relations for calculating the vector potentials from source currents:

$$\nabla^2 \vec{A} + k^2 \vec{A} = -\mu \vec{J}; \quad (2.11)$$

$$\nabla^2 \vec{F} + k^2 \vec{F} = -\varepsilon \vec{M}. \quad (2.12)$$

The advantage of the two above expressions over (2.5) and (2.6) is their simpler form, allowing direct separation of the vector equation into separate scalar wave equations in rectangular coordinates. For example, for the magnetic vector potential we have

$$\begin{aligned} \nabla^2 A_x + k^2 A_x &= -\mu J_x, \\ \nabla^2 A_y + k^2 A_y &= -\mu J_y, \\ \nabla^2 A_z + k^2 A_z &= -\mu J_z. \end{aligned} \quad (2.13)$$

Once the scalar wave equation has been obtained, it can be solved by the Green's functions approach. First, a solution is sought for the Dirac delta-function excitation (i.e. for a point source), and then the solution for any general excitation can be found through a convolution<sup>1</sup> of the Green's function and the actual excitation function [10], [31], [32].

---

<sup>1</sup> Strictly speaking, the representation employing the convolution is valid only in homogeneous space.



For radiation problems in homogeneous space, it is the most convenient to express the functions in terms of spherical coordinates. Assuming the point source located at the origin of the coordinate system, we have

$$\nabla^2 g + k^2 g = -\delta(\vec{r}), \quad (2.14)$$

where  $g$  denotes the Green's function for the differential operator  $D(\cdot) = (\nabla^2 + k^2)(\cdot)$ , and the argument  $\vec{r}$  has been explicitly written in the Delta function to emphasize that the point source is located at the coordinate system origin. The equation has two solutions, an outgoing and an incoming spherical wave, respectively:

$$g_1(r, \theta, \phi) = \frac{e^{-jkr}}{4\pi r}, \quad (2.15)$$

$$g_2(r, \theta, \phi) = \frac{e^{jkr}}{4\pi r}. \quad (2.16)$$

Clearly, only the wave represented by (2.15) is of interest for radiation problems. Taking that solution, we compose the convolution integral between the Green's function and the actual current  $J_i$ , where  $i \in \{x, y, z\}$ , to obtain the solution for the vector potential due to a general point source excitation. Finally, the contributions from all source points confined within volume  $V$  are superimposed to obtain the final expression:

$$A_i(\vec{r}) = (g * (\mu J_i))(\vec{r}) = \frac{\mu}{4\pi} \iiint_V J_i(\vec{r}') \frac{e^{-jk|\vec{r}-\vec{r}'|}}{|\vec{r}-\vec{r}'|} dV', \quad (2.17)$$

and similarly for the vector electric potential  $F$ ,

$$F_i(\vec{r}) = \frac{\varepsilon}{4\pi} \iiint_V M_i(\vec{r}') \frac{e^{-jk|\vec{r}-\vec{r}'|}}{|\vec{r}-\vec{r}'|} dV'. \quad (2.18)$$

In (2.17) and (2.18), the primed coordinates refer to the coordinates of the source point, while regular coordinates refer to the observation point. The distance between the observation point and the source point can be simply calculated as

$$R = |\vec{r} - \vec{r}'| = \sqrt{(x - x')^2 + (y - y')^2 + (z - z')^2}. \quad (2.19)$$

Expressions (2.17) and (2.18) represent the scalar form of the radiation integral, suitable for calculating the scalar components of the auxiliary vector potentials. In order to reach expressions which allow the computing of vector electric and magnetic fields, one has to

revert to Eqs. (2.7)-(2.10). Generally, both electric and magnetic currents can exist, therefore the fields are found by summing up (2.8) and (2.9), and (2.7) and (2.10), respectively:

$$\vec{E} = \vec{E}_A + \vec{E}_F = -j\omega\vec{A} - j\frac{1}{\omega\mu\epsilon}\nabla(\nabla\cdot\vec{A}) - \frac{1}{\epsilon}\nabla\times\vec{F}; \quad (2.20)$$

$$\vec{H} = \vec{H}_F + \vec{H}_A = -j\omega\vec{F} - j\frac{1}{\omega\mu\epsilon}\nabla(\nabla\cdot\vec{F}) + \frac{1}{\mu}\nabla\times\vec{A}. \quad (2.21)$$

Plugging the expressions (2.17) and (2.18) for calculating the vector potentials into (2.20) and (2.21), one obtains:

$$\begin{aligned} \vec{E} = & \frac{\mu}{4\pi} \iiint_V \left( -j\omega - j\frac{1}{\omega\mu\epsilon}\nabla\nabla \right) \left( \vec{J}(\vec{r}') \frac{e^{-jkR}}{R} \right) dV' + \\ & \frac{\epsilon}{4\pi} \iiint_V -\frac{1}{\epsilon}\nabla\times\left( \vec{M}(\vec{r}') \frac{e^{-jkR}}{R} \right) dV' \end{aligned} \quad (2.22)$$

$$\begin{aligned} \vec{H} = & \frac{\epsilon}{4\pi} \iiint_V \left( -j\omega - j\frac{1}{\omega\mu\epsilon}\nabla\nabla \right) \left( \vec{M}(\vec{r}') \frac{e^{-jkR}}{R} \right) dV' + \\ & \frac{\mu}{4\pi} \iiint_V \frac{1}{\mu}\nabla\times\left( \vec{J}(\vec{r}') \frac{e^{-jkR}}{R} \right) dV' \end{aligned} \quad (2.23)$$

Note that here all three components of the electric and magnetic currents have been taken into account ( $\vec{J}(\vec{r}')$  is used instead of  $J_i(\vec{r}')$ ).

To reach the explicit form of the radiation integral, we need to perform analytical differentiation as dictated by the vector differential operators above. Since the operators differentiate the product of a scalar and a vector function, we will make use of the following auxiliary identities:

$$\nabla\cdot(f\vec{g}) = (\nabla f)\cdot\vec{g} + f(\nabla\cdot\vec{g}), \quad (2.24)$$

$$\nabla\times(f\vec{g}) = \vec{g}\times(\nabla f) + f(\nabla\times\vec{g}). \quad (2.25)$$

Bearing in mind that the curl, divergence and gradient in (2.22) and (2.23) all operate in observation coordinates, whereas the currents  $\vec{J}$  and  $\vec{M}$  are defined in source coordinates, applying (2.24) and (2.25) to the functions as given above gives:

$$\nabla\times\left( \vec{J}(\vec{r}') \frac{e^{-jkR}}{R} \right) = \left( \vec{J}(\vec{r}') \times \hat{R} \right) \left( \frac{1 + jkR}{R^2} \right) e^{-jkR}$$

$$\begin{aligned}\nabla \cdot \left( \vec{J}(\vec{r}') \frac{e^{-jkR}}{R} \right) &= \vec{J}(\vec{r}') \cdot \left( \nabla \frac{e^{-jkR}}{R} \right) = -(\vec{J}(\vec{r}') \cdot \hat{R}) \left( \frac{1 + jkR}{R^2} \right) e^{-jkR} \\ \nabla \left( \nabla \cdot \left( \vec{J}(\vec{r}') \frac{e^{-jkR}}{R} \right) \right) &= \left( \frac{jk}{R^2} + \frac{1}{R^3} \right) e^{-jkR} \vec{J}(\vec{r}') + \left( \frac{k^2}{R} - \frac{3jk}{R^2} - \frac{3}{R^3} \right) e^{-jkR} (\vec{J}(\vec{r}') \cdot \hat{R}) \hat{R}.\end{aligned}$$

The last of the three above formulas was obtained using the auxiliary relationship [36]

$$\nabla (\vec{J}(\vec{r}') \cdot \hat{R}) = \frac{1}{R} (\vec{J}(\vec{r}') - (\vec{J}(\vec{r}') \cdot \hat{R}) \hat{R}).$$

Plugging the expressions just derived back into (2.22) and (2.23), upon regrouping the terms and making use of the relationships  $k = \omega\sqrt{\mu\varepsilon}$  and  $\eta = \sqrt{\mu/\varepsilon}$ , we finally arrive at the general vector form of the radiation integral as given in [34]:

$$\begin{aligned}\vec{E}(\vec{r}) &= \frac{\eta}{4\pi} \iiint_V \left[ \vec{J}(\vec{r}') \left( -\frac{j}{kR} - \frac{1}{(kR)^2} + \frac{j}{(kR)^3} \right) \right. \\ &\quad \left. + (\vec{J}(\vec{r}') \cdot \hat{R}) \hat{R} \left( \frac{j}{kR} + \frac{3}{(kR)^2} - \frac{3j}{(kR)^3} \right) \right] k^2 e^{-jkR} dV' \quad (2.26) \\ &\quad - \frac{1}{4\pi} \iiint_V (\vec{M}(\vec{r}') \times \hat{R}) \left( \frac{1 + jkR}{(kR)^2} \right) k^2 e^{-jkR} dV',\end{aligned}$$

$$\begin{aligned}\vec{H}(\vec{r}) &= \frac{1}{4\pi} \iiint_V (\vec{J}(\vec{r}') \times \hat{R}) \left( \frac{1 + jkR}{(kR)^2} \right) k^2 e^{-jkR} dV' \\ &\quad - \frac{1}{4\pi\eta} \iiint_V \left[ \vec{M}(\vec{r}') \left( -\frac{j}{kR} - \frac{1}{(kR)^2} + \frac{j}{(kR)^3} \right) \right. \\ &\quad \left. + (\vec{M}(\vec{r}') \cdot \hat{R}) \hat{R} \left( \frac{j}{kR} + \frac{3}{(kR)^2} - \frac{3j}{(kR)^3} \right) \right] k^2 e^{-jkR} dV'. \quad (2.27)\end{aligned}$$

In (2.26) and (2.27) one can notice terms with  $1/kr$ ,  $1/(kr)^2$  and  $1/(kr)^3$  dependence. The second and the third one attenuate much faster than the first one with distance  $R$ , and can after a certain distance be neglected, which yields somewhat simpler expressions

$$\begin{aligned}\vec{E}(\vec{r}) &= \frac{\eta}{4\pi} \iiint_V \left[ -\vec{J}(\vec{r}') + (\vec{J}(\vec{r}') \cdot \hat{R}) \hat{R} \right] \left( \frac{jk}{R} \right) e^{-jkR} dV' \\ &\quad - \frac{1}{4\pi} \iiint_V (\vec{M}(\vec{r}') \times \hat{R}) \left( \frac{jk}{R} \right) e^{-jkR} dV', \quad (2.28)\end{aligned}$$

$$\begin{aligned}\vec{H}(\vec{r}) &= \frac{1}{4\pi} \iiint_V (\vec{J}(\vec{r}') \times \hat{R}) \left( \frac{jk}{R} \right) e^{-jkR} dV' \\ &\quad - \frac{1}{4\pi\eta} \iiint_V \left[ -\vec{M}(\vec{r}') + (\vec{M}(\vec{r}') \cdot \hat{R}) \hat{R} \right] \left( \frac{jk}{R} \right) e^{-jkR} dV'. \quad (2.29)\end{aligned}$$

If, however, the true far-field radiation pattern is desired, it can be obtained from (2.26) and (2.27) by calculating the far-field limit as [34]

$$\vec{E}_{far} = \lim_{r \rightarrow \infty} \left( kr e^{jkr} \vec{E}(\vec{r}) \right), \quad (2.30)$$

$$\vec{H}_{far} = \lim_{r \rightarrow \infty} \left( kr e^{jkr} \vec{H}(\vec{r}) \right). \quad (2.31)$$

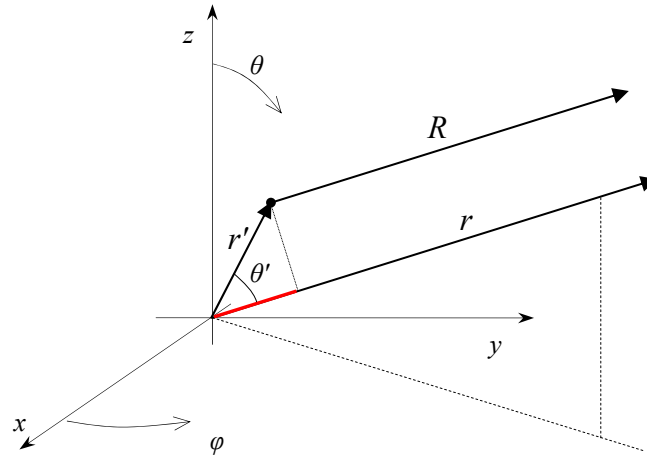


Figure 2.2. Geometry for the far-field approximation

It is obvious that in (2.26) and (2.27) only the terms with  $kr$  factor in the denominator will remain. Applying the approximation for the distance from the source point to the observation point (see Fig. 2.2.) when the observation point is far away,

$$R = r - r' \cos \theta' = r - r' (\hat{r}' \cdot \hat{r}) = r - \vec{r}' \cdot \hat{r}, \quad (2.32)$$

the far-field limit of the radiation integrals can be written as:

$$\begin{aligned} \vec{E}_{far}(\theta, \phi) = & -j \frac{\eta}{4\pi} \iiint_V \left( \vec{J}(\vec{r}') - (\vec{J}(\vec{r}') \cdot \hat{r}) \hat{r} \right) e^{jk(\vec{r}' \cdot \hat{r})} k^2 dV' \\ & + \frac{j}{4\pi} \iiint_V \left( \hat{r} \times \vec{M}(\vec{r}') \right) e^{jk(\vec{r}' \cdot \hat{r})} k^2 dV', \end{aligned} \quad (2.33)$$

$$\begin{aligned} \vec{H}_{far}(\theta, \phi) = & -\frac{j}{4\pi} \iiint_V \left( \hat{r} \times \vec{J}(\vec{r}') \right) e^{jk(\vec{r}' \cdot \hat{r})} k^2 dV' \\ & - \frac{j}{4\pi\eta} \iiint_V \left( \vec{M}(\vec{r}') - (\vec{M}(\vec{r}') \cdot \hat{r}) \hat{r} \right) e^{jk(\vec{r}' \cdot \hat{r})} k^2 dV'. \end{aligned} \quad (2.34)$$

The unit vector  $\hat{R}$  has been replaced by the unit vector  $\hat{r}$  because in the far-field limit they both point in the same direction. Also, the  $r$ -dependence of the radiated field has been

annihilated by the limit operation. The far-field radiation pattern is therefore only a function of angular coordinates  $(\theta, \phi)$ .

In the analysis of reflector antenna problems, the sources of radiation are the metallic surfaces of the reflectors. In that case, the triple integrals of Eqs. (2.26), (2.27), (2.33) and (2.34) reduce to double integrals over the surface of the reflector. That form of the radiation integral is the basis and the starting point of the Physical Optics analysis, which is one of the two principal building blocks of the analysis method presented in this thesis. Physical Optics is explained in more detail in Sec. 2.3.1.2, while additional comments on the adaptation of the radiation integral to the analysed geometrical structures are given in Sec. 4.2.

### 2.1.1. Radiation Integral in Spectral Domain

Eqs. (2.17) and (2.18), as well as (2.26) and (2.27), all represent the radiation integral in spatial domain because the Green's function and also the currents are expressed in spatial coordinates. There are, however, alternative ways of solving the differential equation (2.14) which lead to alternative formulations of the Green's function and consequently to alternative representations of the radiation integral, such as the so-called spectral-domain representation. The mathematical background comes from the theory of the Sturm-Liouville differential operator and various techniques for solving the Sturm-Liouville problems (SLP), presented in detail in [10], [24], [44].

For example, the scalar wave equation

$$\frac{\partial^2 v(x)}{\partial x^2} + k^2 v(x) = -f(x) \quad (2.35)$$

can be viewed as a special case of the more general Sturm-Liouville problem

$$-\frac{1}{w(x)} \frac{d}{dx} \left[ p(x) \frac{du(x)}{dx} \right] + q(x)u(x) - \lambda u(x) = f(x) \quad (2.36)$$

where functions  $p(x)$ ,  $q(x)$  and  $w(x)$  can be identified simply as<sup>2</sup>

$$p(x) = 1; \quad q(x) = 0; \quad w(x) = 1; \quad \lambda = k^2. \quad (2.37)$$

---

<sup>2</sup> This choice of functions  $p(x)$ ,  $q(x)$ ,  $w(x)$  and  $\lambda$  is pertinent to the rectangular coordinate system. In other coordinate systems, the wave equation has a different form, and  $p(x)$ ,  $q(x)$ ,  $w(x)$  and  $\lambda$  have different values.

This can be written more compactly as

$$L_\lambda u = (L - \lambda)u = f, \quad (2.38)$$

where  $L$  is the Sturm-Liouville operator

$$L = -\frac{1}{w(x)} \frac{d}{dx} \left[ p(x) \frac{d}{dx} \right] + q(x). \quad (2.39)$$

Depending on the boundary conditions (bounded or unbounded domain) and the character of parameter  $\lambda$  and function  $f$  (real or complex), there are three kinds of the Sturm-Liouville problem. If the domain is bounded, then the problem is of the first or of the second kind. This relates to the analysis of electromagnetic phenomena in closed spaces, such as resonators, cavities and others. Differential equations describing radiation phenomena into unbounded space fall into the group of Sturm-Liouville problems of the third kind (SLP3), also called singular Sturm-Liouville problems [10].

One of the techniques for solving SLP problems is via eigenfunctions and eigenvalues, leading to the representation of the Green's function in terms of its "natural" modes, which can be shown to form an orthogonal basis in the domain of the operator  $L$  [24]. Such a formulation is thus closely related to the Fourier series expansion and Fourier integral. The complete and mathematically precise description of the solution of the Sturm-Liouville problem via this approach is beyond the scope of this introductory text, therefore in this section only the key steps will be illustrated. The solution is first developed for bounded domains and then extended to domains extending to infinity by a limit operation.

A complex number  $\mu$  is called an *eigenvalue* of the linear operator  $L$  if there exists a nonzero vector (or function)  $v$  in the domain of  $L$  such that

$$Lv = \mu v. \quad (2.40)$$

Vector  $v$  for which the equality holds is called the *eigenvector* (or eigenfunction) of the operator  $L$ . Since the eigenfunctions form a complete set and are orthogonal, any function  $u$  in the domain of the operator<sup>3</sup> can be represented as a sum of eigenfunctions  $v_n$

---

<sup>3</sup> Orthogonal eigenvectors can be found in the most general case for the class of operators called normal operators [8].

$$u = \sum_{n=1}^{\infty} \alpha_n v_n . \quad (2.41)$$

The coefficients  $\alpha_n$  are obtained via the inner product

$$\alpha_n = \langle u, v_n \rangle = \int_a^b u(x) \overline{v_n(x)} dx , \quad (2.42)$$

where the overline denotes the complex conjugate<sup>4</sup>. As already stated, the domain  $[a, b]$  may extend to infinity, in which case the differential equation (2.38) represents an SLP3.

Looking at the Sturm-Liouville problem from (2.38) again

$$(L - \lambda)u = f ,$$

an associated *eigenproblem* can be formed as a homogeneous differential equation

$$(L - \lambda_n)v_n = 0 , \quad (2.43)$$

subject to the same boundary conditions that apply to (2.38) in a given case. The theory goes on to show that the coefficients  $\alpha_n$  can be obtained from the forcing function  $f$  as

$$\alpha_n = \frac{\langle f, v_n \rangle}{\lambda - \lambda_n} , \quad (2.44)$$

which means that the function  $u$  due to the forcing function  $f$  can be expanded as

$$u = \sum_{k=1}^{\infty} \alpha_k v_k = \sum_{k=1}^{\infty} \frac{\langle f, v_k \rangle}{\lambda - \lambda_k} v_k . \quad (2.45)$$

Function  $u$ , apart from being a function of variable  $x$ , is also a function of the variable  $\lambda$ , which was a parameter in the starting differential equation. Since all functions in the domain of the operator  $L$  are well-behaved<sup>5</sup>,  $\langle f, v_n \rangle v_n$  is finite everywhere, and  $u(x, \lambda)$  only has simple poles for  $\lambda = \lambda_n$ . Therefore, by the Residue Theorem one can obtain

$$\oint_{C_R} u(x, \lambda') d\lambda' = \sum_{k=1}^{\infty} \langle f, v_k \rangle v_k \oint_{C_R} \frac{d\lambda'}{\lambda_k - \lambda'} = -2\pi j \sum_{k=1}^{\infty} \langle f, v_k \rangle v_k = -2\pi j f(x) , \quad (2.46)$$

---

<sup>4</sup> Eq. (2.42) is only one possible form of the inner product, chosen here because it is often used in the analysis of electromagnetic problems.

<sup>5</sup> The Sturm-Liouville operator is defined on a Hilbert space  $\mathcal{L}^2$ , which is, in loose terms, the set of all square-integrable piecewise-continuous functions.

where  $C_R$  is a closed circle of radius  $R$  extending to infinity, so as to enclose all the poles, as shown in Fig. 2.3.a. Eq. (2.46) can be written shortly as

$$f(x) = -\frac{1}{2\pi j} \oint_{C_R} u(x, \lambda') d\lambda'. \quad (2.47)$$

The above relation is true for any forcing function  $f$ , therefore for the Delta-function excitation we have

$$\delta(x) = -\frac{1}{2\pi j} \oint_{C_R} g(x, \lambda') d\lambda'. \quad (2.48)$$

This expression defines the *spectral representation of the delta function* and is valid both for bounded and unbounded domains. The case of the unbounded domain is treated as the limiting case of the bounded domain when the domain limits extend to infinity. In that case, the poles  $\lambda_n$  come closer together and eventually form a continuous line on the real axis, therefore a modified integration path is considered to obtain the solution.

The presented theory allows us to develop the spectral representation of the Delta function for the scalar wave equation with radiating boundary conditions, which is a special case of SLP3:

$$\frac{\partial^2 g(x)}{\partial x^2} + k^2 g(x) = -\delta(x). \quad (2.49)$$

Again, we identify the parameter  $\lambda = k^2$ . In rectangular coordinates, the space-domain Green's function for the problem at hand is given by [10]

$$g(x) = \frac{e^{-jk|x|}}{2jk} = \frac{e^{-j\sqrt{\lambda}|x|}}{2j\sqrt{\lambda}}. \quad (2.50)$$

Inserting into (2.48), we have

$$-2\pi j \delta(x) = \oint_{C_R} g(x, \lambda') d\lambda'. \quad (2.51)$$



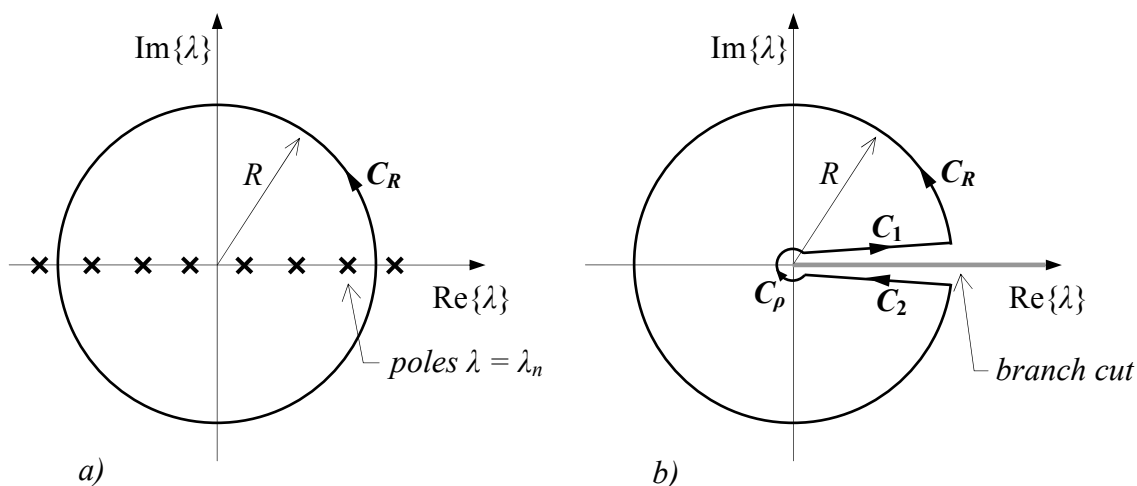


Figure 2.3. Integration path for obtaining the spectral representation of the Green's function for different kinds of Sturm-Liouville problems. a) SLP1 and SLP2 (bounded domain); b) SLP3 (unbounded domain)

Performing the integration on the modified path, shown in Fig. 2.3.b, which takes into account the branch cut and the singularities lying on the positive  $x$  axis, we have

$$0 = \oint g(x, \lambda') d\lambda' = \int_{C_R} + \int_{C_1} + \int_{C_2} + \int_{C_\rho} . \quad (2.52)$$

The contribution of the  $C_\rho$  segment is also zero, and so, upon applying the limit,

$$-2\pi j \delta(x) = \oint_{C_R} g(x, \lambda') d\lambda' = - \int_{C_1} \frac{e^{-j\sqrt{\lambda'}x}}{2j\sqrt{\lambda'}} d\lambda' - \int_{C_2} \frac{e^{-j\sqrt{\lambda'}x}}{2j\sqrt{\lambda'}} d\lambda' , \quad (2.53)$$

where the integration limits for  $C_1$  and  $C_2$  are  $(\infty, 0]$  and  $[0, \infty)$ , respectively. Resolving the sign change due to the branch cut and introducing the substitution  $\sqrt{\lambda'} = k_x$  ( $dk_x = \frac{d\lambda'}{2\sqrt{\lambda'}}$ ),

the integrals can be merged, giving

$$\delta(x) = \frac{1}{2\pi} \int_{-\infty}^{\infty} e^{-jk_x x} dk_x . \quad (2.54)$$

On can easily notice that (2.54) is none other than the inverse Fourier transform of the Dirac's Delta function, the usual interpretation of which is "the spectrum of the Delta function is a constant (unity)". In fact, from (2.54) one can establish the Fourier transform for any function, and thus also for the unknown function  $u$  from the differential equation, by noticing

$$\begin{aligned}
f(x) &= \int_{-\infty}^{\infty} f(\xi) \delta(x - \xi) d\xi = \int_{-\infty}^{\infty} f(\xi) \frac{1}{2\pi} \int_{-\infty}^{\infty} e^{-jk(x-\xi)} dk d\xi \\
&= \frac{1}{2\pi} \int_{-\infty}^{\infty} \left[ \int_{-\infty}^{\infty} f(\xi) e^{jk\xi} d\xi \right] e^{-jkx} dk = \frac{1}{2\pi} \int_{-\infty}^{\infty} F(k) e^{-jkx} dk.
\end{aligned} \tag{2.55}$$

Hence, we have established the Fourier transform pair for the function  $u$ :

$$u(x) = \frac{1}{2\pi} \int_{-\infty}^{\infty} U(k_x) e^{-jk_x x} dk_x, \tag{2.56}$$

$$U(k_x) = \int_{-\infty}^{\infty} u(x) e^{jk_x x} dx. \tag{2.57}$$

Variable  $k_x$  is used in the expressions in order to avoid confusion with the wavenumber  $k$  of the starting equation. The notation with the subscript will be practical later on, when the problem is extended to two and three dimensions, whereby the subscript will indicate along which coordinate the Fourier transform is performed.

Noticing that the integral in (2.56) has the form of the inner product defined in (2.42), one can see that (2.56) is equivalent to the eigenfunction expansion of (2.41), whereby  $e^{-jk_x x}$  plays the role of the eigenfunction  $v_n$  and  $U(k_x)$  plays the role of the coefficient  $\alpha_n$ . This is further justified by inspecting what happens if the operator  $\frac{\partial^2}{\partial x^2}$  is applied to the exponential  $e^{-jk_x x}$ :

$$\frac{\partial^2}{\partial x^2} (e^{-jk_x x}) = -k_x^2 e^{-jk_x x}. \tag{2.58}$$

The operator applied to the function  $e^{jk_x x}$  returns the same function multiplied by a constant, which confirms the eigenfunction-like behaviour<sup>6</sup> of  $e^{jk_x x}$ . All of this serves to find the solution to the initial problem, because one now knows what the result of applying the Fourier transform to the differential equation  $(L - k^2)u = f$  will be. Upon transformation, we have

$$\mathcal{F}(L(u)) + k^2 U(k_x) = F(k_x) \Leftrightarrow -k_x^2 U(k_x) + k^2 U(k_x) = F(k_x), \tag{2.59}$$

which can be rewritten as

---

<sup>6</sup>  $e^{-jk_x x}$  is also referred to as the "improper eigenfunction". It is improper because it does not actually belong to the Hilbert space  $\mathcal{L}^2$  (it is not square-integrable).

$$U(k) = \frac{F(k)}{k^2 - k_x^2}. \quad (2.60)$$

Applying the inverse Fourier transform to (2.60) gives finally the solution for the unknown function  $u(x)$  (in our case the electric or magnetic field) due to the forcing function  $f(x)$  (in our case the electric or magnetic currents), starting from its spectral representation:

$$u(x) = \frac{1}{2\pi} \int_{-\infty}^{\infty} \frac{F(k_x)}{k^2 - k_x^2} e^{-jk_x x} dk_x. \quad (2.61)$$

Fast-forwarding to the case of interest for this thesis, namely the spectral-domain representation of the radiation integral in three-dimensional space, we recall the wave equation for the auxiliary vector potentials, given in (2.13)

$$\left( \frac{\partial^2}{\partial x^2} + \frac{\partial^2}{\partial y^2} + \frac{\partial^2}{\partial z^2} + k^2 \right) A(x, y, z) = -\mu J(x, y, z). \quad (2.62)$$

From the theory exposed above, we know that if  $A(x, y, z)$  is represented in terms of eigenfunctions, its Fourier transform will yield

$$(-k_x^2 - k_y^2 - k_z^2 + k^2) \tilde{A}(k_x, k_y, k_z) = -\mu \tilde{J}(k_x, k_y, k_z). \quad (2.63)$$

To solve it, first the spectral representation of the corresponding Green's function has to be found. Replacing the source  $-\mu J(x, y, z)$  by the Delta function located at the coordinate system origin, and applying again the Fourier transform, we have

$$(-k_x^2 - k_y^2 - k_z^2 + k^2) \tilde{G}(k_x, k_y, k_z) = -1. \quad (2.64)$$

or

$$\tilde{G}(k_x, k_y, k_z) = -\frac{1}{k^2 - k_x^2 - k_y^2 - k_z^2}. \quad (2.65)$$

Its spatial representation is then obtained through inverse Fourier transform, viz.

$$g(x, y, z) = -\frac{1}{(2\pi)^3} \int_{-\infty}^{\infty} \int_{-\infty}^{\infty} \int_{-\infty}^{\infty} \frac{1}{k^2 - k_x^2 - k_y^2 - k_z^2} e^{-jk_x x} e^{-jk_y y} e^{-jk_z z} dk_x dk_y dk_z \quad (2.66)$$

It is interesting to note that (2.63) can be rewritten as:

$$\tilde{A}(k_x, k_y, k_z) = \mu \tilde{J}(k_x, k_y, k_z) \frac{-1}{k^2 - k_x^2 - k_y^2 - k_z^2} = \mathcal{F}[\mu J(x, y, z)] \cdot \mathcal{F}[g(x, y, z)]. \quad (2.67)$$

This way one can see that the spectral domain representation of the unknown potential  $A$  due to the excitation  $-\mu J$  consists of a product of the spectral representation of the excitation and the spectral representation of the Green's function for the considered case. This is consistent with the well-known property of the Fourier transform, which says that a convolution in spatial domain is transformed into a product in spectral domain. This result is in fact the same as the one in (2.60), only extended to three-dimensional space. Therefore, as in (2.61) we can obtain the final solution by applying the inverse Fourier transform:

$$\begin{aligned} A(x, y, z) &= \int_{-\infty}^{\infty} \int_{-\infty}^{\infty} \int_{-\infty}^{\infty} \tilde{A}(k_x, k_y, k_z) e^{-jk_x x} e^{-jk_y y} e^{-jk_z z} dk_x dk_y dk_z \\ &= -\frac{1}{(2\pi)^3} \int_{-\infty}^{\infty} \int_{-\infty}^{\infty} \int_{-\infty}^{\infty} \mu \tilde{J}(k_x, k_y, k_z) \frac{e^{-jk_x x} e^{-jk_y y} e^{-jk_z z}}{k^2 - k_x^2 - k_y^2 - k_z^2} dk_x dk_y dk_z \end{aligned} \quad (2.68)$$

Eq. (2.68) is one form of the spectral-domain radiation integral. There is a number of other forms, which all have practical value. The various forms depend on the given boundary conditions and on the choice of the referent coordinate system (i.e. cylindrical, spherical).

When working in three dimensions, there is also the possibility of applying the Fourier transform not to the equation as a whole, but only to two of the three coordinates. This is practical when analysing aperture radiation, since apertures are often planar, and in one of the three dimensions the excitation is actually a delta function, i.e. a point source, whose radiation is given by the spatial domain Green's function. The combined spatial-spectral formulation is developed again starting from the wave equation with Delta function excitation:

$$\left( \frac{\partial^2}{\partial x^2} + \frac{\partial^2}{\partial y^2} + \frac{\partial^2}{\partial z^2} + k^2 \right) g(x, y, z) = -\delta(x)\delta(y)\delta(z). \quad (2.69)$$

The Fourier transform is applied to  $x$  and  $y$  coordinates:

$$\left( \frac{\partial^2}{\partial z^2} + k^2 - k_x^2 - k_y^2 \right) \tilde{G}(k_x, k_y, z) = -1 \cdot \delta(z) = \delta(z). \quad (2.70)$$

The Green's function is now partially in spectral domain and partially in spatial domain, and will next be solved for its spatial-domain component  $z$ . In fact, substituting

$$k_z^2 = k^2 - k_x^2 - k_y^2. \quad (2.71)$$

we get

$$\left( \frac{\partial^2}{\partial z^2} + k_z^2 \right) \tilde{G}(k_x, k_y, z) = \delta(z). \quad (2.72)$$

which is the same equation as (2.49). Therefore, the solution can be copied from (2.50):

$$\tilde{G}(k_x, k_y, z) = \frac{e^{-jk_z|z|}}{2jk_z}. \quad (2.73)$$

To obtain the Green's function in all three spatial coordinates, as in (2.66) the inverse Fourier transform is applied, only this time only to  $k_x$  and  $k_y$  only:

$$g(x, y, z) = -\frac{1}{(2\pi)^2} \int_{-\infty}^{\infty} \int_{-\infty}^{\infty} \frac{e^{-jk_z|z|}}{2jk_z} e^{-jk_x x} e^{-jk_y y} dk_x dk_y. \quad (2.74)$$

In the next step, we consider the wave equation with an arbitrary *planar* source current lying in the plane  $z = 0$ :

$$\left( \frac{\partial^2}{\partial x^2} + \frac{\partial^2}{\partial y^2} + \frac{\partial^2}{\partial z^2} + k^2 \right) A(x, y, z) = -\mu J(x, y, 0). \quad (2.75)$$

By a development analogous to that in (2.62) – (2.67), we can show that the spatial representation of the vector potential is

$$\tilde{A}(k_x, k_y, z) = -\mu \tilde{J}(k_x, k_y, 0) \frac{e^{-jk_z|z|}}{2jk_z}, \quad (2.76)$$

giving finally, upon the inverse Fourier transform over  $k_x$  and  $k_y$ ,

$$A(x, y, z) = -\frac{\mu}{8j\pi^2} \int_{-\infty}^{\infty} \int_{-\infty}^{\infty} \tilde{J}(k_x, k_y, 0) \frac{e^{-jk_z|z|}}{k_z} e^{-jk_x x} e^{-jk_y y} dk_x dk_y, \quad (2.77)$$

Eq. (2.77) is the starting point for the development of the new propagation model based on complex conical wave objects, which is the main objective of this thesis. The detailed account of the new model is presented in Chapter 3.

### 2.1.2. Radiation Integral and Dyadic Green's Functions

Comparing the spatial-domain and the spectral-domain expressions for the scalar radiation integral in (2.17) and (2.77), one can remark a common form

$$F(x, y, z) = \int_D J(\mathbb{X}_D, \mathbb{Y}_D) \cdot g(\mathbb{X}_D, \mathbb{Y}_D | x, y, z) \cdot dD, \quad (2.78)$$

where  $D$  is the domain of integration, which can be either the finite physical surface of the aperture or the infinite spectral plane, and  $(\mathbb{X}_D, \mathbb{Y}_D)$  is the general "position" of the source,

expressed in the appropriate coordinates (e.g.  $(\mathbb{X}_D, \mathbb{Y}_D)$  can be  $(x, y)$ ,  $(\rho, \phi)$ ,  $(k_x, k_y)$ , etc.). Eq. (2.78) is none other than a statement of linearity, saying that the total output is a sum of individual incremental contributions. In the two cases elaborated so far, in the spatial domain we are summing up spherical waves launched from different points on the surface of the source, whereas in the spectral domain each individual contribution consists of a plane wave, launched from the same aperture plane and travelling in a different direction, determined by the pair of wavenumbers  $(k_x, k_y)$  (with  $k_z = \sqrt{k^2 - k_x^2 - k_y^2}$ ). Depending on the choice of coordinate system, other sums, e.g. of cylindrical or spherical waves, are also possible, however in all the cases  $J(\mathbb{X}_D, \mathbb{Y}_D)$  gives the strength of the incremental source, and  $g(\mathbb{X}_D, \mathbb{Y}_D | x, y, z)$  determines the output field produced by an incremental source of unit strength.

As explained in previous sections, the scalar integral establishes a link between source currents and auxiliary vector potentials, due to the simpler relationship between these quantities than between source currents and actual electric or magnetic fields (see (2.11) and (2.5)). The expression for calculating the fields starting from the source currents is given by a far more complex vector version of the radiation integral, as given in (2.26). It can be shown, however, that the vector radiation integral (2.26) can also be written in the same compact form as its scalar counterpart, because it still represents a linear superposition of incremental field contributions. Assuming only the presence of the electric current  $J$ , starting from (2.22) through a number of vector analysis manipulations [29] it is shown that:

$$\begin{aligned} \vec{E}(\vec{r}) &= -j\omega\mu \iiint_V \vec{J}(\vec{r}') \cdot \left[ \underline{\mathbf{I}} + \frac{\nabla' \nabla'}{k^2} \right] \left( \frac{e^{jk|\vec{r}-\vec{r}'|}}{4\pi|\vec{r}-\vec{r}'|} \right) d\vec{r}' \\ &= -j\omega\mu \iiint_V \vec{J}(\vec{r}') \cdot \underline{\mathbf{G}}(\vec{r} | \vec{r}') d\vec{r}' \end{aligned} \quad (2.79)$$

where  $\underline{\mathbf{I}}$  is a 3x3 identity matrix, and

$$\underline{\mathbf{G}}(\vec{r} | \vec{r}') = \left[ \underline{\mathbf{I}} + \frac{\nabla' \nabla'}{k^2} \right] (g(\vec{r} | \vec{r}')) \quad (2.80)$$

is also a 3x3 matrix, which describes the connection of each component of the source current to each component of the radiated field. Function  $\underline{\mathbf{G}}$  is called the *dyadic* (or tensor) Green's function.

## 2.2. Propagation via Expansion into Wave Objects

Whether in spatial or in spectral domain, the radiation integral is typically a double integral of rapidly oscillating functions (containing  $e^{jkx}$  terms), which becomes ever more numerically cumbersome as the electrical size of the object increases (i.e. when frequency and wavenumber  $k$  increase). In those cases, an alternative way of calculating the radiation is a necessity. The main idea is to replace the double integral representing the summation of elementary waves (plane waves, spherical waves, etc.) by a summation of fewer but more complex objects, which can still be evaluated in closed form, but produce more complicated radiation patterns that individually match better the (expected) radiated field distribution.

Generally speaking, a wave object can be defined as any mathematical function which exhibits wave-like behaviour, in that its amplitude and phase fronts can be identified. It is in a way a generalization of the notion of wave. A wave object may be a specific solution of the wave equation, an approximate solution of the wave equation, a solution of an approximation of the wave equation, or even none of the above [1]-[3], [6]-[12]. Classical planar, cylindrical and spherical waves can be seen as a subset of wave objects, being exact and simple solutions of the wave equation in different coordinate systems with real coordinates.

Clearly, not every mathematical object that arises from a solution of the wave equation, or its approximation, is useful. For a wave object to be useful, first of all an efficient, analytic way of calculating its propagation in a homogenous medium should exist. This is one of the three criteria by which Einziger *et al.* classify beam<sup>1</sup> expansions [13], the other two being a systematic methodology for computing the amplitude of each beam in the expansion, and the existence of clear-cut rules for truncating the beam series. This, however, deals only with the expansion aspect of beams. There is also a distinction regarding the quality of different wave objects themselves. For instance, an expansion employing beams whose individual region of validity is wider is more likely to give physically correct results in a wider region of space. Obviously, beams that satisfy the wave equation without restrictions are preferred from this point of view. Still, there are other qualities to consider in a beam, which may or may not decide its usefulness for a given application. These may be the availability of analytic solution

---

<sup>1</sup> Some authors insist that the term "beam" be used only for wave objects with significant directivity, i.e. focused in a small region of space. However, in this text the two terms will sometimes be used interchangeably.

for reflection and/or diffraction from common reflector shapes, the existence of closed-form expression in both spatial and spectral domains, or a specific kind and level of directivity (e.g. Gaussian tapered beams etc.).

In the following subsections an overview of most common mathematical objects employed to model electromagnetic wave propagation will be presented. The various objects are presented systematically, starting from the simplest ones and proceeding to the more complex and less commonly employed. The intent is to put the different solutions in the same perspective, rather than give a detailed account of each of them and make a definitive exhaustive list. More attention will be given to those wave objects that have been used in the development of the analysis method herein presented. For more details on the other objects, the reader is referred to the given references.

### 2.2.1. Plane, Cylindrical and Spherical Waves

The elementary wave functions come from the direct solution of the homogeneous wave equation:

$$\nabla^2 f + k^2 f = 0 \quad (2.81)$$

in rectangular, cylindrical and spherical coordinate systems, respectively. The solution is sought by the method of separation of variables [27], [44], whereby we assume that the dependence of  $f$  on each of the three coordinates is independent of the other two, viz.:

$$f(x_1, x_2, x_3) = f_1(x_1) \cdot f_2(x_2) \cdot f_3(x_3). \quad (2.82)$$

By using the appropriate definition of the Laplace operator in the chosen coordinate system, with some further manipulation, the desired separation can be achieved, which satisfies the given boundary conditions and thereby confirms the validity of the initial assumption. For example, in rectangular coordinates, one gets the following three independent single-variable differential equations:

$$\begin{aligned} \frac{\partial^2 f_1(x)}{\partial x^2} + k_x^2 f_1(x) &= 0, \\ \frac{\partial^2 f_2(y)}{\partial y^2} + k_y^2 f_2(y) &= 0, \\ \frac{\partial^2 f_3(z)}{\partial z^2} + k_z^2 f_3(z) &= 0, \end{aligned} \quad (2.83)$$



whereby  $k^2 = k_x^2 + k_y^2 + k_z^2$ . Each of these will give a solution of the same form, namely

$$\begin{aligned} f_1(x) &= C_1 e^{-jk_x x} + C_2 e^{jk_x x}, \\ f_2(y) &= C_3 e^{-jk_y y} + C_4 e^{jk_y y}, \\ f_3(z) &= C_5 e^{-jk_z z} + C_6 e^{jk_z z}, \end{aligned} \quad (2.84)$$

which is a linear combination of two plane waves, one travelling in the positive and the other in the negative direction ( $x$ ,  $y$  or  $z$ , respectively). The solution could also be given in terms of sine and cosine functions, in which case the solutions would represent standing waves. A general solution is obtained as a product of these three single-variable functions:

$$f(x, y, z) = C \cdot e^{-(\pm jk_x x \pm jk_y y \pm jk_z z)}, \quad (2.85)$$

where it is important to note that only two of the three  $k_i$  can be chosen independently, while the third is determined through the relationship  $k^2 = k_x^2 + k_y^2 + k_z^2$ . The function in (2.85) represents a plane wave because its equiphase surfaces lie in a plane

$$k_x x + k_y y + k_z z - (k_x x_0 + k_y y_0 + k_z z_0) = 0, \quad (2.86)$$

which is easily seen by inspecting the behaviour of the exponent in (2.85).

Similarly, by expanding the Laplacian operator in the cylindrical coordinate system

$$\nabla^2 f = \frac{\partial^2 f}{\partial \rho^2} + \frac{1}{\rho} \frac{\partial f}{\partial \rho} + \frac{1}{\rho^2} \frac{\partial^2 f}{\partial \phi^2} + \frac{\partial^2 f}{\partial z^2}, \quad (2.87)$$

the wave equation splits into three equations

$$\begin{aligned} \frac{d^2 f_1(\rho)}{d\rho^2} + \frac{1}{\rho} \frac{df_1(\rho)}{d\rho} + (k_\rho^2 - \frac{m^2}{\rho^2}) f_1(\rho) &= 0, \\ \frac{d^2 f_2(\phi)}{d\phi^2} + m^2 f_2(\phi) &= 0, \\ \frac{d^2 f_3(z)}{dz^2} + k_z^2 f_3(z) &= 0, \end{aligned} \quad (2.88)$$

and the general solution is a product of a Bessel (or Hankel) function coming from the first equation, a sine (cosine) function from the second equation, and an exponential function from the last equation:

$$f(\rho, \phi, z) = C \cdot \begin{bmatrix} J_m(k_\rho \rho) \\ H_m^{(2)}(k_\rho \rho) \end{bmatrix} \cdot \begin{bmatrix} \sin(m\phi) \\ \cos(m\phi) \end{bmatrix} \cdot e^{\pm jk_z z}. \quad (2.89)$$

Finally, the spherical wave functions are obtained by the same procedure, only in spherical coordinates, and the result consists of a product of a spherical Bessel (or Hankel) function, an associated Legendre function and a sine (or cosine) function:

$$f(r, \theta, \phi) = C \cdot \begin{bmatrix} j_m(kr) \\ h_m^{(2)}(kr) \end{bmatrix} \cdot \begin{bmatrix} P_n^m(\cos \theta) \\ Q_n^m(\cos \theta) \end{bmatrix} \cdot \begin{bmatrix} \sin(m\phi) \\ \cos(m\phi) \end{bmatrix}. \quad (2.90)$$

The choice between the Bessel and the Hankel function, or between two possible choices for the associated Legendre functions, depends on the expected wave behaviour expressed in the boundary conditions; e.g. if the wave shall be a forward or backward propagating wave, or a standing wave. The simple spherical wave  $e^{-jkr}/r$  is also contained in (2.90), with  $m = n = 0$ .

It is interesting to note that while in the plane wave case parameters  $k_x$ ,  $k_y$  and  $k_z$  are picked from a continuous set of values, in the cylindrical case the parameter  $m$  has to be integer, while in the spherical case both  $m$  and  $n$  are integer, i.e. picked from a set of discrete values. This is due to the fact that while in the rectangular coordinate system all three dimensions are infinite, in the cylindrical coordinate system the  $\phi$ -dimension is finite, while in the spherical coordinate system both  $\theta$  and  $\phi$ -dimensions are finite. The discrete set of values for the parameter  $m$  (and  $n$ ) means that the total field in that dimension is obtained via a summation, rather than an integral. This, together with the fact that these functions are orthogonal for different  $m$  and  $n$ , is the reason why the cylindrical and spherical wave functions are commonly referred to as the cylindrical and spherical harmonics.

### 2.2.2. Fields from Sources Located in Complex Space

Placing simple sources, such as a point source, a dipole, a Huygens source and so on, at a point in space with one or more complex coordinates, offers the possibility of modifying their radiation pattern and creating beams of varying directivity by changing the imaginary part of the complex coordinate. The so-called complex source points were introduced by Deschamps [6], and the brief overview presented in this section is based on the work of Felsen [7]. The complex Huygens source, used in this thesis as the excitation for the analysis of single-reflector and two-reflector systems, is presented separately.

The mathematical ground for considering complex source points is the analytical continuation of elementary wave functions of Sec. 2.2.1. into complex space. To illustrate the process, we repeat the wave equation when the forcing function is a point source located at the point  $\vec{r}' = (x', y', z')$ :

$$\nabla^2 f + k^2 f = -\delta(\vec{r} - \vec{r}'). \quad (2.91)$$

The solutions of this equation are the simple spherical waves of Eqs. (2.15) and (2.16). We consider only the outgoing spherical wave:

$$f(\vec{r} | \vec{r}') = \frac{e^{-jk|\vec{r}-\vec{r}'|}}{4\pi|\vec{r}-\vec{r}'|}. \quad (2.92)$$

Function  $f$  is a complex function of six real variables, namely the observation point coordinates  $(x, y, z)$  and the source point coordinates  $(x', y', z')$ . However, from the mathematical point of view, there is no reason why any of the three source point coordinates (i.e. vector  $\vec{r}'$ ) could not be generalised to a complex number, since the  $\nabla^2$  operator only acts on observation point coordinates. That said, it is interesting to observe what changes in the radiation pattern of the spherical wave when its source is moved into the complex plane. To simplify the derivations, without any loss of generality, the complex displacement can be attributed to one coordinate only, usually the  $z$ -coordinate. The source is placed at the point  $(0, 0, jb)$ . The complex distance from the source to the observation point is then

$$\bar{R} = |\vec{r} - \bar{\vec{r}}'| = \sqrt{x^2 + y^2 + (z - jb)^2}, \quad (2.93)$$

where the overline serves to emphasize the fact that the variable it refers to is a complex number. At large distances ( $z \gg b$ ), the distance can be approximated as

$$\bar{R} = R - \frac{jbz}{R}, \quad (2.94)$$

where  $R = \sqrt{x^2 + y^2 + z^2}$  is the distance from the observation point to the origin of the coordinate system, i.e. the real part of the source point coordinates. Substituting  $\rho^2 = x^2 + y^2$ , the ratio  $z/R$  in (2.94) can be expanded as

$$\frac{z}{R} = \sqrt{1 - \frac{\rho^2}{R^2}}. \quad (2.95)$$

Inserting the complex distance  $\bar{R}$  as written in (2.94) and (2.95) back into the solution given in (2.92), we see that the spherical wave now has an extra amplitude term associated with it:

$$f(\vec{r} | \vec{r}') = e^{-kb\sqrt{1-\rho^2/R^2}} \frac{e^{jkR}}{4\pi R}. \quad (2.96)$$

Note that the complex part of  $\bar{R}$  has been neglected in the denominator of the fraction, since its effect is insignificant compared to the effect of the introduction of complex parameter  $b$  in the exponential (still under the assumption  $z \gg b$ ).

If one observes the amplitude of  $f(\vec{r} | \vec{r}')$  at a fixed distance  $R$ , one can see that the newly introduced term varies with changing distance  $\rho$  from the real axis, and the extent of this amplitude modulation is governed by the magnitude of the parameter  $b$ . The radiation pattern of such a wave object is shown in Fig. 2.4. Instead of an omnidirectional radiation pattern of a simple (real) spherical wave, the radiation pattern shows that now the radiation is the strongest around the  $z$ -axis. Had the source been displaced in  $x$ -direction, the maximum would have been  $x$ -directed, and so on. Therefore it is clear that, while retaining the property that the wave object so obtained still satisfies the wave equation without restrictions, gain has been achieved in that there is now an extra parameter, namely the complex displacement  $b = (b_x, b_y, b_z)$ , which can be used to point the beam so obtained in a desired direction and also to increase or decrease the directivity of the source.

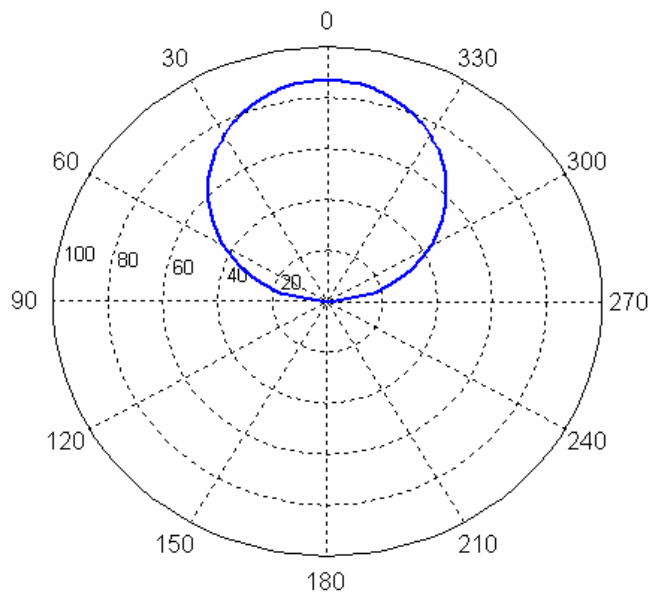


Figure 2.4. Radiation pattern of a complex source point in logarithmic scale. The source is placed at  $(0,0,jb)$ , with  $k = 100$ ,  $R = 1$  and  $b = -0.1$ .

The complex source point also serves to establish a natural link towards the Gaussian beams, which are extensively used in optics and quasi-optical antenna systems, and are explained in

the next section. Here it will be briefly demonstrated that the radiation pattern of a complex source point has a Gaussian taper in the region close to the axis of propagation (assuming naturally that the beam is propagating in the direction of its maximum). To this end, the complex distance  $\bar{R}$  can be approximated slightly differently. We assume not only that  $z \gg b$ , but also that  $\rho^2 \ll |z - jb|^2$ , where  $\rho^2 = x^2 + y^2$ . We then have

$$\bar{R} \approx z - jb + \frac{x^2 + y^2}{2(z - jb)} \approx z - jb + \frac{(z + jb)\rho^2}{2z^2}, \quad (2.97)$$

which substituted back into (2.92) gives

$$f(\vec{r} | \vec{r}') = \frac{e^{-kb}}{4\pi R} e^{-jkz} e^{kb\frac{\rho^2}{2z^2}} e^{-jkz\frac{\rho^2}{2z^2}}. \quad (2.98)$$

With the function factors written explicitly as above, one can read that the function represents a wave travelling in the  $z$ -direction ( $e^{-jkz}$ ), whose amplitude is still determined by the complex parameter  $b$  ( $e^{-kb}$ ), but more importantly, whose amplitude in the transverse direction  $\rho$  is given by the Gaussian function, namely  $e^{kb\frac{\rho^2}{2z^2}}$  (when  $b < 0$ ). Since the same amplitude taper exists in pure Gaussian beams, as will be shown in the next section, this serves as a sort of a validation of their application in the analysis of antenna systems, even if they are solutions of the wave equation, but rather of its paraxial approximation.

### 2.2.3. Gaussian Beams and Higher-order Gauss-Hermite Modes

The particular interest in Gaussian beams, their various derivatives and similar wave objects in the context of reflector antenna systems is motivated by the fact that the antennas commonly used as primary radiators in these systems, namely corrugated horn antennas, really radiate beams whose radiation pattern has an almost Gaussian shape [28], [34]. Corrugated horn antennas are analysed as other aperture antennas, meaning that their radiated field is calculated via the radiation integral, by integrating over the aperture delimited by the antenna walls. However, this integration can be quite slow, as has already been mentioned in Sec. 2.1. By using wave objects which already radiate a beam with a Gaussian profile, one can replace the double integral by one simple object readily calculated in closed form, thereby achieving a tremendous increase in speed. This does come at the expense of accuracy and physical correctness of the analysis, but can still be useful for the early stages of the design of a reflector antenna system, when it is rather the general information (beam width, direction of

propagation upon reflection), that is needed in order to decide on the placement and necessary shape of reflectors in the reflector chain. The fine-tuning of the system is then done at a later stage by a more accurate method, typically the Physical Optics.

Since the simple Gaussian beam was used in this thesis as an auxiliary means for obtaining the basic information on the parameters of the wave reflected from the reflector, in this section a detailed account of the simple Gaussian beam, its behaviour and key parameters will be given. The discussion essentially follows the cornerstone paper by Kogelnik and Li [20] and the remarkable review paper by Goldsmith [1]. Higher-order modes will be briefly introduced at the end of the section. For more information on that topic, see e.g. [20], [45].

The Gaussian beams arise as the solutions to the paraxial approximation of the wave equation

$$\frac{\partial^2 f}{\partial x^2} + \frac{\partial^2 f}{\partial y^2} + \frac{\partial^2 f}{\partial z^2} + k^2 f = 0. \quad (2.99)$$

Assuming that the solution will be a  $z$ -propagating wave, the sought function  $f$  can be written as a product

$$f(x, y, z) = e^{-jkz} g(x, y, z), \quad (2.100)$$

where function  $g$  carries the information on the amplitude and phase distribution of the wave object  $f$  and how they change as the wave propagates. Substituting this back into (2.99), upon cancelling the exponential factor one arrives at

$$\frac{\partial^2 g}{\partial x^2} + \frac{\partial^2 g}{\partial y^2} + \frac{\partial^2 g}{\partial z^2} - 2jk \frac{\partial g}{\partial z} = 0. \quad (2.101)$$

The key assumption in the development of Gaussian beams is that the function  $g$  varies so slowly with  $z$ -coordinate, so that its second derivative can be neglected, which implicitly means that the beam stays focused tight around the axis of propagation:

$$\left| \frac{\partial^2 g}{\partial z^2} \right| \ll 2k \left| \frac{\partial g}{\partial z} \right| \quad (2.102)$$

By imposing this *paraxial approximation*, the equation simplifies and reduces to the *parabolic* wave equation

$$\frac{\partial^2 g}{\partial x^2} + \frac{\partial^2 g}{\partial y^2} - 2jk \frac{\partial g}{\partial z} = 0. \quad (2.103)$$

The general solution of this equation in the rectangular coordinate system is a Gauss-Hermite polynomial (product of the Gaussian function and the Hermite polynomial), and in the cylindrical coordinate system a Gauss-Laguerre polynomial (product of the Gaussian function and the Laguerre polynomial). The basic, lowest-order mode is in both cases the simple Gaussian beam, whose amplitude distribution at the source plane  $z = 0$  has the functional dependence

$$\psi(\rho, 0) = e^{(-\rho^2/w_0^2)}. \quad (2.104)$$

where  $w_0^2$  is called the *beam waist*, and defines a circle around the  $z$  axis where the amplitude of the beam drops to  $1/e$ . The beam is rotationally symmetric, therefore it is described more simply using the transverse radius  $\rho$ . As shown in Fig. 2.5., the beam is the narrowest at the origin and expands as it propagates in  $+z$  direction. The phase front is planar at the plane of the beam waist and curved everywhere else, with the center of curvature of the beam behind the plane of the waist. The distance from the waist, where the beam curvature is minimal, is called the Rayleigh distance or the confocal distance  $z_c$  and is calculated a little bit later.

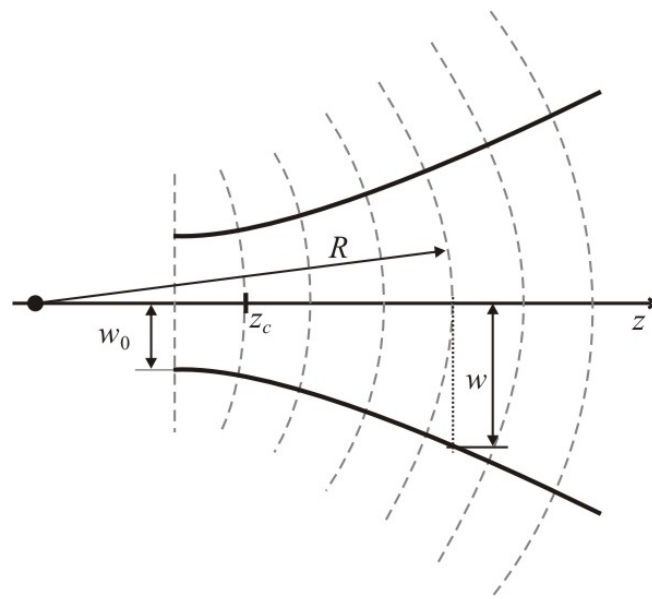


Figure 2.5. Illustration of propagation of a Gaussian beam: dashed lines represent the wave front, and the full lines mark the beam width.

The equation fully describing the propagation of the simple Gaussian beam is

$$f(\rho, z) = \sqrt{\frac{2}{\pi w^2}} e^{(-\rho^2/w^2 - jkz - j\pi\rho^2/\lambda R_c + j\phi_0)}. \quad (2.105)$$

The amplitude term  $\sqrt{2/\pi w^2}$  serves to normalize the beam to unit power. Looking at the four terms in the exponent, one can see that the first one describes the Gaussian distribution in the transverse direction, while the second one shows, as has been assumed, that the wave propagates in  $+z$  direction. The third can be interpreted as the phase difference between the phase at the wave front of the Gaussian beam and the wave front of a spherical wave emanating from the same source. Finally, the last one represents an additional jump in phase which occurs when the beam passes through the waist plane, and is of minor importance in the analysis of radiating structures (as opposed to e.g. resonators). The three parameters in (2.105), namely the beam width  $w$ , the radius of curvature  $R_c$  and the Guoy phase shift  $\phi_0$ , relate to the beam waist  $w_0$  via these simple relations:

$$w = w_0 \sqrt{1 + \left(\lambda z / \pi w_0^2\right)^2}, \quad (2.106)$$

$$R_c = z + \frac{\left(\pi w_0^2 / \lambda\right)^2}{z}, \quad (2.107)$$

$$\phi_0 = \text{arctg}\left(\lambda z / \pi w_0^2\right). \quad (2.108)$$

By introducing the confocal distance as

$$z_c = \pi w_0^2 / \lambda, \quad (2.109)$$

these relations become even simpler

$$w = w_0 \sqrt{1 + (z/z_c)^2}, \quad (2.110)$$

$$R_c = z + \frac{(z_c)^2}{z}, \quad (2.111)$$

$$\phi_0 = \text{arctg}(z/z_c). \quad (2.112)$$

These three quantities completely describe the Gaussian beam at any point in space, and they all depend only on two basic parameters, namely the beam waist and the confocal distance. So, if a real field, radiated by an antenna, is approximated with a Gaussian beam in the analysis of a reflector antenna system, instead of having to calculate the equivalent currents on the surface of each reflector and perform double integration, it is enough to keep track of only two scalar parameters as the beam is reflected between reflectors. The analysis is completely analogous to ray optics analysis and will be presented in more detail in Sec. 2.3.3.



There are also a number of disadvantages related to using Gaussian beams in the analysis of reflector systems. First of all, being only solutions of the paraxial approximation of the wave equation, the values calculated with them can only be reasonably accurate in the near-axis zone. They can not be used for getting any information about side lobe levels, spill-over, and similar parameters. There is also an issue with the phase on the wave front, which does not match well the phase of a spherical wave, and is therefore not physically correct as soon as one moves away from the axis. To extend the region of validity of the Gaussian beam, different correction factors are included in its definition. The most widely recognised and accepted one is the so-called Tuovinen correction, whereby the mentioned phase difference is corrected by an additional factor  $F$  which depends on the angle  $\theta$  measured from the axis of propagation. The same factor is also included in the amplitude term, yielding

$$f(\rho, z) = \frac{1 + \cos \theta}{2} \frac{w_0}{wF} e^{\left(-\rho^2 / (\sqrt{2}wF)^2 - jkz - jkR_c(F-1) + j\phi_0\right)}. \quad (2.113)$$

It is shown that this has a beneficial effect on the overall accuracy of the beam well beyond the paraxial regime, making it a better approximation to the physically correct fields. More details on this correction can be found in [48], [49].

Secondly, since Gaussian beams are usually used to approximate the electric field itself just like standard ray optical techniques, due to their scalar nature there is a major issue related to the polarisation of the radiated field. The polarisation can be artificially imposed onto the beam, but it does not match well the realistic polarisation of fields radiated by real corrugated horn antennas, except in the region very close to the axis of propagation. Moreover, no information whatsoever can be gathered about the cross-polarisation levels upon reflection from a curved reflector. It is for this reason that complex source points are in some cases preferred to Gaussian beams, since they too, as has been demonstrated, can have a Gaussian taper. By combining two orthogonal complex source points, one electric and one magnetic, one creates a *complex Huygens source* [34], [36]. Its radiated field is physically correct and incorporates a natural change of polarisation as the observation point moves away from the axis. The radiated field is calculated via the space-domain radiation integral, but the integral reduces to a simple explicit formula since the integration is performed only over a single point, so the fields are computed only slightly more slowly than with a simple Gaussian beam. This model has been implemented in GRASP [34], and has also been used in this thesis as the

source model for one- and two-reflector system analysis. More details on its implementation will be given in Secs. 4.4. and 5.1.2.

Finally, apart from the limitations from the point of view of physical correctness, there is also the basic limitation that a simple Gaussian beam can only approximate fields with a Gaussian amplitude taper. If one wishes to analyse somewhat more complicated fields while retaining the benefits of the Gaussian beam analysis, there are two general approaches for achieving that: one consists of considering a set of simple Gaussian beams radiated in various directions to locally approximate fields at the surface of interest (e.g. [11]), and the other expands the field into a sum of higher order Gauss-Hermite or Gauss-Laguerre modes [4], [5]. Gauss-Hermite modes are used if the problem is considered in rectangular coordinates, whereas Gauss-Laguerre modes are used in cylindrical coordinate system. Since the underlying mathematics is the same in both cases, here only Gauss-Hermite modes will be briefly presented. For more details, the reader is referred to [20], [45].

The general solution of the parabolic wave equation (2.103) in rectangular coordinates can be tried in the form

$$\psi(x, y, z) = f\left(\frac{x}{w}\right)g\left(\frac{y}{w}\right)e^{-j\left(P+\frac{k}{2q}(x^2+y^2)\right)}, \quad (2.114)$$

where the dependence of  $f$  and  $g$  on the  $z$ -coordinate is contained in the parameter  $w$ , while parameters  $P$  and  $q$  describe the beam's phase variation with the distance  $r$  and its amplitude (Gaussian) variation in the transverse plane. Ineserting this trial solution into (2.103), one notices that  $q$  is the *complex beam parameter* ( $q = j\pi\omega_0^2/\lambda + z$ ), whereas  $P$  relates to the beam width and the Guoy phase shift [20]. Furthermore, one can extract the differential equation for  $f$  (and  $g$ )

$$\frac{\partial^2 H_m}{\partial x^2} - 2x \frac{\partial H_m}{\partial x} + 2mH_m = 0, \quad (2.115)$$

whose solution is the  $m$ -th order Hermite polynomial  $H_m$ , with the respective arguments  $\sqrt{2}x/w$  and  $\sqrt{2}y/w$ , where  $w$  is again the beam width. Hence the general Gauss-Hermite beam can be written, without any additional corrections, as

$$\psi_{mn}(x, y, z) = \frac{1}{\sqrt{2^{m+n} m! n! \pi}} H_m\left(\sqrt{2} \frac{x}{w}\right) \cdot H_n\left(\sqrt{2} \frac{y}{w}\right) \cdot \psi_0(\rho, z), \quad (2.116)$$

where  $\psi_0(\rho, z)$  is the simple Gaussian beam of eq. (2.105), and the normalisation factor has been included to preserve unit power of the beam regardless of the mode order. Plots of the first few lowest-order Gauss-Hermite beams are shown in Fig. 2.6.

Gauss-Hermite and Gauss-Laguerre modes are typically used in a mode-matching analysis. The field on the surface of interest is expanded in the sum of Gauss-Hermite polynomials, and the unknown coefficients are obtained via point-matching or least-squares fitting procedures. The results are more accurate and valid in a wider observation range than the results of a simple Gaussian beam analysis. Furthermore, unlike with simple Gaussian beams, this kind of analysis can give an insight into how (and how much) the beam shape is deformed upon reflection from off-axis reflectors.

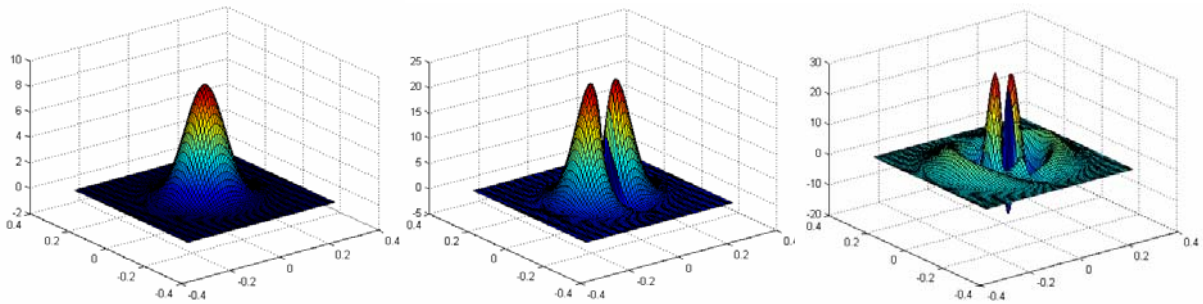


Figure 2.6. Amplitude distributions of Gauss-Hermite beams: a) simple Gaussian beam  $\psi_{00}$ ; b)  $\psi_{01}$ ; c)  $\psi_{12}$

## 2.3. Reflection from Metallic Objects

As has been said in the introduction to this chapter, there are three general approaches to calculating reflection in a reflector antenna system, namely via the radiation integral, via mode-matching techniques and via simple geometrical models. This section will explain them in more details, with extra attention given to the ones used later in this thesis.

### 2.3.1. Reflection via Radiation Integral

This approach consists of calculating the equivalent currents on the surface of the reflector and then reusing them in the subsequent radiation integral to compute the reflected (reradiated) fields at any point in space, using the exact same expressions from Sec. 2.1.

When considering the radiation integral in the context of analysing reflection, the key step is to find the current distribution on the reflector surface, and various models differ in the way they approach this problem. Two most common methods, namely the Method of Moments (MoM) and the Physical Optics (PO), are briefly presented here. Both use as the starting point a derivative of the equivalence theorem which applies to problems in which sources radiate in a space partially filled with an obstacle made of perfect electric conductor (PEC). The equivalence theorem permits to replace the analysed structure (i.e. the sources and the metallic reflector) by its so-called *physical equivalent* [9], [27], the construction of which is illustrated in Fig. 2.7. The obstacle (reflector) is removed from the otherwise homogeneous space, and its effect on the total field (i.e. scattering) is represented by such equivalent currents on its surface, which generate the same field as the original one in the region external to the obstacle. This enables the application of the radiation integral from Sec. 2.1., which was derived assuming that the sources radiated in a homogeneous space.

The field radiated by the sources in presence of an obstacle can be viewed, in the region external to the obstacle, as a superposition of the field radiated by the sources in homogeneous space (incident field  $\vec{E}_i$ ) and the field produced by the currents induced on the obstacle (scattered field  $\vec{E}_s$ ):

$$\vec{E} = \vec{E}_i + \vec{E}_s, \quad (2.117)$$

$$\vec{H} = \vec{H}_i + \vec{H}_s. \quad (2.118)$$

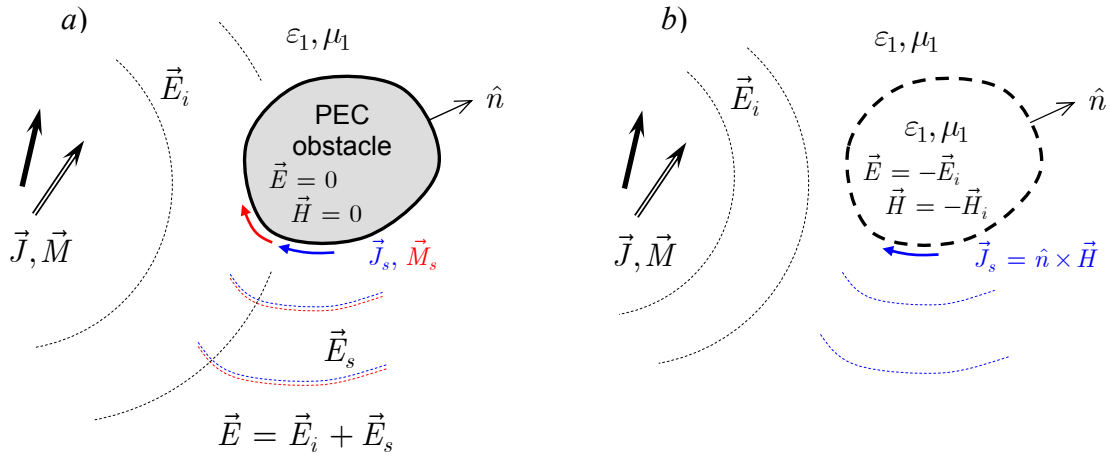


Figure 2.7. Construction of the physical equivalent. a) original situation; b) the equivalent.

It is assumed that the incident fields  $\vec{E}_i$  and  $\vec{H}_i$  are known or can be calculated in the whole region of interest. From the surface equivalence theorem, in order to retain the same field outside of the obstacle, we need to introduce the equivalent currents as

$$\vec{J}_s = \hat{n} \times \vec{H}, \quad (2.119)$$

$$\vec{M}_s = \vec{E} \times \hat{n}. \quad (2.120)$$

However, the boundary conditions for the perfect electric conductor state that the tangential components of the electric field on a PEC surface must be zero, hence

$$\vec{M}_s = \vec{E} \times \hat{n} = 0. \quad (2.121)$$

The equivalent magnetic current vanishes and only  $\vec{J}_s$  suffices to produce the same scattered field  $\vec{E}_s$  as before, as shown in Fig. 2.7.b. The total field is then the sum of the incident and the scattered field:

$$\vec{E} = \vec{E}_i + \oint_{S'} \vec{J}_s(\vec{r}') \cdot \underline{\mathbf{G}}(r | \vec{r}') dS', \quad (2.122)$$

where the radiation integral has been written with the dyadic Green's function notation of Sec. 2.1.2, for sake of compactness.

The crucial point that has to be stressed, before the discussion which follows, is that for the equivalent problem constructed this way, the equivalent current should be obtained from the total field, which is still unknown (only the incident fields  $\vec{E}_i$  and  $\vec{H}_i$  are known). A way has to be found to compute those currents in order to render the developed equivalent model

useful. To do this, there is an exact (Method of Moments) and an approximate (Physical Optics) method.

### 2.3.1.1. Method of Moments Approach

The Method of Moments (MoM) takes advantage of the boundary condition for the electric field on the surface of a PEC body, given in (2.121), to form an integral equation with the equivalent electric current as the unknown<sup>2</sup>. The boundary condition states that the tangential component of the total electric field on the surface of a PEC body must be zero, which gives

$$0 = \hat{n} \times \vec{E}_i \Big|_{S'} + \hat{n} \times \vec{E}_s \Big|_{S'}, \quad (2.123)$$

or

$$\hat{n} \times \vec{E}_i \Big|_{S'} = -\hat{n} \times \oint_{S'} \vec{J}_s(\vec{r}') \cdot \underline{\mathbf{G}}(\vec{r} | \vec{r}') dS' \Big|_{S'}. \quad (2.124)$$

This vector integral equation<sup>3</sup> can be split into components, and for each of the components a scalar integral equation is formed, which is then solved via a numerical procedure called the Method of Moments [14], [16], [32]. The unknown current is expanded into a sum of predetermined basis functions  $f_n$  with unknown weights  $a_n$ :

$$M_s^{tan} = \sum_{n=1}^{\infty} a_n f_n \cong \sum_{n=1}^N a_n f_n. \quad (2.125)$$

Since all the functions under the integral are now known, the integration can be performed, and the integral equation reduces to an algebraic equation with  $N$  unknowns:

$$E_i^{tan} \Big|_{S'} \cong \sum_{n=1}^N a_n I_n. \quad (2.126)$$

where superscript <sup>tan</sup> denotes any of the tangential components of the field, and

$$I_n = \oint_{S'} f_n(\vec{r}') \cdot \underline{\mathbf{G}}(\vec{r} | \vec{r}') dS' \Big|_{S'}. \quad (2.127)$$

---

<sup>2</sup> There are a number of different formulations for the starting integral equation [16], [27]. Other than the presented one, usually referred to as the Electric Field Integral Equation (EFIE), commonly used are also the Magnetic Field Integral Equation (MFIE) and the Combined Field Integral Equation (CFIE).

<sup>3</sup> Eq. (2.124) should be understood only as a symbolical representation of the starting point of the analysis. In practice one has to deal with singularities of the Green's function, since the source and observation surfaces coincide. A rigorous account of this problem can be found in [37].

To be able to solve for the weights  $a_n$ , a system of  $N$  equations has to be constructed from the starting equation. There are various techniques for doing that [14], [15], the simplest of all being the so-called *point-matching* technique, whereby the equality between the left-hand side and the right-hand side of (2.126) is enforced on a set of  $N$  different points  $\vec{r}_m$ ,  $m = 1 \dots N$ . Upon solving for  $a_n$ , the scattered field can be computed as well by using (2.122).

Since no approximations other than the purely numerical ones have been done to the starting equation, the solution of the above system of equations yields a physically correct, exact current distribution over the whole surface of the reflector. The reflected field calculated via this method is therefore usually considered the referent exact solution when different results are compared. However, this comes at the expense of having to perform  $N \times N$  integrations to get the equivalent currents, before even attempting to calculate the radiation integral (which is already slow itself, as explained in Sec. 2.1.). The number of unknowns  $N$  for two-dimensional problems generally increases with the square of the electrical size of the analysed object, and as the analysed reflector becomes electrically larger (e.g. with increasing frequency), so does the system of equations that needs to be solved. For reflectors of dimensions close to ten wavelengths, this approach becomes too slow and impractical.

### 2.3.1.2. Physical Optics Approach

In quasi-optical region one rarely uses MoM to calculate exact reflection, but resorts instead to approximate models to calculate the equivalent current *approximately*, yet without the numerous integrations. The justification of this approach lies in the fact that the radiated field is obtained via an integration process, whereby small errors from individual contributions tend to cancel out in the overall sum. Thus, if the current is approximated well enough in the region from which the strongest contribution comes, the result will be very close to the exact one in a reasonably wide observation region. The most common representative of this approach is the so-called Physical Optics approximation [34], and is explained next.

The approximation consists of considering the generally curved reflector to be locally planar and assuming that the current at a given point is the same as it would be if the equivalent planar reflector extended to infinity. The construction of the physical equivalent for the case of a flat reflector surface is illustrated in Fig. 2.8.

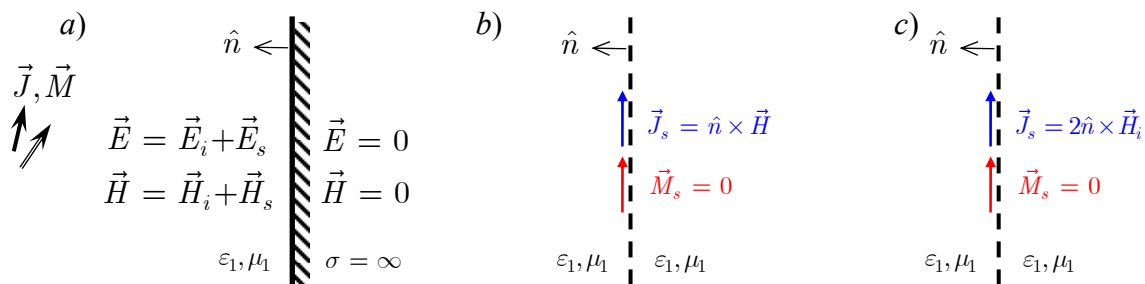


Figure 2.8. Construction of the Physical Optics (PO) equivalent for a flat, infinite PEC reflector. a) original situation; b) physical equivalent; c) PO equivalent.

Since the tangential components of the incident and scattered magnetic field are in phase and of equal amplitudes on a PEC surface, the total tangential magnetic field is simply the double of the incident field, which gives this simple relation for the equivalent electric current:

$$\vec{J}_s = \hat{n} \times \vec{H} = \hat{n} \times (\vec{H}_i + \vec{H}_s) = 2\hat{n} \times \vec{H}_i. \quad (2.128)$$

This allows calculating the equivalent surface currents on the reflector directly from the incident field, without the need to solve integral or any other equations. The reflected field is then calculated applying the same radiation integral as in the first case, but with the new approximated currents. The approximation gives very good results for electrically large smoothly curved reflectors, and is clearly much faster than the Method of Moments approach. However, the accuracy drops as the angle of incidence of the incoming wave becomes more and more oblique. Also, if the whole surface of the reflector is not directly illuminated by the sources, calculating the currents on the shadowed portions of the reflector using (2.128) will cause a further drop in the accuracy of the approximation. Therefore, the PO equivalent declares zero current on the shadowed portions of the reflector. If one insists on calculating those currents, the approach consists of illuminating first the directly visible part of the reflector and then calculating the field produced by that part of the reflector on the shadowed parts. The detection of illuminated and shadowed portions of the reflector can either be done manually, or a parallel ray-tracing analysis may be implemented to keep track of which parts are seen by which other parts. However, as the geometry becomes more complex, this results in a much slower analysis.

It should be said that, despite its shortcomings, Physical Optics analysis is still considered the referent "quasi full-wave" solution in the analysis of quasi-optical systems, since it still uses the most accurate radiation model provided by the radiation integral. The radiation integral



ensures that the radiated fields are Maxwellian and gives physically correct polarisation behaviour of the radiated/reflected fields, with the limitation in accuracy only due to the approximation of the source current. Most other (simpler and faster) models used in this area, for example the Gaussian beam reflection model, rely on wave objects which cannot generate truly Maxwellian fields and provide sensible information on all their aspects. They are usually used to get a quick estimate of the radiation pattern in the preliminary design of a quasi-optical system, while the final analysis is performed by the Physical Optics method. Physical Optics has therefore been chosen as the analysis method for calculating reflection in this thesis. More details on its implementation are given in Secs. 4.1. and 4.2.

### 2.3.2. Mode-matching Techniques

For sake of completeness, included here is a brief sketch of the mode-matching approach to calculating reflection from metallic surfaces. Mode-matching is, generally speaking, more often used for analysing fields in closed or semi-closed domains, like for example waveguide transitions and discontinuities, where the boundary conditions allow natural representation of an arbitrary field in terms of modal functions. Modal functions can be composed of elementary functions (sines, cosines, etc.), special functions (Bessel functions, Legendre polynomials, etc.) or their combinations, and they need to form a complete set in order for the expansion to be feasible. An additional advantage is if the modal functions also form an orthogonal set, in which case the extraction of modal coefficients (amplitudes) simplifies.

In the analysis of reflector antenna systems, the basic idea behind the mode-matching approach is to expand both the incident field and the reflected field in a series of wave objects or modes, for which propagation can be computed analytically in closed form. Most often, the field is expanded into Gauss-Hermite or Gauss-Laguerre modes [4], [5], [21]. The field at the reflection point, obtained by summing up contributions of all the modes, has to be the same for both expansions. The two expansions can be matched using point-matching techniques or in a least-squares sense, resulting in slightly different formulations of the same approach. Presented here is the approach adopted by Withington and Murphy [5].

We assume that the incident and the reflected field can be represented by a summation of modal functions  $\psi_k$ :

$$E^{inc}(\vec{r}') = \sum_k a_k \psi_k^{inc}(\vec{r}'), \quad (2.129)$$

$$E^{ref}(\vec{r}) = \sum_n b_n \psi_n^{ref}(\vec{r}), \quad (2.130)$$

where both  $\vec{r}'$  and  $\vec{r}$  denote the surface of interest, namely that of the reflector, each in its own coordinate system. To determine the modal coefficients, the overlap integrals are calculated over the considered surface:

$$\iint_{S'} E^{ref}(\vec{r}) \bar{\psi}_o(\vec{r}) dS' = \sum_n b_n \iint_{S'} \psi_n^{ref}(\vec{r}) \bar{\psi}_o(\vec{r}) dS' = \sum_n b_n B_{no}, \quad (2.131)$$

where  $\bar{\psi}_o$  is the  $o$ -th modal function, used as the testing function, and the overline denotes the complex conjugate. Note that, in general, when integrating over an arbitrary *curved* surface  $dS'$ , the modes are not orthogonal, i.e. the crosstalk between modes must be taken into account, meaning that the whole matrix  $\underline{\mathbf{B}} = [B_{no}]$  has to be computed (not just the elements on the diagonal where  $n = o$ ).

In the next step, the same integrals are repeated, but with the reflected field on the reflector surface expressed in terms of the incident field. In [5], a simple model is adopted, whereby a mirror is regarded as a simple phase-transforming surface, that is

$$E^{ref}(\vec{r}) = E^{inc}(\vec{r}') \cdot e^{j\Delta\phi}, \quad (2.132)$$

where the phase shift depends on the shape of the reflector. This forms the following overlap integral

$$\iint_{S'} E^{ref}(\vec{r}) \bar{\psi}_l(\vec{r}) dS' = \iint_{S'} E^{inc}(\vec{r}') e^{j\Delta\phi} \bar{\psi}_l(\vec{r}) dS', \quad (2.133)$$

where, analogously to the case of the reflected field,  $\bar{\psi}_l$  is  $l$ -th modal function and serves to determine how much energy of the incident field is carried in the  $l$ -th mode. With the substitution of (2.129), the above integral becomes

$$\iint_{S'} E^{inc}(\vec{r}') e^{j\Delta\phi} \bar{\psi}_l(\vec{r}) dS' = \sum_k a_k \iint_{S'} \psi_k^{inc}(\vec{r}') e^{j\Delta\phi} \bar{\psi}_l(\vec{r}) dS' = \sum_k a_k A_{kl}. \quad (2.134)$$

Equating (2.134) and (2.131) gives

$$\sum_k a_k A_{kl} = \sum_n b_n B_{no}, \quad (2.135)$$

or in matrix notation

$$\underline{\mathbf{a}}\underline{\mathbf{A}} = \underline{\mathbf{b}}\underline{\mathbf{B}}, \quad (2.136)$$

and the vector of unknown modal coefficients of the reflected field is obtained via matrix inversion

$$\mathbf{b} = \mathbf{a}\underline{\mathbf{A}}\underline{\mathbf{B}}^{-1}. \quad (2.137)$$

In [5], Gauss-Hermite modes were selected as the modal functions.

Compared to the radiation integral-based approach from the previous section, the mode-matching approach alleviates the need for calculating the lengthy radiation integral. However, some integration is still necessary, and the integrals are similar in form to those of the Method of Moments. However, as the modes exist over the whole surface of the reflector, they act in a fashion similar to the entire-domain basis functions in MoM, meaning that in general only a low to moderate number of modes will be necessary to completely represent the field, and the size of the matrices that have to be computed will be fairly manageable. As a consequence, the resulting method is an order of magnitude faster than the one based on the radiation integral. It should be noted, though, that even if the reflection is calculated in an exact way and without approximations, when the reflected modes are propagated from the reflection point to the point of observation, the result ceases to be entirely physically correct, due to the limitations of the modes themselves. In other words, Gauss-Hermite and Gauss-Laguerre modes are solutions to the same paraxial approximation of the wave equation, as has been explained in Sec. 2.2.3., so the reflected fields will be physically correct only in a narrow region around the axis of propagation; elsewhere, they will suffer from the same problems as the simple Gaussian beam. Better results could be expected if the field were expanded in modes which respect the wave equation without restrictions, such as the new wave-objects introduced later in Ch. 3.

### 2.3.3. Simplified High-frequency Model: Ray and Beam Reflection

If the scatterers under consideration are electrically very large and smoothly curved, one can resort to classical optics to analyse the interaction between the incident wave and the scatterer. We assume that the source of the incident wave is located far away from the reflector, and that the radiated wave has a narrow main beam and low side-lobe levels, so that most of its energy is concentrated around the axis of propagation. Under these assumptions, one can apply an approximation to both the wave and the scatterer: the scatterer is assumed planar and infinite in extent, while the incident wave is approximated with a plane wave. This allows for the use of simple formulas for reflection and refraction of a plane wave at the interface

between two media. As the beam of the incident wave gets narrower, this leads to the ray-optical propagation model, where relations of classical optics, such as the law of reflection, Snell's law etc., are used to describe the trajectory of the wave (i.e. ray) in a system of scatterers (in optical systems lenses and mirrors).<sup>4</sup> [9], [27], [46].

Since in an isotropic medium rays spread along straight lines, the position of the ray at a given distance from the source point can be determined from its initial position  $r$  (the starting point coordinate) and its slope  $r'$  (i.e. direction of propagation at the source point). Furthermore, assuming that the system in which the ray propagates is linear, one can describe the effect of each device in the system (lens, reflector, etc.) on the beam's parameters with a 2 by 2 matrix relating the ray's input parameters  $r_{in}$  and  $r'_{in}$  to its output parameters  $r_{out}$  and  $r'_{out}$ :

$$r_{out} = Ar_{in} + Br'_{in}, \quad (2.138)$$

$$r'_{out} = Cr_{in} + Dr'_{in}, \quad (2.139)$$

that is,

$$\begin{bmatrix} r_{out} \\ r'_{out} \end{bmatrix} = \begin{bmatrix} A & B \\ C & D \end{bmatrix} \begin{bmatrix} r_{in} \\ r'_{in} \end{bmatrix}. \quad (2.140)$$

The radius of curvature of the beam is defined as  $R_c = r/r'$ , and it can be seen from (2.138) and (2.139) that the input and output radii of curvature are related by

$$R_{c,out} = \frac{AR_{c,in} + B}{CR_{c,in} + D}, \quad (2.141)$$

hence any device in the system can be analysed by its effect on the radius of curvature of the ray. For simple optical devices, the  $ABCD$  parameters can be easily determined from classical optics. For example, the propagation of a ray in a homogeneous medium is described by the

matrix  $\begin{bmatrix} 1 & L \\ 0 & 1 \end{bmatrix}$ , where  $L$  is the distance from the source point to the observation point. The

matrix simply states the obvious fact that in a homogeneous medium, the slope of the ray remains unchanged, while the position changes proportionally to  $L$ , depending on the slope

---

<sup>4</sup> Even if the beam of the incident wave is not narrow, ray analysis can still be used to analyse its propagation in a quasi-optical system via ray-tracing algorithms. The basis of the analysis is to represent the radiation pattern by a sufficient number of rays of appropriate magnitude and calculate propagation of each of them through the whole system to obtain the output radiation pattern. Ray-tracing is, however, not considered in this thesis.

of the input ray. Similarly, the matrix describing the transition from one medium to another, whereby the radius of curvature of the border between the two media is  $R$ , is [1]

$$\underline{\mathbf{T}} = \begin{bmatrix} 1 & 0 \\ (n_b - n_a)/Rn_b & n_a/n_b \end{bmatrix}. \quad (2.142)$$

This is illustrated in Fig. 2.9. The transfer matrix shows that at the interface between two media, the position of the ray does not change, but the slope does.

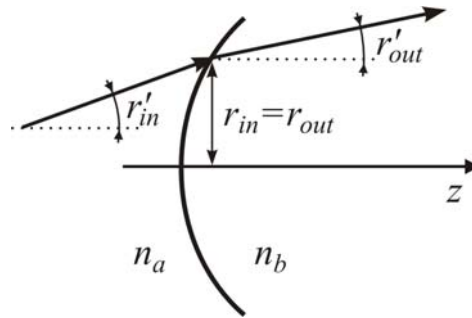


Figure 2.9. Transition of a ray from medium with refractive index  $n_a$  to the medium with refractive index  $n_b$ . At the border, the position of the ray remains the same, while the slope changes.

The strength of the analysis based on ABCD matrices lies in the fact that the ABCD matrix of a succession of elements is obtained by simple multiplication of individual ABCD matrices of each element in the chain:

$$\underline{\mathbf{T}} = \underline{\mathbf{T}}_N \cdot \underline{\mathbf{T}}_{N-1} \cdot \dots \cdot \underline{\mathbf{T}}_1. \quad (2.143)$$

Based on this, the ABCD matrix for a thin lens of refractive index  $n_2$ , embedded in a medium of index  $n_1$ , is obtained as the product of two matrices for curved interfaces of radii  $R_1$  and  $R_2$ , respectively, and can be written shortly as

$$\underline{\mathbf{T}} = \begin{bmatrix} 1 & 0 \\ -1/f & 1 \end{bmatrix}, \quad (2.144)$$

where

$$\frac{1}{f} = \frac{n_2 - n_1}{n_1} \left( \frac{1}{R_2} - \frac{1}{R_1} \right). \quad (2.145)$$

Parameter  $f$  denotes, as usually, the focal distance of the lens.

Within the framework of this thesis, it is important to note that the ABCD matrix for a curved mirror has the same general form as the matrix for the thin lens, while the difference between

various mirror shapes (i.e. spherical, elliptical, etc.) is implicitly accounted for in the formula for calculating the focal distance  $f$ . Hence, if the lens/mirror parameters from (2.144) are substituted into (2.141), one obtains

$$R_{c,out} = \frac{R_{c,in}}{-\frac{1}{f}R_{c,in} + 1} = \frac{1}{-\frac{1}{f} + \frac{1}{R_{c,in}}},$$

which is none other than the classical lens equation

$$\frac{1}{R_{c,in}} - \frac{1}{R_{c,out}} = \frac{1}{f}. \quad (2.146)$$

Note that the sign of  $f$  and  $R_{c,out}$  may be either positive or negative, depending on whether the lens/mirror is concave or convex.

When propagation and reflection of beams are analysed, a beam can be regarded as a ray with an attached amplitude profile, and can be treated in a completely analogous fashion. For Gaussian beams, starting from the confocal distance  $z_c$ , the *complex beam parameter*  $q$  is introduced as

$$q = z + jz_c. \quad (2.147)$$

It contains the information on both key parameters of the beam, namely the beam width and the radius of curvature, which can be demonstrated by manipulating (2.110) and (2.111). We note that

$$w^2 = w_0^2 \frac{z_c^2 + z^2}{z_c^2} = \frac{w_0^2}{z_c} \frac{z_c^2 + z^2}{z_c} = \frac{w_0^2}{\pi w_0^2} \frac{z_c^2 + z^2}{z_c} = \frac{\lambda}{\pi} \frac{z_c^2 + z^2}{z_c}$$

and

$$R_c = \frac{z^2 + z_c^2}{z},$$

while the reciprocal of the complex beam parameter can be written as

$$\frac{1}{q} = \frac{1}{z + jz_c} = \frac{z - jz_c}{z^2 + z_c^2}.$$

From here, it is easily seen that

$$\frac{1}{q} = \frac{1}{R_c} - j \frac{\lambda}{\pi w^2}. \quad (2.148)$$

Since in the high-frequency limit  $\lambda \rightarrow 0$ , the limiting value of  $q$  is the radius of curvature  $R_c$ . This justifies the idea of treating the complex beam parameter  $q$  in the same way as the radius of curvature for simple rays. Therefore, analogously to (2.141), we have

$$q_{out} = \frac{Aq_{in} + B}{Cq_{in} + D}. \quad (2.149)$$

Bearing in mind the discussion on the ABCD matrix of a succession of optical devices, one can develop the general matrix for the basic analysis block of a multielement system. It consists of an optical device and two paths of lengths  $d_{in}$  and  $d_{out}$ , one from each side of the device, as shown in Fig. 2.10. Here, the distance  $d_{out}$  from the output beam's waist to the optical device and the size  $w_{0,out}$  of the output beam's waist are unknown, and the goal is to obtain expressions which will allow calculating them from the known input parameters  $d_{in}$  and  $w_{0,in}$  and the ABCD matrix of the optical element.

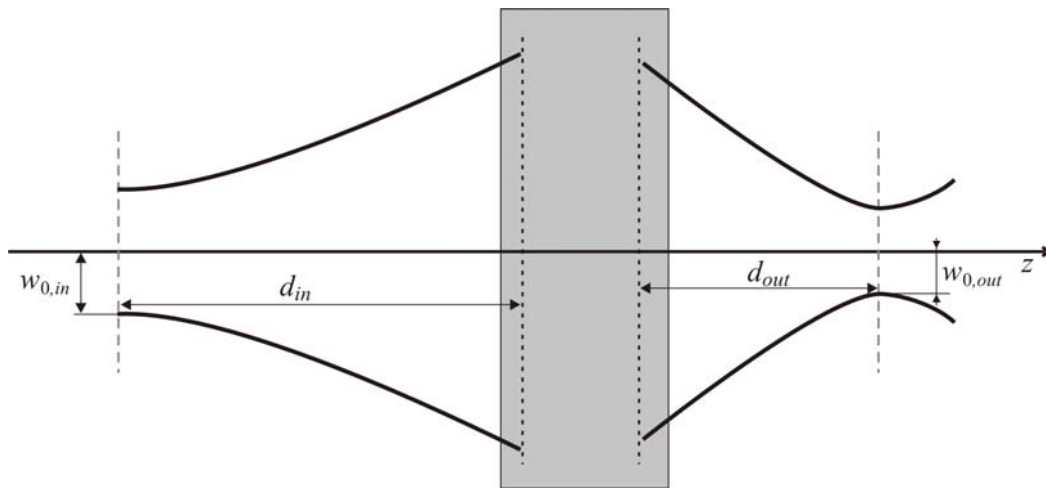


Figure 2.10. Illustration of the basic building block of a multielement quasi-optical system. The input beam waist is  $w_{01}$ , while the output beam waist is  $w_{02}$ .

Assuming that the device alone is represented by the parameters  $A'$ ,  $B'$ ,  $C'$  and  $D'$ , the matrix of the system is:

$$\begin{aligned} \begin{bmatrix} A & B \\ C & D \end{bmatrix} &= \begin{bmatrix} 1 & d_{out} \\ 0 & 1 \end{bmatrix} \cdot \begin{bmatrix} A' & B' \\ C' & D' \end{bmatrix} \cdot \begin{bmatrix} 1 & d_{in} \\ 0 & 1 \end{bmatrix} \\ &= \begin{bmatrix} A' + C'd_{out} & A'd_{in} + B' + d_{out}(C'd_{in} + D') \\ C' & C'd_{in} + D' \end{bmatrix}. \end{aligned} \quad (2.150)$$

According to the definition in (2.147), at the plane of the beam waist ( $z = 0$ ), the complex beam parameter is purely imaginary ( $q = jz_c$ ). Thus, plugging in the values of  $A$ ,  $B$ ,  $C$  and  $D$  for the whole system into (2.149), and separating the real part from the imaginary, permits to determine the output waist's position  $d_{out}$  and size  $w_{out}$ :

$$d_{out} = \frac{(A' d_{in} + B')(C' d_{in} + D') + A' C' z_{c,in}^2}{(C' d_{in} + D')^2 + C'^2 z_{c,in}^2}, \quad (2.151)$$

$$w_{0,out} = \frac{w_{0,in}}{\sqrt{(C' d_{in} + D')^2 + C'^2 z_{c,in}^2}}. \quad (2.152)$$

Alternatively, for simple mirrors, one can use (2.149) directly (i.e. for the mirror alone), which gives, as in (2.146),

$$\frac{1}{q_{in}} - \frac{1}{q_{out}} = \frac{1}{f}. \quad (2.153)$$

Separating the real and the imaginary parts, we obtain

$$\frac{1}{R_{c,in}} - \frac{1}{R_{c,out}} = \frac{1}{f}, \quad (2.154)$$

$$-j \frac{\lambda}{\pi w_{in}^2} + j \frac{\lambda}{\pi w_{out}^2} = 0. \quad (2.155)$$

The second of these two equations states the simple fact that the beam width of the reflected beam and the incident beam, at the point of reflection, are equal. The first one shows that for a Gaussian beam, the reflected beam's radius of curvature is calculated in exactly the same way as for a simple ray. Now, since two parameters suffice to fully describe a Gaussian beam, this means that by knowing the radius of curvature and the beam width at the point of reflection, one has sufficient information to retrieve the beam waist and its distance from the point of reflection. Notice that for Gaussian beams, contrary to simple rays, the distance from the source (i.e. the plane of the beam waist) is not equal to the radius of curvature, since the radius of curvature is always larger than the distance from the source, as given by (2.111). The beam waist and its position can be obtained from the beam width and its radius of curvature at the point of reflection by combining the two expressions for the complex beam parameter. We have:

$$1 = q \cdot \frac{1}{q} = (z + jz_c) \cdot \left( \frac{1}{R_c} - j \frac{\lambda}{\pi w^2} \right),$$



which can again be split into two equations, one for the real part and the other for the imaginary part, giving

$$\begin{aligned}\frac{1}{R_c}z + \frac{\lambda}{\pi w^2}z_c &= 1, \\ -\frac{\lambda}{\pi w^2}z + \frac{1}{R_c}z_c &= 0.\end{aligned}$$

Here,  $z$  is the distance from the beam waist at which the beam width is just  $w$  and the radius of curvature just  $R_c$ . Solving the system for the distance  $z$  then gives

$$z = \frac{R_c}{1 + \left(\frac{\lambda R_c}{\pi w^2}\right)^2}. \quad (2.156)$$

Similarly, solving the system for the confocal distance  $z_c$  and applying its defining equation  $z_c = \pi w_0^2/\lambda$  from (2.109), one obtains

$$w_0^2 = \frac{w^2}{1 + \left(\frac{\pi w^2}{\lambda R_c}\right)^2}. \quad (2.157)$$

It may seem as though all these equations only consider the beam width and the radius of curvature, but say nothing about the amplitude of the reflected beam. This is, however, not true, and can easily be verified by inspecting the definition of the Gaussian beam, given in (2.105). One can see that the amplitude of the beam is  $\sqrt{\frac{2}{\pi w^2}}$ , meaning that the amplitude information is already contained in the beam width information. The narrower the beam, the higher the amplitude, and vice versa, which is of course the expected behaviour.

Another important comment is that all the derivations in this section tacitly assume that the beam is impinging on the lens/reflector on-axis. However, for most reflector antenna applications, the incidence is never on-axis, but always oblique. This results in the appearance of higher order modes (Gauss-Laguerre or Gauss-Hermite) in the reflected wave, a subject which has been thoroughly covered by Murphy [21]. Still, if the analysis is restricted to the fundamental Gaussian mode only, Eqs. (2.154) thru (2.157) can still be used, and the only additional thing that has to be done is to apply the law of reflection in order to determine the direction of propagation of the reflected beam. With the propagation unit vectors  $\hat{r}_{inc}$  and  $\hat{r}_{ref}$

defined as shown in Fig. 2.11., and the normal pointing outwards, the reflected beam's propagation vector  $\hat{r}_{ref}$  is given by

$$\hat{r}_{ref} = \hat{r}_{inc} - 2(\hat{n} \cdot \hat{r}_{inc})\hat{n}. \quad (2.158)$$

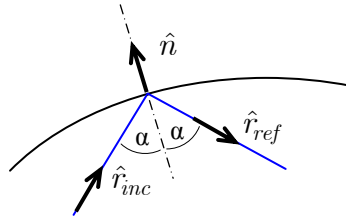


Figure 2.11. Geometry definition for the law of reflection

To summarise, reflection of Gaussian beams can be analysed very simply by means of formulas (2.154) thru (2.158). The method is very fast, but not physically exact, and the results can only be sufficiently accurate for a first-order analysis of the system. Alternatively, the Gaussian beam analysis can be used in conjunction with other, more exact methods, to provide an estimate of the beam width and the location of its focus/waist, which may be required as input parameters for the other method in the pair. In this thesis, the Gaussian beam analysis was implemented as an auxiliary step for the accurate analysis based on the hybrid method involving Physical Optics and the new complex conical beams, to be introduced in Chapter 3.

As a final comment, we note that the focal distance  $f$ , used in Eqs. (2.154) thru (2.158), has to be calculated with an appropriate method for each considered reflector geometry. For the numerical tests and examples presented in Ch. 5, ellipsoidal mirrors were considered, and the related formulae are given in Sec. 4.3.2.

### 3. COMPLEX CONICAL BEAMS

In this chapter a novel method for computing the field radiated by an aperture via expansion in new wave objects is presented. The expansion is done in two steps, starting from the spectral domain radiation integral presented in Sec. 2.1.1. Assuming the electric field spectrum in the aperture plane is given in polar spectral coordinates, the first step consists of expanding it in a Fourier series in the angular spectral coordinate  $\alpha$ . Next, the remaining dependence on the radial spectral coordinate  $k_\rho$  is approximated by a sum of exponential functions with complex exponents, which are obtained by the Generalized Pencil-of-Function (GPOF) method. The radiation integral is thus transformed to a double sum of simpler integrals, each of which rigorously respects the wave equation, just like the starting radiation integral. The benefit of applying these transformations lies in the fact that a closed-form solution can be derived for the new simpler integrals. This is explained in detail in the following sections.

#### 3.1. Formulation – Scalar Case

The starting point for the derivation is the scalar spectral-domain radiation integral [24], explained in Sec. 2.1.1:

$$I'(x, y, z) = \frac{1}{8\pi^2 j} \int_{-\infty}^{\infty} \int_{-\infty}^{\infty} \tilde{F}(k_x, k_y) \frac{e^{-j(k_x x + k_y y) - jz\sqrt{k^2 - k_x^2 - k_y^2}}}{\sqrt{k^2 - k_x^2 - k_y^2}} dk_x dk_y \quad (3.1)$$

In order to be able to apply the Fourier series expansion, (3.1) has to be rewritten in polar coordinates. Substituting  $k_x = k_\rho \cos \alpha$ ,  $k_y = k_\rho \sin \alpha$ , we obtain

$$I'(x, y, z) \equiv I(\rho, \phi, z) = \frac{1}{8\pi^2 j} \int_0^\infty \int_0^{2\pi} \tilde{G}(k_\rho, \alpha) e^{-j\rho k_\rho \cos(\alpha - \phi)} \frac{e^{-jz\sqrt{k^2 - k_\rho^2}}}{\sqrt{k^2 - k_\rho^2}} k_\rho dk_\rho d\alpha, \quad (3.2)$$

where  $\tilde{F}(k_x, k_y) \equiv \tilde{G}(k_\rho, \alpha)$ . Making use of the inherent periodicity in  $\alpha$ , the spectrum  $\tilde{G}(k_\rho, \alpha)$  is expanded in a Fourier series in that coordinate:

$$\tilde{G}(k_\rho, \alpha) = \sum_{n=-\infty}^{\infty} c_n(k_\rho) e^{jn\alpha}. \quad (3.3)$$

This gives

$$I(\rho, \phi, z) = \frac{1}{8\pi^2 j} \int_0^\infty \frac{e^{-jz\sqrt{k^2-k_\rho^2}}}{\sqrt{k^2-k_\rho^2}} k_\rho \sum_n c_n(k_\rho) \left[ \int_0^{2\pi} e^{jn\alpha} e^{-j\rho k_\rho \cos(\alpha-\phi)} d\alpha \right] dk_\rho. \quad (3.4)$$

The Fourier expansion in (3.3) has separated the  $\alpha$  dependence of the spectrum  $\tilde{G}(k_\rho, \alpha)$  from the  $k_\rho$  dependence. Therefore we can apply another transformation to the  $k_\rho$ -dependent part of the spectrum, contained in the terms  $c_n(k_\rho)$ . For this case, the function is approximated with a sum of exponential functions with complex exponents, which are obtained via the Generalized Pencil of Functions method:

$$c_n(k_\rho) = \sum_{m=1}^M d_{mn} e^{b_{mn}\sqrt{k^2-k_\rho^2}}. \quad (3.5)$$

From here on, this approximation will be referred to simply as the GPOF expansion. More details on the underlying mathematics are given in Appendix C and refs. [18] and [19]. For the moment, it is important to note that this is an indirect application of the approximation – the function which is originally a function of variable  $k_\rho$  is represented as a sum of exponents of  $k_z = \sqrt{k^2 - k_\rho^2}$ . The direct application of the expansion would have resulted in an approximation of the function  $c_n(k_\rho)$  in terms of complex exponents  $b_{mn}k_\rho$ . This will be explained in Sec. 3.1.2.

After interchanging the positions of the summations and the outer integral, (3.4) becomes

$$I(\rho, \phi, z) = \frac{1}{8\pi^2 j} \sum_n \sum_{m=1}^M d_{nm} c_n(k_\rho) \int_0^\infty \frac{e^{-j(z+jb_{mn})\sqrt{k^2-k_\rho^2}}}{\sqrt{k^2-k_\rho^2}} k_\rho \left[ \int_0^{2\pi} e^{jn\alpha} e^{-j\rho k_\rho \cos(\alpha-\phi)} d\alpha \right]. \quad (3.6)$$

The integral inside the parenthesis is directly related to the Bessel function of  $n$ -th order [26]:

$$\int_0^{2\pi} e^{jn\alpha} e^{-j\rho k_\rho \cos(\alpha-\phi)} d\alpha = e^{jn\phi} \int_0^{2\pi} e^{jn(\alpha-\phi)} e^{-j\rho k_\rho \cos(\alpha-\phi)} d(\alpha-\phi) = 2\pi (-j)^n e^{jn\phi} J_n(\rho k_\rho).$$

Applying that result to the above integral, (3.6) simplifies to

$$I(\rho, \phi, z) = \sum_n \sum_{m=1}^M -\frac{(-j)^{n-1}}{4\pi} d_{nm} e^{jn\phi} \int_0^\infty \frac{e^{-j(z+jb_{mn})\sqrt{k^2-k_\rho^2}}}{\sqrt{k^2-k_\rho^2}} J_n(\rho k_\rho) k_\rho dk_\rho, \quad (3.7)$$

which can be rewritten in the following simpler form:

$$I(\rho, \phi, z) = \sum_n \sum_{m=1}^M a_{mn} W_n(\rho, \phi, z + jb_{mn}), \quad (3.8)$$

where

$$a_{mn} = (-j)^{n+1} \frac{1}{4\pi} d_{mn}, \quad (3.9)$$

and  $W_n(\rho, \phi, \tilde{z})$  represents the new wave object of order  $n$ :

$$W_n(\rho, \phi, \tilde{z}) = e^{jn\phi} \int_0^\infty \frac{e^{-j\tilde{z}\sqrt{k^2-k_\rho^2}}}{\sqrt{k^2-k_\rho^2}} J_n(\rho k_\rho) k_\rho dk_\rho. \quad (3.10)$$

In the following text, coordinates labeled with  $(\tilde{\cdot})$  represent the complex analytical continuation of the corresponding real variable. In (3.10), wave object  $W_n$  is evaluated at a point whose  $z$ -coordinate is moved from the real axis into the complex plane by a value of  $jb_{mn}$  (i.e.  $\tilde{z} = z + jb_{mn}$ ), obtained from the GPOF expansion, hence the term "complex" in its name [23], [40]. The other descriptive term, "conical", will be clarified in the following subsections.

Before proceeding to the analytical solution of (3.10), a brief demonstration that the mathematical object therein defined really does satisfy the Helmholtz wave equation  $[\nabla^2 + k^2]W_n(\rho, \phi, z) = 0$  will be given. Expanding the wave equation in cylindrical coordinates, we have

$$\frac{\partial^2 W_n}{\partial \rho^2} + \frac{1}{\rho} \frac{\partial W_n}{\partial \rho} + \frac{1}{\rho^2} \frac{\partial^2 W_n}{\partial \phi^2} + \frac{\partial^2 W_n}{\partial z^2} + k^2 W_n = 0. \quad (3.11)$$

Substituting (3.10) in (3.11), the following equation is obtained:

$$e^{jn\phi} \int_0^\infty \frac{e^{-j\tilde{z}\sqrt{k^2-k_\rho^2}}}{\sqrt{k^2-k_\rho^2}} h(\rho, n) k_\rho dk_\rho = 0, \quad (3.12)$$

where

$$h(\rho, n) = \frac{k_\rho^2}{4} \left( J_{n-2}(\rho k_\rho) - 2J_n(\rho k_\rho) + J_{n+2}(\rho k_\rho) \right) + \frac{k_\rho}{2\rho} \left( J_{n-1}(\rho k_\rho) - J_{n+1}(\rho k_\rho) \right) - \frac{n^2}{\rho^2} J_n(\rho k_\rho)$$

To prove that (3.12) equals zero regardless of the coordinates  $(x, y, \tilde{z})$ , the condition  $h(\rho, n) = 0$  has to be satisfied. This is indeed so, and can be demonstrated by applying the following identity for Bessel functions [26] to the  $(n-2)$  and  $(n+2)$  terms twice:

$$J_{\nu-1}(z) + J_{\nu+1}(z) = \frac{2\nu}{z} J_{\nu}(z).$$

### 3.1.1. Analytic Solution of Wave Objects in Space Domain

The integral in (3.10) is simpler in form than the starting one in (3.1), but is still an indefinite integral with a rapidly oscillating integrand, so from the numerical point of view not much has been gained. In order for the expansion in (3.8) to have real practical value, an efficient way must be found to calculate it. This is achieved by relating it to a similar integral whose closed-form solution has been tabulated by Gradshteyn [15] (Eq. 6.637):

$$I_{\nu}^{(g)} = \int_0^{\infty} \frac{e^{-\alpha\sqrt{\beta^2+x^2}}}{\sqrt{\beta^2+x^2}} J_{\nu}(\gamma x) dx = I_{\nu/2} \left[ \frac{\beta}{2} (\sqrt{\alpha^2+\gamma^2}-\alpha) \right] \cdot K_{\nu/2} \left[ \frac{\beta}{2} (\sqrt{\alpha^2+\gamma^2}+\alpha) \right]. \quad (3.13)$$

Here, I and K are modified Bessel functions of the first and second kind, respectively. Note that the convergence of the integral depends on parameters  $\alpha$ ,  $\beta$ ,  $\gamma$  and  $\nu$ . This will be considered in Sec. 3.1.2. Performing the substitutions  $x \equiv k_{\rho}$ ,  $\beta \equiv \varepsilon + jk$ ,  $\varepsilon \rightarrow 0+$ ,  $\gamma \equiv \rho$  and  $\alpha \equiv z$ , the so-called Gradshteyn integral becomes

$$I_n^{(g)} = \int_0^{\infty} \frac{e^{-jz\sqrt{k^2-k_{\rho}^2}}}{j\sqrt{k^2-k_{\rho}^2}} J_n(\rho k_{\rho}) dk_{\rho} = (-j)^{n+1} \frac{\pi}{2} J_{n/2} \left( -\frac{k}{2}(r-z) \right) \cdot H_{n/2}^{(2)} \left( \frac{k}{2}(r+z) \right), \quad (3.14)$$

where  $r = \sqrt{\rho^2 + z^2}$ .

The integrand in (3.13) is very similar to the one in (3.10). In fact, the only difference is the presence of the factor  $k_{\rho}$  in (3.10), which can be easily introduced by differentiating the whole expression with respect to  $\rho$ . This gives

$$\frac{\partial I_n^{(g)}}{\partial \rho} = \frac{1}{2} \left( \int_0^{\infty} \frac{e^{-jz\sqrt{k^2-k_{\rho}^2}}}{j\sqrt{k^2-k_{\rho}^2}} J_{n-1}(\rho k_{\rho}) k_{\rho} dk_{\rho} - \int_0^{\infty} \frac{e^{-jz\sqrt{k^2-k_{\rho}^2}}}{j\sqrt{k^2-k_{\rho}^2}} J_{n+1}(\rho k_{\rho}) k_{\rho} dk_{\rho} \right). \quad (3.15)$$

Multiplying both sides by  $e^{jn\phi}$  and expanding, the equation becomes

$$\begin{aligned} e^{jn\phi} \frac{\partial I_n^{(g)}}{\partial \rho} &= \frac{e^{j(n-1)\phi}}{e^{-j\phi}} \frac{1}{2j} \int_0^{\infty} \frac{e^{-jz\sqrt{k^2-k_{\rho}^2}}}{\sqrt{k^2-k_{\rho}^2}} J_{n-1}(\rho k_{\rho}) k_{\rho} dk_{\rho} \\ &\quad - \frac{e^{j(n+1)\phi}}{e^{j\phi}} \frac{1}{2j} \int_0^{\infty} \frac{e^{-jz\sqrt{k^2-k_{\rho}^2}}}{\sqrt{k^2-k_{\rho}^2}} J_{n+1}(\rho k_{\rho}) k_{\rho} dk_{\rho}, \end{aligned} \quad (3.16)$$

or simply

$$e^{jm\phi} \frac{\partial}{\partial \rho} I_n^{(g)} = \frac{e^{j\phi}}{2j} W_{n-1} - \frac{e^{-j\phi}}{2j} W_{n+1}. \quad (3.17)$$

Turning this expression around we get the recurrence relation which is the basis for the analytical computation of wave objects in space domain:

$$W_{n+1} = e^{j2\phi} W_{n-1} - 2j e^{j(n+1)\phi} \frac{\partial}{\partial \rho} I_n^{(g)}. \quad (3.18)$$

In order to have a well-defined recurrence, we need to find the analytic solution for the first two terms of the series, namely  $W_0$  and  $W_1$ , and know how to compute the  $\rho$ -derivative of the Gradshteyn integral. The latter is easily obtained from (3.14):

$$\begin{aligned} \frac{\partial I_n^{(g)}}{\partial \rho} &= (-j)^{n+1} \frac{\pi}{2} \left[ \frac{\partial J_{n/2}(d^-)}{\partial \rho} \cdot H_{n/2}^{(2)}(d^+) + J_{n/2}(d^-) \cdot \frac{\partial H_{n/2}^{(2)}(d^+)}{\partial \rho} \right] \\ &= (-j)^{n+1} \frac{k\pi}{8} \frac{\rho}{r} \left[ J_{n/2+1}(d^-) H_{n/2}^{(2)}(d^+) - J_{n/2-1}(d^-) H_{n/2}^{(2)}(d^+) \right. \\ &\quad \left. + J_{n/2}(d^-) H_{n/2-1}^{(2)}(d^+) - J_{n/2}(d^-) H_{n/2+1}^{(2)}(d^+) \right], \end{aligned} \quad (3.19)$$

where substitutions  $d^- = -\frac{1}{2}k(r-z)$  and  $d^+ = \frac{1}{2}k(r+z)$  have been introduced to make the expression more compact, and will be used throughout the chapter. Note also that  $\frac{\partial d^-}{\partial \rho} = -\frac{k}{2} \frac{\rho}{r}$  and  $\frac{\partial d^+}{\partial \rho} = \frac{k}{2} \frac{\rho}{r}$ .

The starting term of the recurrence,  $W_0$ , can be resolved by relating it to the similar-looking Sommerfeld integral [24], [30]:

$$\frac{e^{-jkr}}{4\pi r} = \frac{j}{8\pi} \int_{-\infty}^{\infty} \frac{e^{-jz\sqrt{k^2-k_\rho^2}}}{\sqrt{k^2-k_\rho^2}} H_0^{(2)}(\rho k_\rho) k_\rho dk_\rho. \quad (3.20)$$

The differences between this integral and the one in (3.10) (for  $n = 0$ ) are that in this one the integration limits are from  $-\infty$  to  $\infty$ , and that instead of the Bessel function, there is a Hankel function of the second kind in the subintegral function. To revert to the integration limits from 0 to  $\infty$ , we need to separate the even from the odd part of the subintegral function. The integration of the odd part from  $-\infty$  to  $\infty$  will give a zero result, while the integration of the even part from  $-\infty$  to  $\infty$  will amount to twice the integration of the same integrand from 0 to  $\infty$ . Looking at (3.20), one can notice that the first factor in the

subintegral function,  $e^{-jz\sqrt{k^2-k_\rho^2}}/\sqrt{k^2-k_\rho^2}$ , is even in  $k_\rho$ , while the last factor ( $k_\rho$ ) is odd.

The Hankel function is neither even nor odd, but can be split in its even and odd parts:

$$H_0^{(2)}(z) = H_{0,e}^{(2)}(z) + H_{0,o}^{(2)}(z),$$

which gives

$$\begin{aligned} \frac{e^{-jkr}}{4\pi r} &= \frac{j}{8\pi} \int_{-\infty}^{\infty} \frac{e^{-jz\sqrt{k^2-k_\rho^2}}}{\sqrt{k^2-k_\rho^2}} (H_{0,e}^{(2)}(\rho k_\rho) + H_{0,o}^{(2)}(\rho k_\rho)) k_\rho dk_\rho \\ &= \frac{j}{4\pi} \int_0^{\infty} \frac{e^{-jz\sqrt{k^2-k_\rho^2}}}{\sqrt{k^2-k_\rho^2}} H_{0,o}^{(2)}(\rho k_\rho) k_\rho dk_\rho, \end{aligned} \quad (3.21)$$

because  $H_{0,e}^{(2)}(\rho k_\rho)$  multiplied by the other two factors will give an overall odd function.

The even and the odd parts of the Hankel function are found using the following relations:

$$\begin{aligned} H_{0,e}^{(2)}(z) &= \frac{1}{2} (H_0^{(2)}(z) + H_0^{(2)}(-z)), \\ H_{0,o}^{(2)}(z) &= \frac{1}{2} (H_0^{(2)}(z) - H_0^{(2)}(-z)). \end{aligned}$$

The relationship with the Bessel function used in (3.10) is established through the definition of the Hankel function of the second kind:

$$H_0^{(2)}(z) = J_0(z) - jY_0(z).$$

Applying the following relations for the Bessel and Neumann functions of order zero [26]:

$$\begin{aligned} J_0(-z) &= J_0(z), \\ Y_0(-z) &= Y_0(z) + 2jJ_0(z), \end{aligned}$$

we get

$$H_0^{(2)}(-z) = J_0(-z) - jY_0(-z) = H_0^{(2)}(z) + 2J_0(z),$$

which can be rewritten as

$$J_0(z) = \frac{1}{2} (H_0^{(2)}(-z) - H_0^{(2)}(z)) = -H_{0,o}^{(2)}(z). \quad (3.22)$$

Therefore, the odd part of the Hankel function of the second kind and order zero amounts to a negative Bessel function of order zero, which is a rather peculiar result because the Bessel function of order zero itself is an even function, as stated above. Nevertheless, with this result applied to (3.21), we finally obtain



$$\frac{e^{-jkr}}{4\pi r} = -\frac{j}{4\pi} \int_0^{\infty} \frac{e^{-jz\sqrt{k^2-k_\rho^2}}}{\sqrt{k^2-k_\rho^2}} J_0(\rho k_\rho) k_\rho dk_\rho, \quad (3.23)$$

and thus

$$W_0 = j \frac{e^{-jkr}}{r}. \quad (3.24)$$

The second starting term of the recurrence,  $W_1$ , is found by setting  $n = 0$  in the recurrence (3.18), which yields

$$\frac{\partial}{\partial \rho} I_0^{(g)} = \frac{e^{j\phi}}{2j} W_{-1} - \frac{e^{-j\phi}}{2j} W_1. \quad (3.25)$$

Applying (3.10) and the following relation for the Bessel functions [26]

$$J_{-1}(z) = -J_1(z), \quad (3.26)$$

we get

$$\frac{\partial}{\partial \rho} I_0^{(g)} = -2 \frac{e^{-j\phi}}{2j} W_1, \quad (3.27)$$

which, using the result of (3.14), finally yields the closed-form expression for  $W_1$ :

$$\begin{aligned} W_1 &= -j e^{j\phi} \frac{\partial}{\partial \rho} I_0^{(g)} \\ &= -j e^{j\phi} \frac{\partial}{\partial \rho} \left( (-j) \frac{\pi}{2} J_0(d^-) H_0^{(2)}(d^+) \right) \\ &= -e^{j\phi} \frac{k\pi}{4} \frac{\rho}{r} \left[ J_1(d^-) H_0^{(2)}(d^+) - J_0(d^-) H_1^{(2)}(d^+) \right]. \end{aligned} \quad (3.28)$$

For convenience, the derivatives of the substitutions  $d^-$  and  $d^+$  are repeated here:

$$\frac{\partial d^-}{\partial \rho} = -\frac{k}{2} \frac{\rho}{r}; \quad \frac{\partial d^+}{\partial \rho} = \frac{k}{2} \frac{\rho}{r}.$$

To summarise, all positive higher-order wave objects can be calculated analytically using the recurrence relation (3.18) with (3.24) and (3.28) as the starting terms, and employing (3.19) to calculate the derivatives of the Gradshteyn integral. However, the Fourier series expansion of the field spectrum, introduced in (3.3), contains both positive and negative indices  $n$ . Therefore, it is necessary to find a way to calculate negative-order wave objects, especially since the one of the conditions on the convergence of the Gradshteyn integral (3.13) requires that the order  $\nu$  of the Bessel function be greater than -1 [25]. Fortunately, owing to the fact

that in this case only Bessel functions of integer order  $n$  are used, it is possible to relate the negative-order wave objects to the positive-order ones by using this identity for the Bessel functions [26]:

$$J_{-n}(z) = (-1)^n J_n(z). \quad (3.29)$$

Inserting this into (3.10), we have

$$W_{-n}(\rho, \phi, \tilde{z}) = e^{-jn\phi} \int_0^{\infty} \frac{e^{-j\tilde{z}\sqrt{k^2 - k_\rho^2}}}{\sqrt{k^2 - k_\rho^2}} J_{-n}(\rho k_\rho) k_\rho dk_\rho = (-1)^n e^{-2jn\phi} W_n(\rho, \phi, \tilde{z}). \quad (3.30)$$

### 3.1.2. Numerical Considerations

#### 3.1.2.1. Convergence of the Gradshteyn Integral

In the previous section it was stated that conditions applied to the convergence of the Gradshteyn integral. Apart from the condition on the order of the Bessel function being greater than  $-1$ , as just explained, the other conditions related to the integral in (3.13) are

$$\begin{aligned} \operatorname{Re}\{\alpha\} &> 0, \\ \operatorname{Re}\{\beta\} &> 0, \\ \gamma &> 0. \end{aligned} \quad (3.31)$$

With  $\beta \equiv \varepsilon + jk$ ,  $\varepsilon \rightarrow 0+$ ,  $\gamma \equiv \rho$  and  $\alpha \equiv \tilde{z}$ , potential convergence problems are related to the last of the three parameters. Since  $\tilde{z} = z + jb_{mn}$  and  $b_{mn}$  is a *complex* exponent coming from the GPOF expansion, this translates to the condition

$$\operatorname{Im}\{b_{mn}\} < z, \quad (3.32)$$

which means that, generally speaking, there exists a minimal distance  $z_0$  before which the wave-object expansion cannot be applied. Whether or not there really will be a near-field limit in practice depends on the actual spectrum submitted to the GPOF routine and the GPOF parameters (number of exponents, number of points, etc.) used for the given case. In some cases, all exponents will have negative imaginary parts and there will not be any limitations on the validity of the wave-object expansion, in others it may happen. This is due to the fact that only a *truncated* portion of the spectrum is being approximated – if the fitting were done on the whole spectrum ( $k_\rho \in [0, \infty)$ ), all exponents would have to have negative imaginary parts (assuming the initial electric field spectrum is physical). However, this potential

limitation usually does not pose a real problem: in all simulated cases for this thesis, the largest exponents were of the order of magnitude of the wavelength, and accurate representations of radiated fields were obtained as close as  $0.3\lambda$  from the aperture plane. Since the distances between reflectors in a beam waveguide are of the order of  $100\lambda$  and more, condition (3.32) did not impede the application of the wave objects expansion.

The GPOF expansion was not the primary concern of this thesis and was used as a black box, and the results obtained were numerically stable in a fairly broad range of GPOF expansion parameters. However, it is recommended to work with the minimal number of output exponents, as increasing the number of exponents increases the probability of the fitting procedure picking up on the numerical noise, increasing also the probability of obtaining exponents with positive imaginary parts. The other reason for using the minimal number of exponents is that the speed of the wave-object expansion is directly proportional to the number of GPOF exponents per spectrum harmonic.

### 3.1.2.2. Corrections for Arguments of the Bessel Function in the Second Quadrant

Another mathematical detail that was omitted in the derivations in Sec. 3.1.1 relates to the relationship between the Bessel function and the modified Bessel function, applied when passing from (3.13) to (3.14). The relationship between the two functions actually depends on the quadrant in which the complex input argument is lying [26]:

$$\begin{aligned} I_\nu(z) &= e^{-j\frac{\pi}{2}\nu} J_\nu\left(e^{j\frac{\pi}{2}}z\right), \quad \text{for } -\pi < \arg z \leq \frac{\pi}{2} \\ I_\nu(z) &= e^{j\frac{3\pi}{2}\nu} J_\nu\left(e^{-j\frac{3\pi}{2}}z\right), \quad \text{for } \frac{\pi}{2} < \arg z \leq \pi \end{aligned} \quad (3.33)$$

For half-order Bessel functions (i.e.  $I_{n/2}$  with  $n$  integer), which are used in the derivations herein presented, we get

$$I_{n/2}(z) = \begin{cases} e^{-j\frac{\pi}{4}n} J_{n/2}(jz), & \text{for } -\pi < \arg z \leq \frac{\pi}{2} \\ (-1)^n e^{-j\frac{\pi}{4}n} J_{n/2}(z), & \text{for } \frac{\pi}{2} < \arg z \leq \pi \end{cases}, \quad (3.34)$$

which means that a correction factor  $(-1)^n$  should be included in all formulae to account for the case of the argument supplied to the Bessel function falling into the second quadrant.

Since the argument of the modified Bessel function is  $j\frac{k}{2}(r - \tilde{z})$ , where  $\tilde{z} = z + jb_{mn}$ , the modification has to be applied whenever  $r - \tilde{z}$  lies in the first quadrant of the complex plane.

### 3.1.2.3. Truncation of the Radiation Integral

As explained previously, the GPOF approximation is applied to the Fourier coefficients  $c_n(k_\rho)$  of the starting field spectrum  $\tilde{G}(k_\rho, \alpha)$ . The integral in  $k_\rho$  theoretically spans from zero to infinity, and naturally has to be truncated at a certain  $k_{\rho, max}$ . Hence, the spectrum  $\tilde{G}(k_\rho, \alpha)$  can also be truncated at  $k_{\rho, max}$ , which is of importance in all practical applications of the beam expansion. Here, the goal is to determine where, that is, at which  $k_{\rho, max}$ , the spectrum can be truncated, depending on the distance of the observation point from the source plane and the chosen accuracy criterion.

The integral in (3.1) can be viewed as a sum of plane waves

$$\tilde{h}(k_x, k_y) e^{-j(k_x x + k_y y) - jk_z z}, \quad (3.35)$$

for all possible values of  $(k_x, k_y)$ , with  $k_z = \sqrt{k^2 - k_x^2 - k_y^2}$ . The spectrum can be divided in the so-called visible and invisible regions, i.e. where  $k_x^2 + k_y^2 \leq k^2$  and  $k_x^2 + k_y^2 > k^2$ , respectively. The waves belonging to the visible region are propagating waves, while those in the invisible spectrum are evanescent, since  $-jk_z z$  becomes real and negative. In fact, the exponential term in (3.35) can be seen as the attenuating factor of the plane wave with the amplitude  $\tilde{h}(k_x, k_y)$  at the source plane  $z = 0$ ; at the distance  $z = z_0$ , that plane wave will be attenuated by a factor  $e^{-|k_z|z_0}$ . We choose to neglect contributions of all plane waves whose amplitude at the distance  $z = z_0$  from the source plane has dropped by more than a factor  $c_{min}$ , and want to see up until what  $k_{\rho, max}$  the contributions have to be taken into account. We can write the following criterion:

$$\left| \tilde{h}(k_x, k_y) e^{-j(k_x x + k_y y) - jk_z z} \right| \leq c_{min} \cdot \left| \tilde{h}(k_x, k_y) \right|. \quad (3.36)$$

Since  $\left| e^{-j(k_x x + k_y y)} \right| = 1$ , (3.36) for waves belonging to the invisible spectrum reduces to

$$e^{-z_0 |k_z|} = e^{-z_0 k \sqrt{k_{\rho, max}^2 / k^2 - 1}} \leq c_{min}. \quad (3.37)$$

Substituting  $c_{min} = e^{-p}$  to get a simpler final expression, we see that

$$z_0 k \sqrt{k_{\rho, \max}^2 / k^2 - 1} \leq p, \quad (3.38)$$

which can be rewritten as

$$\frac{k_{\rho, \max}}{k} \leq \sqrt{1 + \frac{(p/2\pi)^2}{(z_0/\lambda_0)^2}}, \quad (3.39)$$

For example, choosing a value of  $p = 4\pi$ , which is equivalent to  $c_{\min} \approx 3.4 \cdot 10^{-6}$ , gives the following simple criterion for truncating the starting radiation integral

$$k_{\rho, \max} = k \sqrt{1 + \frac{4}{(z_0/\lambda_0)^2}}. \quad (3.40)$$

With this as the accuracy criterion, we can investigate how far into the invisible region the spectrum has to be calculated for different distances  $z_0$ . To calculate the field on a plane  $2\lambda$  away from the source plane, we need to integrate up to  $k_{\rho, \max} = k\sqrt{2}$ , while at  $z_0 = 20\lambda$  this drops to  $k_{\rho, \max} \approx 1.005k$ .

In practice, in beam waveguides the distances between elements are almost always much larger than the two shown here as examples, so even with a stronger accuracy criterion than this one, it is hardly ever necessary to integrate past the invisible spectrum border. Consequently, in most practical cases it will be sufficient to get field spectrum information only up to  $k_{\rho, \max} = k$ .

#### 3.1.2.4. Indirect GPOF expansion

As shown in (3.5), the Fourier coefficients  $c_n(k_\rho)$  are approximated with a sum of complex exponentials of the kind

$$c_n(k_\rho) = \sum_{m=1}^M d_{mn} e^{b_{mn} \sqrt{k^2 - k_\rho^2}}, \quad (3.41)$$

which constitutes an *indirect* GPOF expansion, since it takes samples of the function along  $k_\rho$ , but represents it rather as a function of  $k_z = \sqrt{k^2 - k_\rho^2}$ . Conversely, the direct GPOF expansion would take samples of  $c_n(k_\rho)$  and give its approximate representation in terms of a sum of exponentials of  $k_\rho$ .

$$c_n(k_\rho) = \sum_{m=1}^M d''_{mn} e^{b''_{mn} k_\rho}, \quad (3.42)$$

Since the available GPOF algorithms do not by themselves calculate the indirect function approximation, it is necessary to adapt it in order to get the desired expansion. This adaptation is explained here.

The key concern with the indirect GPOF expansion is that taking samples of  $k_\rho$  in the visible spectrum region gives corresponding  $k_z$  real, while passing into the invisible region causes it to change character and become imaginary. The two sampling paths are illustrated in Fig. 3.1. by the solid black line and the dotted black line. This change from the real axis to the imaginary axis presents a problem for the GPOF expansion, which requires equidistant samples, i.e. samples taken along a straight line. In order to satisfy this requirement, the sampling path has to be modified, and is represented in the same figure by the dotted red line. The new samples are taken with respect to the variable  $k_z$ , which corresponds to the curved sampling path (solid red line) in terms of  $k_\rho$ .

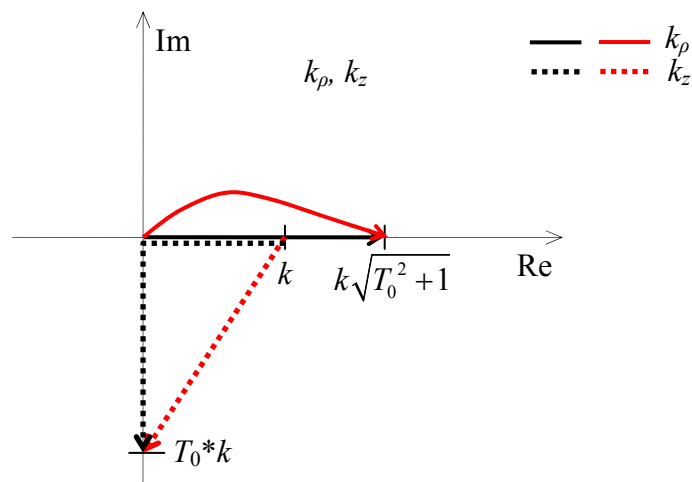


Figure 3.1. Direct (solid black line) and indirect (dotted red line) sampling paths for the GPOF procedure

The new sampling path in  $k_z$  is a straight line, along which there are no problems with the branch cut or the singularity, but the sampling variable is complex. However, it can still be expressed as a linear function of an auxiliary real variable  $t$ . If an auxiliary parameter  $T_0$  is

set, to limit how far (into the invisible spectrum region) the function will be sampled, the following equation is valid for the dotted red line:

$$k_z = k\left(1 - t/T_0\right) - jkt, \quad 0 \leq t \leq T_0. \quad (3.43)$$

For each value of  $t$ ,  $k_z$  and the corresponding  $k_\rho$  are computed, and the corresponding sample is taken. The function is then expanded via regular GPOF in terms of parameter  $t$ , which yields the coefficients  $d'_{mn}$  and  $b'_{mn}$ . These, should be transformed back to  $d_{mn}$  and  $b_{mn}$ , which is done by equating the amplitudes and the exponents of the two different GPOF representations of the same function:

$$c_n(k_\rho) = \sum_{m=1}^M d'_{mn} e^{b'_{mn}t} = \sum_{m=1}^M d_{mn} e^{b_{mn}k_z}. \quad (3.44)$$

Substituting (3.43) into (3.44), we get

$$\sum_{m=1}^M d_{mn} e^{b_{mn}k_z} = \sum_{m=1}^M d'_{mn} e^{b'_{mn}(k(1-t/T_0) - jkt)} = \sum_{m=1}^M d'_{mn} e^{b'_{mn}k} e^{-b'_{mn}k \frac{1+jT_0}{T_0} t}, \quad (3.45)$$

from where these relationships between  $(b_{mn}, d_{mn})$  and  $(b'_{mn}, d'_{mn})$  can be read:

$$b_{mn} = -b'_{mn} \frac{T_0}{k(1+jT_0)}, \quad (3.46)$$

$$d_{mn} = d'_{mn} e^{b'_{mn} \frac{T_0}{1+jT_0}}. \quad (3.47)$$

Since the evanescent waves arising from the invisible part of the spectrum attenuate very rapidly, as shown in Sec. 3.1.2.3, in most cases it is sufficient to expand only the visible part of the spectrum (i.e. in Fig. 3.1. the black straight line from 0 to  $k$  only). In that case, the black dotted line does not extend to the imaginary axis, and relations (3.46) and (3.47) are simply

$$b_{mn} = -b'_{mn}, \quad (3.48)$$

$$d_{mn} = d'_{mn} e^{b'_{mn}k}. \quad (3.49)$$

### 3.1.3. Properties of the Wave Objects

As stated in previous sections, the wave objects used in the realistic case to expand a given spectrum contain each the complex argument  $jb_{mn}$ . With  $b_{mn} = \text{Re}\{b_{mn}\} + j\text{Im}\{b_{mn}\}$ , this means in practice that one has two degrees of freedom when forming a given wave object.

The influence of the real and the imaginary part of  $b$  on the shape of the wave object is shown in Fig. 3.2. It can be seen that the real part of  $b$  attenuates or amplifies the wave object (comparing the plots by rows, the leftmost plot in a row is severely attenuated while the rightmost one is strongly amplified), while the imaginary part of  $b$  influences the direction of the maximum radiation, with a minor effect on its magnitude (comparing the plots by columns, the top plot has the main lobe the closest to the  $z$ -axis, and vice-versa; the amplitudes are not the same in all cases). Also visible in Fig. 3.2. is the minimal distance limitation considered in Sec. 3.1.2. The plots in the top row, obtained with the imaginary part of  $b$  equal to the wavelength, only exist for  $z > \lambda$ , which is, at the chosen distance of  $2\lambda$ , equal to the maximum angle  $\theta$  of  $60^\circ$ . Naturally, as the distance  $z$  from the aperture plane increases, the maximum angle  $\theta$  also increases and tends to  $90^\circ$  in the far-field limit.

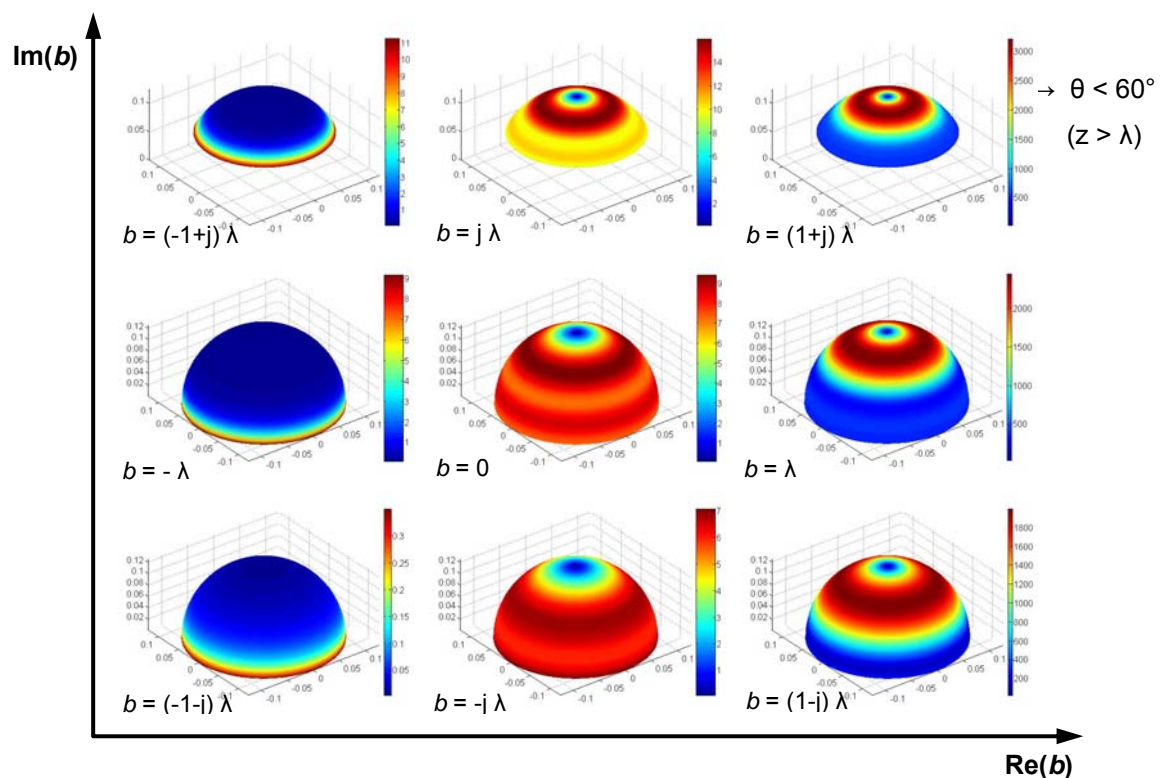


Figure 3.2. Radiation patterns of the first-order wave object ( $W_1$ ) as a function of parameter  $b$ . The values are computed on a sphere of radius  $2\lambda$

Figure 3.3. displays the first three wave objects calculated for the same value of the complex parameter  $b$  and sampled in the  $x$ - $y$  plane for the same value of distance  $z$ . The magnitudes of the three wave objects have been chosen such that the maximum value of the radiated scalar field is approximately equal in all three cases. The  $z$ -axis of the plot represents the absolute



value of the wave object at a given point. As given by (3.24),  $W_0$  produces a field equal to that of the complex source point, with a typical Gaussian profile.  $W_1$  and  $W_2$  on the other hand, as well as all higher-order wave objects, have a zero field on the  $z$ -axis, while the maximum field exists on a circular ring. Since the wave object expands radially as it propagates, a cone of maximum directivity is formed. This is significantly different from all other commonly used wave objects, most of which were briefly introduced in Sec. 2.2, and is the reason why the term "conical beams" has been chosen to describe the wave objects presented in this thesis.

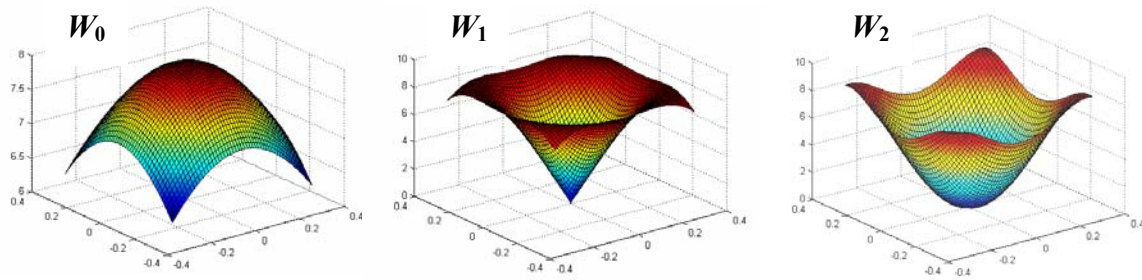


Figure 3.3. Illustration of beams  $W_0$ ,  $W_1$  and  $W_2$  for the same value of complex parameter  $b$ . Except for  $W_0$ , the maximum field points are located on a circle.

## 3.2. Vectorisation of Conical Beams

The complex conical beams satisfy the scalar Helmholtz wave equation. However, to be able to apply them to realistic antenna configurations, an extension to vector fields is necessary. If the vectorised wave objects are to represent actual electromagnetic fields, they must satisfy not only the wave equation, but also Maxwell's equations. For this thesis, two different vectorisation strategies were considered and will be presented in the following subsections. The two strategies differ in the way they interpret the spectrum  $\tilde{F}(k_x, k_y)$  in (3.1).

### 3.2.1. Vectorisation Strategy 1: Fourier Transform Approach

In the first vectorisation strategy, the function  $\tilde{F}(k_x, k_y)$  is constructed as

$$\vec{\tilde{F}}(k_x, k_y) = 2j \vec{\tilde{E}}(k_x, k_y) \sqrt{k^2 - k_x^2 - k_y^2}, \quad (3.50)$$

and each rectangular component of  $\vec{\tilde{F}}$  is submitted to (3.1) individually, giving

$$I'_i(x, y, z) = \frac{1}{4\pi^2} \int_{-\infty}^{\infty} \int_{-\infty}^{\infty} \tilde{E}_i(k_x, k_y) e^{-j(k_x x + k_y y) - jz\sqrt{k^2 - k_x^2 - k_y^2}} dk_x dk_y, \quad (3.51)$$

where index  $i$  stands for any of the three coordinates  $(x, y, z)$ . This is easily recognized as the standard inverse Fourier transform, which relates the spectrum in the aperture plane to the radiated field in another plane. The wave-object expansion can in this context be viewed as an alternative to the Fast Fourier Transform approach commonly used to perform near-field to far-field transformations, with the inherent advantage that, unlike with FFT, there is no limit on spatial resolution – once the compound spectrum  $\vec{F}(k_x, k_y)$  is approximated via the GPOF expansion, the field can be instantly computed at any given point in the upper half-space.

From the electromagnetic perspective though, there is a slight drawback that each component of the radiated field is calculated separately, which means that the quality of the FFT-GPOF approximation will determine to what extent the calculated fields obey Maxwell's equation, i.e. to what extent they really represent physically correct electromagnetic fields. To ensure that the radiated fields satisfy Maxwell's equations regardless of the accuracy of each separate FFT-GPOF expansion, a better, albeit somewhat more mathematically cumbersome, strategy has been found.

### 3.2.2. Vectorisation Strategy 2: Auxiliary Vector Potentials Approach

If the spectrum  $\vec{F}(k_x, k_y)$  in (3.1) is interpreted as one rectangular component of the equivalent magnetic current on the aperture

$$\vec{F}_i(k_x, k_y) = \vec{M}_i(k_x, k_y), \quad (3.52)$$

where  $\vec{M} = 2\vec{E}(k_x, k_y) \times \hat{n}$ ,  $\hat{n}$  being the unit normal vector to the aperture, we can recognize the calculated value of the integral  $I'$  as the corresponding rectangular component of the auxiliary vector potential  $\vec{F}$  (see Sec. 2.1.1):

$$F_i(x, y, z) = \frac{1}{8\pi^2 j} \int_{-\infty}^{\infty} \int_{-\infty}^{\infty} \vec{M}_i(k_x, k_y) \frac{e^{-j(k_x x + k_y y) - jz\sqrt{k^2 - k_x^2 - k_y^2}}}{\sqrt{k^2 - k_x^2 - k_y^2}} dk_x dk_y. \quad (3.53)$$

The fields are obtained indirectly by means of known relationships between the auxiliary vector potentials and the field quantities [26]. Only the tangential components of the equivalent currents are needed to obtain all three components of the output fields in this case:

$$\vec{E} = \hat{x} \left( \frac{1}{\varepsilon} \frac{\partial F_y}{\partial z} \right) - \hat{y} \left( \frac{1}{\varepsilon} \frac{\partial F_x}{\partial z} \right) + \hat{z} \left( \frac{1}{\varepsilon} \left( \frac{\partial F_x}{\partial y} - \frac{\partial F_y}{\partial x} \right) \right). \quad (3.54)$$

It can be demonstrated that a vector field constructed this way from any two functions  $F_x$  and  $F_y$ , which individually satisfy the Helmholtz wave equation, will also satisfy Maxwell's equations. The integral in (3.53) satisfies the scalar wave equation for any analytic function  $\tilde{M}$ , owing to the theory of Green's functions [31]. This means that in practice, no matter how good an approximation of the actual equivalent magnetic current  $\tilde{M}$  is ( $\tilde{M}$  is obtained via FFT expansion and GPOF fitting), the final output components of the calculated electric field will be linked between themselves in such a way that the overall vector electric field so obtained will satisfy Maxwell's equations.

The downside of this approach compared to the first one is that the first one can make use of the scalar form of conical beams, while this one necessitates the development of analytic expressions for the derivatives of conical beams with respect to all three coordinates. Furthermore, extra attention must be given to the subcase of small argument  $d^- = -\frac{k}{2}(r - \tilde{z})$  of the Bessel function.

However, due to the important advantage of working with auxiliary vector potentials from the physical point of view, this was the chosen approach for all test cases presented in the thesis. The necessary mathematical derivations are presented in the following section.

### 3.2.3. Differentiation of Complex Conical Beams

From Eqs. (3.8) and (3.53) we see that the auxiliary vector electric potential can be calculated via a summation of conical beams as

$$F_i(\rho, \phi, z) = \sum_n \sum_{m=1}^M a_{mm,i} W_n(\rho, \phi, z + j b_{mm,i}), \quad (3.55)$$

where  $i$  stands for  $x$  or  $y$  component of the potential. Bearing in mind Eq. (3.54), we can see that in order to calculate the radiated electric field, the recurrence relation (3.18) also has to be differentiated. The relation is repeated here for convenience:

$$W_{n+1} = e^{j2\phi} W_{n-1} - 2j e^{j(n+1)\phi} \frac{\partial}{\partial \rho} I_n^{(g)}. \quad (3.56)$$

### 3.2.3.1. Derivation of $\frac{\partial W_n}{\partial z}$

Differentiating (3.56) with respect to  $z$  yields:

$$\left[ \frac{\partial W}{\partial z} \right]_{n+1} = e^{j2\phi} \left[ \frac{\partial W}{\partial z} \right]_{n-1} - 2j e^{j(n+1)\phi} \frac{\partial}{\partial z} \left( \frac{\partial}{\partial \rho} I_n^{(g)} \right). \quad (3.57)$$

As in the case of the original recurrence, the explicit expressions for  $\frac{\partial W_0}{\partial z}$  and  $\frac{\partial W_1}{\partial z}$ , and the last term  $\frac{\partial}{\partial z} \left( \frac{\partial}{\partial \rho} I_n^{(g)} \right)$  have to be derived. For the zero-order term, we have from (3.24)

$$W_0 = j \frac{e^{-jkr}}{r} = j \frac{e^{-jk\sqrt{\rho^2+z^2}}}{\sqrt{\rho^2+z^2}}, \quad (3.58)$$

which gives

$$\begin{aligned} \frac{\partial W_0}{\partial z} &= j \frac{\left( \frac{-jkz}{\sqrt{\rho^2+z^2}} e^{-jk\sqrt{\rho^2+z^2}} \right) \sqrt{\rho^2+z^2} - e^{-jk\sqrt{\rho^2+z^2}} \frac{z}{\sqrt{\rho^2+z^2}}}{\rho^2+z^2}, \\ &= W_0 \left( \frac{-jkz}{r} - \frac{z}{r^2} \right). \end{aligned} \quad (3.59)$$

The  $W_1$  term was found in Sec. 3.1.1 as:

$$W_1 = -e^{j\phi} \frac{k\pi\rho}{4r} \left[ J_1 \left( -\frac{k}{2}(r-z) \right) H_0^{(2)} \left( \frac{k}{2}(r+z) \right) - J_0 \left( -\frac{k}{2}(r-z) \right) H_1^{(2)} \left( \frac{k}{2}(r+z) \right) \right]. \quad (3.60)$$

It contains three terms which depend on  $z$ . To keep the derivation legible, first each of their derivatives will be derived separately, and the results will be merged in the final sum. The Bessel and Hankel function are differentiated for the general order  $n$ , so as to reuse the results at a later time. We have:

$$\frac{\partial}{\partial z} \frac{1}{r} = \frac{\partial}{\partial z} (\rho^2+z^2)^{-1/2} = -\frac{1}{2} (\rho^2+z^2)^{-3/2} 2z = -\frac{z}{r^3}; \quad (3.61)$$

$$\frac{\partial}{\partial z} J_n \left( -\frac{k}{2}(r-z) \right) = \frac{k}{2} \left( 1 - \frac{z}{r} \right) \frac{1}{2} \left[ J_{n-1} \left( -\frac{k}{2}(r-z) \right) - J_{n+1} \left( -\frac{k}{2}(r-z) \right) \right]; \quad (3.62)$$

$$\frac{\partial}{\partial z} H_n^{(2)} \left( \frac{k}{2}(r+z) \right) = \frac{k}{2} \left( 1 + \frac{z}{r} \right) \frac{1}{2} \left[ H_{n-1}^{(2)} \left( \frac{k}{2}(r+z) \right) - H_{n+1}^{(2)} \left( \frac{k}{2}(r+z) \right) \right]. \quad (3.63)$$

Recalling the substitutions  $d^- = -\frac{k}{2}(r-z)$ ,  $d^+ = \frac{k}{2}(r+z)$ , the first-order conical beam  $W_1$  is differentiated as follows:

$$\begin{aligned}
\frac{\partial W_1}{\partial z} &= e^{j\phi} \frac{k\pi\rho}{4} \frac{\partial}{\partial z} \left( \frac{1}{r} \left[ J_1(d^-) H_0^{(2)}(d^+) - J_0(d^-) H_1^{(2)}(d^+) \right] \right) = \\
&= e^{j\phi} \frac{k\pi\rho}{4} \left( -\frac{z}{r^3} \right) \left[ J_1(d^-) H_0^{(2)}(d^+) - J_0(d^-) H_1^{(2)}(d^+) \right] \\
&\quad + e^{j\phi} \frac{k\pi}{4} \frac{\rho}{r} \frac{\partial}{\partial z} \left( \left[ J_1(d^-) H_0^{(2)}(d^+) - J_0(d^-) H_1^{(2)}(d^+) \right] \right) = \\
&= -\frac{z}{r^2} W_1 + e^{j\phi} \frac{k\pi}{4} \frac{\rho}{r} \frac{\partial}{\partial z} \left( \left[ J_1(d^-) H_0^{(2)}(d^+) - J_0(d^-) H_1^{(2)}(d^+) \right] \right).
\end{aligned}$$

Applying (3.62), (3.63) and the auxiliary relations  $J_{-1}(z) = -J_1(z)$ ,  $H_{-1}^{(2)}(z) = -H_1^{(2)}(z)$  [26], many of the terms cancel out and the final expression can be written in this way:

$$\begin{aligned}
\frac{\partial W_1}{\partial z} &= -\frac{z}{r^2} W_1 + e^{j\phi} \frac{k^2\pi}{16} \frac{\rho}{r} \left( J_0(d^-) H_2^{(2)}(d^+) - J_2(d^-) H_0^{(2)}(d^+) \right) \\
&\quad + e^{j\phi} \frac{k^2\pi}{16} \frac{\rho z}{r^2} \left( J_2(d^-) H_0^{(2)}(d^+) + J_0(d^-) H_2^{(2)}(d^+) \right) \\
&\quad - 2J_0(d^-) H_0^{(2)}(d^+) - 4J_1(d^-) H_1^{(2)}(d^+).
\end{aligned} \tag{3.64}$$

In the last of the three steps, we proceed to differentiate the  $\rho$ -derivative of the Gradstheyn integral. The starting point is Eq. (3.19):

$$\frac{\partial I_n^{(g)}}{\partial \rho} = (-j)^{n-1} \frac{k\pi}{8} \frac{\rho}{r} \cdot f(d^-, d^+), \tag{3.65}$$

where

$$\begin{aligned}
f(d^-, d^+) &= J_{n/2+1}(d^-) H_{n/2}^{(2)}(d^+) - J_{n/2-1}(d^-) H_{n/2}^{(2)}(d^+) \\
&\quad + J_{n/2}(d^-) H_{n/2-1}^{(2)}(d^+) - J_{n/2}(d^-) H_{n/2+1}^{(2)}(d^+)
\end{aligned}$$

Differentiating with respect to  $z$  gives

$$\frac{\partial}{\partial z} \left( \frac{\partial}{\partial \rho} I_n^{(g)} \right) = (-j)^{n-1} \frac{k\pi\rho}{8} \frac{\partial}{\partial z} \left[ \frac{1}{r} \right] \cdot f(d^-, d^+) + (-j)^{n-1} \frac{k\pi}{8} \frac{\rho}{r} \frac{\partial}{\partial z} \left[ f(d^-, d^+) \right]. \tag{3.66}$$

To avoid obtaining terms of order  $n/2-2$  after the differentiation in  $z$ , we use alternative expressions for the derivatives of Bessel and Hankel functions:

$$b'_k(z) = b_{k-1}(z) - \frac{k}{z} b_k(z) = -b_{k+1}(z) + \frac{k}{z} b_k(z), \tag{3.67}$$

where  $b_k$  denotes either a Bessel or a Hankel function of order  $k$ . This approach ensures that no Bessel functions of order  $-3/2$  are present in the computation of the starting terms of the recurrence, which means a milder and more easily tractable singularity (the lowest-order

Bessel function is  $J_{-1/2}$  in this case), as will be shown later in this section. Applying (3.61) and (3.67) in (3.66), after some manipulations we eventually obtain

$$\begin{aligned} \frac{\partial}{\partial z} \left( \frac{\partial}{\partial \rho} I_n^{(g)} \right) &= -\frac{z}{r^2} \frac{\partial}{\partial \rho} I_n^{(g)} \\ &+ (-j)^{n-1} \frac{k^2 \pi}{8} \frac{\rho z}{r^2} \left( 2 J_{n/2} H_{n/2}^{(2)} - J_{n/2-1} H_{n/2+1}^{(2)} - J_{n/2+1} H_{n/2-1}^{(2)} \right) \\ &+ (-j)^{n-1} \frac{k \pi}{8} \frac{\rho}{r^2} \left( J_{n/2-1} H_{n/2}^{(2)} - J_{n/2+1} H_{n/2}^{(2)} + J_{n/2} H_{n/2-1}^{(2)} - J_{n/2} H_{n/2+1}^{(2)} \right). \end{aligned} \quad (3.68)$$

Note that the arguments of the Bessel and Hankel functions have been completely omitted in the above expression to keep it relatively compact; the functions are, however, still computed with respective arguments  $d^-$  and  $d^+$ , as before.

When  $n = 1$ ,  $J_{n/2-1}$  terms diverge for points close to the  $z$ -axis (where  $d^- = -\frac{k}{2}(r-z)$  is small), and special care needs to be taken to be able to calculate  $\frac{\partial W_n}{\partial z}$  in that area. The whole expression  $\frac{\partial}{\partial z} \left( \frac{\partial}{\partial \rho} I_n^{(g)} \right)$  stays finite, because  $\rho$  goes to zero when  $d^- \rightarrow 0$  and suppresses the growth of  $J_{-1/2}$ , but numerical difficulties may be encountered while dividing very small numbers and the error may be carried from  $\frac{\partial W_1}{\partial z}$  onto higher-order terms, due to the use of the recurrence formula for their computation. It is therefore necessary to find the analytical limit for  $\frac{\partial W_1}{\partial z}$  for the case of small argument  $d^-$ . To find the limit for  $d^- \rightarrow 0$ , we make use of the following identities [26]:

$$J_{\nu-1}(z) = \frac{2\nu}{z} J_\nu(z) - J_{\nu+1}(z) \Rightarrow J_{-1/2}(d^-) = -\frac{2}{k(r-z)} J_{1/2}(d^-) - J_{3/2}(d^-); \quad (3.69)$$

$$J_\nu(z) \approx \left(\frac{z}{2}\right)^\nu / \Gamma(\nu+1) \Rightarrow J_{1/2}(d^-) \approx j \sqrt{\frac{k}{\pi}} \sqrt{r-z}. \quad (3.70)$$

where  $\Gamma(3/2) = \sqrt{\pi/4}$ . Using (3.69) in (3.68), we get

$$\begin{aligned}
\frac{\partial}{\partial z} \left( \frac{\partial}{\partial \rho} I_1^{(g)} \right) &= -\frac{z}{r^2} \frac{\partial}{\partial \rho} I_1^{(g)} \\
&+ \frac{k\pi}{8} \frac{\rho}{r} k \left( 2J_{1/2} H_{1/2}^{(2)} - J_{3/2} H_{-1/2}^{(2)} - J_{3/2} H_{3/2}^{(2)} \right) \\
&+ \frac{k\pi}{8} \frac{\rho}{r} \frac{1}{r} \left( -2J_{3/2} H_{1/2}^{(2)} + J_{1/2} H_{-1/2}^{(2)} - J_{1/2} H_{3/2}^{(2)} \right) \\
&+ \frac{k\pi}{8} \frac{\rho}{r} \left( k \frac{2}{k(r-z)} J_{1/2} H_{3/2}^{(2)} - \frac{1}{r} \frac{2}{k(r-z)} J_{1/2} H_{1/2}^{(2)} \right)
\end{aligned}$$

and, upon applying (3.70) and noticing that  $\rho = \sqrt{r^2 - z^2} = \sqrt{k(r-z)(r+z)}$ ,

$$\begin{aligned}
\frac{\partial}{\partial z} \left( \frac{\partial}{\partial \rho} I_1^{(g)} \right) &= -\frac{z}{r^2} \frac{\partial}{\partial \rho} I_1^{(g)} \\
&+ \frac{k\pi}{8} \frac{\rho}{r} k \left( 2J_{1/2} H_{1/2}^{(2)} - J_{3/2} H_{-1/2}^{(2)} - J_{3/2} H_{3/2}^{(2)} \right) \\
&+ \frac{k\pi}{8} \frac{\rho}{r^2} \left( -2J_{3/2} H_{1/2}^{(2)} + J_{1/2} H_{-1/2}^{(2)} - J_{1/2} H_{3/2}^{(2)} \right) \\
&+ j \frac{\sqrt{k\pi}}{4} \left[ k H_{3/2}^{(2)} - \frac{1}{r} H_{1/2}^{(2)} \right] \frac{\sqrt{r+z}}{r}.
\end{aligned} \tag{3.71}$$

### 3.2.3.2. Derivation of $\frac{\partial W_n}{\partial x}$

The steps needed to obtain the necessary relations for calculating  $\frac{\partial W_n}{\partial x}$  are in principle the same as those applied in the previous section, however the final expressions will be rather more complicated than in the previous case. Looking at the starting recurrence

$$W_{n+1} = e^{j2\phi} W_{n-1} - 2j e^{j(n+1)\phi} \frac{\partial}{\partial \rho} I_n^{(g)},$$

one can notice that now not only  $W_{n-1}$  and  $\frac{\partial}{\partial \rho} I_n^{(g)}$  depend on  $x$ , but also the two exponential factors  $e^{j2\phi}$  and  $e^{j(n+1)\phi}$ . Before proceeding, the necessary auxiliary differentials will be derived here for future reference. Since  $\phi = \tan^{-1} \frac{y}{x}$ , we have

$$\frac{\partial \phi}{\partial x} = \frac{1}{1 + (y/x)^2} \left( -\frac{y}{x^2} \right) = -\frac{y}{x^2 + y^2} = -\frac{y}{\rho^2}; \tag{3.72}$$

$$\frac{\partial \phi}{\partial y} = \frac{1}{1 + (y/x)^2} \left( \frac{1}{x} \right) = \frac{x}{x^2 + y^2} = \frac{x}{\rho^2}. \tag{3.73}$$

Hence, the recurrence equation for the derivatives of complex conical beams with respect to coordinate  $x$  becomes

$$\begin{aligned} \left[ \frac{\partial W}{\partial x} \right]_{n+1} &= 2j \left( -\frac{y}{\rho^2} \right) e^{j2\phi} W_{n-1} + e^{j2\phi} \left[ \frac{\partial W}{\partial x} \right]_{n-1} \\ &\quad - 2j \left( j(n+1) \right) \left( -\frac{y}{\rho^2} \right) e^{j(n+1)\phi} \frac{\partial}{\partial \rho} I_n^{(g)} - 2j e^{j(n+1)\phi} \frac{\partial}{\partial x} \left( \frac{\partial}{\partial \rho} I_n^{(g)} \right) \end{aligned}$$

which can be simplified by rewriting  $(n+1)j = 2j + (n-1)j$  and splitting the third term in the above expression in two, which gives

$$\begin{aligned} \left[ \frac{\partial W}{\partial x} \right]_{n+1} &= -2j \frac{y}{\rho^2} W_{n+1} + e^{j2\phi} \left[ \frac{\partial W}{\partial x} \right]_{n-1} \\ &\quad - 2(n-1) \frac{y}{\rho^2} e^{j(n+1)\phi} \frac{\partial}{\partial \rho} I_n^{(g)} - 2j e^{j(n+1)\phi} \frac{\partial}{\partial x} \left( \frac{\partial}{\partial \rho} I_n^{(g)} \right). \end{aligned} \quad (3.74)$$

$W_{n+1}$  and  $\frac{\partial}{\partial \rho} I_n^{(g)}$  are already available from the scalar wave-objects expansion, therefore

again we only have to find the expressions for  $\frac{\partial W_0}{\partial x}$ ,  $\frac{\partial W_1}{\partial x}$  and  $\frac{\partial}{\partial x} \left( \frac{\partial}{\partial \rho} I_n^{(g)} \right)$  in order to have a well-defined recurrence relation.

To find  $\frac{\partial W_0}{\partial x}$ , it is sufficient to replace  $z$ 's with  $x$ 's in (3.59), owing to the symmetry in the expression:

$$\frac{\partial W_0}{\partial x} = W_0 \left( \frac{-jkx}{r} - \frac{x}{r^2} \right), \quad (3.75)$$

For  $\frac{\partial W_1}{\partial x}$  and higher-order objects, the following auxiliary identities are used

$$\frac{\partial}{\partial x} e^{j\phi} = -\frac{jy}{\rho^2} e^{j\phi}, \quad (3.76)$$

$$\frac{\partial}{\partial x} \frac{\rho}{r} = \frac{\frac{x}{r} r - \rho \frac{x}{r}}{r^2} = \frac{\rho}{r} \left( \frac{x}{\rho^2} - \frac{x}{r^2} \right), \quad (3.77)$$

$$\frac{\partial}{\partial x} J_n(d^-) = -\frac{kx}{4r} \left( J_{n-1}(d^-) - J_{n+1}(d^-) \right), \quad (3.78)$$

$$\frac{\partial}{\partial x} H_n^{(2)}(d^+) = \frac{kx}{4r} \left( H_{n-1}^{(2)}(d^+) - H_{n+1}^{(2)}(d^+) \right). \quad (3.79)$$



The arguments of Bessel and Hankel functions will again be suppressed in the following expressions. The derivative of  $W_1$  with respect to  $x$  is, after some manipulations,

$$\frac{\partial W_1}{\partial x} = \left( \frac{x - jy}{\rho^2} - \frac{x}{r^2} \right) W_1 + e^{j\phi} \frac{k^2 \pi}{16} \frac{x \rho}{r^2} \left[ -2 J_0 H_0^{(2)} + J_2 H_0^{(2)} + J_0 H_2^{(2)} - 4 J_1 H_1^{(2)} \right]. \quad (3.80)$$

As the starting point for the derivation of  $\frac{\partial}{\partial x} \left( \frac{\partial}{\partial \rho} I_n^{(g)} \right)$ , we repeat  $\frac{\partial}{\partial \rho} I_n^{(g)}$  from (3.65):

$$\frac{\partial I_n^{(g)}}{\partial \rho} = (-j)^{n-1} \frac{k\pi}{8} \frac{\rho}{r} \cdot f(d^-, d^+), \quad (3.81)$$

where

$$\begin{aligned} f(d^-, d^+) &= J_{n/2+1}(d^-) H_{n/2}^{(2)}(d^+) - J_{n/2-1}(d^-) H_{n/2}^{(2)}(d^+) \\ &\quad + J_{n/2}(d^-) H_{n/2-1}^{(2)}(d^+) - J_{n/2}(d^-) H_{n/2+1}^{(2)}(d^+). \end{aligned}$$

Two parts which depend on  $x$  can be identified in Eq. (3.81):

$$\frac{\partial}{\partial x} \left( \frac{\partial}{\partial \rho} I_n^{(g)} \right) = (-j)^{n-1} \frac{k\pi}{8} \frac{\partial}{\partial x} \left[ \frac{\rho}{r} \right] \cdot f(d^-, d^+) + (-j)^{n-1} \frac{k\pi}{8} \frac{\rho}{r} \frac{\partial}{\partial x} [f(d^-, d^+)] \quad (3.82)$$

As in the case of  $\frac{\partial}{\partial z} \left( \frac{\partial}{\partial \rho} I_n^{(g)} \right)$ , alternative expressions for the derivatives of Bessel and Hankel functions from (3.67) are used, yielding

$$\begin{aligned} \frac{\partial}{\partial x} \left( \frac{\partial}{\partial \rho} I_n^{(g)} \right) &= \left( \frac{x}{\rho^2} - \frac{x}{r^2} \right) \frac{\partial}{\partial \rho} I_n^{(g)} + (-j)^{n-1} \frac{k\pi}{8} \frac{\rho x}{r^2} \cdot \\ &\quad \cdot \left[ \frac{k}{2} J_{n/2} H_{n/2}^{(2)} + \frac{n/2 - 1}{r - z} J_{n/2-1} H_{n/2}^{(2)} - \frac{k}{2} J_{n/2-1} H_{n/2+1}^{(2)} + \frac{n/2}{r + z} J_{n/2-1} H_{n/2}^{(2)} \right. \\ &\quad + \frac{k}{2} J_{n/2} H_{n/2}^{(2)} + \frac{n/2 + 1}{r - z} J_{n/2+1} H_{n/2}^{(2)} - \frac{k}{2} J_{n/2+1} H_{n/2-1}^{(2)} + \frac{n/2}{r + z} J_{n/2+1} H_{n/2}^{(2)} \\ &\quad - \frac{k}{2} J_{n/2+1} H_{n/2-1}^{(2)} - \frac{n/2}{r - z} J_{n/2} H_{n/2-1}^{(2)} + \frac{k}{2} J_{n/2} H_{n/2}^{(2)} - \frac{n/2 + 1}{r + z} J_{n/2} H_{n/2-1}^{(2)} \\ &\quad \left. - \frac{k}{2} J_{n/2-1} H_{n/2+1}^{(2)} - \frac{n/2}{r - z} J_{n/2} H_{n/2+1}^{(2)} + \frac{k}{2} J_{n/2} H_{n/2}^{(2)} - \frac{n/2 + 1}{r + z} J_{n/2} H_{n/2+1}^{(2)} \right]. \end{aligned}$$

Sorting and grouping together some of the elements in the square brackets above, after a few more manipulations (using also  $J_{\nu-1}(z) + J_{\nu+1}(z) = \frac{2\nu}{z} J_{\nu}(z)$ ), the final result is

$$\begin{aligned}
\frac{\partial}{\partial x} \left( \frac{\partial}{\partial \rho} I_n^{(g)} \right) &= \left( \frac{x}{\rho^2} - \frac{x}{r^2} \right) \frac{\partial}{\partial \rho} I_n^{(g)} + (-j)^{n-1} \frac{k\pi}{8} \frac{\rho x}{r^2} \\
&\cdot \left[ \left( 2k J_{n/2} H_{n/2}^{(2)} - k J_{n/2-1} H_{n/2+1}^{(2)} - k J_{n/2+1} H_{n/2-1}^{(2)} \right) \right. \\
&\quad - \frac{2n^2}{k(r^2-z^2)} J_{n/2} H_{n/2}^{(2)} \\
&\quad + \frac{1}{2(r-z)} \left( (n-2) J_{n/2-1} H_{n/2}^{(2)} + (n+2) J_{n/2+1} H_{n/2}^{(2)} \right) \\
&\quad \left. - \frac{1}{2(r+z)} \left( (n-2) J_{n/2} H_{n/2-1}^{(2)} + (n+2) J_{n/2} H_{n/2+1}^{(2)} \right) \right].
\end{aligned} \tag{3.83}$$

Similarly to the  $z$ -derivative of the Gradshteyn integral shown in the previous section, additional steps are required to calculate small-argument values (in the vicinity of the  $z$ -axis) of the above derivative for  $n = 1$ . It turns out that it is simpler to do this by modifying first the starting expression for  $\frac{\partial}{\partial \rho} I_1^{(g)}$ , so as to not have any negative order Bessel functions inside.

Using the identity  $J_{\nu-1}(z) + J_{\nu+1}(z) = \frac{2\nu}{z} J_{\nu}(z)$ , we get

$$\frac{\partial}{\partial \rho} I_1^{(g)} = \frac{k\pi}{8} \frac{\rho}{r} \left[ -\frac{2}{k(r-z)} J_{1/2} H_{1/2}^{(2)} - 2 J_{3/2} H_{1/2}^{(2)} - J_{1/2} H_{-1/2}^{(2)} - J_{1/2} H_{3/2}^{(2)} \right]. \tag{3.84}$$

Despite the factor  $(r-z)$  in the denominator, the expression is still well-behaved when  $(r-z) \rightarrow 0$  because the pole is cancelled by the zeros coming from the factors  $\rho$  and  $J_{1/2}$ .

The following manipulations are performed on that term in order to arrive at a numerically stable expression:

$$\begin{aligned}
\frac{k\pi}{8} \frac{\rho}{r} \left( \frac{1}{d^-} J_{1/2}(d^-) H_{1/2}^{(2)}(d^+) \right) &= -\frac{k}{4} \frac{\rho}{r} \left( \sqrt{-\frac{\pi}{2d^-}} \right)^2 J_{1/2}(d^-) H_{1/2}^{(2)}(d^+) \\
&= -\frac{k}{4} \frac{\rho}{r} \sqrt{-\frac{\pi}{2d^-}} \left( \sqrt{-\frac{\pi}{2d^-}} J_{1/2}(d^-) \right) H_{1/2}^{(2)}(d^+) \\
&= -j \frac{k}{4} \frac{\sqrt{(r-z)(r+z)}}{r} \sqrt{\frac{\pi}{k(r-z)}} \frac{\sin(d^-)}{d^-} H_{1/2}^{(2)}(d^+) \\
&= -j \frac{\sqrt{k\pi}}{4} \frac{\sqrt{(r+z)}}{r} \frac{\sin(d^-)}{d^-} H_{1/2}^{(2)}(d^+),
\end{aligned}$$

The key step in the above derivation is applying the defining equation of the spherical Bessel function of order zero [26]:

$$j_0(z) = \sqrt{\frac{\pi}{2z}} J_{1/2}(z) = \frac{\sin z}{z}.$$

Therefore, the expression that will be differentiated with respect to  $x$ , and to which the small-argument approximation is sought, is

$$\begin{aligned} \frac{\partial}{\partial \rho} I_1^{(g)} = & -j \frac{\sqrt{k\pi}}{4} \frac{\sqrt{(r+z)}}{r} \frac{\sin(d^-)}{d^-} H_{1/2}^{(2)}(d^+) \\ & - \frac{k\pi}{8} \frac{\rho}{r} \left[ 2 J_{3/2}(d^-) H_{1/2}^{(2)}(d^+) + J_{1/2}(d^-) H_{-1/2}^{(2)}(d^+) + J_{1/2}(d^-) H_{3/2}^{(2)}(d^+) \right]. \end{aligned} \quad (3.85)$$

The differentiation of the first block above gives

$$\begin{aligned} \frac{\partial A}{\partial x} = & +j \frac{\sqrt{k\pi}}{4} \frac{2xz + xr}{2r^3 \sqrt{(r+z)}} \frac{\sin(d^-)}{d^-} H_{1/2}^{(2)}(d^+) \\ & + j \frac{\sqrt{k\pi}}{4} \frac{\sqrt{(r+z)}}{r} \frac{kx \cos(d^-) \cdot (d^-) - \sin(d^-)}{(d^-)^2} H_{1/2}^{(2)}(d^+) \\ & - j \frac{\sqrt{k\pi}}{4} \frac{\sqrt{(r+z)}}{r} \frac{\sin(d^-)}{d^-} \frac{kx}{4r} \left( H_{-1/2}^{(2)}(d^+) - H_{3/2}^{(2)}(d^+) \right). \end{aligned}$$

For small values of  $d^-$  we apply the Taylor expansion to the sine and cosine functions:

$$\begin{aligned} \sin x & \approx x - \frac{x^3}{6} + \dots \\ \cos x & \approx 1 - \frac{x^2}{2} + \dots \end{aligned}$$

which cancels the small factors in the denominators and finally yields

$$\begin{aligned} \frac{\partial A}{\partial x} = & j \frac{\sqrt{k\pi}}{4} \frac{2xz + xr}{2r^3 \sqrt{(r+z)}} \left( 1 - \frac{(d^-)^2}{6} \right) H_{1/2}^{(2)}(d^+) \\ & + j \frac{\sqrt{k\pi}}{4} \frac{\sqrt{(r+z)}}{r} \frac{kx}{r} \left( -\frac{d^-}{6} \right) H_{1/2}^{(2)}(d^+) \\ & - j \frac{\sqrt{k\pi}}{4} \frac{\sqrt{(r+z)}}{r} \left( 1 - \frac{(d^-)^2}{6} \right) \frac{kx}{4r} \left( H_{-1/2}^{(2)}(d^+) - H_{3/2}^{(2)}(d^+) \right). \end{aligned} \quad (3.86)$$

The differentiation of the second block in (3.85) gives (omitting the arguments  $d^-$  and  $d^+$  from the expression to make it more compact)

$$\begin{aligned}
\frac{\partial B}{\partial x} = & -\frac{k\pi\rho}{8r}\left(\frac{x}{\rho^2}-\frac{x}{r^2}\right)\left[2J_{3/2}H_{1/2}^{(2)}+J_{1/2}H_{-1/2}^{(2)}+J_{1/2}H_{3/2}^{(2)}\right] \\
& +\frac{k^2\pi x\rho}{16r^2}\left[3J_{1/2}H_{1/2}^{(2)}-2J_{3/2}H_{-1/2}^{(2)}+2J_{3/2}H_{3/2}^{(2)}-J_{5/2}H_{1/2}^{(2)}\right] \\
& +\frac{k\pi x\rho}{16r^2}\frac{1}{(r-z)}\left[J_{1/2}H_{3/2}^{(2)}-J_{1/2}H_{-1/2}^{(2)}\right] \\
& +\frac{k\pi x\rho}{16r^2}\frac{1}{(r+z)}\left[J_{1/2}H_{-1/2}^{(2)}-3J_{1/2}H_{3/2}^{(2)}\right].
\end{aligned}$$

Here, the critical factor when  $d^- \rightarrow 0$  is contained in the first term of the last row. To cancel the pole, the small-argument approximation (3.70) is applied to the Bessel function, giving

$$\begin{aligned}
\frac{\partial B}{\partial x} = & -\frac{k\pi\rho}{8r}\left(\frac{x}{\rho^2}-\frac{x}{r^2}\right)\left[2J_{3/2}H_{1/2}^{(2)}+J_{1/2}H_{-1/2}^{(2)}+J_{1/2}H_{3/2}^{(2)}\right] \\
& +\frac{k^2\pi x\rho}{16r^2}\left[3J_{1/2}H_{1/2}^{(2)}-2J_{3/2}H_{-1/2}^{(2)}+2J_{3/2}H_{3/2}^{(2)}-J_{5/2}H_{1/2}^{(2)}\right] \\
& +j\frac{k\pi}{16r^2}\sqrt{\frac{k}{\pi}}\left[H_{3/2}^{(2)}-H_{-1/2}^{(2)}\right]+\frac{k\pi x\rho}{16r^2}\frac{1}{(r+z)}\left[J_{1/2}H_{-1/2}^{(2)}-3J_{1/2}H_{3/2}^{(2)}\right].
\end{aligned} \tag{3.87}$$

Finally, the small-argument approximation for calculating the critical derivative  $\frac{\partial}{\partial x}\left(\frac{\partial}{\partial \rho}I_1^{(g)}\right)$

is obtained by summing up (3.86) and (3.87):

$$\begin{aligned}
\frac{\partial}{\partial x}\left(\frac{\partial}{\partial \rho}I_1^{(g)}\right) = & \frac{\partial A}{\partial x}+\frac{\partial B}{\partial x} \\
= & j\frac{\sqrt{k\pi}}{4}\frac{2xz+xr}{2r^3\sqrt{(r+z)}}\left(1-\frac{(d^-)^2}{6}\right)H_{1/2}^{(2)}+j\frac{\sqrt{k\pi}}{4}\frac{\sqrt{(r+z)}}{r}\frac{kx}{r}\left(-\frac{d^-}{6}\right)H_{1/2}^{(2)} \\
& -j\frac{\sqrt{k\pi}}{4}\frac{\sqrt{(r+z)}}{r}\left(1-\frac{(d^-)^2}{6}\right)\frac{kx}{4r}\left(H_{-1/2}^{(2)}-H_{3/2}^{(2)}\right) \\
& -\frac{k\pi\rho}{8r}\left(\frac{x}{\rho^2}-\frac{x}{r^2}\right)\left[2J_{3/2}H_{1/2}^{(2)}+J_{1/2}H_{-1/2}^{(2)}+J_{1/2}H_{3/2}^{(2)}\right] \\
& +\frac{k^2\pi x\rho}{16r^2}\left[3J_{1/2}H_{1/2}^{(2)}-2J_{3/2}H_{-1/2}^{(2)}+2J_{3/2}H_{3/2}^{(2)}-J_{5/2}H_{1/2}^{(2)}\right] \\
& +j\frac{k\pi}{16r^2}\sqrt{\frac{k}{\pi}}\left[H_{3/2}^{(2)}-H_{-1/2}^{(2)}\right]+\frac{k\pi x\rho}{16r^2}\frac{1}{(r+z)}\left[J_{1/2}H_{-1/2}^{(2)}-3J_{1/2}H_{3/2}^{(2)}\right].
\end{aligned} \tag{3.88}$$

To conclude, in order to calculate the derivatives of conical beams with respect to  $x$ , the recurrence in (3.74) is used in conjunction with the original recurrence for the scalar wave objects defined in (3.18). Equations (3.75), (3.80) and (3.83) are used to the terms specific to

the differentiated recurrence. For small arguments  $d^-$ , (3.88) should be used instead of (3.84) to avoid numerical problems.

### 3.2.3.3. Derivation of $\frac{\partial W_n}{\partial y}$

The expressions for calculating  $\frac{\partial W_n}{\partial y}$  are in principle identical to the ones for calculating  $\frac{\partial W_n}{\partial x}$  (replacing  $x$  with  $y$  where necessary), save for the differences introduced by differentiating the angle  $\phi$  with respect to  $y$  instead of  $x$  (see Eqs. (3.72), (3.73), (3.76) and (3.77)). Therefore, the details of the mathematical manipulations will be omitted, and only the final expressions will be presented.

The recurrence relation for  $\frac{\partial W_n}{\partial y}$  is:

$$\begin{aligned} \left[ \frac{\partial W}{\partial y} \right]_{n+1} &= 2j \frac{x}{\rho^2} e^{j2\phi} W_{n+1} + e^{j2\phi} \left[ \frac{\partial W}{\partial y} \right]_{n-1} \\ &+ 2(n-1) \frac{x}{\rho^2} e^{j(n+1)\phi} \frac{\partial}{\partial \rho} I_n^{(g)} - 2j e^{j(n+1)\phi} \frac{\partial}{\partial y} \left( \frac{\partial}{\partial \rho} I_n^{(g)} \right). \end{aligned} \quad (3.89)$$

The three necessary elements specific to the differentiated recurrence are:

$$\frac{\partial W_0}{\partial y} = W_0 \left( \frac{-jk y}{r} - \frac{y}{r^2} \right), \quad (3.90)$$

$$\frac{\partial W_1}{\partial x} = \left( \frac{jx+y}{\rho^2} - \frac{y}{r^2} \right) W_1 + e^{j\phi} \frac{k^2 \pi y \rho}{16 r^2} \left[ -2 J_0 H_0^{(2)} + J_2 H_0^{(2)} + J_0 H_2^{(2)} - 4 J_1 H_1^{(2)} \right], \quad (3.91)$$

and

$$\begin{aligned} \frac{\partial}{\partial y} \left( \frac{\partial}{\partial \rho} I_n^{(g)} \right) &= \left( \frac{y}{\rho^2} - \frac{y}{r^2} \right) \frac{\partial}{\partial \rho} I_n^{(g)} + (-j)^{n-1} \frac{k \pi \rho y}{8 r^2} \\ &\cdot \left[ \left( 2k J_{n/2} H_{n/2}^{(2)} - k J_{n/2-1} H_{n/2+1}^{(2)} - k J_{n/2+1} H_{n/2-1}^{(2)} \right) \right. \\ &\quad - \frac{2n^2}{k(r^2-z^2)} J_{n/2} H_{n/2}^{(2)} \\ &\quad + \frac{1}{2(r-z)} \left( (n-2) J_{n/2-1} H_{n/2}^{(2)} + (n+2) J_{n/2+1} H_{n/2}^{(2)} \right) \\ &\quad \left. - \frac{1}{2(r+z)} \left( (n-2) J_{n/2} H_{n/2-1}^{(2)} + (n+2) J_{n/2} H_{n/2+1}^{(2)} \right) \right]. \end{aligned} \quad (3.92)$$

The small-argument approximation for  $\frac{\partial}{\partial y} \left( \frac{\partial}{\partial \rho} I_1^{(g)} \right)$  is

$$\begin{aligned}
& \frac{\partial}{\partial y} \left( \frac{\partial}{\partial \rho} I_1^{(g)} \right) = \\
& = j \frac{\sqrt{k\pi}}{4} \frac{2yz + yr}{2r^3 \sqrt{(r+z)}} \left( 1 - \frac{(d^-)^2}{6} \right) \mathbf{H}_{1/2}^{(2)} + j \frac{\sqrt{k\pi}}{4} \frac{\sqrt{(r+z)}}{r} \frac{ky}{r} \left( -\frac{d^-}{6} \right) \mathbf{H}_{1/2}^{(2)} \\
& \quad - j \frac{\sqrt{k\pi}}{4} \frac{\sqrt{(r+z)}}{r} \left( 1 - \frac{(d^-)^2}{6} \right) \frac{ky}{4r} \left( \mathbf{H}_{-1/2}^{(2)} - \mathbf{H}_{3/2}^{(2)} \right) \\
& \quad - \frac{k\pi}{8} \frac{\rho}{r} \left( \frac{y}{\rho^2} - \frac{y}{r^2} \right) \left[ 2 \mathbf{J}_{3/2} \mathbf{H}_{1/2}^{(2)} + \mathbf{J}_{1/2} \mathbf{H}_{-1/2}^{(2)} + \mathbf{J}_{1/2} \mathbf{H}_{3/2}^{(2)} \right] \\
& \quad + \frac{k^2 \pi}{16} \frac{y\rho}{r^2} \left[ 3 \mathbf{J}_{1/2} \mathbf{H}_{1/2}^{(2)} - 2 \mathbf{J}_{3/2} \mathbf{H}_{-1/2}^{(2)} + 2 \mathbf{J}_{3/2} \mathbf{H}_{3/2}^{(2)} - \mathbf{J}_{5/2} \mathbf{H}_{1/2}^{(2)} \right] \\
& \quad + j \frac{k\pi}{16r^2} \sqrt{\frac{k}{\pi}} \left[ \mathbf{H}_{3/2}^{(2)} - \mathbf{H}_{-1/2}^{(2)} \right] + \frac{k\pi}{16} \frac{y\rho}{r^2} \frac{1}{(r+z)} \left[ \mathbf{J}_{1/2} \mathbf{H}_{-1/2}^{(2)} - 3 \mathbf{J}_{1/2} \mathbf{H}_{3/2}^{(2)} \right].
\end{aligned}$$

(3.93)

## 4. APPLICATION OF CONICAL BEAMS IN THE ANALYSIS OF REFLECTOR SYSTEMS

Having presented the various techniques for treating propagation and reflection in Ch. 2, and having established new complex conical wave objects in Ch. 3, in this chapter the aim is to show how the new propagation model of the complex conical beams can be linked to a suitable reflection model in order to develop a complete method for analysing reflector antenna systems. Following the overview given in this introduction, the subsequent sections will focus on the parts of the method that require additional clarification. A few comments on the developed computer algorithm and code optimisation are given at the end of the chapter.

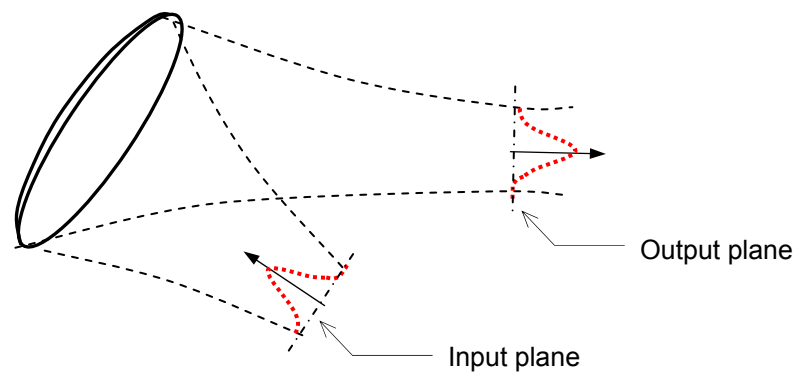


*Figure 4.1. Basic analysis segment of a beam waveguide*

As stated in the Introduction, the analysis method should be modular, meaning that it should allow treating a succession of reflector antennas one reflector at a time, in which case the total calculation time will only increase linearly with the number of reflectors. Bearing that in mind, the basic analysis block of a beam waveguide is shown in Fig. 4.1.. For simplicity, let us assume that the reflector under observation is a concave reflector. The reflector is illuminated by a shaped wave, which expands as it propagates towards the reflector and is refocused upon reflection. Having passed through its focus (or waist), the reflected wave continues to propagate towards the next reflector and starts expanding again. Most often, for such refocusing purposes rotationally symmetric ellipsoidal reflectors are used. In a well-designed beam waveguide, the reflector will be illuminated from its first focal point, and the reflected beam will focus in the plane containing the second focal point. It should be noted though, that as soon as any of the geometric parameters of the system (i.e. position of the

source, angle of incidence, symmetry of the reflector) changes, this is no longer true, i.e. the reflected wave's focus and the focal point of the reflector do not necessarily coincide.

The analysis of a basic building block of a beam waveguide using complex conical beams can be divided in four steps, which can be repeated indefinitely:

- 1) calculate field spectrum in the input plane
- 2) expand the incident field into complex conical beams
- 3) compute equivalent currents on the reflector surface using complex conical beams
- 4) calculate reflected field via Physical Optics

For the method presented in this thesis, Physical Optics has been chosen because, among the methods explained in Sec. 2.3, it offers the highest accuracy for treating scattering from objects of such big electrical size.

In order to translate the four-step procedure outlined above into a working code, a number of practical issues have to be resolved. The most important ones, excluding handling the system geometry (e.g. defining the reflector position, finding intersections etc.), are listed below:

- 1) choose the optimal position for the input/output plane and develop auxiliary routines for estimating it for a given system geometry
- 2) find an efficient way of calculating the spectrum in the input plane
- 3) find an efficient way of calculating the PO integral
- 4) establish criteria for truncating the FFT-GPOF expansion
- 5) develop auxiliary routines for managing the geometry of multiple reflector systems (e.g. coordinate system transformations etc.)

Being closely related, the first two points of this list are discussed together in Sec. 4.1. The calculation of the PO integral is addressed in Sec. 4.2, while coordinate transformations and other auxiliary calculations are the subject of Sec. 4.3. The criteria for truncating the expansion were already commented on in Sec. 3.1.2., but a few additional remarks will be given also in Secs. 4.1.1 and 4.1.2. As far as system geometry is concerned, the related auxiliary calculations are presented at the end of the chapter, in Sec. 4.4, dedicated to the description of the developed computer program for the analysis of reflector systems.

Finally, to have something to calculate, one must define the initial excitation, that is, implement a source model. The developed method has been created such that it is easily



extendable to accept different source models; hence the source model is not considered a part of the method itself. The two implemented source models are thus briefly presented in Ch. 5, in the context of numerical verification and different test cases.

#### 4.1. Merging Physical Optics With Conical Beams – A-PO Approach

As opposed to pure Physical Optics analysis, whereby currents on a given reflector are calculated directly from the known currents on the previous reflector via the radiation integral, the method presented herein is a two-step method. The currents on the reflector are computed by summing up contributions of conical beams, which have to be obtained first from the spectrum of the (already PO-reflected) field in a chosen plane. The natural question that arises is how can this method be expected to perform faster than the direct PO analysis, which only has one step in the procedure? The answer is that the speed of the PO analysis depends very much on where the reflected fields are calculated. As demonstrated in [35], the PO integral will be evaluated the fastest in the zone nearest to the focus of the reflected field, because in that zone all incremental contributions scattered from different parts of the reflector are almost in phase. As the observation point moves away from the focus in either direction, the rapidly oscillating subintegral functions will oscillate ever more rapidly, requiring more and more points in the summation in order for the integral to converge. This is illustrated in Fig. 4.2. Note also that the increasing frequency will also contribute to slower convergence of the radiation integral, everywhere, except at the focus. At the focus, the contributions are in phase independently of the frequency, due to geometrical reasons.

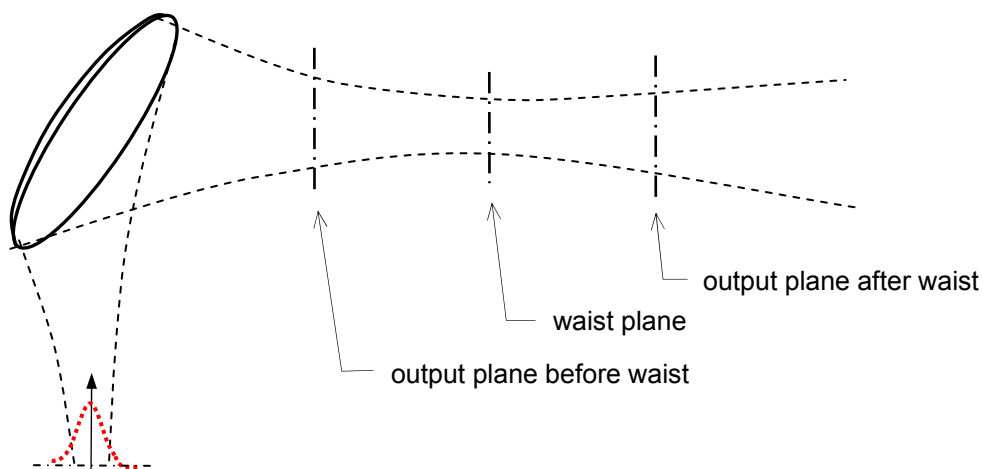


Figure 4.2. Illustration of possible locations of the plane where the conical beam expansion is performed. The fastest convergence of the PO integral is achieved in the waist plane.

Furthermore, the second radiation integral, which covers propagation from the intermediate plane to the actual observation point, is also shown to be much faster than the integral over the surface of the reflector. This is because the field in the plane around the focus (or waist) decays the most rapidly, so even though theoretically it should extend to infinity, the integration surface can be truncated quite close to the focus. In most cases the integration surface in the waist plane is much smaller than the surface of the analysed reflector. Therefore, the computation of the field at the observation point is done faster indirectly, passing through a conveniently chosen auxiliary plane, than directly. This technique has been named Auxiliary-plane Physical Optics, or A-PO [35]. Due to the truncation of the auxiliary plane, its accuracy is indeed somewhat inferior to the accuracy of the direct Physical Optics approach, but still higher than the accuracy of other available methods.

The analysis method in this thesis has been built with Auxiliary-plane Physical Optics as the guiding idea. However, there is an important difference, which is that for the conical beam expansion we need the *spectrum* of the field in the given plane, but not necessarily the field itself. Hence, in practice, step 4 and step 1 of the next cycle in the procedure outlined in the introduction can be connected in different ways. Two possible approaches have been found for the so-called recollection of conical beams: the PO field can be recollected either at the waist plane, or in the far-field region. In the first case, the Fourier transform can be used to arrive at the spectrum of the scattered field, while in the second case the inverse near-field to far-field transformation can be applied for the same purpose. The two approaches have each its advantages and disadvantages, which are discussed next.

#### 4.1.1. Obtaining Field Spectrum Directly from Field in the Focal Plane

The simplest and most intuitive idea how to get the spectrum of the field is to perform the Fast Fourier Transform on the PO-calculated reflected field in the waist plane. However, one should bear in mind that the FFT operates on and also returns a rectangular grid of points (i.e. the spectrum is a function of  $k_x$  and  $k_y$ ), whereas for the conical beam expansion, one needs spectrum points on a polar grid (i.e. as a function of polar spectral coordinates  $k_\rho$  and  $\alpha$ , see Eq. (3.2)). Clearly, the FFT alone is not sufficient to get the spectrum information in the form needed for the subsequent expansion, and the necessary points on the required polar grid have to be interpolated using 2D interpolation. In order to maintain reasonable accuracy and

prevent instabilities in the GPOF expansion, the number of points in the FFT has to be significantly increased, which makes the intuitive approach slower than the others for the same level of accuracy.

An alternative FFT-based approach, employing the pseudo-polar FFT algorithm, will be introduced later in this section, but nevertheless in both cases it is necessary to determine proper spatial sampling parameters for the FFT, depending on the selected maximum value of  $k_\rho$  and the chosen density/spacing of spectral lines  $\Delta k$ . It is these two parameters that control and define at which points in the auxiliary plane the field has to be calculated via PO. Even though the solution steps dictate calculating the PO-reflected field first, followed by the FFT and as the last step the GPOF expansion, the calculation can be made economical only by planning ahead and working out the minimal sufficient set of points that need to be analysed, depending on the requirements of the steps which follow it. Thus, the set of points in the auxiliary plane at which the field has to be calculated ultimately depends on the chosen parameters of the subsequent GPOF expansion. We note that the spacing between points in the spectrum is directly related to the parameters of the GPOF expansion, namely to the number of sample points  $n_{GPOF}$  (loosely related to the number of GPOF exponents  $m_{GPOF}$ , see Appendix A). Usually, the spectral points obtained via FFT and the spectral points necessary for the GPOF expansion do not coincide, and the input samples for the GPOF approximation have to be interpolated between the calculated spectral points. In this case, as a rule of thumb, the density of the calculated spectral points should be at least ten points per wavenumber and not more than three times scarcer than the density of GPOF input samples in order to have satisfactory accuracy of the approximation. This density in spectral domain in return defines the maximum sample distance from the origin in the spatial domain. Similarly, the maximum value of  $k_\rho$  determines the spacing of samples in spatial domain.

To be able to tweak the numerical solution, it is convenient to parameterise the FFT settings. We start from the known relationship relating the point spacing in the spatial and spectral domains [38]

$$\Delta k \Delta x = \frac{2\pi}{n_{FFT}}, \quad (4.1)$$

where  $n_{FFT}$  is the number of points submitted to the FFT. The denser the spectral lines, the wider the spacing between samples in spatial domain, and the farther away from the focus the reflected fields have to be collected for the beam expansion. We shall consider only an even

number of points, because that is the requirement of the alternative pseudo-polar FFT approach (explained later), which was implemented in the developed computer program:

$$\Delta k \Delta x = \frac{2\pi}{2m}. \quad (4.2)$$

With an even number of points, according to the definition of the discrete Fourier Transform, the  $m+1$ -th point in the array corresponds to the origin (zero displacement or zero frequency). However, as the field is sampled symmetrically about the origin for reasons of symmetry, there is an extra half-step shift in the spatial domain, which would cause a phase drift in the FFT spectrum, compared to the actual spectrum. The phase drift has to be cancelled manually after the transformation, by multiplying the spectrum by a factor  $e^{-jk_i \Delta x/2}$ , where  $k_i$  is the frequency (wavenumber) of the  $i$ -th point in the array. With that in mind, for a chosen value of  $\Delta k$  the  $2m$  frequency points are spread between  $-k_{\rho,max}$  and  $k_{\rho,max}$ , where

$$k_{\rho,max} = \left(m - \frac{1}{2}\right) \frac{2\pi}{2m \Delta x}. \quad (4.3)$$

We introduce parameter  $p$ , so that

$$k_{\rho,max} = p \cdot k, \quad (4.4)$$

where  $k = 2\pi/\lambda$  is the wavenumber of the wave being Fourier-transformed. This parameter regulates how far into the invisible region the spectrum is to be calculated (see Sec. 3.1.2.3). Next, we introduce the parameter  $q$ , to control the density of points in the spectrum, again with respect to the free-space wavenumber  $k$ :

$$\Delta k = \frac{k}{q}. \quad (4.5)$$

By substituting (4.4) and (4.5) into (4.2) and (4.3), and noticing that just like  $k_{\rho,max}$ , the most distant point from the origin in spatial domain is  $x_{max} = \left(m - \frac{1}{2}\right)\Delta x$ , we can determine the necessary spacing between field points in spatial domain and see how far away from the estimated location of the focus the field has to be computed. We have

$$\Delta x = \frac{2m-1}{2} \frac{2\pi}{2m} \frac{1}{pk} = \frac{2m-1}{4mp} \lambda, \quad (4.6)$$

and

$$x_{max} = \frac{2m-1}{2} \Delta x = \frac{(2m-1)^2}{8mp} \lambda. \quad (4.7)$$

Factor  $q$  is implicitly included in both (4.6) and (4.7), since

$$pq = \frac{k_{\rho,max}}{\Delta k} = \frac{2m-1}{2}. \quad (4.8)$$

One could argue that one of the two introduced parameters is redundant; however, when looking from the perspective of adjusting the input parameters of the GPOF and tweaking the interpolation settings, it seems more natural to control the spectrum parameters and have the total number of points come out as a byproduct of these adjustments:

$$2m = 2pq + 1. \quad (4.9)$$

If we decide to set parameters  $p$  and  $q$  completely independently, the number of necessary points is determined by calculating the product on the right-hand side of (4.9) and taking the nearest even integer (either smaller or larger), upon which the value of  $q$  is slightly corrected so that  $\Delta k$  would satisfy Eq. (4.8). For example, for values of  $p = 2.25$  and  $q' = 7$  (i.e.  $k_{\rho,max} = 2.25k$ , aimed  $\Delta k = k/7$ ), we have:

$$\begin{aligned} 2m' &= 2pq' + 1 = 32.5 \\ \Rightarrow 2m &= 32 \\ q &= (2m-1)/2p \approx 6.888 \end{aligned}$$

which gives the parameters of the spatial sampling for the FFT:

$$\begin{aligned} \Delta x &= \frac{2m-1}{4mp} \lambda \approx 0.2153\lambda \\ x_{max} &= \frac{2m-1}{2} \Delta x \approx 3.3368\lambda \end{aligned}$$

There is one more reason for opting to parameterise the FFT settings. Even though in Sec. 3.1.2.3 it is claimed that it is hardly ever necessary to take into account the invisible part of the spectrum (i.e. the value of parameter  $p$  should always be  $p = 1$ ), this was stated assuming the spectrum was exact. The FFT, however, provides only an approximation to the spectrum and exhibits the same deficiency as any truncated Fourier series, namely that the approximation gets worse towards the edges of the interval. This is roughly illustrated in Fig. 4.3. Of course, by increasing the number of harmonics in the expansion, the approximation becomes better, but at the expense of increased simulation time. An alternative, faster,

approach takes advantage of the behaviour illustrated in Fig. 4.3. The idea is to calculate the FFT spectrum from  $-pk$  to  $pk$ , with  $p > 1$ , and reuse only the points from the central region between  $-k$  to  $k$  in the subsequent interpolation and GPOF expansion. Numerical tests have shown that a choice of  $p$  between 1.5 and 3 gives satisfactory results.

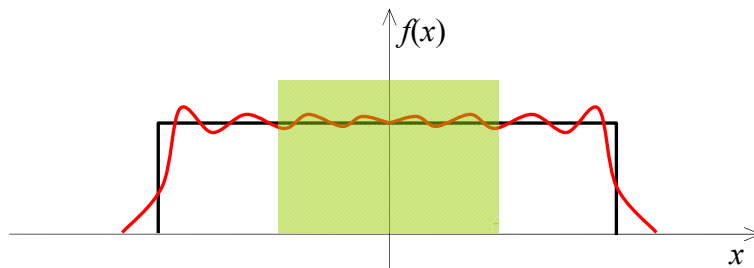


Figure 4.3. Illustration of a function (black line) and its Fourier approximation (red curve). The approximation is better in the central zone (shaded area).

The direct approach to calculating the spectrum of the reflected field takes advantage of the fact that the reflected field in that very plane can be calculated fast. However, it can hardly be called economical. Fig. 4.4. illustrates a typical situation, with  $p = 2$  and  $q = 9$ . In order to have a sufficiently good approximation of the spectrum, represented on a sufficiently dense grid, a whole order of magnitude more points than actually needed have to be calculated.

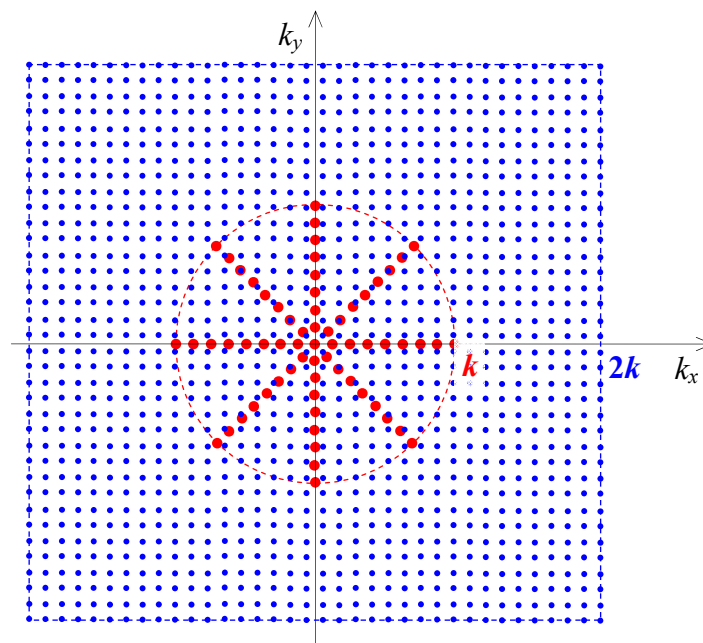


Figure 4.4. Illustration of the typical ratio between the number of points needed for the conical beam expansion (red dots) and the number of points that have to be calculated for the FFT (blue dots) in order to achieve good accuracy.

Other than the field computation stage and the FFT computation stage taking more time, the interpolation stage is also very sensitive to the increase in the number of points. In fact, the speed of 2D interpolation drops very rapidly with the increasing size of the input matrix, and becomes a dominant factor in the overall computation time.

Fortunately, there is an alternative to the simple direct FFT, which allows replacing 2D interpolation with simpler and much faster 1D interpolation. It consists in applying the recently developed Pseudo-polar Fast Fourier Transform (PPFFT), an algorithm developed by Averbuch *et al.* [39], [I-3]. The Pseudo-polar FFT operates on the same rectangular input matrix as the classical two-dimensional FFT, but performs instead a series of one-dimensional FFT's and one-dimensional interpolations, and returns the resulting spectrum values on a pseudo-polar grid. The computational complexity of the PPFFT algorithm is only slightly higher than that of the standard 2D FFT algorithm, therefore there is no significant loss of time in that segment, compared to the direct FFT approach.

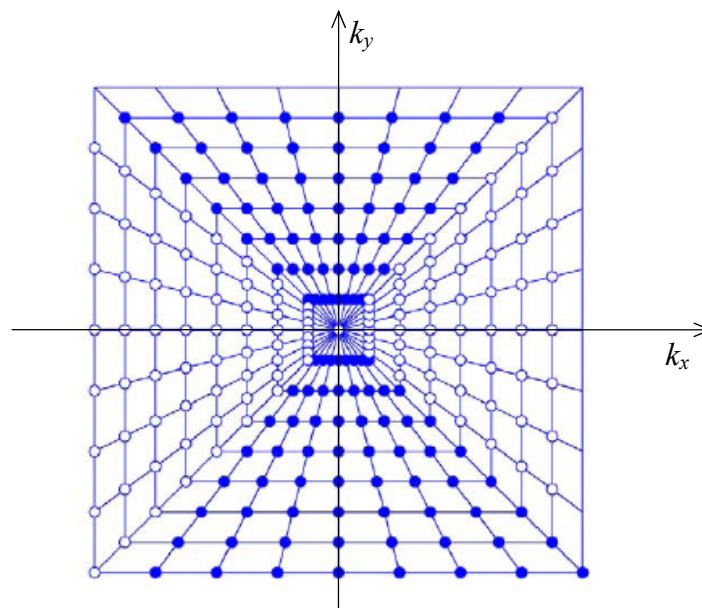


Figure 4.5. Illustration of the recto-polar grid of the Donoho type [39]. Basically horizontal rays (white dots) and basically vertical rays (blue dots) can be identified.

The pseudo-polar grid, shown in Fig. 4.5., is a recto-polar grid where the points are distributed on concentric squares in such a manner that it is possible to group them into *rays*, which emanate from the coordinate system origin. With spectrum points already placed on these rays, and bearing in mind that the spectrum samples for the GPOF are also needed on a polar grid, i.e. lying on rays emanating from the origin, instead of the 2D interpolation, simple

one-dimensional interpolation can be applied<sup>1</sup>. Moreover, the field points need not be calculated on a grid as dense as in the direct approach. These two facts result in a significant reduction of computation time, without any adverse effect on the accuracy of the so-obtained spectrum, if several practical rules are respected. The most important one is that the PPFFT algorithm encounters significant numerical difficulties when the maxima of the input 2D array lie near the corners of the matrix. Therefore, if one rearranges the input array (which is sampled symmetrically about the origin) to compensate for the built-in assumption of FFT that the sampling interval starts from zero *prior to calling* the FFT calculation, very poor results will be obtained. (The rearranging of the array is done in Matlab via the *FFTSHIFT* command.). This common practice with standard FFT should always be avoided. Instead, the frequency shift arising from different interpretations of input array must be compensated for manually, *after* running the PPFFT.

More details on the PPFFT algorithm and its practical handling are given in Appendix C. For a detailed account of the algorithm itself, the reader is referred to [39].

#### 4.1.2. Obtaining Field Spectrum from Far-field Radiation Pattern

The second option for getting the spectrum of the reflected field in the auxiliary plane consists of calculating the reflected field on a spherical grid in the far-field zone, and using the inverse near-field to far-field transformation [28], [33] to extract the spectral data.

The near-field to far-field transformation is a closed-form formula relating the radiated field and its spectrum at the aperture plane. It is obtained via asymptotic evaluation of the inverse Fourier transform of the spectrum. The starting point is to write down the electric field as a superposition of plane waves:

$$E_i(x, y, z) = \frac{1}{4\pi^2} \int_{-\infty}^{\infty} \int_{-\infty}^{\infty} \tilde{f}_i(k_x, k_y) e^{-j\vec{k} \cdot \vec{r}} dk_x dk_y. \quad (4.10)$$

---

<sup>1</sup> Provided that the rays obtained via PPFFT and rays required by the FFT-GPOF expansion coincide; this is rarely true, but the number of PPFFT rays is much higher than the number of rays needed for the expansion, and typically the angular error can be kept below 0.5 degrees. For more details, see Appendix C.



Here,  $\tilde{f}_i(k_x, k_y)$  determines the amplitude of each plane wave in the sum, and  $\vec{k}$  is the vector wavenumber. Index  $i$  denotes any of the three scalar (rectangular) components of the electric field vector, and will be omitted in the following text. The scalar product  $\vec{k} \cdot \vec{r}$  is expanded as

$$\vec{k} \cdot \vec{r} = k_x x + k_y y + k_z z, \quad (4.11)$$

where

$$k_x^2 + k_y^2 + k_z^2 = k^2, \quad (4.12)$$

and  $k = |\vec{k}| = 2\pi/\lambda$ . Substituting (4.11) into (4.10), the integral can be rewritten as

$$E(x, y, z) = \frac{1}{4\pi^2} \int_{-\infty}^{\infty} \int_{-\infty}^{\infty} \left( \tilde{f}(k_x, k_y) e^{-jk_z z} \right) e^{-j(k_x x + k_y y)} dk_x dk_y. \quad (4.13)$$

The term inside the parentheses in (4.13) is easily identified as the Fourier transform of the electric field  $E$ , that is, the spectrum of the field in the plane parallel to the  $x$ - $y$  plane, at the elevation  $z$ :

$$\tilde{E}(k_x, k_y, z) = \tilde{f}(k_x, k_y) e^{-jk_z z}. \quad (4.14)$$

The function  $\tilde{f}(k_x, k_y)$  is actually the spectrum of the field at  $z = 0$ :

$$\tilde{E}(k_x, k_y, 0) = \tilde{f}(k_x, k_y). \quad (4.15)$$

We note again, as in Sec. 3.1.2.3, that depending on  $k_x$  and  $k_y$ , the propagation constant  $k_z$  can be either real or imaginary, causing the particular plane wave to be either propagating or evanescent. When the fields are observed in the far-field region, the evanescent waves can be neglected, which simplifies the evaluation of the integral.

The integral in (4.13) is evaluated in the far-field zone asymptotically by means of the method of Stationary Phase [24], [44]. The detailed derivation is given by Balanis [28], and here the procedure will be only briefly sketched. The stationary phase method assumes that the dominant contribution to the integral with a subintegral function in the form of a product of a slowly varying function ( $\tilde{f}(k_x, k_y)$ ) and a rapidly oscillating function ( $e^{-j\vec{k} \cdot \vec{r}}$ ) comes from values of integration variables  $k_x$  and  $k_y$  where the otherwise rapidly oscillating function remains stationary for first-order changes in  $k_x$  and  $k_y$ , if such point exists in the integration domain. Away from the stationary point the neighbouring positive and negative contributions

due to the rapidly oscillating function will cancel each other out, since the slowly varying function cannot introduce sufficient unbalance to prevent that. The stationary point is the point where the first derivative of the rapidly oscillating function vanishes, which in this case translates to the vanishing derivative of the product  $\vec{k} \cdot \vec{r}$ :

$$\frac{\partial(\vec{k} \cdot \vec{r})}{\partial k_x} = 0, \quad (4.16)$$

$$\frac{\partial(\vec{k} \cdot \vec{r})}{\partial k_y} = 0. \quad (4.17)$$

The solution to these two equations is found after expressing the vector wavenumber in spherical coordinates:

$$k_x = k \sin \theta \cos \phi = k_1, \quad (4.18)$$

$$k_y = k \sin \theta \sin \phi = k_2. \quad (4.19)$$

We note that the stationary point moves in the spectrum as the observation point moves, since angles  $\theta$  and  $\phi$  are the spherical angular coordinates of the observation point.

Having found the stationary point, the product  $\vec{k} \cdot \vec{r}$  is next represented by its Taylor series up to the second order, whereby the first-order terms vanish, as imposed by (4.16) and (4.17). The integration domain reduces to the small area around the stationary point, where the slowly varying function is approximately constant. This gives

$$\begin{aligned} E(x, y, z) &= \frac{1}{4\pi^2} \iint_{S_{SP}} \tilde{f}(k_x, k_y) e^{-j(kr - A(k_x - k_1)^2 - B(k_y - k_2)^2 - C(k_x - k_1)(k_y - k_2))} dk_x dk_y \\ &\approx \frac{1}{4\pi^2} \tilde{f}(k_1, k_2) e^{-jkr} \iint_{S_{SP}} e^{+j(A(k_x - k_1)^2 + B(k_y - k_2)^2 + C(k_x - k_1)(k_y - k_2))} dk_x dk_y. \end{aligned} \quad (4.20)$$

Coefficients  $A$ ,  $B$  and  $C$  are, respectively [28],

$$A = \frac{r}{2k} \left( 1 + \frac{\sin^2 \theta \cos^2 \phi}{\cos^2 \theta} \right), \quad (4.21)$$

$$B = \frac{r}{2k} \left( 1 + \frac{\sin^2 \theta \sin^2 \phi}{\cos^2 \theta} \right), \quad (4.22)$$

$$C = \frac{r \sin^2 \theta}{k \cos^2 \theta} \cos \phi \sin \phi. \quad (4.23)$$

The asymptotic value of the remaining integral in (4.20) is [28]

$$\iint_{S_{SP}} e^{+j(A(k_x-k_1)^2+B(k_y-k_2)^2+C(k_x-k_1)(k_y-k_2))} dk_x dk_y = j2\pi \frac{k \cos \theta}{r}, \quad (4.24)$$

hence the far-field asymptotic evaluation of the Fourier integral eventually becomes

$$E(x, y, z) \approx j \frac{1}{2\pi r} k \cos \theta \tilde{E}(k \sin \theta \cos \phi, k \sin \theta \cos \phi, 0) e^{-jkr}, \quad (4.25)$$

where we have used the substitution from (4.15). This important expression defines the near-field to far-field (NF-FF) transformation: it gives a direct, closed-form relationship between the field in the far-field zone ( $z \gg \lambda$ ) and its spectrum in the (aperture) plane  $z = 0$ .

In the context of the recollection of reflected conical beams, theoretically speaking, any plane can be used as the plane  $z = 0$ ; however, once again it is advantageous to set it to coincide with the auxiliary plane containing the reflected wave's focus (i.e. the waist plane). This is because the field is the most spatially confined in that very plane, and consequently the far-field distance is minimal, i.e. the conditions for the validity of (4.25) will be satisfied at the smallest possible distance from the waist (and consequently from the reflector too). This is convenient because, as already explained in the introductory part of Sec. 4.1, the closer the observation point is to the reflected wave's focus, the faster the radiation integral is evaluated.

Getting the spectrum via the inverse NF-FF transformation has a number of advantages over the FFT-based approach of the previous section. First and foremost, it is economical and precise: since every observation point is directly related to one spectral point, one can immediately pick only the spectrum points necessary for the subsequent GPOF expansion and evaluate the radiation integral only at the corresponding observation points. Suppose that the spectrum needs to be evaluated at the point  $(k_\rho, \alpha)$ , as required by the FFT and GPOF expansions (see (3.2) thru (3.5)). We recall that

$$\begin{aligned} k_x &= k_\rho \cos \alpha, \\ k_y &= k_\rho \sin \alpha. \end{aligned}$$

Turning around (4.25), we have

$$\tilde{E}(k \sin \theta \cos \phi, k \sin \theta \cos \phi, 0) = \tilde{E}(k_x, k_y, 0) \approx -j \frac{2\pi r}{k \cos \theta} E(x, y, z) e^{jkr}, \quad (4.26)$$

from where we see that

$$\begin{aligned} k \sin \theta \cos \phi &= k_\rho \cos \alpha, \\ k \sin \theta \sin \phi &= k_\rho \sin \alpha. \end{aligned}$$

Through simple algebraic manipulations we reach

$$\begin{aligned}\theta &= \arcsin(k_\rho/k), \\ \phi &= \alpha.\end{aligned}$$

Hence, for the given spectral point with coordinates  $(k_\rho, \alpha)$ , the coordinates of the observation point where the reflected field has to be computed are

$$(r, \theta, \phi) = (r, \arcsin(k_\rho/k), \alpha),$$

or, equivalently in rectangular coordinates,

$$(x, y, z) = \left( r \frac{k_\rho}{k} \cos \alpha, r \frac{k_\rho}{k} \sin \alpha, r \sqrt{1 - \left( k_\rho/k \right)^2} \right).$$

Due to the direct relationship between the spectrum and the field, there are no extra points to be evaluated and no need for interpolation whatsoever, which saves a lot of computation time and partially compensates for the slower evaluation of the radiation integral.

The second advantage of this approach is that the values of the field spectrum correspond to the actual spectrum defined by the Fourier integral, unlike in the FFT-based approach, where the spectrum calculated via FFT is the Fourier series approximation to the actual one, and its accuracy depends on the truncation of the series. In other words, reducing the number of points in the FFT-based approach will lower the accuracy of the calculated field spectrum, and consequently the accuracy of the whole analysis. On the other hand, the same will have no influence at all on the accuracy of the calculated spectrum if the inverse NF-FF transformation is used. Hence, the number of simulated points can be further reduced for smooth spectra that can be well approximated via GPOF with only a few exponents.

As far as the downsides of the NF-FF transformation-based approach, there are three main concerns. Firstly, only the visible part of the spectrum can be retrieved by this method. This means that the fields calculated in the vicinity of the auxiliary plane will not be accurate. In practice though, this is most often not a very serious drawback, since the distances between reflectors in a beam waveguide are, like their dimensions, also on the order of hundreds of wavelengths. The second problem is the existence of the singularity in the inverse NF-FF transformation (4.26) for  $\theta = 90^\circ$ , which in practice means that other than the whole invisible spectrum, a small portion of the visible spectrum around  $k_\rho \rightarrow k$  is lost too. The truncation of the visible spectrum should be done as close as possible to the limit  $k_\rho = k$ , but before the numerical difficulties become apparent. Truncating too far away from  $k_\rho = k$  may

lead to incorrect results after the GPOF expansion. Finally, there is the issue of the speed of the PO integral when calculating the reflected fields in the far zone. The points for which the field has to be calculated are located on the whole hemisphere where  $z > 0$  (the local  $z$ -axis is aligned so that it coincides with the vector of propagation of the reflected field). Of those points, the ones located on the axis or close to it will be calculated fast, while the integral will converge ever more slowly as the local angle  $\theta$  increases. As stated before, to ensure good GPOF approximation, one should sample points as close as possible to  $\theta = 90^\circ$ , meaning that the slowly calculated observation points unfortunately cannot be avoided, and the integration of the PO integral can last an order of magnitude longer than in the FFT-based approach. In the end, the trade-off between the two approaches is whether to calculate the fields fast, but at an exceeded number of points, or slowly, but only at the small number of points which are really necessary for the subsequent analysis.

## 4.2. Efficient Calculation of the PO Integral

As explained in Sec. 2.3.1, the electric field scattered by the metallic reflector is found via the radiation integral (2.26), reduced to double integration over the surface of the reflector:

$$\begin{aligned} \vec{E}(\vec{r}) = & \frac{\eta}{4\pi} \iint_S \left[ \vec{J}(\vec{r}') \left( -\frac{j}{kR} - \frac{1}{(kR)^2} + \frac{j}{(kR)^3} \right) \right. \\ & \left. + \left( \vec{J}(\vec{r}') \cdot \hat{R} \right) \hat{R} \left( \frac{j}{kR} + \frac{3}{(kR)^2} - \frac{3j}{(kR)^3} \right) \right] k^2 e^{-jkR} dS' \quad (4.27) \\ & - \frac{1}{4\pi} \iint_S \left( \vec{M}(\vec{r}') \times \hat{R} \right) \left( \frac{1 + jkR}{(kR)^2} \right) k^2 e^{-jkR} dS' . \end{aligned}$$

However, this generic formula says nothing about the actual curved surface or the shape of the reflector defined by its rim (e.g. circular, rectangular etc.). As the numerical integration routines can typically only do double integration on a plane (i.e.  $\int dx dy$ ), in order to translate formula (4.27) into a working numerical code, additional preparation is necessary. In this thesis, the approach adopted for doing that follows the approach implemented in GRASP (TM) [34], which is straightforward and very efficient. Moreover, it can be easily adapted to various explicitly defined surfaces and reflector shapes by means of a few dedicated factors, while maintaining the core of the integration routine intact.

For simpler notation, in the following derivations the whole subintegral function will be replaced by a generic function  $f(x', y', z')$ , where  $(x', y', z') \equiv \vec{r}'$  are the coordinates of a point on the reflector surface. Hence, we consider the integral

$$I = \iint_S f(x', y', z') dS', \quad (4.28)$$

where the surface of the reflector is defined by

$$z' = g(x', y'). \quad (4.29)$$

Both source and observation point coordinates here refer to the local coordinate system of the reflector. The integral has been reduced to scalar form because the fact whether the subintegral function is scalar or vector plays no part in the discussion of this section. The final expression can be applied to the case of the radiation integral by simply replacing the generic function  $f(x', y', z')$  with the subintegral function of Eq. (4.27).

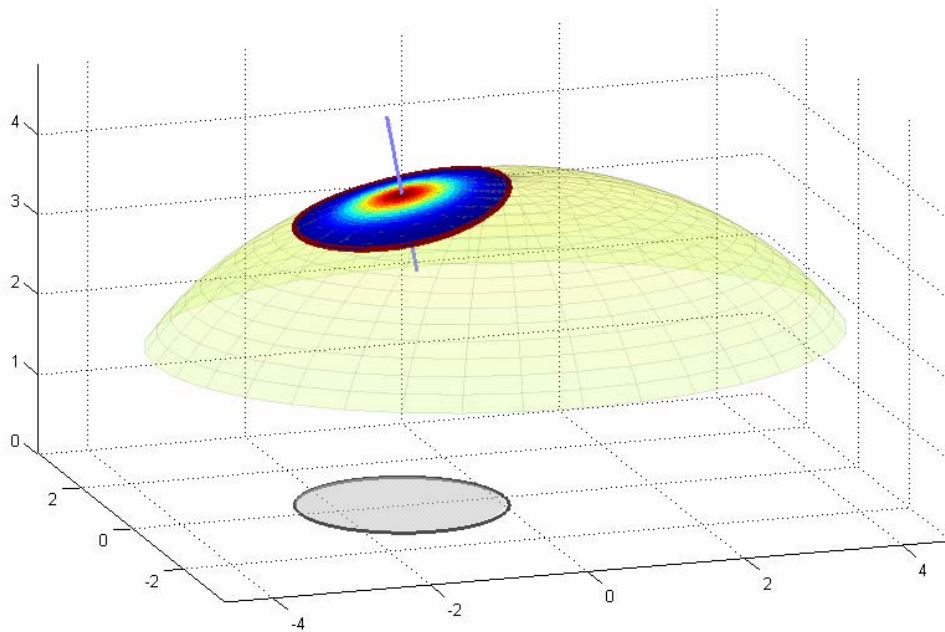


*Figure 4.6. Integration over the surface of an ellipsoidal reflector is replaced by integration over its projection on the x-y plane (shaded grey circle). Blue line shows the direction of the normal on the surface at the center of the reflector.*

Fig. 4.6. shows a circular-ellipsoidal reflector, formed by intersecting a vertical circular cylinder and an ellipsoid. Suppose the integration has to be performed over its surface. The goal is to replace the integration over the surface by an equivalent integration over a simple *rectangular area* in a plane, which will allow the implementation of standard numerical integration routines. This is achieved in two steps: first, the surface of the reflector is

projected back onto the local  $x$ - $y$  plane (where the reflector rim is defined, as shown in Fig. 4.6.); second, the reflector rim is "unwrapped" and transformed into a rectangular patch. The first operation results in the occurrence of a factor containing the information on the area of the elementary surface  $dS'$ , while the second makes appear a Jacobian determinant in the subintegral function. These two factors suffice to represent any explicitly defined surface with a simple rim, and allow for easy extension of the model to new reflector types.

The differential area of a surface is

$$dS' = |\nabla S'| = |\vec{n}| dx' dy' , \quad (4.30)$$

where  $\vec{n}$  is the surface normal (*not* the unit normal). For a surface defined as in (4.29), the normal is found as

$$\vec{n} = -\frac{\partial g}{\partial x'} \hat{x}' - \frac{\partial g}{\partial y'} \hat{y}' + \hat{z}' , \quad (4.31)$$

so the surface element becomes

$$dS' = |\vec{n}| dx' dy' = \sqrt{\left(\frac{\partial g}{\partial x'}\right)^2 + \left(\frac{\partial g}{\partial y'}\right)^2 + 1} dx' dy' . \quad (4.32)$$

Hence, after the first step, the integral in (4.28) is

$$I = \iint_{S_{x'y'}} f(x', y', g(x', y')) \sqrt{\left(\frac{\partial g}{\partial x'}\right)^2 + \left(\frac{\partial g}{\partial y'}\right)^2 + 1} dx' dy' , \quad (4.33)$$

where  $S_{x'y'}$  denotes the projected surface in the  $x'$ - $y'$  plane (the shaded grey area in Fig. 4.6.).

The second step varies depending on the actual shape of the rim, whether it is defined by a smooth curve or by triangular or rectangular sections. All cases are covered in [34], and here only the case of the curved reflector rim is presented, because it is the one actually used in the numerical test cases. The geometry of the problem is illustrated in Fig. 4.7. The projection of the reflector rim onto the  $x'$ - $y'$  plane is bounded by the curve  $r_0(\tau)$ , where  $\tau$  is the angle measured from positive  $x'$ -axis.

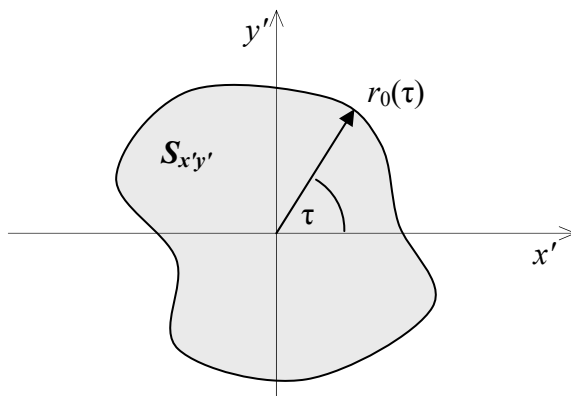


Figure 4.7. Integration over the  $x'$ - $y'$ -projection of the reflector. Conversion to a rectangular area is done by performing the integral in polar coordinates.

To reduce the integral over an arbitrary curved surface as shown above to an integral over a rectangular domain, we change integration variables to polar by introducing

$$x' = r \cos \tau, \tag{4.34}$$

$$y' = r \sin \tau, \tag{4.35}$$

and (4.33) becomes

$$I = \int_0^{2\pi} \int_0^{r_0(\tau)} f(r \cos \tau, r \sin \tau, g(r \cos \tau, r \sin \tau)) |\vec{n}| r dr d\tau, \tag{4.36}$$

where the identity of Eq. (4.32) was used to get a more compact expression. The integration surface now looks as in Fig. 4.8.

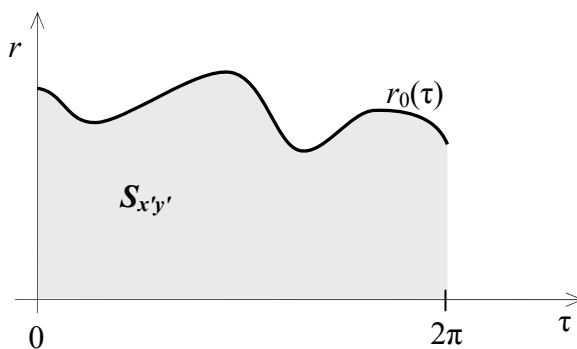


Figure 4.8. Integration surface after switching to polar coordinates

Finally, integration from 0 to  $r_0(\tau)$  is transformed to integration from 0 to 1 by passing to scaled polar coordinates  $(\rho, v)$ :

$$\rho(r, \tau) = \frac{r}{r_0(\tau)}, \tag{4.37}$$



$$v(r, \tau) = \tau. \quad (4.38)$$

Here, we see that when  $r = 0$ , also  $\rho = 0$ , whereas when  $r = r_0(\tau)$ ,  $\rho = 1$ . The variable change is accounted for in the subintegral function by the introduction of the Jacobian:

$$J = \begin{vmatrix} \partial r / \partial \rho & \partial r / \partial \tau \\ \partial v / \partial \rho & \partial v / \partial \tau \end{vmatrix} = \begin{vmatrix} r_0(\tau) & \rho \partial r_0(\tau) / \partial \tau \\ 0 & 1 \end{vmatrix} = r_0(\tau), \quad (4.39)$$

and the integral finally assumes the desired form:

$$I = \int_0^{2\pi} \int_0^1 f(\rho r_0(v) \cos v, \rho r_0(v) \sin v, g(\rho r_0(v) \cos v, \rho r_0(v) \sin v)) |\vec{n}| (r_0(v))^2 \rho d\rho dv. \quad (4.40)$$

For reflectors with a circular rim, we note that  $r_0(\tau) = r_0$ , and the integral simplifies to

$$I = \int_0^{2\pi} \int_0^1 f(\rho r_0 \cos v, \rho r_0 \sin v, g(\rho r_0 \cos v, \rho r_0 \sin v)) |\vec{n}| r_0^2 \rho d\rho dv. \quad (4.41)$$

### 4.3. Auxiliary Calculations

Presented in this section are two auxiliary calculations, which are themselves neither a part of the PO integration, nor a part of the conical beam expansion, but are essential for the successful analysis of scattering by an arbitrarily placed and oriented reflector. By arbitrarily placed, we understand not only with respect to the global coordinate system, but also with respect to the incident wave source<sup>2</sup>. This is a common situation whenever a system of more than one reflector is considered, whereby the shape and placement of the reflectors are governed by the imposed design requirements.

The first of the two auxiliary calculations serves to handle the complex geometry, i.e. to provide the necessary coordinate system transformations between the global coordinate system and the various local coordinate systems. The second one uses geometrical optics and simple Gaussian beam analysis to supply the data on the direction of propagation and waist

---

<sup>2</sup> In the developed computer program, the relative positioning of the source and the reflector is not entirely arbitrary. The source can move with respect to the reflector, but must stay in the symmetry plane (i.e. central cross-section) of the reflector. Should the source be allowed to move out of the symmetry plane and be oriented in any direction, the estimation of the auxiliary plane position would become much more involved.

location of the beam upon each reflection, so as to be able to apply the auxiliary plane technique described in Sec. 4.1.

#### 4.3.1. Coordinate System Transformations

Most beam-based propagation models assume that the beam is propagating in the  $z$ -direction in the (local) coordinate system, which is due to the fact that such choice of coordinate system results in the most compact expressions for the field components when passing from rectangular to spherical coordinates and vice versa. As shown in Secs. 2.2.3 and 3.1, both Gaussian beams and the complex conical beams (as introduced in this thesis) propagate in the local  $z$ -direction. However, as soon as the beam encounters a scatterer in an off-axis position, it will be reflected at a certain angle and propagate in a direction different from the direction of the incident wave. Clearly, what represented the  $z$ -axis to the incident beam is no longer the  $z$ -axis to the reflected one. In order to analyse such cases, the local coordinate system needs to follow the beam, and it is necessary to develop auxiliary routines to relate each of those coordinate systems to the global coordinate system, as well as to pass from one local coordinate system to another.

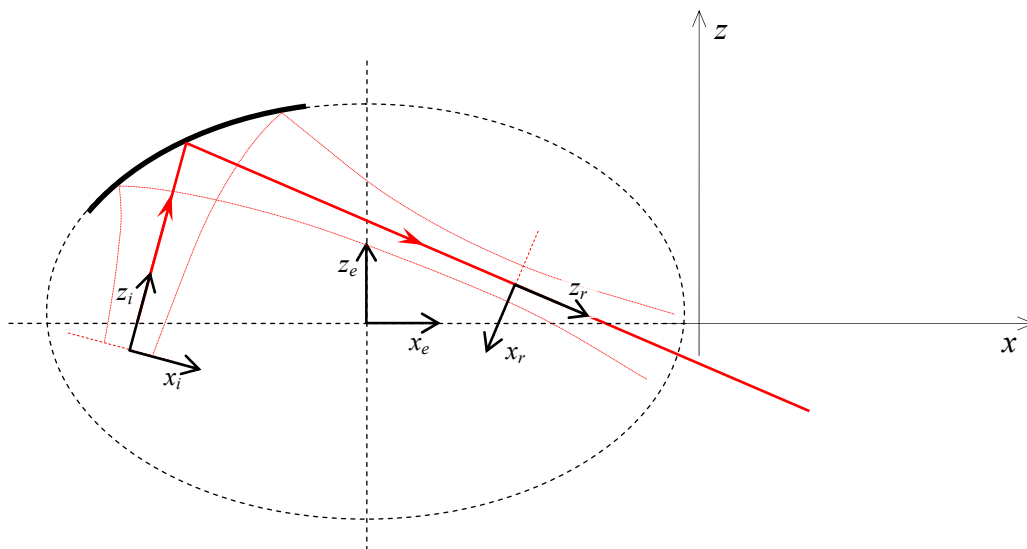


*Figure 4.9. Local coordinate systems employed for the analysis of one reflector: coordinate system of the incident beam  $(x_i, z_i)$ , coordinate system of the reflected beam  $(x_r, z_r)$  and coordinate system of the ellipsoidal reflector  $(x_e, z_e)$*

Related to the analysis of reflector systems employing complex conical beams, for each reflector three distinct local coordinate systems are used, as shown in Fig. 4.9. These are the local coordinate system of the incident beam  $(x_i, z_i)$ , the local coordinate system of the

reflected beam  $(x_r, z_r)$ , and the local coordinate system in which the reflector (in this case ellipsoidal) is defined  $(x_e, z_e)$ . When finding the reflection point on the surface of the reflector or when defining the reflector rim, it is practical to switch to the local coordinate system of the reflector, for the equations to-be-solved will be the simplest there. On the other hand, for the conical beam expansion we need the tangential components of the field in the source (or waist) plane, which is defined by  $z_{local} = 0$ , therefore one must inevitably convert field components to that local coordinate system. Conversely, when calculating the PO reflection, it is necessary to pass to the global coordinate system, because ultimately the observation points are defined in global coordinates. Hence, one must convert the coordinates of the observation points (either a rectangular grid in the auxiliary plane or a spherical grid in the far-field, recall Secs. 4.1.1 and 4.1.2) from the local coordinate system to the global one.

As can be seen in the above paragraph, in some cases we have to convert field values from one coordinate system to another, whereas in other cases the coordinates of a given point have to be expressed in a different coordinate system. The difference between converting a vector and a point between two coordinate systems is that for the latter, one must align the origins of the two coordinate systems (i.e. translate one of the two) prior to applying transformation formulas. If one of the two involved coordinate systems (CS) is named "global" and the other one "local", generally speaking, there are four possible conversions:

- local CS to global CS, for a point
- global CS to local CS, for a point
- local CS to global CS, for a vector
- global CS to local CS, for a vector

In the developed program, all four variations were included in one dedicated function, which was adapted for working with array variables, so as to be able to convert many input points in only one function call and by so doing save computation time. The conversion formulas are known from standard vector algebra, and are briefly derived next, for reference purposes.

Assume a vector  $\vec{A}$  which can be expressed as

$$\vec{A} = a_{x_1} \hat{x}_1 + a_{y_1} \hat{y}_1 + a_{z_1} \hat{z}_1 = a_{x_2} \hat{x}_2 + a_{y_2} \hat{y}_2 + a_{z_2} \hat{z}_2, \quad (4.42)$$

where  $(\hat{x}_1, \hat{y}_1, \hat{z}_1)$  are the unit vectors pertaining to the first coordinate system, and  $(\hat{x}_2, \hat{y}_2, \hat{z}_2)$  the unit vectors pertaining to the second coordinate system. To find the lengths  $a_{x_2}$ ,  $a_{y_2}$  and  $a_{z_2}$ , vector  $\vec{A}$  is projected onto the corresponding unit vectors:

$$a_{x_2} = \vec{A} \cdot \hat{x}_2 = a_{x_1} (\hat{x}_1 \cdot \hat{x}_2) + a_{y_1} (\hat{y}_1 \cdot \hat{x}_2) + a_{z_1} (\hat{z}_1 \cdot \hat{x}_2), \quad (4.43)$$

$$a_{y_2} = \vec{A} \cdot \hat{y}_2 = a_{x_1} (\hat{x}_1 \cdot \hat{y}_2) + a_{y_1} (\hat{y}_1 \cdot \hat{y}_2) + a_{z_1} (\hat{z}_1 \cdot \hat{y}_2), \quad (4.44)$$

$$a_{z_2} = \vec{A} \cdot \hat{z}_2 = a_{x_1} (\hat{x}_1 \cdot \hat{z}_2) + a_{y_1} (\hat{y}_1 \cdot \hat{z}_2) + a_{z_1} (\hat{z}_1 \cdot \hat{z}_2), \quad (4.45)$$

The scalar products in the above relations can be calculated easily if both sets of unit vectors are related to the reference global coordinate system, spanned by the unit vectors  $\hat{x}$ ,  $\hat{y}$  and  $\hat{z}$ :

$$\begin{aligned} \hat{x}_1 &= x_1^x \hat{x} + x_1^y \hat{y} + x_1^z \hat{z}, \\ \hat{y}_1 &= y_1^x \hat{x} + y_1^y \hat{y} + y_1^z \hat{z}, \\ \hat{z}_1 &= z_1^x \hat{x} + z_1^y \hat{y} + z_1^z \hat{z}, \end{aligned} \quad (4.46)$$

and

$$\begin{aligned} \hat{x}_2 &= x_2^x \hat{x} + x_2^y \hat{y} + x_2^z \hat{z}, \\ \hat{y}_2 &= y_2^x \hat{x} + y_2^y \hat{y} + y_2^z \hat{z}, \\ \hat{z}_2 &= z_2^x \hat{x} + z_2^y \hat{y} + z_2^z \hat{z}. \end{aligned} \quad (4.47)$$

Substituting (4.46) and (4.47) into (4.43)-(4.45), we can write the transformation in matrix form

$$\begin{bmatrix} a_{x_2} \\ a_{y_2} \\ a_{z_2} \end{bmatrix} = \begin{bmatrix} x_1^x x_2^x + x_1^y x_2^y + x_1^z x_2^z & y_1^x x_2^x + y_1^y x_2^y + y_1^z x_2^z & z_1^x x_2^x + z_1^y x_2^y + z_1^z x_2^z \\ x_1^x y_2^x + x_1^y y_2^y + x_1^z y_2^z & y_1^x y_2^x + y_1^y y_2^y + y_1^z y_2^z & z_1^x y_2^x + z_1^y y_2^y + z_1^z y_2^z \\ x_1^x z_2^x + x_1^y z_2^y + x_1^z z_2^z & y_1^x z_2^x + y_1^y z_2^y + y_1^z z_2^z & z_1^x z_2^x + z_1^y z_2^y + z_1^z z_2^z \end{bmatrix} \cdot \begin{bmatrix} a_{x_1} \\ a_{y_1} \\ a_{z_1} \end{bmatrix}. \quad (4.48)$$

Upon closer inspection of the above matrix, one sees that it is actually a product of two matrices

$$\underline{\mathbf{T}}_{12} = \begin{bmatrix} x_2^x & x_2^y & x_2^z \\ y_2^x & y_2^y & y_2^z \\ z_2^x & z_2^y & z_2^z \end{bmatrix} \cdot \begin{bmatrix} x_1^x & y_1^x & z_1^x \\ x_1^y & y_1^y & z_1^y \\ x_1^z & y_1^z & z_1^z \end{bmatrix} = \underline{\mathbf{B}}_2 \cdot \underline{\mathbf{B}}_1^T. \quad (4.49)$$

Matrix  $\underline{\mathbf{T}}_{12}$  is the transformation matrix for passing from the first coordinate system to the second coordinate system, while  $\underline{\mathbf{B}}_1$  and  $\underline{\mathbf{B}}_2$  represent the bases of the two coordinate

systems. Superscript  $T$  denotes a matrix transpose. By a completely analogous derivation, for the transformation of a vector from the second coordinate system to the first one, one would arrive at the transformation matrix  $\underline{\mathbf{T}}_{21}$  defined through bases  $\underline{\mathbf{B}}_1$  and  $\underline{\mathbf{B}}_2$  as:

$$\underline{\mathbf{T}}_{21} = \underline{\mathbf{B}}_1 \cdot \underline{\mathbf{B}}_2^T = (\underline{\mathbf{B}}_2 \cdot \underline{\mathbf{B}}_1^T)^T. \quad (4.50)$$

As seen in (4.49), the basis of a coordinate system is a 3 by 3 matrix where the rows contain components of unit vectors of a given coordinate system, expressed in terms of global unit vectors  $\hat{x}$ ,  $\hat{y}$  and  $\hat{z}$ . Hence, the matrix describing the basis of the global coordinate system is simply an identity matrix. The bases of beam-based coordinate systems are constructed from the known direction of propagation of the beam, which is shown next.

Assume the incident beam is defined by its direction of propagation, expressed through angles of incidence  $\theta_{inc}$  and  $\phi_{inc}$ , with the usual definition of  $\theta$  and  $\phi$  in the global coordinate system. This means that the unit propagation vector of the beam in global coordinates is:

$$\hat{k}_{inc} = \hat{x} \sin \theta_{inc} \cos \phi_{inc} + \hat{y} \sin \theta_{inc} \sin \phi_{inc} + \hat{z} \cos \theta_{inc}. \quad (4.51)$$

We set the local unit vector  $\hat{z}_{loc}$  to coincide with the vector of propagation:

$$\hat{z}_{loc} = \hat{k}_{inc}, \quad (4.52)$$

and define the unit vectors  $\hat{x}_{loc}$  and  $\hat{y}_{loc}$  via cross products:

$$\hat{x}_{loc} = \frac{\hat{y} \times \hat{z}_{loc}}{|\hat{y} \times \hat{z}_{loc}|}, \quad (4.53)$$

$$\hat{y}_{loc} = \hat{z}_{loc} \times \hat{x}_{loc}. \quad (4.54)$$

This ensures that the local coordinate system has the same (right-handed) orientation as the global coordinate system. The construction fails if  $\hat{z}_{loc}$  happens to coincide with global unit vector  $\hat{y}$  because a zero vector is encountered in (4.53). However, in that case one can construct  $\hat{x}_{loc}$  and  $\hat{y}_{loc}$  starting with global unit vector  $\hat{x}$  and making sure that the local coordinate system is still right-handed:

$$\hat{y}_{loc} = \frac{\hat{z}_{loc} \times \hat{x}}{|\hat{z}_{loc} \times \hat{x}|}, \quad (4.55)$$

$$\hat{x}_{loc} = \hat{y}_{loc} \times \hat{z}_{loc}. \quad (4.56)$$

If one has to convert the coordinates of a point from one coordinate system to another, the two coordinate system origins have to be taken into account. Without loss of generality, we can consider one of the two coordinate systems as the reference "global" system, with the origin at  $(0,0,0)$ , whereas the origin of the other, "local", coordinate system, is displaced and is located at the point  $O' = (X_o, Y_o, Z_o)$ . The situation is depicted in Fig. 4.10.

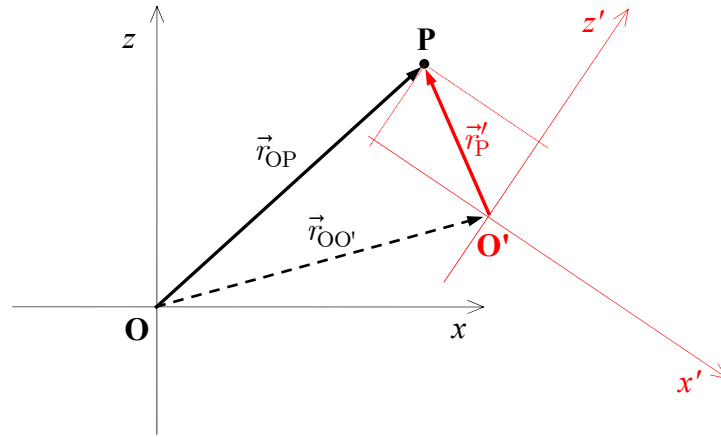


Figure 4.10. Coordinate transformation for point  $P$  between the global coordinate system  $(x, z)$  and the local coordinate system  $(x', z')$ .

Assume the coordinates of the point in the local coordinate system are  $(X'_P, Y'_P, Z'_P)$ . They are identical to the components of the vector  $\vec{r}'_P$ , referred to the local coordinate system. The same point is described by the vector  $\vec{r}_{OP}$  referred to the global coordinate system, which can be written as

$$\vec{r}_{OP} = \vec{r}_{OO'} + \vec{r}'_{OP} = \vec{r}_{OO'} + \underline{\mathbf{T}}_{\mathbf{LG}} \cdot \vec{r}'_P, \quad (4.57)$$

where  $\underline{\mathbf{T}}_{\mathbf{LG}}$  is the transformation matrix which converts the components of a vector from the local (L) coordinate system to the global (G) coordinate system. The inverse transformation, from the global to the local coordinate system, is derived by applying the transformation matrix  $\underline{\mathbf{T}}_{\mathbf{GL}}$ :

$$\underline{\mathbf{T}}_{\mathbf{GL}} \cdot \vec{r}_{OP} = \underline{\mathbf{T}}_{\mathbf{GL}} \cdot \vec{r}_{OO'} + \underline{\mathbf{T}}_{\mathbf{GL}} \cdot \underline{\mathbf{T}}_{\mathbf{LG}} \cdot \vec{r}'_P, \quad (4.58)$$

which gives, bearing in mind that  $\underline{\mathbf{T}}_{\mathbf{GL}}$  and  $\underline{\mathbf{T}}_{\mathbf{LG}}$  cancel each other out,

$$\vec{r}'_P = \underline{\mathbf{T}}_{\mathbf{GL}} \cdot (\vec{r}_{OP} - \vec{r}_{OO'}). \quad (4.59)$$

In the developed computer program, the four conversion formulas (4.49), (4.50), (4.57) and (4.59) have been included in a single function which covers all possible conversions. Since

usually the program deals with many points at once, to save computation time all considered points are passed to the function in an array variable, and inside the function, the origin of the local coordinate system is replicated, to form a matrix with as many rows as there are points in the input array. The benefit of this organisation is that there is only one initialization of the function in the computer memory and that fewer arithmetic operations have to be performed.

#### 4.3.2. Estimation of Position of the Reflected Beam's Waist

In order to be able to apply and take advantage of the Auxiliary-plane approach to Physical Optics, one must first determine the position of the auxiliary plane. As indicated in Sec. 2.3.3, this is done by an independent Gaussian beam analysis of the same reflector. Since this step is of vital importance for the whole analysis and is repeated for every reflector, in this section the involved calculations will be explained more thoroughly, with particular attention to the specific case of ellipsoidal reflector geometry, used in the test cases in Secs. 5.4 and 5.5.

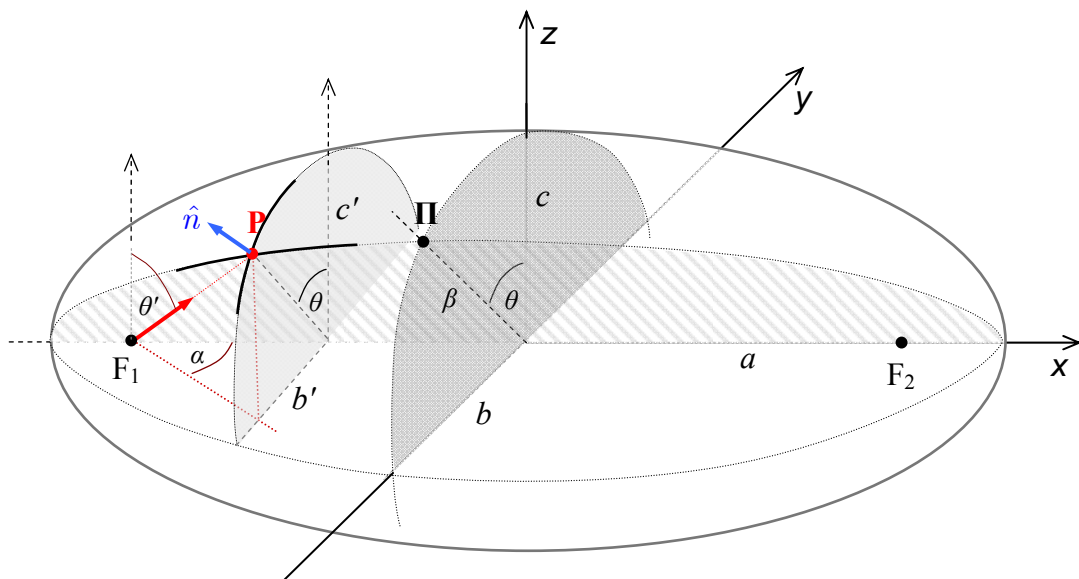


Figure 4.11. Reflection from an ellipsoidal reflector with semi-axes  $a$ ,  $b$  and  $c$ : the incident beam is launched from point  $F_1$  and reflects at point  $P$ . Highlighted are the two principal planes at  $P$ .

The considered geometry is shown in Fig. 4.11. We assume that the beam is launched from point  $F_1$  in the direction defined by angles  $\theta'$  and  $\phi'$  (in the figure, angle  $\alpha = 2\pi - \phi'$  is marked). The central ray of the beam intersects the surface of the ellipsoid at point  $P$ , which can be found analytically. The simplest solution is obtained if the problem is observed in the local coordinate system of the ellipsoid, where its equation is simply

$$\frac{x^2}{a^2} + \frac{y^2}{b^2} + \frac{z^2}{c^2} = 1. \quad (4.60)$$

The equation of the straight line  $\overline{F_1P}$  is expressed parametrically:

$$[x, y, z] = [x_{F_1}, y_{F_1}, z_{F_1}] + t \cdot \hat{k}_{inc}, \quad (4.61)$$

with  $\hat{k}_{inc} = k_x \hat{x} + k_y \hat{y} + k_z \hat{z}$  the unit propagation vector of the incident beam, calculated via (4.51). Inserting (4.61) into (4.60), a quadratic equation in  $t$  is obtained:

$$a_P t^2 + b_P t + c_P = 0, \quad (4.62)$$

with

$$\begin{aligned} a_P &= k_x^2 b^2 c^2 + k_y^2 a^2 c^2 + k_z^2 a^2 b^2, \\ b_P &= 2x_{F_1} k_x b^2 c^2 + 2y_{F_1} k_y a^2 c^2 + 2z_{F_1} k_z a^2 b^2, \\ c_P &= x_{F_1}^2 b^2 c^2 + y_{F_1}^2 a^2 c^2 + z_{F_1}^2 a^2 b^2 - a^2 b^2 c^2. \end{aligned} \quad (4.63)$$

Depending on the geometry, one of the two solutions is discarded (in the case corresponding to Fig. 4.11. the solution for positive  $t$  is kept), and the intersection point is next calculated via (4.61). The direction of propagation of the reflected beam is calculated as in (2.158):

$$\hat{k}_{ref} = \hat{k}_{inc} - 2(\hat{n} \cdot \hat{k}_{inc}) \hat{n}, \quad (4.64)$$

where  $\hat{n}$  is the unit normal on the surface  $S$ . The unit normal is defined as

$$\hat{n} = \frac{\nabla S}{|\nabla S|}, \quad (4.65)$$

and is also most easily calculated in the local coordinate system of the ellipsoid, where the gradient  $\nabla S$ , calculated at point P, is simply

$$\nabla S = \frac{2x_P}{a^2} \hat{x} + \frac{2y_P}{b^2} \hat{y} + \frac{2z_P}{c^2} \hat{z}. \quad (4.66)$$

Proceeding with the analysis, from the known distance  $d_{in} = |\overline{F_1P}|$ , we want to calculate the distance  $d_{out}$  along the direction of unit vector  $\hat{k}_{ref}$  at which the reflected beam will refocus. This is done via Eq. (2.154):

$$\frac{1}{R_{c,inc}} - \frac{1}{R_{c,ref}} = \frac{1}{f}, \quad (4.67)$$



where  $R_{c,inc}$  and  $R_{c,ref}$  are the radii of curvature of the incident and reflected Gaussian beam, and  $f$  is the focal distance of the reflector, calculated from the radius of curvature of the reflecting surface at the point of reflection. Classical optics [46] shows that, for a realistic three-dimensional case, the reflected beam's focus can be found by approximating the beam by a pencil of rays (i.e. a ray tube). In general, the reflected beam is astigmatic, i.e. there are two distinct focal lines for the two principal planes of the ray tube, as shown in Fig. 4.12. This may occur even if the incident beam is not astigmatic (a simple Gaussian beam is not astigmatic). The two foci can be found from the radii of curvature of the two principal planes of the reflector. The principal planes of a reflector at a given point are the two planes in which the radius of curvature of the curve obtained by intersecting the plane and the reflector is either minimal or maximal, and they are orthogonal. For the ellipsoidal reflector, the two principal planes at the point of reflection P are illustrated in Fig. 4.11. It is evident that they are both ellipses, one with the semi-axes  $a$  and  $\beta$ , and the other with semi-axes  $b'$  and  $c'$ .

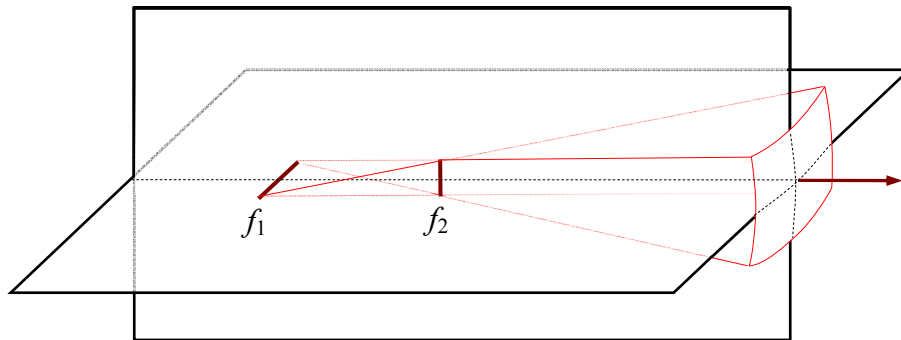


Figure 4.12. Astigmatic ray tube and its principal planes: horizontal wave-fronts focus at  $f_1$ , vertical at  $f_2$ .

If one of the two principal planes of the beam coincides with one of the two principal planes of the reflector, a condition always satisfied for a simple Gaussian beam, the two focal distances of the reflected beam are given by [46], [47]:

$$f_s = \frac{\rho_s \cos \theta_{inc}}{2}, \quad (4.68)$$

$$f_t = \frac{\rho_t}{2 \cos \theta_{inc}}, \quad (4.69)$$

where  $\rho_s$  and  $\rho_t$  denote the radii of curvature of the ellipsoid in the two principal planes, namely the sagittal and the tangential plane, respectively. The sagittal plane is the plane of reflection (in Fig. 4.11. it is the plane containing the ellipse with semi-axes  $a$  and  $\beta$ ), while

the tangential plane is the plane perpendicular to the reflection plane (in Fig. 4.11. it is the plane containing the ellipse with semi-axes  $b'$  and  $c'$ ).  $\theta_{inc}$  is the angle between the incident beam (unit vector  $\hat{k}_{inc}$ , marked by the red arrow in Fig. 4.11.) and the normal on the ellipsoid at point P (unit vector  $\hat{n}$ , marked by the blue arrow in Fig. 4.11.).

The radii of curvature  $\rho_s$  and  $\rho_t$  can be calculated from the parametric equations of the two ellipses. For a planar curve defined parametrically by  $x = x(t)$ ,  $y = y(t)$ , the radius of curvature is calculated by [I-4]

$$\rho = \frac{(\dot{x}^2 + \dot{y}^2)^{3/2}}{\dot{x}\ddot{y} - \dot{y}\ddot{x}}, \quad (4.70)$$

where one and two dots over  $x$  and  $y$  denote the first and second derivative with respect to parameter  $t$ , respectively. For an ellipse with parametric equations  $x = a \cos(t)$ ,  $y = b \sin(t)$ , this becomes

$$\rho = \frac{(a^2 \sin^2 t + b^2 \cos^2 t)^{3/2}}{ab}. \quad (4.71)$$

To summarize, the position of the reflected beam's focus is obtained via (4.67), where the focal distance for the two principal planes is calculated by (4.69) and (4.68), and the related radius of curvature is found through (4.71). The values of the semi-major axis and the semi-minor axis ( $a$  and  $b$ ) can be determined analytically from geometrical relations in Fig. 4.11. For example, for the ellipse in the sagittal plane, the semi-minor axis  $\beta$  is found as follows. We note first that the ellipse is lying in the plane which is tilted by an angle  $\theta'$  from the  $z$ -axis, which can be retrieved from the coordinates of the reflection point P:

$$\tan \theta' = \frac{y_P}{z_P}.$$

The ellipse in the  $y$ - $z$  plane has semi-axes  $b$  and  $c$  (i.e. its parametric equation is  $y = b \cos \tau$ ,  $z = c \sin \tau$ ). Angle  $\theta'$  is exactly the value of parameter  $\tau$  for which point II on that ellipse falls onto the same sagittal plane mentioned above, while  $\beta$  is none other than the distance of that point from the origin:

$$\beta = \sqrt{y_{II}^2 + z_{II}^2} = \sqrt{b^2 \sin^2 \theta' + c^2 \cos^2 \theta'}.$$

Finally, we have to determine the value of parameter  $t$  in (4.71). We note that the equation of the tilted ellipse in its local coordinate system is

$$\frac{x^2}{a^2} + \frac{u^2}{\beta^2} = 1,$$

or, parametrically, using the same  $t$  as the variable,

$$x = a \cos t, \quad u = \beta \sin t.$$

Since the local  $x$ -coordinate on the ellipse is the same as the global  $x$ -coordinate (because the ellipse is not rotated around  $z$ -axis), the necessary parameter is obtained directly from the coordinates of the reflection point P

$$t_p = \arccos(x_p/a),$$

which completes the solution. By similar reasoning one can also calculate the radius of curvature in the tangential plane.

In general, a Gaussian beam after reflection becomes astigmatic and therefore does not refocus at a single point, which would complicate things if the analysis was to continue using Gaussian beams. For a simple Gaussian beam, one would have to establish a criteria where to set the waist of the reflected beam, i.e. if it should coincide with the tangential focus or the sagittal focus, or if it should be placed somewhere between the two. However, as far as the analysis via conical beams is concerned, the goal of this step is merely to approximately determine a convenient location for the auxiliary plane needed for the conical beam expansion. As long as one radius of curvature is not much larger than the other, the two reflected foci will not lie too far away from one another and the reflected beam will remain spatially confined in the whole region between the two foci. Therefore, one can choose either of the two foci as the position of the auxiliary plane, or any point in between.

For the test-cases in Secs. 5.4 and 5.5 a special case was considered, allowing to completely avoid the problem of having to choose the position of the auxiliary plane. The ellipsoid was designed to be rotationally symmetric (with  $b = c$ , referring still to Fig. 4.11.), and the incident beam was launched from the focal point of the ellipsoid towards its apex on the semiminor axis (i.e. the beam reflects at the point  $(0,0,b)$ ). In such configuration, it can be shown that the focal distances in the two perpendicular planes are equal, and the reflected (Gaussian) beam is not astigmatic. Therefore, the auxiliary plane was simply put at that (sole) focus of the reflected beam.

## 4.4. Description of the Developed Simulation Program

For the purpose of verifying the exposed analysis method based on combining Physical Optics with new complex conical beams, a computer program has been developed in Matlab®. To arrive at a working code, it is always necessary to incorporate a number of things not crucial to the method itself, such as routines for the definition of initial simulation parameters, various visualisation routines, auxiliary routines for comparison and testing purposes, and others. In this section, an overview of the developed program is given in order to bridge the gap between the theory and the final working code. First, the algorithm is explained, followed by additional comments where necessary (e.g. integration routines for Physical Optics, acceleration techniques, etc.).

### 4.4.1. Algorithm Description

Here we present the step-by-step account of the operations done by the developed computer program, for the case of analysing a system of two ellipsoidal reflectors. If more than two reflectors are analysed, the part of the algorithm regarding the analysis of the second reflector can simply be repeated.

The algorithm is divided into blocks which run sequentially, as listed below:

- 1) definition of input parameters
  - a. reflector geometry (ellipsoid focal points and semi-axes, rim radius and offset);
  - b. input beam parameters (vector of propagation, beam waist, taper angle, and/or other parameters, depending on the type of excitation);
  - c. observation points
  - d. simulation parameters (FFT/GPOF parameters (see Sec. 4.1.1), or only GPOF parameters (see Sec. 4.1.2))
  - e. input, output and intermediate files' filenames
  - f. other general parameters (frequency, global coordinate system, etc.)
- 2) analysis of the first reflector geometry
  - a. find intersection of the incident beam with the reflector
  - b. calculate the normal and the direction of propagation of the reflected field
  - c. determine points on the ellipsoid surface belonging to the reflector (based on rim definition)
  - d. define coordinate system: incident beam for the second reflector

- 3) determining of auxiliary plane parameters for the reflected beam
  - a. calculate focal point and reflected beam's waist with Gaussian Beam analysis
  - b. define points in the auxiliary plane for which the field will be computed<sup>3</sup>
  - c. define points in the far-field for which the field will be computed<sup>3</sup>
- 4) calculating reflected fields at the intermediate observation points
  - a. determine reflector points for which the incident field has to be computed<sup>4</sup> and calculate normal vectors and unit normal vectors
  - b. convert reflector points to the local coordinate system of the incident beam
  - c. calculate incident field on the reflector (from the selected feed model) in the local coordinate system
  - d. convert calculated field into global coordinate system and compute equivalent currents (PO equivalent)
  - e. convert coordinates of intermediate observation points to global coordinate system
  - f. apply Physical Optics and calculate reflected fields at the chosen points
  - g. convert calculated fields to the coordinate system of the incident beam for the second reflector
- 5) calculating reflected field spectrum in the auxiliary plane for the chosen  $(k_\rho, \alpha)$  set<sup>5</sup>
  - a. apply FFT or PFFT to the converted fields in the auxiliary plane, OR
  - b. apply inverse NF-FF transformation to the converted fields in the far field
  - c. interpolate spectrum values to fit the selected grid (only if using 5.a)
- 6) performing complex conical beam expansion on the reflected field
  - a. calculate equivalent magnetic currents from the electric field spectrum
  - b. apply one-dimensional FFT to the calculated currents in the  $\alpha$ -dimension
  - c. for each  $\alpha$ -column ( $mFFT$  columns), call GPOF expansion and calculate nGPOF exponents (to get  $mFFT \cdot nGPOF$  coefficients  $b_{mn}$ )
- 7) analysis of the second reflector geometry (as in step 2; local coordinate system of the output beam is defined first)
- 8) determining of auxiliary plane for the output field (as in step 3)
- 9) calculating reflected fields after second reflection at the intermediate observation points (as in step 4, with modifications related to using complex conical beams)
  - a. determine reflector points for which the incident field has to be computed<sup>4</sup> and calculate normal vectors and unit normal vectors

---

<sup>3</sup> Depending on the chosen method for calculating the spectrum.

<sup>4</sup> The points on the reflector at which the incident field has to be computed are dictated by the integration routine implemented in the Physical Optics integral

<sup>5</sup> The  $k_\rho$  points at which the spectrum has to be computed are dictated by input parameters of GPOF; the  $\alpha$  points are dictated by the subsequent FFT.

- b. convert reflector points to the local coordinate system of the *incident beam for the second reflector*
  - c. *apply wave-object summation to calculate the incident field at the second reflector* (at the given observation points<sup>6</sup>)
  - d. convert calculated field into global coordinate system and compute equivalent currents (PO equivalent)
  - e. apply Physical Optics and calculate reflected fields at the chosen points
  - f. convert calculated fields to the coordinate system of the output beam
- 10) calculating reflected field spectrum in the auxiliary plane (as in step 5)
- 11) performing complex conical beams expansion on the reflected field (as in step 6)
- 12) calculating output field at observation points defined in step 1
- a. convert observation points to the local coordinate system of the *output beam*
  - b. *apply wave-object summation to calculate the field* at the observation points
  - c. convert calculated field to global coordinate system

#### 4.4.2. Program Optimization and Enhancements

Direct coding of the relations presented in Ch. 3 and 4 results in a program which is easy to read and follow, but very slow. This refers primarily to the evaluation of the Physical Optics integral and, to some extent, the evaluation of complex conical beams themselves. In order to improve the performance of the developed program, both the algorithm and the developed routines were optimized using various programming techniques and solutions. The enhancements ranged from adapting the key functions (wave-object evaluation, coordinate transformation) to work with array input variables, to replacing standard Matlab integration routines by newly developed own functions, specifically designed for two-dimensional integration. The optimization was done with help of Matlab Profiler, a utility which counts all functions called during the execution of the designated part of the code, and gives an overview of the performance in tabular form, listing the number of calls to each function and the total time spent inside it. Shown in Fig. 4.13. are two example profiles, obtained for two intermediate versions of the Physical Optics subprogram. A reduction in the calculation time of a factor of ten can be noticed between the older version, which calls function "gauss2d\_PO\_v2", and the newer version, which calls "gauss2d\_PO\_v3".

---

<sup>6</sup> If analysing more than one reflector, the observation points after first reflection are points on the surface of the second reflector, dictated again by the integration routine implemented in the (second) Physical Optics integral

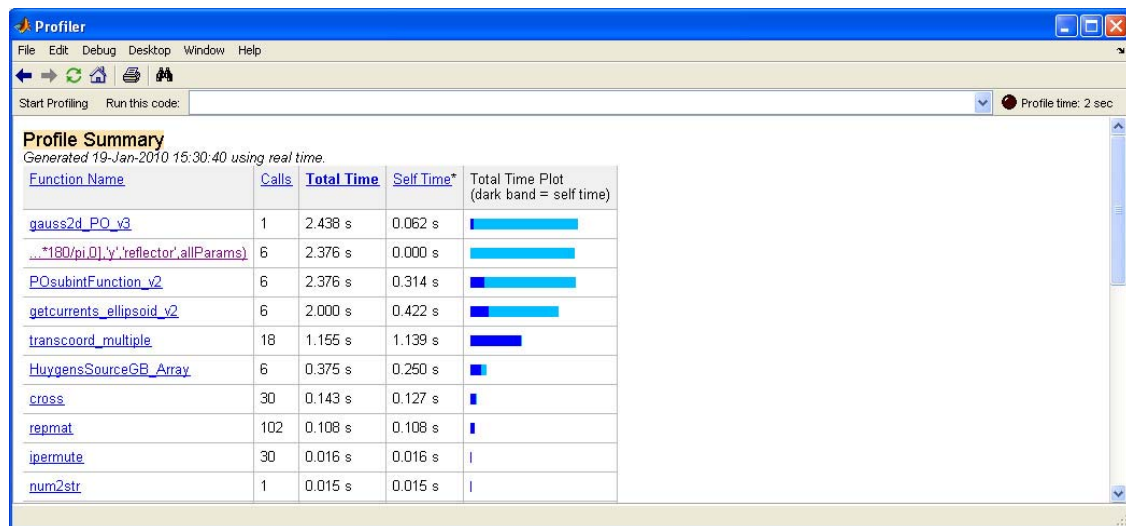
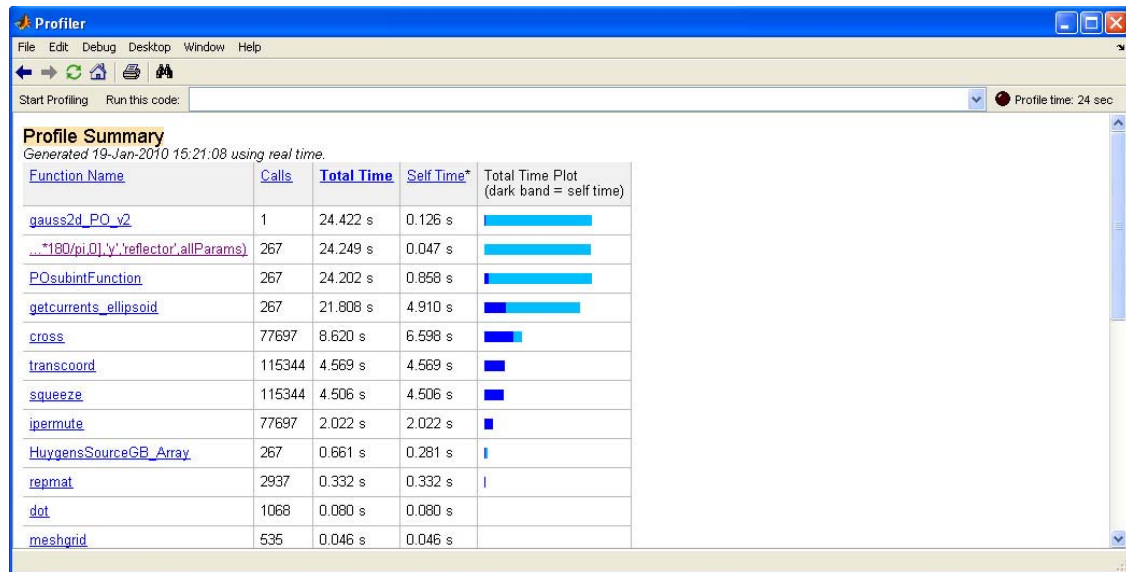


Figure 4.13. Matlab Profiler report for the integration of PO integral for the same analysed geometry with two versions of the integration function and the dependent functions. As seen in the two tables, function `gauss2d_PO_v3` (bottom report) has much fewer function calls than `gauss2d_PO_v2`. The computation has been accelerated by a factor of ten.

Code optimisation is achieved on two levels: the first one is adapting the code to better match the internal organisation of the programming language (in this case Matlab); the second one includes following general good programming practices. Adapting the code to match the internal organisation of Matlab means, for example, replacing *for* loops with matrix operations such as multielement multiplication, array summation and so on wherever possible, because Matlab is matrix-oriented and shows best performance when manipulating arrays. This also extends to calculating Bessel functions and evaluating dot-products and cross-products, which have built-in capabilities of treating array input variables. For example,

it is possible to compute values of the Bessel function for multiple orders and multiple arguments in a single function call, and reorganizing the code so as to take advantage of that possibility proves to be worth the effort. In Fig. 4.13. it is shown that the number of evaluated cross-products has been reduced from almost 78000 to only 30, which was achieved by reorganizing the code and grouping the input arguments submitted to the *cross* function.

Regarding good programming practices, they essentially consist of one and the same thing, i.e. reduction, on several closely related levels: reducing the number of performed operations within a function, reducing the number of calls to a given function, and reducing the number of used functions altogether. The number of operations can be reduced by precalculating, storing and reusing the results of an operation, if that operation is repeated more than once.

For example, in the Physical Optics integral (see Eq. (2.26)), one has to calculate terms

$$\vec{J}(\vec{r}') \left( -\frac{j}{kR} - \frac{1}{(kR)^2} + \frac{j}{(kR)^3} \right) \quad \text{and} \quad \left( \vec{J}(\vec{r}') \cdot \hat{R} \right) \hat{R} \left( \frac{j}{kR} + \frac{3}{(kR)^2} - \frac{3j}{(kR)^3} \right) \quad \text{for each}$$

observation point, where  $\vec{J}(\vec{r}')$  represents the equivalent magnetic current on the reflector and  $R$  is the distance between the observation point and the source point (on the reflector surface). The current is due to the incident field and is clearly independent of the observation point. Therefore, for evaluating the integral at more than a single point, it is a waste of time to calculate the current every time. A better strategy is to calculate the current only once and store it in a new variable<sup>7</sup>, which can be invoked whenever needed. Similarly, further reduction of simulation time can be achieved by applying the same principle to the  $R$ -dependent terms in the above expressions, noticing that all of the  $\frac{1}{(kR)}$ ,  $\frac{1}{(kR)^2}$  and  $\frac{1}{(kR)^3}$

terms are used more than once. In case an external function is called for calculating the currents, the reduced number of operations can be measured also in the reduced number of calls to that very function. In Fig. 4.13. one can see that in the older version of the code there are 267 calls to the function "getcurrents\_ellipsoid", while in the upgraded version there are only 6 calls to the equivalent function "getcurrents\_ellipsoid\_v2", with a significant effect on

---

<sup>7</sup> The current is computed at points dictated by the integration routine, hence for each iteration of the integration, a new (denser) grid of current values is computed, and the resulting 2D array variable is larger for each subsequent iteration. To save these arrays of different dimensions in a single array, in order to be able to recall them simply, an empty cell array is defined before the start of the integration, and each of the calculated 2D arrays is stored as an element in that cell array.



the needed computation time. Finally, as for reducing the number of used functions, it too can be achieved on different levels. One aspect includes grouping similar functions into one bigger function. This was done for the evaluation of the  $x$ ,  $y$  and  $z$ -derivatives of conical beams, which all have to compute the same scalar wave-object recurrence. Another aspect consists of writing out explicit expressions for some simple operations that can normally be done also with built-in Matlab functions. For example, if one wants to isolate a point (i.e. retrieve its  $(x, y, z)$  components) in an array of points, faster than any solution based on built-in functions (such as *squeeze* for example) will be the simple hand-picking of the desired values from the three-dimensional array. A similar conclusion is valid for some other operations, e.g. dot and cross products.

The second major enhancement of the code was the construction of own integration routines. The standard Matlab quadrature functions (*quad*, *quadl* and *dblquad*) were found to be too slow for treating two-dimensional integration of highly oscillating functions like the ones encountered in the Physical Optics integral. Upon closer inspection, it was noticed that the algorithm for two-dimensional integration was basically performing line integration in  $x$  for each point in  $y$ , and was not taking full advantage of Matlab's array-oriented structure. The new integration functions were built to work directly with two-dimensional input variables, performing genuine surface integration. For the quadrature algorithm, 12-point Gaussian quadrature [50] was chosen (in both dimensions). The optimal number of points for the quadrature algorithm was determined heuristically, bearing in mind that a too low number of points will require too many iterations to converge, while a too high number of points will have as a consequence a rapid increase in the number of subintegral function evaluations between iteration steps, both with an adverse effect on the algorithm speed. The algorithm was also revised and enhanced with help of Matlab Profiler and the techniques described in this section.

By applying these enhancements and optimisations, the numerical evaluation of conical beams was sped up by a factor of 10, while the Physical Optics integral computation time was reduced by more than 300 times.

## 5. NUMERICAL VALIDATION

In this section, the theory presented in chapters 3 and 4 is numerically tested and compared to other available solutions and different methods. First, two tests are performed to verify the expansion into complex conical beams for the scalar and the vector case, respectively. Next, the analysis of a single reflector is performed and the results are compared to the referent Physical Optics solution, obtained via the GRASP9 SE electromagnetic simulator [34]. The last test case consists of an analysis of a two-reflector system, and the results are verified against the referent Physical Optics solution and compared to the simpler Gauss-Hermite modal analysis. For the sake of comparing computation times, the Physical Optics analysis based mostly on the algorithm implemented in GRASP was reproduced in Matlab, and additional comments and discussion on that subject are given in Sec. 0.

### 5.1. Test Sources

Two source configurations have been chosen for the numerical tests exposed in this chapter: transverse magnetic circular waveguide modes and the complex Huygens source.

Circular waveguide modes have been chosen as excitation to verify the scalar and vector conical beam expansion because they possess closed form expressions both in spatial and spectral domain (see Appendix B). This allows for the direct calculation of the radiation integral, providing an exact reference solution and enabling the verification of all intermediate steps in the beam expansion.

The complete method for analysing reflector antenna systems was tested with a complex Huygens source excitation. The Huygens source is a source composed of a pair of mutually orthogonal elementary dipoles, one electric and one magnetic. When moved into complex space, it radiates a field with a Gaussian amplitude distribution, similar to a simple Gaussian beam. The Gaussian amplitude distribution resembles that of fields radiated by corrugated horn antennas, often used as excitation in beam waveguide systems. However, unlike the simple Gaussian beam, the Huygens source radiates a physically correct vector field, and can give more useful results when designing a reflector antenna system.

### 5.1.1. Circular Waveguide Modes

The first of the two sources used for numerical verification is a transverse magnetic (TM) circular waveguide mode. The  $TM_{mn}$  mode is defined by [9]

$$\vec{E}_{mn}(\rho, \phi) = \alpha_{mn} J'_m(\alpha_{mn}\rho) \cos(m\phi) \hat{\rho} - \frac{m}{\rho} J_m(\alpha_{mn}\rho) \sin(m\phi) \hat{\phi}, \quad (4.72)$$

where  $J_m$  and  $J'_m$  are the  $m$ -th order Bessel function and its derivative, respectively, and  $\alpha_{mn} = \chi_{mn}/r_w$ , where  $r_w$  is the radius of the circular waveguide (i.e. aperture), and  $\chi_{mn}$  is the  $n$ -th zero of the  $m$ -th order Bessel function. The Fourier transform of the mode can be found in closed form (see Appendix B), and the rectangular components of the electric field spectrum are

$$\begin{aligned} \tilde{E}_{x,mn}(k_\rho, \alpha) &= j^{m-1} 2\pi \frac{\alpha_{mn} r_w}{\alpha_{mn}^2 - k_\rho^2} \cos(m\alpha) \cos(\alpha) \\ &\cdot \{ \alpha_{mn} J'_{m+1}(\alpha_{mn} r_w) J_{m+1}(k_\rho r_w) - k_\rho J_{m+1}(\alpha_{mn} r_w) J'_{m+1}(k_\rho r_w) \}, \end{aligned} \quad (4.73)$$

$$\begin{aligned} \tilde{E}_{y,mn}(k_\rho, \alpha) &= j^{m-1} 2\pi \frac{\alpha_{mn} r_w}{\alpha_{mn}^2 - k_\rho^2} \cos(m\alpha) \sin(\alpha) \\ &\cdot \{ \alpha_{mn} J'_{m+1}(\alpha_{mn} r_w) J_{m+1}(k_\rho r_w) - k_\rho J_{m+1}(\alpha_{mn} r_w) J'_{m+1}(k_\rho r_w) \}. \end{aligned} \quad (4.74)$$

The spatial and spectral distributions of the  $x$ -component of  $TM_{01}$  mode are shown in Fig. 4.1.

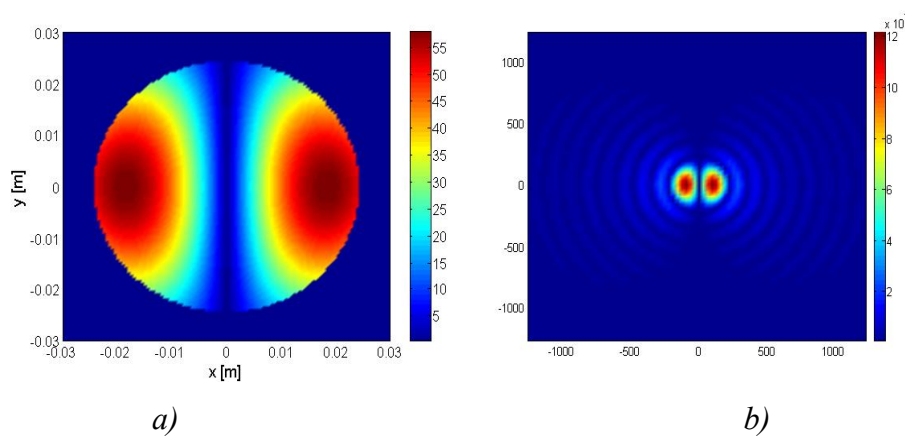


Figure 4.1. a) Magnitude of the  $E_x$  component of a  $TM_{01}$  circular waveguide mode aperture field ( $r_w = 0.024049$  m,  $k = 100$ ). b) Magnitude of the  $x$ -component of the corresponding spectrum.

### 5.1.2. Huygens Source in Complex Space

The second source employed in the tests presented in this chapter is the so-called Huygens Source in Complex Space. This source serves to generate a tapered beam similar to actual

fields radiated by real sources typically employed in beam waveguides and similar quasi-optical reflector systems (e.g. corrugated horn antennas). This is illustrated in Figs. 4.2.a and 4.2.b., which compare the near and far-field radiation patterns of a complex source point and real radiated fields from a corrugated horn.

Often, simple Gaussian beams are used to model the excitation of a quasi-optical system, in order to get a quick estimate of the system's behaviour. However, due to their shortcomings and limitations (see Sec. 2.2.3.), the correctness of the results is very limited. The Huygens source provides an alternative to the simple Gaussian beam. When displaced into the complex plane, it too radiates a beam with a Gaussian taper, but the field it generates satisfies Maxwell's equations and is physically correct in both in near field and far field, which is a significant advantage when analysing such systems.

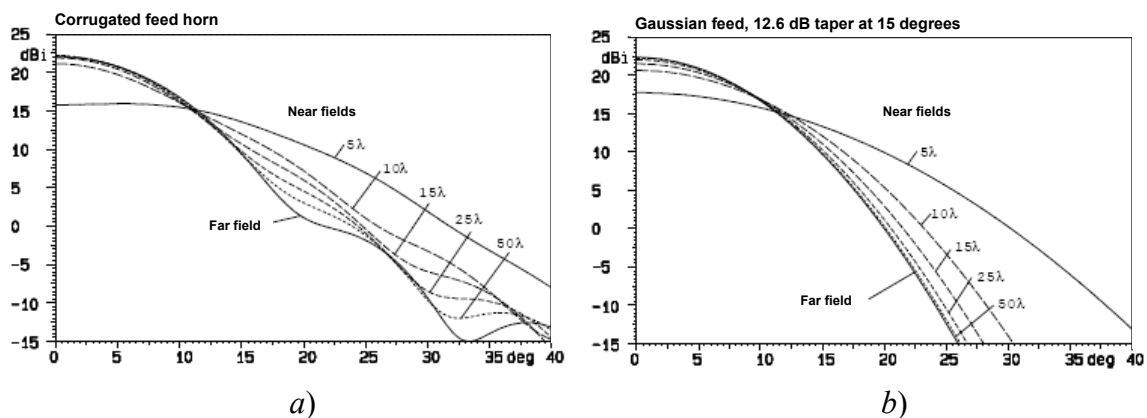


Figure 4.2. Fields of a) conical corrugated feed horn, and b) Huygens source with complex displacement  $b$  giving the same taper of 12.7 dB, at different near field sphere radii (source: Ref. [34])

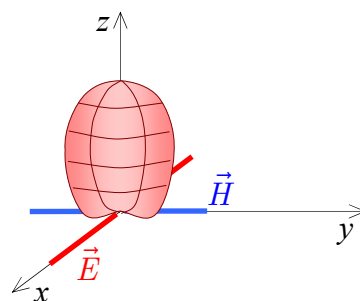


Figure 4.3. The Huygens source consisting of an electric and a magnetic dipole

The Huygens' source consists of an electrical  $x$ -directed short dipole (a Hertzian dipole) and a  $y$ -directed short magnetic dipole, as shown in Fig. 4.3., and produces a  $z$ -directed beam. The

polarisation of the field generated by such a composition of elementary sources is co-polar, in all directions, to the linear  $x$ -polarisation as defined according to Ludwig's 3rd definition [34]. The complete field expressions for the Huygens source are obtained by inserting  $\vec{J}(\vec{r}') = A_0\sqrt{2/\eta}\delta(x)\delta(y)\delta(z)\hat{x}$  and  $\vec{M}(\vec{r}') = A_0\sqrt{2\eta}\delta(x)\delta(y)\delta(z)\hat{y}$  into the radiation integral of Eqs. (2.26) and (2.27), where  $A_0$  is a constant. The Delta functions interact with the integral in such a way that the result is simply the value of the subintegral function at  $\vec{r}' = (0, 0, 0)$ , e.g. for the electric field:

$$\begin{aligned}\vec{E}(\vec{r}) &= \frac{\eta}{4\pi}\vec{J}\left(-\frac{j}{kR} - \frac{1}{(kR)^2} + \frac{j}{(kR)^3}\right)k^2e^{-jkR} \\ &+ \frac{\eta}{4\pi}(\vec{J} \cdot \hat{R})\hat{R}\left(\frac{j}{kR} + \frac{3}{(kR)^2} - \frac{3j}{(kR)^3}\right)k^2e^{-jkR} \\ &- \frac{1}{4\pi}(\vec{M} \times \hat{R})\left(\frac{1 + jkR}{(kR)^2}\right)k^2e^{-jkR}.\end{aligned}\quad (4.75)$$

By applying the far-field approximation as in Sec. 2.1, we arrive at a simple expression for the field of the Huygens source at large distances  $r$ :

$$\vec{E}(r, \theta, \phi) = E_0 \frac{e^{-jkr}}{r} (1 + \cos\theta) (\cos\phi \hat{\theta} - \sin\phi \hat{\phi}) \quad (4.76)$$

where  $E_0$  is a constant. When this source is located at a point with the complex position  $(x, y, z) = (0, 0, jb)$ , it will generate a Gaussian beam propagating in the positive  $z$ -direction.

The derivations are analogous to those presented in Sec. 2.2.2., and the expression becomes

$$\vec{E}(r, \theta, \phi) = E_0 \frac{e^{-jkr}}{r} e^{kb \cos\theta} (1 + \cos\theta) (\cos\phi \hat{\theta} - \sin\phi \hat{\phi}). \quad (4.77)$$

Usually, one prefers to define the beam through its (measurable) radiation parameters, rather than an imaginary complex displacement. For example, in GRASP one can define the beam taper and the beam taper angle. A beam taper of  $A = -10$  dB with a beam taper angle of  $\theta_t = 5^\circ$  define a beam with a Gaussian profile, which is attenuated by 10 dB at  $\theta = 5^\circ$ , where  $\theta$  is measured from the axis of propagation. Parameter  $b$  can be then obtained from these two parameters by substituting them into (4.77), giving

$$b = \frac{20 \log\left(\frac{1 + \cos\theta_t}{2}\right) - A}{20k(1 - \cos\theta_t) \log(e)}. \quad (4.78)$$

We also note here an important relationship between the complex parameter  $b$  of a Gaussian beam and its waist  $w_0$  [34]. It is important to know at least approximately the waist size of

the beam, in order to estimate the far-field distance when using the inverse near-field to far-field transformation of Sec. 4.1.2:

$$w_0 = \sqrt{\frac{2b}{k}}. \quad (4.79)$$

## 5.2. Verification: Scalar Beams (TM mode)

In the first step of verification, we inspect the accuracy of the scalar version of the conical beam expansion, to confirm the possibility of using the GPOF approximation in this context. For this purpose, we compare the fields calculated by formulas (3.2) and (3.8). The direct integration of the radiation integral was programmed in Mathematica, and the wave-object summation program was developed in Matlab. For the direct integration, explicit expressions for the spectrum of circular waveguide modes, given by (4.73) and (4.74), were used. The integral in  $\alpha$  was resolved in closed form, yielding a product of a cosine and a Bessel function. This extra step helped both improve the accuracy and reduce computation time of the direct integration.

The comparison was performed at two different  $z$ -planes, lying at a distance  $0.3\lambda$  and  $2.0\lambda$  away from the aperture plane ( $z = 0$ ), respectively. Field values were computed over a  $10\lambda$  by  $10\lambda$  square, on a rectangular grid of 61 by 61 points, with the wavenumber  $k = 100$ . The results are compared in Figs. 4.4. and 4.5. The agreement between the two plots is excellent in both cases, and is confirmed by plots showing the relative error between the direct and conical beam solution along a straight line  $x = 0.1 \text{ m}$ , marked with a dashed white line in Figs. 4.4.a and 4.5.a. For the conical beam expansion, only 16 wave objects were used.

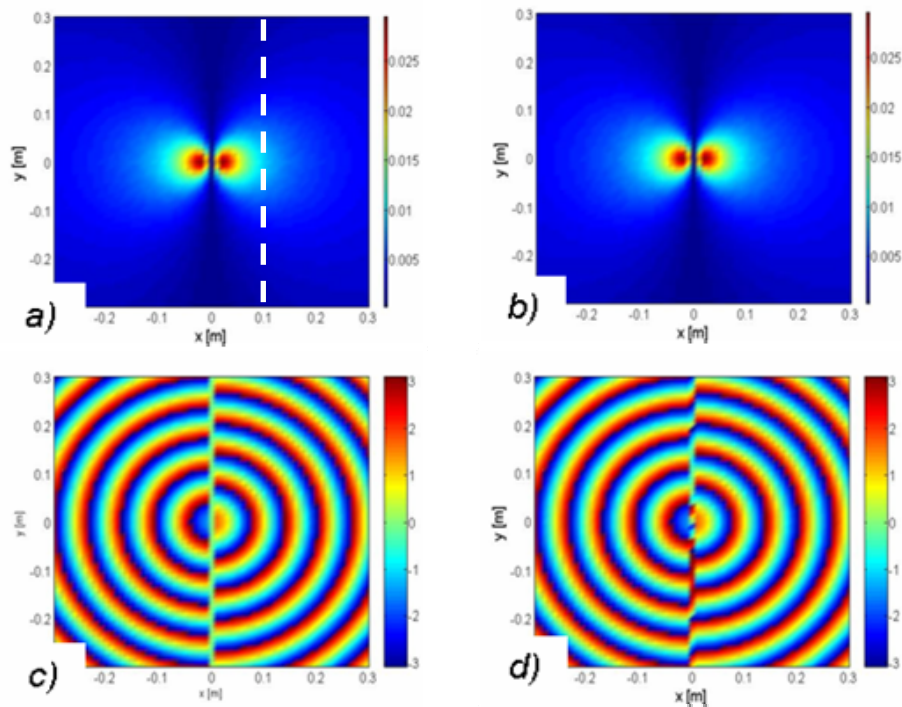


Figure 4.4. Field plots of a  $TM_{01}$  circular waveguide mode in the plane  $z = 0.3\lambda$ : Magnitude (a) and phase (c) obtained via direct integration; Magnitude (b) and phase (d) obtained via wave-objects expansion

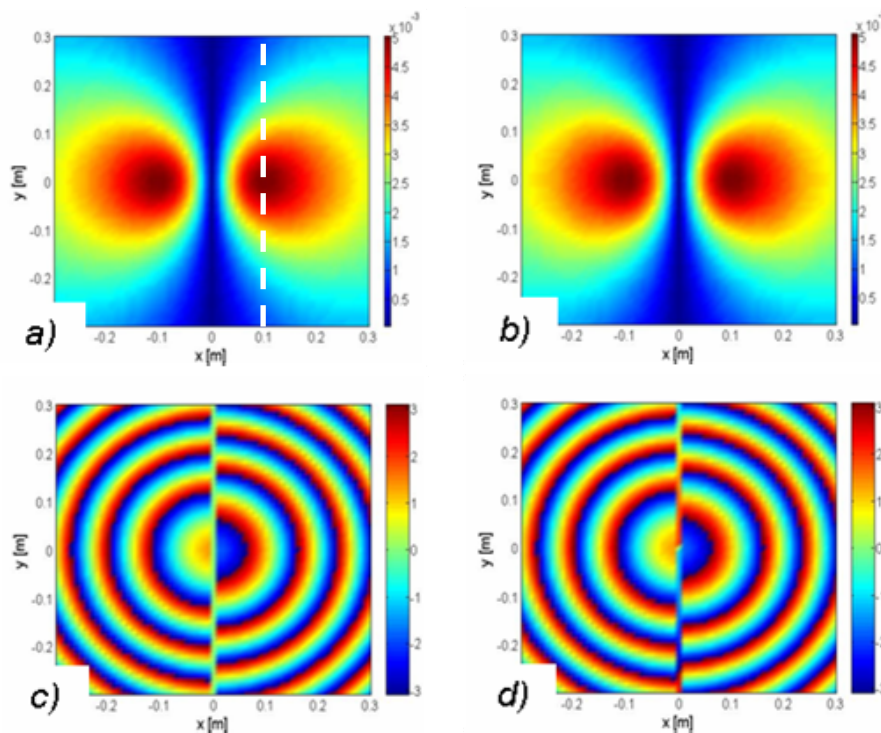


Figure 4.5. Field plots of a  $TM_{01}$  circular waveguide mode in the plane  $z = 2.0\lambda$ : Magnitude (a) and phase (c) obtained via direct integration; Magnitude (b) and phase (d) obtained via wave-objects expansion

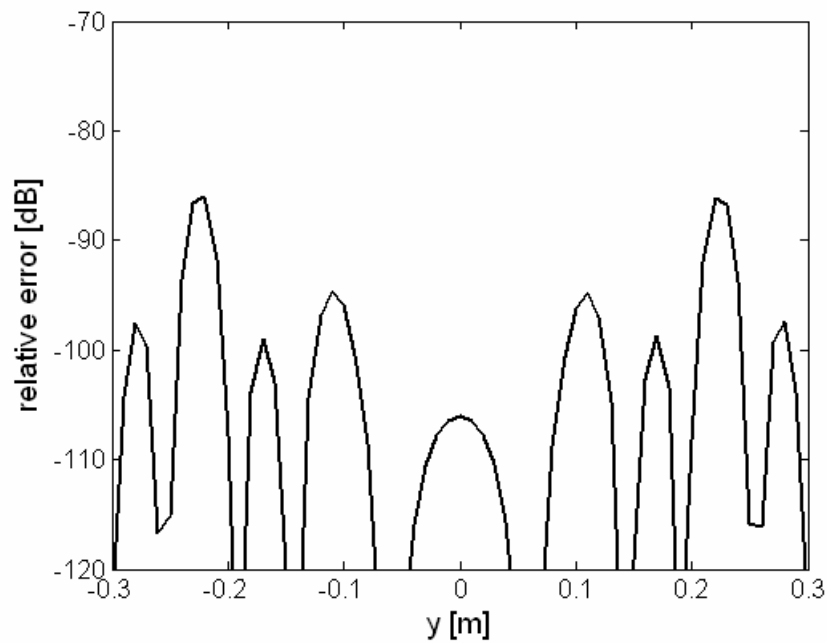


Figure 4.6. Relative error between the directly integrated scalar radiation integral and the same radiation integral computed via conical beam expansion, for a  $TM_{01}$  circular waveguide mode;  $z = 0.3\lambda$ ,  $x = 0.1\text{m}$ .

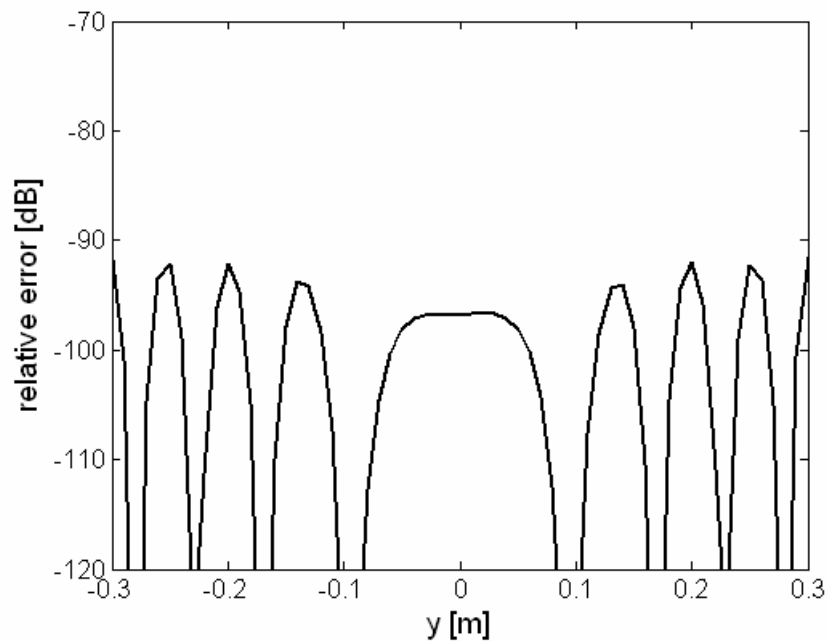


Figure 4.7. Relative error between the directly integrated scalar radiation integral and the same radiation integral computed via conical beam expansion, for a  $TM_{01}$  circular waveguide mode;  $z = 2\lambda$ ,  $x = 0.1\text{m}$ .



### 5.3. Verification: Vectorised Beams (TM mode)

This example [22] serves to verify the validity of the chosen vectorisation strategy described in Sec. 3.2.2. Here, again a TM circular waveguide mode distribution is chosen as the excitation, but we observe the actual radiated electric field. We compare the field obtained via the direct integration of the vector radiation integral given by (2.26) and the field obtained via the recurrence formulas for the three components of the radiated electric field given in Secs. 3.2.3.1 thru 3.2.3.3. It is also worth mentioning that circular waveguide modes are the basic output of a horn mode-matching analysis, and consequently their expansion in wave-objects is of significant practical concern.

Figs. 4.8. thru 4.10. show the comparison of the directly radiated field of a  $TM_{01}$  mode (via spatial radiation integral), and the conical-beam radiated field, for all three components of the electric field. For this example, the wavenumber was  $k = 100$  and the magnitude of the radiated mode was unity. The field points were calculated on a  $x$ -directed straight line ( $y = 5\lambda$ ) lying in the plane  $z = 10\lambda$ . As can be seen in the figures, again an excellent agreement between direct integration and the wave-objects expansion was achieved, confirming the choice of the vectorisation strategy. The discontinuity in the curve close to  $x = 0$  m for the  $x$ -component of the field is due to rather scarce sampling, which was chosen as such due to very slow convergence of the direct integration in Mathematica. Only 14 wave-objects were necessary to completely reconstruct the field of the  $TM_{01}$  mode.

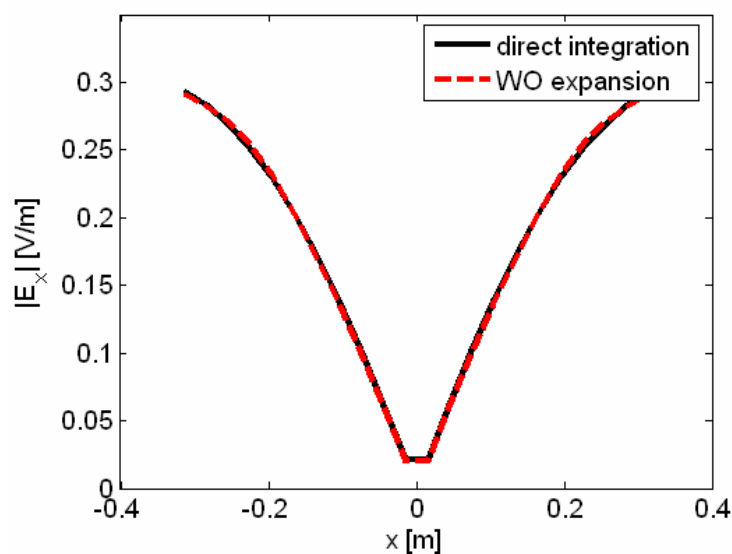


Figure 4.8. Radiated field components of a  $TM_{01}$  circular waveguide mode:  $E_x$ . Waveguide radius is 0.02405 m, and wavenumber is  $k = 100$ .

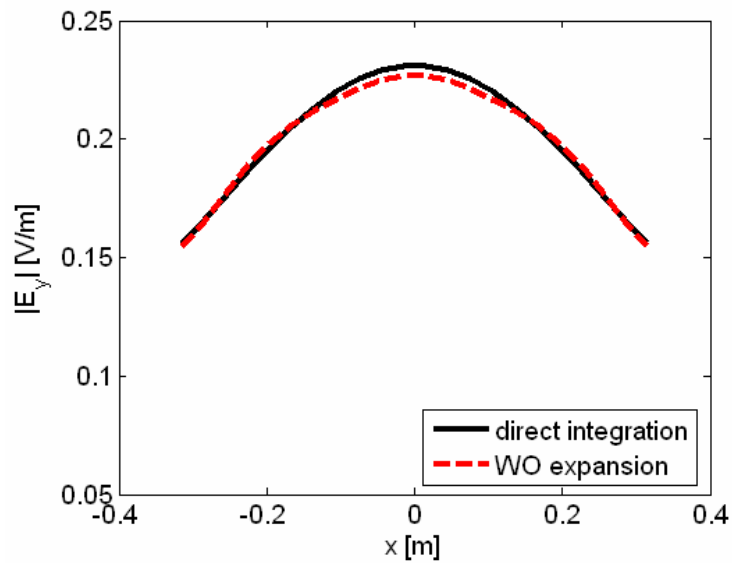


Figure 4.9. Radiated field components of a  $TM_{01}$  circular waveguide mode:  $E_y$ . Waveguide radius is 0.02405 m, and wavenumber is  $k = 100$ .

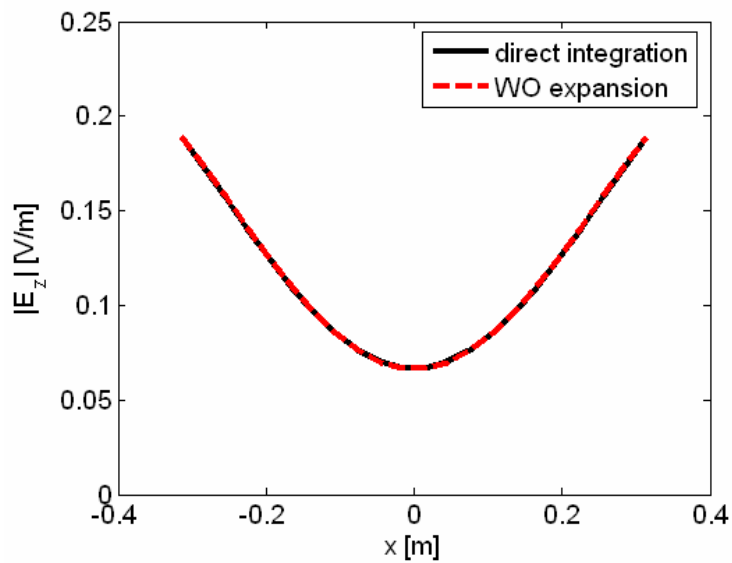


Figure 4.10. Radiated field components of a  $TM_{01}$  circular waveguide mode:  $E_z$ . Waveguide radius is 0.02405 m, and wavenumber is  $k = 100$ .

## 5.4. Analysis of a Single Reflector

In this example an analysis of a single ellipsoidal reflector is presented [22]. It serves to validate the so-called recollection of the scattered WO-fields and their re-expansion into wave-objects via the described procedure. In this case we considered an ellipsoidal reflector defined as the intersection of an ellipsoid (with semi-axes  $a = 8\lambda$ ,  $b = 4\lambda$ ) with a cone whose nose angle is  $\theta_c$  (here  $30^\circ$ ) and whose apex coincides with one of the two focal points of the ellipsoid, as shown in Fig. 4.11.

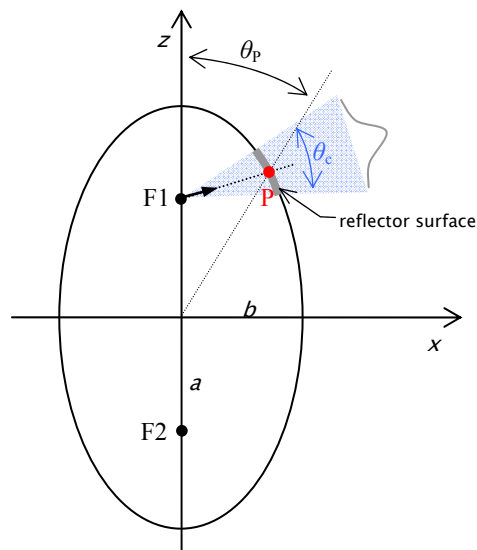


Figure 4.11. Geometry of the ellipsoidal reflector. The beam is radiated from focal point  $F1$  towards the point on the ellipsoid for which  $\theta_p = 40^\circ$ , while the cone nose angle is  $30^\circ$ .

The reflector was illuminated by a complex source point located at focal point  $F1$ , whose complex displacement gave a Gaussian-type taper to the incident field, with the equivalent Gaussian beam waist  $w_0 = 1\lambda$ . Note that a complex point source is equivalent to the wave-object of order zero,  $\mathcal{W}_0$ , as has been demonstrated in [23], [40]. Therefore, the aim was to illuminate the reflector with a complex conical beam and determine whether or not the reflected field could be re-expanded into conical beams and reconstructed in the far-field zone. The result was confronted with directly calculated PO fields.

The reflected PO field and the re-expanded WO field were computed on a semi-sphere of radius  $100\lambda$ . The spectral components of the reflected field in the beam waist plane (which contains the second focal point  $F2$ ) were found through the inverse near-field to far-field transformation. Only 36 wave-objects were employed to reconstruct the radiated fields. The agreement between the results is very good, as shown in Fig. 4.12.

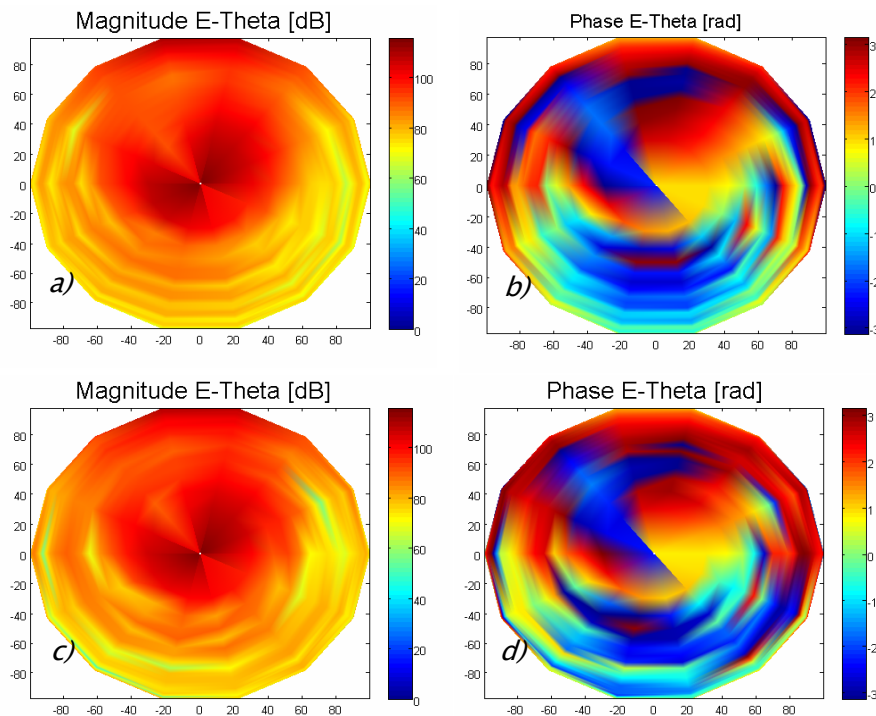


Figure 4.12. Magnitude (a) and phase (b) of the PO-radiated field. Magnitude (c) and phase (d) of the same field reconstructed with complex conical beams. Both field values are computed on a semi-sphere of radius  $100\lambda$  whose origin coincides with focal point  $F2$ .

## 5.5. Analysis of a Two-Reflector System (Huygens' Source)

The last test case serves to demonstrate a real-life application of the developed mathematical model. The geometry under consideration is a two-reflector system consisting of ellipsoidal reflectors, as shown in Figs. 4.13. and 4.16.. The frequency is 3 GHz, i.e.  $\lambda = 0.1\text{ m}$ , and the semi-axes of both ellipsoids are  $a = 5\text{ m} = 50\lambda$ ,  $b = c = 4\text{ m} = 40\lambda$ . The first reflector is illuminated from its geometrical focus  $F1$  by a complex Huygens source with a beam taper of  $A = -10\text{ dB}$  and a beam taper angle of  $\theta = 6^\circ$ , which corresponds to the beam waist  $w_{0,inc} = 0.326\text{ m} = 3.26\lambda$ . The incident beam is launched towards the apex of the first ellipsoid (on the  $z$ -axis; point  $(0, 0, 4\text{ m})$ ).

Two reflector setups were considered. In the first setup, the two reflectors were identical, and their common radius was  $r_0 = 10\lambda$ . They were placed in such a way that the focal point (waist) of the beam reflected from the first reflector ( $z_{waist,1}$ , as calculated via the auxiliary

Gaussian beam analysis) lay halfway between the  $z$ -axis apices of the two reflectors, so as to ensure maximum symmetry in the system from the beam analysis perspective (i.e. equal beam width on both reflectors). The geometry and the beam trajectory through this system of reflectors are illustrated in Fig. 4.13. and the results are compared to the reference PO solution obtained via GRASP SE in Figs. 4.14. and 4.15., showing very good agreement.

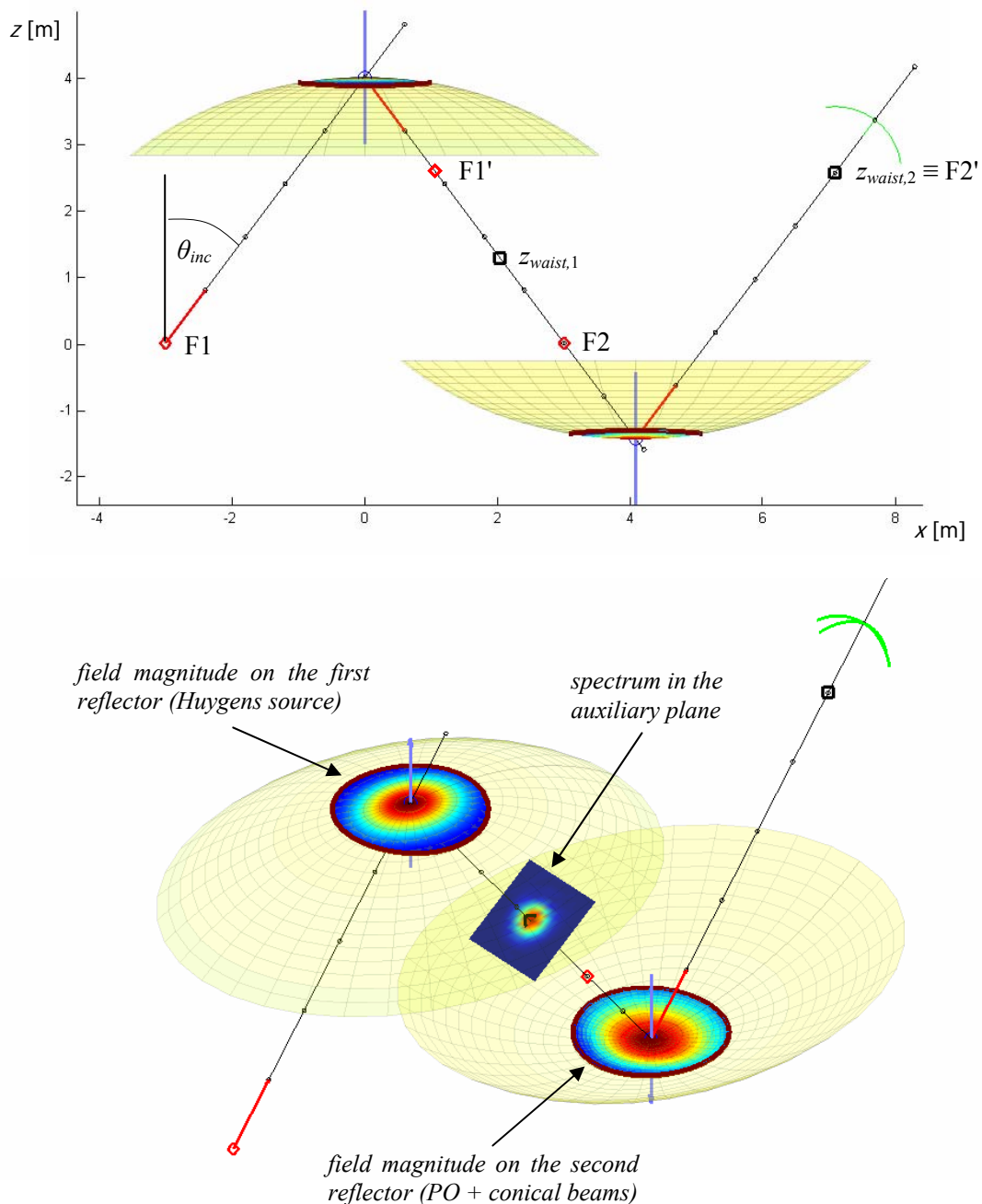


Figure 4.13. Side view (top) and perspective view (bottom) of a system of two ellipsoidal reflectors with a circular rim. Shown in the perspective view is also the field in the auxiliary plane upon first reflection. The green lines denote the observation points in the far field (two theta-cuts, for  $\phi = 0^\circ$  and  $\phi = 90^\circ$ ).

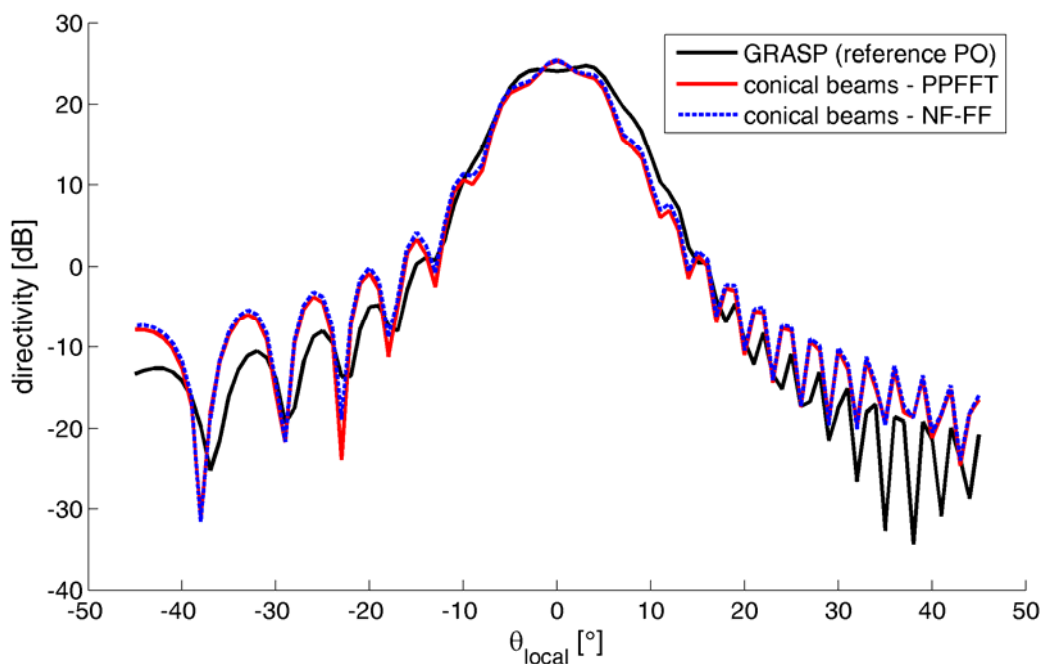


Figure 4.14. Radiation pattern (directivity) of the output beam after two reflections (first test case). Angle  $\theta$  is measured from the estimated (obtained by ray analysis) direction of propagation of the outgoing beam;  $\phi_{local} = 0^\circ$

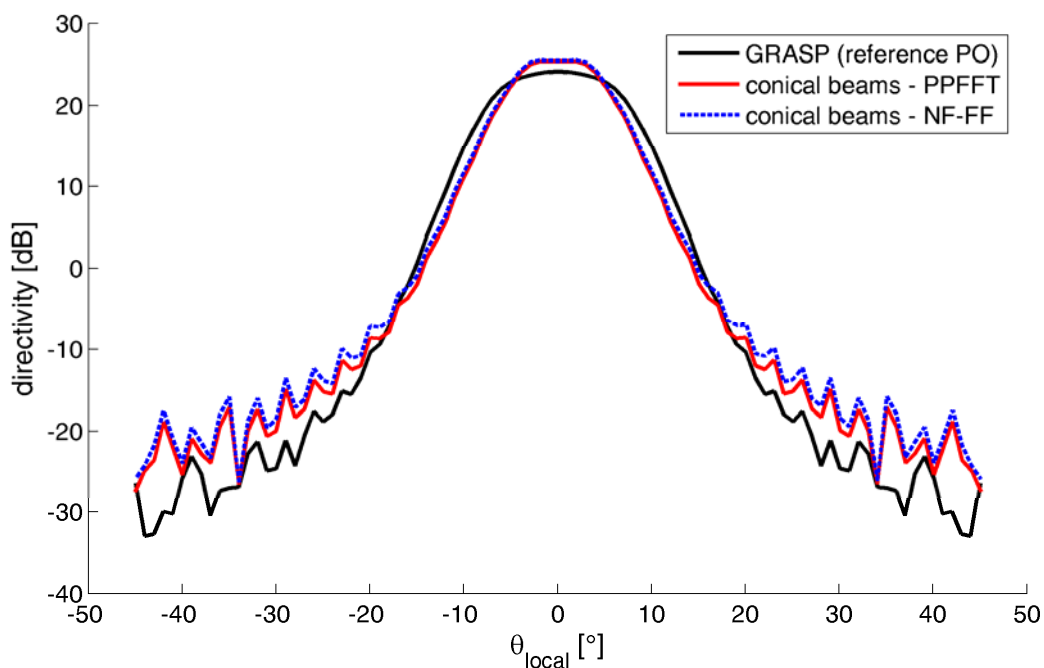


Figure 4.15. Radiation pattern (directivity) of the output beam after two reflections (first test case). Angle  $\theta$  is measured from the estimated (obtained by ray analysis) direction of propagation of the outgoing beam;  $\phi_{local} = 90^\circ$

In the second scenario, shown in Fig. 4.16., the first part of the system remained unchanged, while the second part was altered. The radius of the second reflector was  $r'_0 = 15\lambda$ , and the second ellipsoid was moved so that its  $z$ -axis apex lay at the point (6 m, 0, 4 m). That is, the two ellipsoids were geometrically symmetric about the focal point F2 of the first reflector (which was at the same time the first focal point of the second reflector, i.e.  $F2 \equiv F1'$ ). Such placement is optimal from the point of view of ray-optical analysis, since in the ray-optical approximation, all rays emitted from F1 refocus at F2 and then again at F2'. In order to investigate the effects of non-ideal positioning of reflectors and the ability of the developed method to assess such problems, the center of the second reflector's rim was shifted by  $\Delta x = 5\lambda$  in positive  $x$  direction relative to its default position (by default, the rim center is set to coincide with the intersection of the central ray and the reflector surface, to achieve the most symmetric field distribution on its surface). Comparing Figs. 4.16. and 4.13. (bottom images), one can see that in Fig. 4.16. the fields on the inner part of the second reflector are truncated more abruptly than in Fig. 4.13.. Consequently, for the second test case one can expect to have more ripples in the radiation pattern in the  $\phi = 0^\circ$  cut-plane.

The calculated fields for the two cuts ( $\phi = 0^\circ$  and  $\phi = 90^\circ$ ) for the second test case are shown in Figs. 4.17. and 4.18., respectively. The reference solution was again obtained with GRASP SE. The new method compares favourably to the reference results, and is capable of predicting correct field values down to 40 dB below peak value. Also, as explained above, in the transverse plane (i.e. for  $\phi = 90^\circ$ ), the radiation pattern is much smoother in Fig. 4.18. than in Fig. 4.15.

As shown in Figs. 4.14.-4.15. and 4.17.-4.18., both variants of the developed hybrid method consisting of Physical Optics and the new complex conical beams have been tested (the one based on pseudo-polar FFT and the one based on inverse near-field to far-field transformation). The results show excellent consistency, proving that either variation of the method can be successfully used in the analysis of such reflector systems.

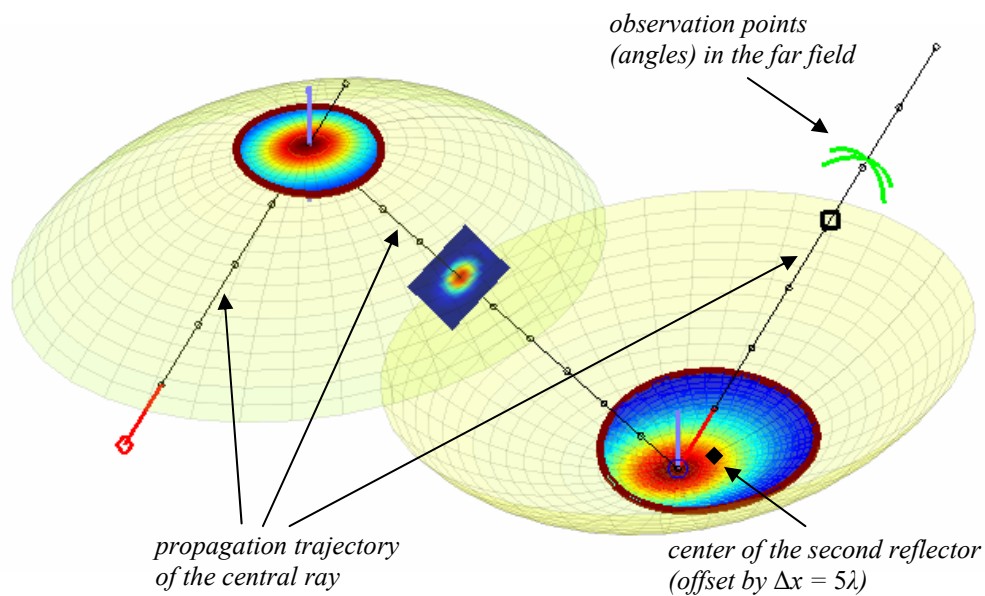
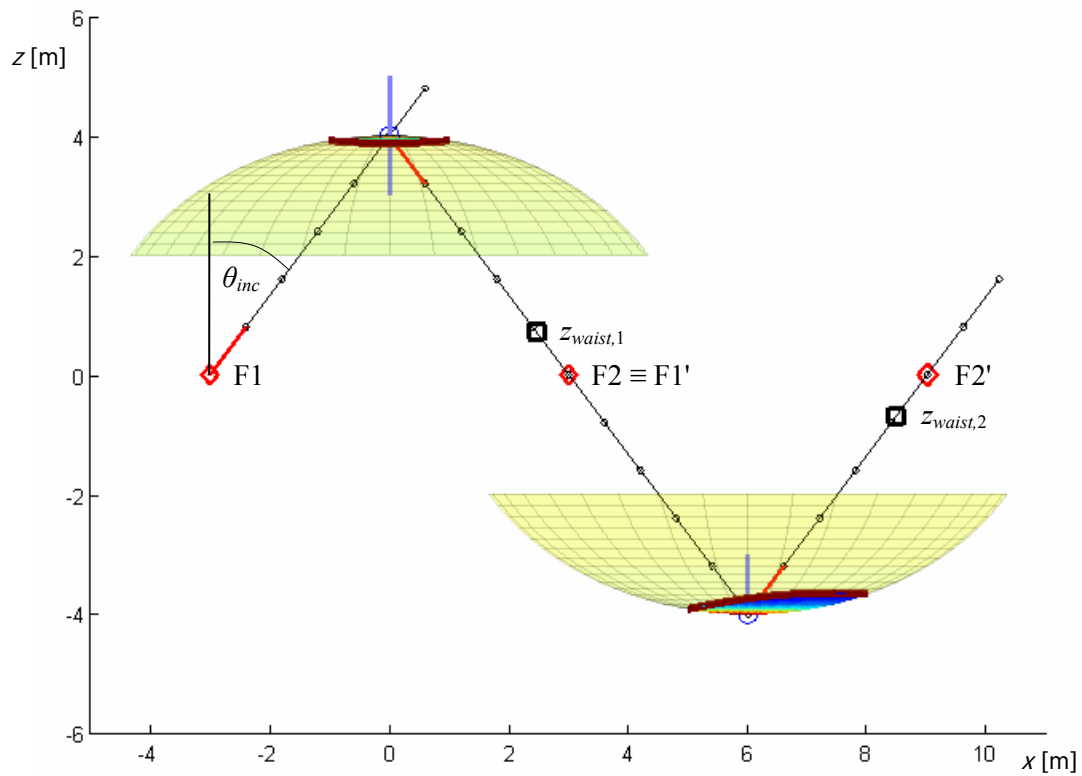


Figure 4.16. Side view (top) and perspective view (bottom) of a system of two ellipsoidal reflectors with a circular rim (second test case). The second reflector is larger ( $r_0 = 15\lambda$ ) than in the first case and offset by  $\Delta x = 5\lambda$ . The field is observed at the same far-field points as in the first case.



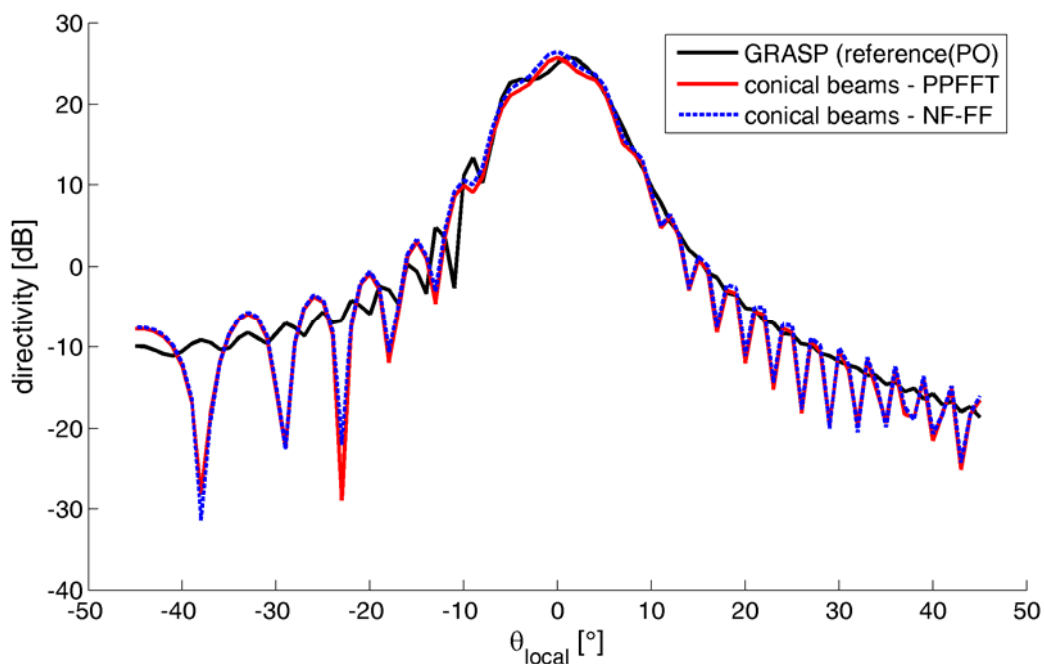


Figure 4.17. Radiation pattern (directivity) of the output beam after two reflections (second test case). Angle  $\theta$  is measured from the estimated (obtained by ray analysis) direction of propagation of the outgoing beam;  $\phi_{local} = 0^\circ$

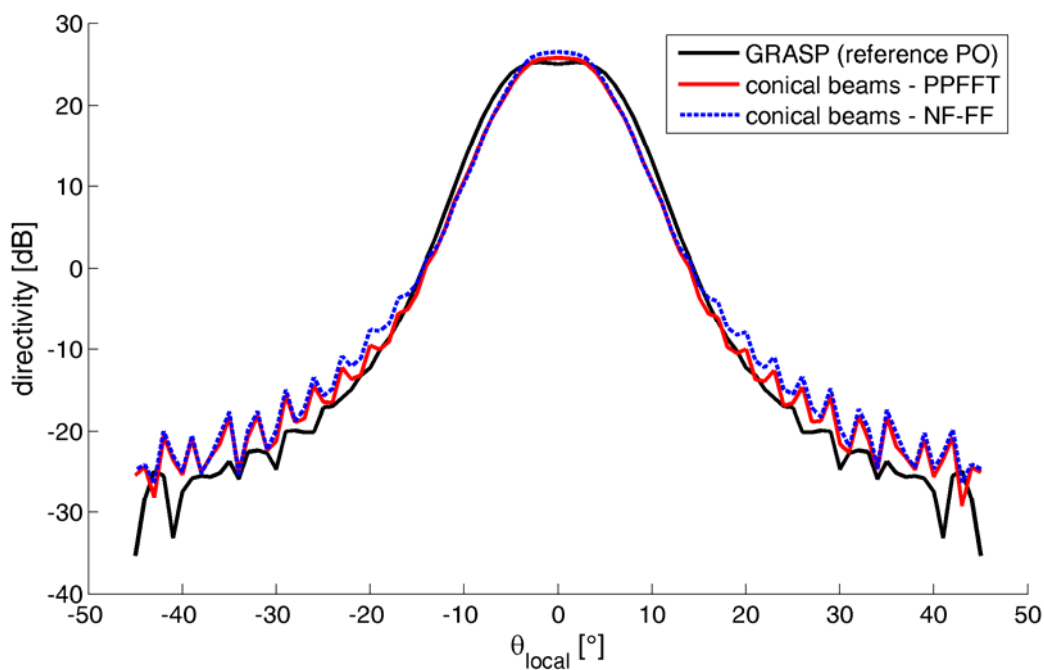


Figure 4.18. Radiation pattern (directivity) of the output beam after two reflections (second test case). Angle  $\theta$  is measured from the estimated (obtained by ray analysis) direction of propagation of the outgoing beam;  $\phi_{local} = 90^\circ$

## 5.6. Discussion

In Table 5.1. the computation times of the examples presented in the previous section are compared. In order to be able to compare the simulation times of the new hybrid method with the direct Physical Optics analysis, an entire PO analysis for a two-reflector system was implemented following step-by-step the model described in the GRASP Technical Description [34]. As can be seen, the hybrid method based on PO and conical beams is by almost an order of magnitude faster than the referent PO solution.

*Table 5.1. Computation Times for Test Cases of Sec. 5.5.*

	COMPUTATION TIME [min]		
	Direct PO	PO + CCB (PPFFT)	PO + CCB (NF-FF)
<b>CASE 1</b>	587	117*	115*
<b>CASE 2</b>	576	84*	78*

\* The simulation does not include one optimization step implemented in the PO analysis, which reduces the calculation time by a factor of two (PO analysis was developed at a later stage)

The simulations were performed on a P4 equipped with 8-core 3.0 GHz Xeon CPUs in Matlab 2009b. It should be pointed out, however, that in other (older) versions of Matlab this advantage may not be so pronounced. This is because more recent versions of Matlab employ algorithms for parallel processing in built-in functions, such as Bessel and Hankel functions, which are heavily used in the computation of conical beams. Unlike that, the Physical Optics algorithm developed for the sake of comparisons does not involve many Bessel and Hankel function evaluations (unless it is not pertinent to the original source), nor was it built with parallel processing in mind. Consequently, with more recent versions of Matlab the new approach does have some unfair advantage over PO. Furthermore, the most exact approach was assumed in the PO algorithm, which calculates the currents via the radiation integral for every necessary point. Further time savings could have been achieved by using some interpolation scheme instead of the direct radiation integral approach.

## 6. CONCLUSIONS

The analysis of quasi-optical reflector antenna systems such as beam waveguides presents significant numerical challenges and requires the development of new methods particularly suited for that frequency and size range, because classical numerical methods like Method of Moments lead to systems of equations with more than a million unknowns per reflector, rendering them useless for any practical application. Instead, the common approach in the analysis of quasi-optical reflector antenna systems is to express the radiated field, typically highly directed with a narrow main lobe, in terms of a relatively low number of wave objects of higher complexity and calculate reflection for each of them analytically, in this way reducing the number of unknowns in the system. The aim is to develop a repeatable modular process, whereby one module completely covers the analysis of the interaction of the incident wave with one reflector. The analysis starts by expanding the incident field into a sum of wave objects of a given kind, then uses the appropriate method to calculate the reflection from the metallic surface of the reflector under consideration, and finally re-expands the reflected fields in a new sum of wave objects of the same kind.

In this thesis, a new kind of wave objects suitable for this analysis approach has been introduced. These wave objects have been named Complex Conical Beams: conical, due to their angular selectivity property; complex, due to the presence of complex exponents in their formulation; beams, due to the capacity of being highly directive. The complex exponents are obtained naturally, starting from a standard scalar spectral domain radiation integral, upon applying the Fourier series expansion and the GPOF expansion to the electric field spectrum. These manipulations allow reducing the initial double integral to a double sum of complex conical beams, whose analytical solution has been derived in this thesis. Apart from the natural generation of the beams, the main advantage of the new formulation over most other approaches is that the new wave objects respect the wave equation in the whole domain. Furthermore, the conical beams possess closed form expressions in both space and spectral domain and, by constructing the vector solution using auxiliary vector potentials, the vector form of conical beams satisfies Maxwell's equations.

In order to analyse reflector antenna systems, the developed conical beam expansion has been linked to Physical Optics (PO), which is considered the reference solution among high-

frequency antenna analysis methods. In this approach, the incident field from the source, which is represented by an aperture field (or its spectrum), is in the first step of the process expanded into complex conical beams. The beams are used to rapidly calculate the input PO equivalent currents, and the reflected fields are then obtained via the standard space-domain radiation integral. The advantage over pure PO analysis comes from a convenient strategy for recollecting and re-expanding the reflected fields into a new sum of conical beams, which significantly reduces simulation times for multi-reflector environments. Two possible strategies of using complex conical beams have been developed and presented in the thesis. In the first one, the reflected fields are calculated on a spherical grid in the far-field zone, and the spectrum in the near-field zone of the reflector is obtained directly from far-field values via the inverse near-field to far-field transformation. In the second one, the fields are calculated on a rectangular grid in the focal plane of the reflected wave, after which the spectrum in the same plane is computed via the Pseudo-polar FFT algorithm combined with 1-D interpolation. The first strategy requires the computation of the reflected wave on fewer observation points, whereas the second one calculates more points but does it much faster, due to the inherent property that the fields reflected from different parts of the reflector are all almost in phase close to the focus of the reflected wave, ensuring fast convergence of the numerically evaluated integrals. For both techniques it is necessary to determine the direction of propagation of the reflected wave and the location its focus. This is achieved by an auxiliary simple Gaussian beam analysis, which has also been implemented.

The developed mathematical model has been coded into a computer programme and its validity has been verified on various levels with two different excitations and against different referent solutions. To verify the scalar and vector conical beam expansion, TM circular waveguide modes have been chosen as excitation, because they possess closed form expressions in both space and spectral domain. This allows direct calculation of the radiation integral and provides an exact reference, which in return enables to verify all intermediate steps in the beam expansion. The overall method for analysing reflector antenna systems has been tested with a complex Huygens source excitation, which provides a physically correct vector field with a Gaussian taper, mimicking well real-life fields radiated by corrugated horn antennas. Two test systems were analysed, involving one or two ellipsoidal reflectors. The results were verified against pure Physical Optics simulations and compared to simpler high-frequency methods, such as Gaussian beam analysis and the analysis involving higher-order Gauss-Hermite modes. The resulting method has been shown to have the level of accuracy

comparable to straight Physical Optics, which is considered to be the reference solution in the analysis of quasi-optical systems. However, due to the modular approach, the simulation time is more than an order of magnitude shorter than that of the PO analysis, proving this method to be especially advantageous for analysing systems with more than one reflector, i.e. beam waveguides.

## APPENDIX A: FUNCTION APPROXIMATION VIA THE GENERALIZED PENCIL-OF-FUNCTIONS METHOD

Any transient signal  $y(t)$  can be represented by

$$y_k = y(t = k\Delta t) = \sum_{i=1}^M b_i e^{s_i k \Delta t}, \quad k = 0, 1, \dots, N-1 \quad (\text{A.1})$$

where  $b_i$  are complex residues<sup>1</sup>,  $s_i$  are complex poles and  $\Delta t$  is the sampling interval. For notational brevity, we can write  $z_i = e^{s_i \Delta t}$ , that is

$$y_k = \sum_{i=1}^M b_i z_i^k, \quad k = 0, 1, \dots, N-1 \quad (\text{A.2})$$

The objective is to find the best estimates of  $M$ ,  $b_i$  and  $z_i$  from the noise-contaminated data  $y_k = y(k\Delta t)$ . To do that, we consider the following set of information vectors

$$Y_0, Y_1, \dots, Y_L$$

where

$$y_i = [y_i, y_{i+1}, \dots, y_{i+N-L-1}]^T, \quad i = 0, 1, \dots, L; \quad 0 < L < N$$

The superscript denotes the transpose of a matrix. Based on these vectors, we can define two information matrices  $Y_1$  and  $Y_2$  as

$$Y_1 = [y_0, y_1, \dots, y_{L-1}]_{(N-L) \times L} \quad (\text{A.3})$$

$$Y_2 = [y_1, y_2, \dots, y_L]_{(N-L) \times L} \quad (\text{A.4})$$

It can be shown that the two matrices can be expressed as

$$Y_1 = Z_1 B Z_2 \quad (\text{A.5})$$

$$Y_2 = Z_1 B Z_0 Z_2 \quad (\text{A.6})$$

---

<sup>1</sup> The terms “complex residue” and “complex pole” have been introduced by the authors of the method [19]. Alternatively, they can be called simply complex amplitudes and complex exponents.

where

$$Z_1 = \begin{bmatrix} 1 & 1 & \dots & 1 \\ z_1 & z_2 & \dots & z_M \\ \vdots & & \ddots & \\ z_1^{N-L-1} & z_2^{N-L-1} & \dots & z_M^{N-L-1} \end{bmatrix}_{(N-L) \times M} \quad (\text{A.7})$$

$$Z_2 = \begin{bmatrix} 1 & z_1 & \dots & z_1^{L-1} \\ 1 & z_2 & \dots & z_2^{L-1} \\ \vdots & & \ddots & \\ 1 & z_M & \dots & z_M^{L-1} \end{bmatrix}_{M \times L} \quad (\text{A.8})$$

$$Z_0 = \text{diag}[z_1, z_2, \dots, z_M]_{M \times M} \quad (\text{A.9})$$

$$B = \text{diag}[b_1, b_2, \dots, b_M]_{M \times M}. \quad (\text{A.10})$$

If  $N - L \geq M$ , and  $L \geq M$ , the following relation is satisfied

$$(Z_1 B Z_2)^+ = Z_2^+ B^{-1} Z_1^+. \quad (\text{A.11})$$

where superscript  $+$  denotes the Moore-Penrose pseudo-inverse of a matrix.

There exist vectors  $\{p_i \mid i = 1, \dots, M\}$  such that

$$Y_1^+ Y_1 p_i = p_i, \quad (\text{A.12})$$

and

$$Y_1^+ Y_2 p_i = z_i p_i. \quad (\text{A.13})$$

The  $p_i$  are called the generalized eigenvectors of a matrix pencil  $Y_2 - z Y_1$  and  $z_i$  are  $M$  corresponding eigenvalues. To compute the pseudo-inverse  $Y_1^+$ , one can use the condensed singular value decomposition (SVD) of  $Y_1$  as follows

$$Y_1 = U D V^H, \quad (\text{A.14})$$

$$Y_1^+ = V D^{-1} U^H, \quad (\text{A.15})$$

where  $U = [u_1, \dots, u_M]$ ,  $V = [v_1, \dots, v_M]$ , corresponding to the  $M$  non-zero singular values  $D = \text{diag}\{\sigma_1, \sigma_2, \dots, \sigma_M\}$ .

Since  $Y_1^+ Y_1 = V V^H$  and  $V V^H = I$ , substituting (A.15) into (A.13) and left multiplying (A.13) yields

$$(Z - z_i I) z_i = 0, \quad (\text{A.16})$$

where  $i = 1, \dots, M$ ,

$$Z = D^{-1} U^H Y_2 V, \quad (\text{A.17})$$

and

$$z_i = V^H p_i, \quad (\text{A.18})$$

Note that  $Z$  is an  $M \times M$  matrix and  $z_i$  and  $z_i$  are eigenvalues and eigenvectors of  $Z$ , respectively. Once that complex poles  $z_i$  are found as eigenvalues of the matrix  $Z$ , the unknown residues  $b = [b_1, b_2, \dots, b_M]$  can be found by solving the system of linear equations

$$y_k = \sum_{i=1}^M b_i z_i^k, \quad k = 1, \dots, M. \quad (\text{A.19})$$

This algorithm is the basis of the GPOF method for extracting poles and residues of a system from its transient response.



## APPENDIX B: FOURIER TRANSFORM OF TM CIRCULAR WAVEGUIDE MODES

### B.1. 2-D Fourier Transform of a Vector Function in Polar Coordinates

The 2-D Fourier transformation is defined, in rectangular coordinates, as

$$\tilde{F}(k_x, k_y) = \int_{-\infty}^{\infty} \int_{-\infty}^{\infty} f(x, y) e^{-j(k_x x + k_y y)} dx dy \quad (\text{B.1})$$

Introducing the variable change  $x = r \cos \phi$ ,  $y = r \sin \phi$ , and likewise in the spectral domain

$k_x = k_\rho \cos \alpha$ ,  $k_y = k_\rho \sin \alpha$ , the 2-D Fourier transformation in polar coordinates becomes:

$$\tilde{G}(k_\rho, \alpha) = \int_0^{\infty} \int_{-\pi}^{\pi} g(\rho, \phi) e^{-jk_\rho \rho \cos(\phi - \alpha)} \rho d\rho d\phi \quad (\text{B.2})$$

This is straightforward if function  $f$  (and consequently  $g$ ) is scalar. For vector functions, one can transform separately the  $x$ -component and the  $y$ -component, but this approach is only valid in rectangular coordinates. In polar coordinates, the basis vectors change orientation with their position, and the function has to be “traced back” to rectangular coordinates.

In this sense, assuming that the original function is defined as

$$\vec{f}(x, y) = \hat{x} f_x(x, y) + \hat{y} f_y(x, y) \quad (\text{B.3})$$

and its equivalent in polar coordinates as

$$\vec{g}(\rho, \phi) = \hat{\rho} g_\rho(\rho, \phi) + \hat{\phi} g_\phi(\rho, \phi) \quad (\text{B.4})$$

the correct expressions for the components of the Fourier transform  $\vec{\tilde{G}}$  are found by coordinate substitution from the components of  $\vec{\tilde{F}}$ . We have

$$f_x(x, y) = g_\rho(\rho, \phi) \cos \phi - g_\phi(\rho, \phi) \sin \phi, \quad (\text{B.5})$$

$$f_y(x, y) = g_\rho(\rho, \phi) \sin \phi + g_\phi(\rho, \phi) \cos \phi, \quad (\text{B.6})$$

and similarly

$$\tilde{F}_x(k_x, k_y) = \tilde{G}_{k_\rho}(k_\rho, \alpha) \cos \alpha - \tilde{G}_\alpha(k_\rho, \alpha) \sin \alpha, \quad (\text{B.7})$$

$$\tilde{F}_y(k_x, k_y) = \tilde{G}_{k_\rho}(k_\rho, \alpha) \sin \alpha + \tilde{G}_\alpha(k_\rho, \alpha) \cos \alpha. \quad (\text{B.8})$$

Therefore, applying (B.1) on  $f_x$  and  $f_y$  components of  $f$ , we have

$$\tilde{F}_x = \tilde{G}_{k_\rho} \cos \alpha - \tilde{G}_\alpha \sin \alpha = \int_0^\infty \int_{-\pi}^\pi (g_\rho \cos \phi - g_\phi \sin \phi) e^{-jk_\rho \rho \cos(\phi-\alpha)} \rho d\rho d\phi \quad (\text{B.9})$$

$$\tilde{F}_y = \tilde{G}_{k_\rho} \sin \alpha + \tilde{G}_\alpha \cos \alpha = \int_0^\infty \int_{-\pi}^\pi (g_\rho \sin \phi + g_\phi \cos \phi) e^{-jk_\rho \rho \cos(\phi-\alpha)} \rho d\rho d\phi \quad (\text{B.10})$$

Solving the above system of two equations in two variables yields the final direct expressions for  $\tilde{G}_{k_\rho}$  and  $\tilde{G}_\alpha$ :

$$\tilde{G}_{k_\rho}(k_\rho, \alpha) = \int_0^\infty \int_{-\pi}^\pi (g_\rho \cos(\phi - \alpha) - g_\phi \sin(\phi - \alpha)) e^{-jk_\rho \rho \cos(\phi-\alpha)} \rho d\rho d\phi \quad (\text{B.11})$$

$$\tilde{G}_\alpha(k_\rho, \alpha) = \int_0^\infty \int_{-\pi}^\pi (g_\rho \sin(\phi - \alpha) + g_\phi \cos(\phi - \alpha)) e^{-jk_\rho \rho \cos(\phi-\alpha)} \rho d\rho d\phi \quad (\text{B.12})$$

## B.2. Fourier Transform of TM Circular Waveguide Modes

The TM modes in a circular waveguide are described with [27]:

$$\vec{E}_{kl}(\rho, \phi) = \alpha_{kl} J'_k(\alpha_{kl}\rho) \cos(k\phi) \hat{\rho} - \frac{k}{\rho} J_k(\alpha_{kl}\rho) \sin(k\phi) \hat{\phi} \quad (\text{B.13})$$

where  $\alpha_{kl} = \frac{\chi_{kl}}{r_w}$ , and  $\chi_{kl}$  is the  $l$ -th zero of the  $k$ -th order Bessel function  $J_k$ . We plug the  $\rho$  and  $\phi$  components of  $\vec{E}$  into (B.11) and (B.12) to derive expressions for the components of  $\vec{E}$  in polar spectral coordinates.

*Derivation of  $\tilde{E}_{k_\rho}$ .*

For  $\tilde{E}_{k_\rho}$  component, we have

$$\begin{aligned} \tilde{E}_{k_\rho}(k_\rho, \alpha) = & \int_0^\infty \int_{-\pi}^\pi \alpha_{kl} J'_k(\alpha_{kl}\rho) \cos(k\phi) \cos(\phi - \alpha) e^{-jk_\rho \rho \cos(\phi-\alpha)} \rho d\rho d\phi + \\ & + \int_0^\infty \int_{-\pi}^\pi \frac{k}{\rho} J_k(\alpha_{kl}\rho) \sin(k\phi) \sin(\phi - \alpha) e^{-jk_\rho \rho \cos(\phi-\alpha)} \rho d\rho d\phi \end{aligned} \quad (\text{B.14})$$

which can be rewritten as

$$\begin{aligned} \tilde{E}_{k\rho}(k\rho, \alpha) = & \alpha_{kl} \int_0^\infty \rho J'_k(\alpha_{kl}\rho) \left[ \int_{-\pi}^\pi \cos(k\phi) \cos(\phi-\alpha) e^{-jk\rho \cos(\phi-\alpha)} d\phi \right] d\rho + \\ & + k \int_0^\infty J_k(\alpha_{kl}\rho) \left[ \int_{-\pi}^\pi \sin(k\phi) \sin(\phi-\alpha) e^{-jk\rho \cos(\phi-\alpha)} d\phi \right] d\rho. \end{aligned} \quad (\text{B.15})$$

The integrals in  $\phi$  can be simplified by noticing the following relations:

$$\int_{-\pi}^\pi \cos(k\phi) \cos(\phi-\alpha) e^{-jk\rho \cos(\phi-\alpha)} d\phi = \frac{1}{-jk\rho} \frac{\partial}{\partial \rho} \int_{-\pi}^\pi \cos(k\phi) e^{-jk\rho \cos(\phi-\alpha)} d\phi \quad (\text{B.16})$$

$$\int_{-\pi}^\pi \sin(k\phi) \sin(\phi-\alpha) e^{-jk\rho \cos(\phi-\alpha)} d\phi = \frac{1}{-jk\rho} \frac{\partial}{\partial \alpha} \int_{-\pi}^\pi \sin(k\phi) e^{-jk\rho \cos(\phi-\alpha)} d\phi \quad (\text{B.17})$$

The simplified integrals can be related to the  $k$ -th order Bessel function [25], after rewriting  $k\phi = k(\phi-\alpha) + k\alpha$  and expanding the sine and cosine functions in (B.16) and (B.17):

$$\begin{aligned} \int_{-\pi}^\pi \cos(k\phi) e^{-jk\rho \cos(\phi-\alpha)} d\phi &= |\phi' = \phi - \alpha| \\ &= \cos(k\alpha) \int_{-\pi-\alpha}^{\pi-\alpha} \cos(k\phi') e^{-jk\rho \cos\phi'} d\phi' - \sin(k\alpha) \int_{-\pi-\alpha}^{\pi-\alpha} \sin(k\phi') e^{-jk\rho \cos\phi'} d\phi' \quad (\text{B.18}) \\ &= j^k 2\pi \cos(k\alpha) J_k(k\rho\rho) \end{aligned}$$

$$\begin{aligned} \int_{-\pi}^\pi \sin(k\phi) e^{-jk\rho \cos(\phi-\alpha)} d\phi &= |\phi' = \phi - \alpha| \\ &= \cos(k\alpha) \int_{-\pi-\alpha}^{\pi-\alpha} \sin(k\phi') e^{-jk\rho \cos\phi'} d\phi' - \sin(k\alpha) \int_{-\pi-\alpha}^{\pi-\alpha} \cos(k\phi') e^{-jk\rho \cos\phi'} d\phi' \quad (\text{B.19}) \\ &= j^k 2\pi \sin(k\alpha) J_k(k\rho\rho). \end{aligned}$$

Notice that one of the two integrals obtained after expanding the sine and cosine functions in both (B.18) and (B.19) equals zero due to the parity of the subintegral function.

Taking these results back to (B.16) and (B.17) and performing the differentiation, we get

$$\int_{-\pi}^\pi \cos(k\phi) \cos(\phi-\alpha) e^{-jk\rho \cos(\phi-\alpha)} d\phi = -j^{k-1} 2\pi \cos(k\alpha) J'_k(k\rho\rho) \quad (\text{B.20})$$

$$\int_{-\pi}^\pi \sin(k\phi) \sin(\phi-\alpha) e^{-jk\rho \cos(\phi-\alpha)} d\phi = -\frac{k}{k\rho} j^{k-1} 2\pi J_k(k\rho\rho) \cos(k\alpha). \quad (\text{B.21})$$

Plugged back into (B.15), this gives

$$\begin{aligned} \tilde{E}_\rho(k_\rho, \alpha) = & -j^{k-1} 2\pi \cos(k\alpha) \alpha_{kl} \int_0^\infty \rho J'_k(\alpha_{kl}\rho) J'_k(k_\rho\rho) d\rho + \\ & - j^{k-1} \frac{k^2}{k_\rho} 2\pi \cos(k\alpha) \int_0^\infty \frac{1}{\rho} J_k(\alpha_{kl}\rho) J_k(k_\rho\rho) d\rho. \end{aligned} \quad (\text{B.22})$$

In the next step, we make use of the following recurrence equations for Bessel functions and its derivatives [26]

$$\begin{aligned} 2J'_k(z) &= J_{k-1}(z) - J_{k+1}(z) \\ \frac{2k}{z} J_k(z) &= J_{k-1}(z) + J_{k+1}(z) \end{aligned}$$

in order to combine the two integrals and reach the final solution. Here, it should be noted that even though the transformation integral extends to infinity, the subintegral function only exists for  $r \in [0, r_w]$ . Hence, (B.22) becomes

$$\begin{aligned} \tilde{E}_{k_\rho}(k_\rho, \alpha) = & -j^{k-1} \frac{\pi}{2} \cos(k\alpha) \alpha_{kl} \int_0^{r_w} \rho (J_{k-1}(\alpha_{kl}\rho) - J_{k+1}(\alpha_{kl}\rho)) (J_{k-1}(k_\rho\rho) - J_{k+1}(k_\rho\rho)) d\rho \\ & - j^{k-1} \frac{\pi}{2} \cos(k\alpha) \alpha_{kl} \int_0^{r_w} \rho (J_{k-1}(\alpha_{kl}\rho) + J_{k+1}(\alpha_{kl}\rho)) (J_{k-1}(k_\rho\rho) + J_{k+1}(k_\rho\rho)) d\rho. \end{aligned} \quad (\text{B.23})$$

The two integrals can now be summed up, and in doing this the  $(k-1) \cdot (k+1)$  terms cancel out, leaving

$$\begin{aligned} \tilde{E}_{k_\rho}(k_\rho, \alpha) = & -j^{k-1} \pi \cos(k\alpha) \alpha_{kl} \int_0^{r_w} \rho J_{k-1}(\alpha_{kl}\rho) J_{k-1}(k_\rho\rho) d\rho - \\ & - j^{k-1} \pi \cos(k\alpha) \alpha_{kl} \int_0^{r_w} \rho J_{k+1}(\alpha_{kl}\rho) J_{k+1}(k_\rho\rho) d\rho. \end{aligned} \quad (\text{B.24})$$

The above integrals can be solved in closed form by applying the following expression [26]:

$$\begin{aligned} \int_0^z \left[ (k^2 - l^2)t - \frac{\mu^2 - \nu^2}{t} \right] C_k(kt) D_k(lt) dt = \\ = z [k C_{k+1}(kz) D_k(lz) - l C_k(kz) D_{k+1}(lz)] - (\mu - \nu) C_k(kz) D_k(lz), \end{aligned} \quad (\text{B.25})$$

where  $C_n$  and  $D_n$  are any of the Bessel or Hankel functions of order  $n$ . Substituting  $\mu=\nu=k$  and  $C, D \rightarrow J$ ;  $k \rightarrow \alpha_{kl}$ ;  $l \rightarrow k_\rho$ , the above expression simplifies to

$$\int_0^{r_w} \rho J_k(\alpha_{kl}\rho) J_k(k_\rho\rho) d\rho = \frac{r_w}{\alpha_{kl}^2 - k_\rho^2} [\alpha_{kl} J_{k+1}(\alpha_{kl}r_w) J_k(k_\rho r_w) - k_\rho J_k(\alpha_{kl}r_w) J_{k+1}(k_\rho r_w)]. \quad (\text{B.26})$$

Applying (B.26) in (B.24), we get

$$\begin{aligned} \tilde{E}_{k_\rho}(k_\rho, \alpha) = & -j^{k-1} \pi \cos(k\alpha) \frac{\alpha_{kl} r_w}{\alpha_{kl}^2 - k_\rho^2} [\alpha_{kl} J_k(\alpha_{kl} r_w) J_{k-1}(k_\rho r_w) - k_\rho J_{k-1}(\alpha_{kl} r_w) J_k(k_\rho r_w)] \\ & -j^{k-1} \pi \cos(k\alpha) \frac{\alpha_{kl} r_w}{\alpha_{kl}^2 - k_\rho^2} [\alpha_{kl} J_{k+2}(\alpha_{kl} r_w) J_{k+1}(k_\rho r_w) - k_\rho J_{k+1}(\alpha_{kl} r_w) J_{k+2}(k_\rho r_w)] \end{aligned} \quad (\text{B.27})$$

One can note that the term  $J_k(\alpha_{kl} r_w)$  equals zero, because  $\alpha_{kl} r_w = \chi_{kl}$  and  $\chi_{kl}$  is the zero of  $J_k$ , but the expression simplifies more by first regrouping terms with  $\alpha_{kl}$  and those with  $k_\rho$ , and next adding and subtracting  $J_k(\alpha_{kl} r_w) J_{k+1}(k_\rho r_w)$  in the first, and  $J_{k+1}(\alpha_{kl} r_w) J_k(k_\rho r_w)$  term in the second case. We obtain:

$$\begin{aligned} \tilde{E}_{k_\rho}(k_\rho, \alpha) = & -j^{k-1} \pi \cos(k\alpha) \frac{\alpha_{kl} r_w}{\alpha_{kl}^2 - k_\rho^2} \cdot \\ & \cdot \left\{ \alpha_{kl} \left[ J_k(\alpha_{kl} r_w) (J_{k-1}(k_\rho r_w) + J_{k+1}(k_\rho r_w)) + J_{k+1}(k_\rho r_w) (J_{k+2}(\alpha_{kl} r_w) - J_k(\alpha_{kl} r_w)) \right] \right. \\ & \left. - k_\rho \left[ J_k(k_\rho r_w) (J_{k-1}(\alpha_{kl} r_w) + J_{k+1}(\alpha_{kl} r_w)) + J_{k+1}(\alpha_{kl} r_w) (J_{k+2}(k_\rho r_w) - J_k(k_\rho r_w)) \right] \right\} \end{aligned} \quad (\text{B.28})$$

Using again the recurrence relations for the Bessel functions and bearing in mind that  $J_k(\alpha_{kl} r_w) = 0$ , the first and the third product in the above equation vanish, while the second and the fourth yield  $J'_{k+1}$  terms. Finally, we get the closed form expression for the  $k_\rho$  component of the electric field spectrum of a  $\text{TM}_{kl}$  circular waveguide mode:

$$\begin{aligned} \tilde{E}_{k_\rho}(k_\rho, \alpha) = & j^{k-1} 2\pi \cos(k\alpha) \frac{\alpha_{kl} r_w}{\alpha_{kl}^2 - k_\rho^2} \\ & \cdot \left\{ \alpha_{kl} J'_{k+1}(\alpha_{kl} r_w) J_{k+1}(k_\rho r_w) - k_\rho J_{k+1}(\alpha_{kl} r_w) J'_{k+1}(k_\rho r_w) \right\}. \end{aligned} \quad (\text{B.29})$$

### Derivation of $\tilde{E}_\alpha$

For the  $\tilde{E}_\alpha$  component, we plug equation (B.13) and plug it into (B.12):

$$\begin{aligned} \tilde{E}_\alpha(k_\rho, \alpha) = & \int_0^\infty \int_{-\pi}^\pi \alpha_{kl} J'_k(\alpha_{kl}\rho) \cos(k\phi) \sin(\phi-\alpha) e^{-jk_\rho\rho \cos(\phi-\alpha)} \rho d\rho d\phi - \\ & - \int_0^\infty \int_{-\pi}^\pi \frac{k}{\rho} J_k(\alpha_{kl}\rho) \sin(k\phi) \cos(\phi-\alpha) e^{-jk_\rho\rho \cos(\phi-\alpha)} \rho d\rho d\phi \end{aligned} \quad (\text{B.30})$$

Performing the same trick as in (B.16) and (B.17), this can be rewritten as

$$\begin{aligned} \tilde{E}_\alpha(k_\rho, \alpha) = & -\frac{\alpha_{kl}}{jk_\rho} \int_0^\infty \rho J'_k(\alpha_{kl}\rho) \frac{\partial}{\partial \alpha} \left( \int_{-\pi}^{\pi} \cos(k\phi) e^{-jk_\rho \rho \cos(\phi-\alpha)} d\phi \right) d\rho + \\ & + \frac{k}{jk_\rho} \int_0^\infty J_k(\alpha_{kl}\rho) \frac{\partial}{\partial \rho} \left( \int_{-\pi}^{\pi} \sin(k\phi) e^{-jk_\rho \rho \cos(\phi-\alpha)} d\phi \right) d\rho \end{aligned} \quad (\text{B.31})$$

which becomes, making use of the results in (B.20) and (B.21),

$$\begin{aligned} \tilde{E}_\alpha(k_\rho, \alpha) = & -\frac{\alpha_{kl}}{jk_\rho} \int_0^\infty \rho J'_k(\alpha_{kl}\rho) \frac{\partial}{\partial \alpha} (j^k 2\pi \cos(k\alpha) J_k(k_\rho \rho)) d\rho + \\ & + \frac{k}{jk_\rho} \int_0^\infty J_k(\alpha_{kl}\rho) \frac{\partial}{\partial \rho} (j^k 2\pi \sin(k\alpha) J_k(k_\rho \rho)) d\rho. \end{aligned} \quad (\text{B.32})$$

It is now obvious that the two integrals can be joined, and that the combined subintegral function is in fact the derivative of the product  $J_k(\alpha_{kl}\rho) J_k(k_\rho \rho)$ . Therefore, the result of the integration is the product itself, which gives the final result

$$\tilde{E}_\alpha(k_\rho, \alpha) = j^{k-1} \frac{k}{k_\rho} 2\pi \sin(k\alpha) J_k(\alpha_{kl} r_w) J_k(k_\rho r_w) = 0, \quad (\text{B.33})$$

due to the fact that  $J_k(\alpha_{kl} r_w) = 0$ , as was noted in the derivation of the  $\tilde{E}_{k_\rho}$  component.

Having obtained the polar spectral components of the electric field of a  $\text{TM}_{kl}$  circular waveguide mode, it is now straightforward to extract the  $x$  and  $y$  components of the spectrum, using (B.7) and (B.8):

$$\begin{aligned} \tilde{E}_x(k_x, k_y) = & \tilde{E}_{k_\rho}(k_\rho, \alpha) \cos \alpha \\ = & j^{k-1} 2\pi \cos(k\alpha) \cos \alpha \frac{\alpha_{kl} r_w}{\alpha_{kl}^2 - k_\rho^2} \\ & \cdot \left\{ \alpha_{kl} J'_{k+1}(\alpha_{kl} r_w) J_{k+1}(k_\rho r_w) - k_\rho J_{k+1}(\alpha_{kl} r_w) J'_{k+1}(k_\rho r_w) \right\} \end{aligned} \quad (\text{B.34})$$

$$\begin{aligned} \tilde{E}_y(k_x, k_y) = & \tilde{E}_{k_\rho}(k_\rho, \alpha) \sin \alpha \\ = & j^{k-1} 2\pi \cos(k\alpha) \sin \alpha \frac{\alpha_{kl} r_w}{\alpha_{kl}^2 - k_\rho^2} \\ & \cdot \left\{ \alpha_{kl} J'_{k+1}(\alpha_{kl} r_w) J_{k+1}(k_\rho r_w) - k_\rho J_{k+1}(\alpha_{kl} r_w) J'_{k+1}(k_\rho r_w) \right\}. \end{aligned} \quad (\text{B.35})$$

## APPENDIX C: PSEUDO-POLAR FFT ALGORITHM

One of the key steps in the analysis of a sequence of reflector antennas with the hybrid method incorporating the Auxiliary-plane PO and the new complex conical beams, presented in Sec. 4.1, is the Fourier transformation of the reflected field in the focal plane in order to obtain its spectrum. The step is delicate because the FFT algorithm operates on a rectangular grid of field points, while the spectrum is needed on a polar grid (polar spectral coordinates  $(k_\rho, \alpha)$ ) for the subsequent FFT-GPOF expansion procedure. Since there is no known polar Fourier transform, it is necessary to perform some kind of interpolation in order to get the spectrum values on the required grid. However, classical 2-D interpolation requires a fairly oversampled spectrum in order to provide satisfactory accuracy at all points, which makes it too slow for real-time applications.

The recent development of unequally-spaced (US-FFT [41]) and non-uniform (NUFFT, [43]) FFT algorithms has enabled the development of the Pseudo-polar FFT algorithm (PPFFT, [39]), which overcomes the shortcomings of the two-step 2-D FFT + 2-D interpolation approach. The Pseudo-polar FFT plays the role of a halfway point — a nearly-Polar system from which conversion to Polar coordinates uses processes relying purely on 1D FFT's and interpolation operations. The algorithm boasts the same level of complexity as the standard FFT algorithm ( $O(N^2 \log N)$ ), owing to the use of only 1-D FFT and 1-D interpolation, which at the same time also guarantees higher accuracy than the 2-D based approach. The output spectrum is saved on a pseudo-polar grid consisting of radial rays which are non-uniformly distributed in  $\alpha$ , but on each ray the samples (in  $k_\rho$  variable) are equidistant.

The purpose of this Appendix is not to go through all the mathematical details of the PPFFT method, but rather to give just a basic sketch and an understanding of the output pseudo-polar grid on which the output data is saved, since that data has to be reverted to the classical polar grid for the subsequent analysis. For the interested reader, the detailed account of the method is given in [39], while the translation of the method into a toolbox of Matlab routines is available at [I-3].

The term Polar Fourier transform refers to the operation

$$\tilde{F}(r, \theta) = \mathcal{PF}(f(x, y)) \quad (\text{C.1})$$

namely, getting  $f(x, y)$  in Cartesian variables and computing  $\tilde{F}(r, \theta)$  defined with polar variables. While the change of variables is banal per se, its significance lies in the change of viewpoint it provides. As shown in Fig. C.1., the Polar grid of frequencies is defined as  $\xi_{p,q} = \{\xi_x[p, q], \xi_y[p, q]\}$  in the circle inscribed in the fundamental region  $\xi \in [-\pi, \pi)^2$ , and, given digital Cartesian data  $f[i_1, i_2]$  the Polar Fourier Transform is defined as the collection of samples  $\{\tilde{F}(\xi_{p,q})\}$ , where  $\tilde{F}(\xi_{p,q})$  is the trigonometric polynomial

$$\tilde{F}(\xi_{p,q}) = \sum_{i_1=0}^{N-1} \sum_{i_2=0}^{N-1} f[i_1, i_2] \exp(-j(i_1 \xi_x[p, q] - i_2 \xi_y[p, q])). \quad (\text{C.2})$$

The sampled frequency points are given by

$$\left\{ \begin{array}{l} \xi_x[p, q] = \frac{\pi p}{N} \cos(\pi q/2N) \\ \xi_y[p, q] = \frac{\pi p}{N} \sin(\pi q/2N) \end{array} \right\}, \quad \text{for } -N \leq p \leq N-1; \quad 0 \leq q \leq 2N-1. \quad (\text{C.3})$$

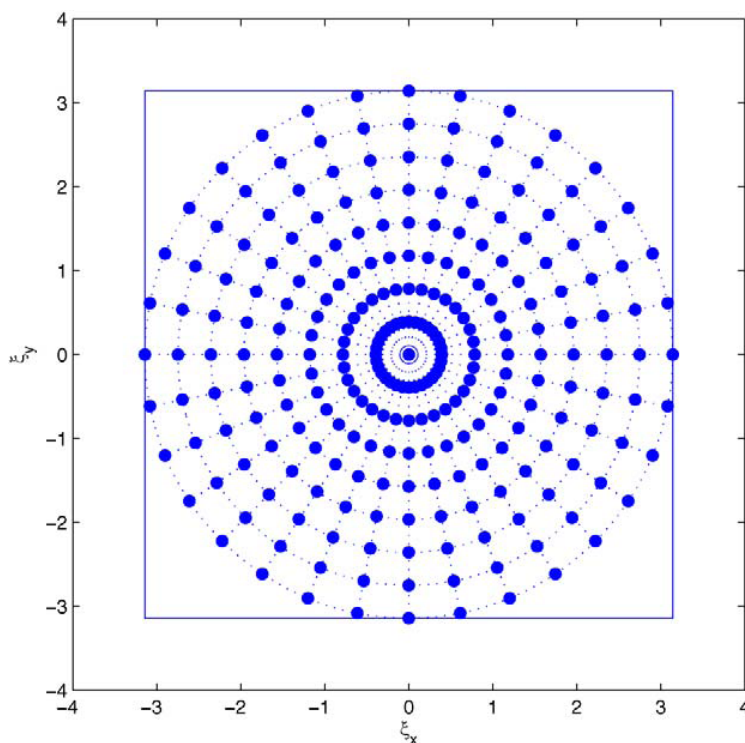


Figure C.1. Polar grid—intersection of 8 concentric circles and 16 angularly equispaced rays



The Polar sampling set is certainly a non-equispaced, non-Cartesian set. Thus, the problem of computing  $\tilde{F}(\xi_{p,q})$  from digital data  $f[i_1, i_2]$  is explicitly a problem of evaluating the Fourier transform of  $f$  at unequally spaced frequencies. In other words, the problem of computing the PDFT is a special case of the unequally-spaced FFT problem. Adapting ideas from the USFFT literature [41], [42], the forward Polar-FFT can be generally accomplished by the following stages:

- 1) pre-multiplication of  $f[i_1, i_2]$  by pre-computed weights  $s[i_1, i_2]$ ;
- 2) computation of the 2D-FFT on an oversampled Cartesian grid;
- 3) interpolation of the values on the Polar grid based on those given on the Cartesian one.

The method developed by Averbuch, Elad et al. uses a slightly modified approach, where a different launching grid is used, rather than the Cartesian one. The method reduces the process into only two steps:

- 1) a pseudo-polar FFT is applied on a pseudo-polar sampling set;
- 2) a conversion from pseudo-polar to Polar FT.

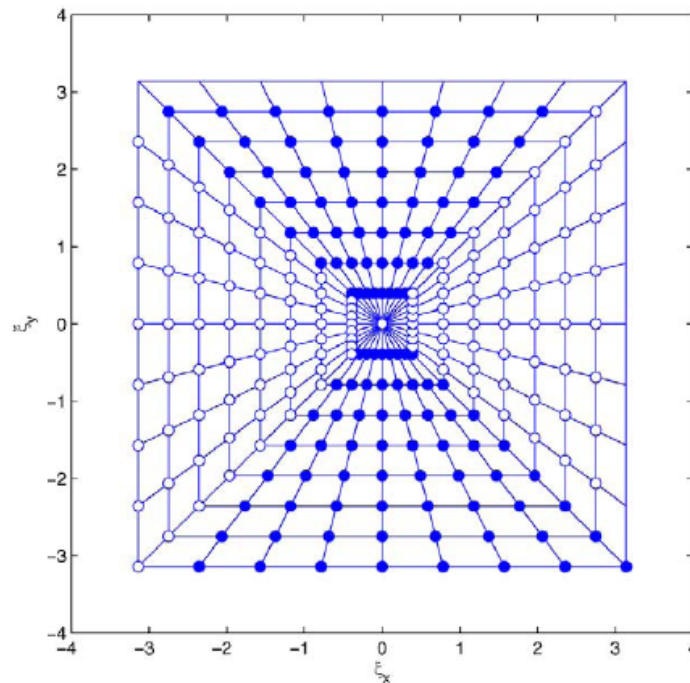


Figure C.2. The pseudo-Polar grid and its separation into BV (filled circles) and BH (empty circles) coordinates ( $N = 8$ )—intersection of 8 concentric squares and 16 slope-equispaced rays

In the pseudo-polar Fourier transform, the evaluation frequencies lie in an oversampled set of *nonangularly equispaced points*, as shown in Fig. C.2. The pseudo-polar FFT offers a near-

polar frequency coordinate system for which exact rapid FT evaluation is possible. Whereas the polar grid points in Fig. C.1. sit at the intersection between linearly growing concentric circles and angularly equispaced rays, the pseudo-polar points sit at the intersection between linearly growing concentric squares and a specific choice of angularly nonequispaced rays.

The points on the pseudo-polar grid are separated into two groups — the basically vertical (BV) and the basically horizontal (BH) subsets, given by

$$BV = \left\{ \xi_y = \frac{\pi l}{N}, \text{ for } -N \leq l \leq N; \quad \xi_x = \xi_y \cdot \frac{2m}{N}, \text{ for } -\frac{N}{2} \leq m < \frac{N}{2} \right\}. \quad (\text{C.4})$$

$$BH = \left\{ \xi_x = \frac{\pi l}{N}, \text{ for } -N \leq l \leq N; \quad \xi_y = \xi_x \cdot \frac{2m}{N}, \text{ for } -\frac{N}{2} \leq m < \frac{N}{2} \right\}. \quad (\text{C.5})$$

Figure C.2. depicts this grid; BV points are marked with the filled dots and BH ones are marked as circles. This grid has several remarkable properties, the most important of which are listed below:

- 1) The grid points are at intersections of linearly growing concentric squares with angularly non-equispaced rays. The length of the sides of the squares is  $\frac{\pi k}{N}$ ,  $k = 0, 1, \dots, N$ . The BH rays also have an equispaced slope:  $\frac{2k}{N}$ ,  $k = -\frac{N}{2} + 1, -\frac{N}{2} + 2, \dots, \frac{N}{2}$ . The BV rays are similar, but with clockwise rotation of  $90^\circ$ .
- 2) Referring to the BV (and similarly to the BH) points, they are organized on lines with angles ranging from  $-\pi$  to  $\pi$ . Along each such line, the points are spread uniformly, though in an angle-dependent way.

In computing and storing the Fourier transform for these points, the data structure is given by two simple 2D arrays — one for the BV and the other for the BH sample set. Referring to the BV array, the vertical axis corresponds to the index  $l$  and the horizontal to  $m$  (see (C.4) and (C.5)). Thus, each of the two arrays has  $2N$  rows and  $N$  columns and the overall number of frequency sample points is  $4N^2$ , which originate from the input image of size  $N \times N$ . This oversampling by a factor of 4 is also helpful for numerical stability.

The data structure so defined implies that a row or a column from the output arrays does not refer to a horizontal or vertical set of frequency points, but rather refers to points computed

along one ray or points along one of the concentric squares. It is therefore necessary to perform a few matrix manipulations and rearrange the obtained frequency points in order to get the classical polar grid. The process is illustrated in Fig. C.3. Points from each ray, stored in one column in the PFFFT output array, stand for two rays in the classical polar grid (one for angle  $\alpha$  and the other for  $\alpha+180^\circ$ ), one of which is stored backwards (with decreasing  $k_\rho$ ). Also notice that in the classical polar grid, each ray starts from the center point ( $k_\rho = 0$ ), while in the polar grid each ray passes through the center point only once. Hence, after splitting the ray in two and inverting the order of one of the two halves, it is necessary to duplicate the center point and merge it to one of the two arrays. But then, there is one frequency point too many in all such arrays and the outmost points have to be discarded.

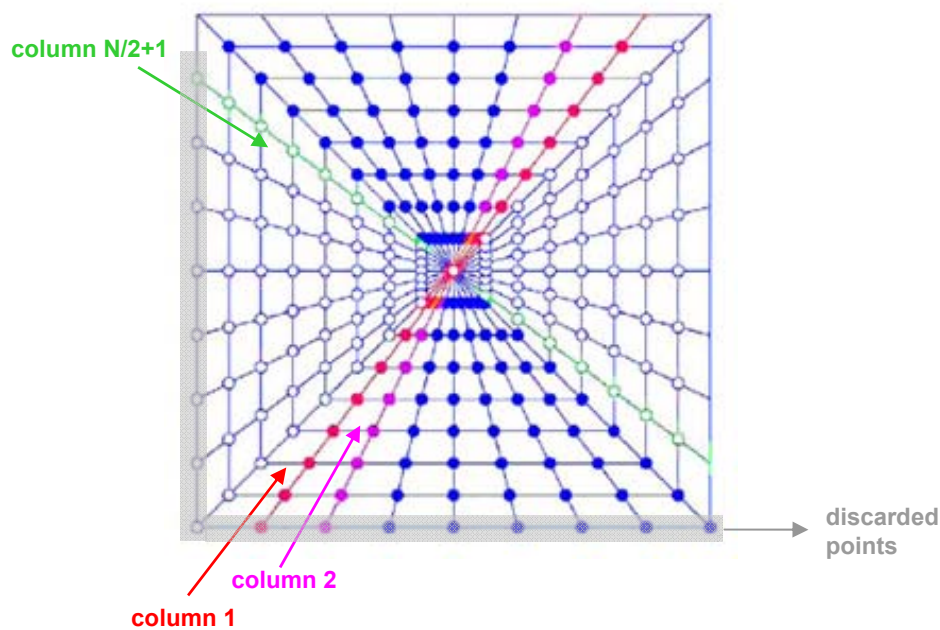


Figure C.3. Process of rearranging the array containing the data on a pseudo-polar grid to the classical polar grid.

The following code performs the described manipulations on the PFFFT output. The variable marked with the suffix "RP" is the one saved on the pseudo-polar grid (i.e. Recto-Polar grid of the Donoho type)

```
% create Polar array
spectxP = zeros(size(spectxRP,1)/2,2*size(spectxRP,2));
% read and rearrange the Recto-Polar grid data
spectxP(:,1:size(spectxP,2)/2) = ...
    fftshift(spectxRP((size(spectxRP,1)/2+1):size(spectxRP,1),:),2);
spectxP(:,(size(spectxP,2)/2+1):size(spectxP,2)) = ...
    fftshift(flipud(spectxRP(2:(size(spectxRP,1)/2+1),:)),2);
% rotate array horizontally so that the angle starts counting from 0
spectxP = circshift(spectxP,[0 -(size(spectxRP,2)/4 -1)]);
```

After the PPFFT-calculated spectrum has been rearranged into a classical polar grid structure with radial variable spanning from 0 to  $r_{max}$  and the angular variable from 0 to  $2\pi$ , the array can be passed on to the FFT-GPOF expansion routine. The spectrum is, however, quite oversampled, especially in the angular coordinate  $\alpha$ . For example, a TM circular waveguide mode only carries energy in 4 harmonics, while the PPFFT routine with decent accuracy will provide a few hundred rays. Therefore, prior to calling FFT-GPOF expansion routine, from the PPFFT-obtained spectrum a subset of points should be extracted or interpolated, depending on the parameters of the FFT-GPOF expansion to follow. In the implemented computer programme, the  $k_\rho$  data was resampled and interpolated using splines, while the  $\alpha$  data was obtained by copying the values from the appropriate column using the nearest-neighbour method. Since the angular spacing between neighbouring rays in the pseudo-polar grid is not constant, the latter introduces a small error. However, owing to the PPFFT spectrum being fairly oversampled, in all test cases the angular distance between rays was less than  $1^\circ$ , meaning a maximum possible angular error of  $0.5^\circ$ , which has been found tolerable.

## REFERENCES

- [1] P. F. Goldsmith, "Quasi-Optical Techniques," *Proc. IEEE*, vol. 80, pp. 1729-1747, Nov. 1992.
- [2] H-T. Chou and P. H. Pathak, "Uniform Asymptotic Solution for Electromagnetic Reflection and Diffraction of an Arbitrary Gaussian Beam by a Smooth Surface with an Edge", *Radio Science*, vol. 32, no. 4, pp. 1319-1336, 1997.
- [3] N. J. McEwan and P. F. Goldsmith, "Gaussian Beam Techniques for Illuminating Reflector Antennas", *IEEE Trans. Antennas & Propagation*, **vol. 37**, No. 3, pp. 297-304, 1989
- [4] W. A. Imbriale and D. J. Hoppe, "Recent Trends in the Analysis of Quasioptical Systems", *Proc. Millenium Conference on Antennas and Propagation*, Davos, Switzerland, 2000.
- [5] S. Withington, J. A. Murphy and K. G. Isaak, "Representation of Mirrors in Beam Waveguides as Inclined Phase-Transforming Surfaces", *Infrared Phys. Technol.*, vol. 36, no. 3, pp. 723-734, Apr. 1995
- [6] G. A. Deschamps, "The Gaussian Beam as a Bundle of Complex Rays", *Electronics Letters*, vol. 7, No. 23, 1971
- [7] L. B. Felsen, "Complex-Source-Point Solutions of the Field Equations and their Relation to the Propagation and Scattering of Gaussian Beams", *Proc. Symp. Math*, 1975
- [8] J. N. Franklin, *Matrix Theory*, Prentice-Hall, Englewood Cliffs, New Jersey, USA, 1968.
- [9] R. F. Harrington, *Time-harmonic Electromagnetic Fields*, IEEE Press & John Wiley and Sons, New York, USA, 2001.
- [10] D. G. Dudley, *Mathematical Foundations for Electromagnetic Theory*, IEEE Press & Oxford University Press, Oxford, UK, 1994.
- [11] H-T. Chou and P. H. Pathak, "Fast Gaussian beam based synthesis of shaped reflector antennas for contoured beam applications", *IEE Proc. Microw. Antennas Propag.*, Vol. 151, No. 1, pp. 13-20, Feb. 2004.
- [12] H-T. Chou, P. H. Pathak and R. J. Burkholder, "Application of Gaussian-ray Basis Functions for the Rapid Analysis of Electromagnetic Radiation from Reflector Antennas", *IEE Proc. Microw. Antennas and Propag.*, vol. 150, pp. 177-183, 2003

- [13] P. D. Einziger, S. Raz, and M. Shapira, "Gabor representation and Aperture Theory," *J. Opt. Soc. Am.*, vol. 3, No. 4, Apr. 1986, pp. 508-522
- [14] R. F. Harrington, *Field Computation by Moment Methods*, Robert E. Krieger Publishing Company, Malabar, Florida, 1968.
- [15] J. J. H. Wang, *Generalized Moment Methods in Electromagnetics*, John Wiley & Sons, Inc., New York, USA, 1991.
- [16] R. Mittra (Ed.), *Computer Techniques for Electromagnetics*, Pergamon Press, Oxford, United Kingdom, 1973.
- [17] W. L. Stutzman and G. A. Thiele, *Antenna Theory and Design*, 2<sup>nd</sup> ed., John Wiley and Sons Inc., New York, USA, 1997.
- [18] Y. Hua and T. K. Sarkar, "Generalized Pencil-of-Function Method for Extracting Poles of an EM System from Its Transient Response", *IEEE Trans. Antennas and Propagation*, vol. 37, no. 2, pp. 229-234, Feb. 1989
- [19] T. K. Sarkar and O. Pereira, "Using the Matrix Pencil Method to Estimate the Parameters of a Sum of Complex Exponentials", *IEEE Antennas and Propagation Magazine*, vol. 37, no. 1, pp. 48-55, Feb. 1995
- [20] H. Kogelnik and T. Li, "Laser Beams and Resonators", *Applied Optics*, Vol. 5, No. 10, pp. 1550-1567, Oct. 1966.
- [21] J. A. Murphy, "Distortion of a Simple Gaussian Beam on Reflection From Off-axis Ellipsoidal Mirrors", *Int. Journal of Infrared and Millimeter Waves*, vol. 8, no. 9, pp. 1165-1187, 1987.
- [22] S. Škokić, M. Casaletti, S. B. Sørensen, S. Maci, "Complex Conical Beam Expansion for the Analysis of Beam Waveguides", *Proc. 3rd European Conference on Antennas and Propagation (EuCAP 2009)*, Berlin, Germany, 2009
- [23] S. Škokić, M. Casaletti, S. B. Sørensen, S. Maci, "Complex Conical Beams for Aperture Field Representations", *submitted to IEEE Trans. Antennas & Propagation*, 2009.
- [24] L. B. Felsen and N. Marcuwitz, *Radiation and Scattering of Waves*, Wiley-IEEE Press, Place, 1994.
- [25] I. S. Gradshteyn and I. M. Ryzhik, *Tables of Integrals, Series and Products*, Academic Press, London, 1994.
- [26] M. Abramowitz and I. A. Stegun, *Handbook of Mathematical Functions*, Dover Publications, New York, 1970

- [27] C. A. Balanis, *Advanced Electromagnetic Engineering*, John Wiley and Sons, NY, USA, 1989
- [28] C. A. Balanis, *Antenna Theory – Analysis and Design*, 2<sup>nd</sup> edition, John Wiley and Sons, NY, USA, 1997.
- [29] W. C. Chew, *Waves and Fields in Inhomogeneous Media*, IEEE Press, NY, USA, 1995.
- [30] A. Sommerfeld, *Partial Differential Equations in Physics*, Academic Press, New York, USA, 1964.
- [31] Z. Šipuš, "Greenove funkcije za mikrotrakaste strukture i primjena u analizi mikrotrakastih antena," *Master Thesis, Univ. of Zagreb, Zagreb, Croatia*, 1991.
- [32] S. Škokić, "Moment Method Analysis of Spherical Structures", *Master Thesis, Univ. of Zagreb, Zagreb, Croatia*, 2005.
- [33] J. J. H. Wang, "An Examination of the Theory and Practices of Planar Near-Field Measurement", *IEEE Trans. Antennas & Propagation*, vol. 36, no. 6, pp.746-753, 1988.
- [34] K. Pontoppidan (Ed.), *GRASP9 Technical Description*, TICRA Engineering Consultants, Copenhagen, Denmark, 2005.
- [35] T. Bondo and S. B. Sørensen, "Physical Optics Analysis of Beam Waveguides Using Auxiliary Planes", *IEEE Trans. Antennas and Propagation*, Vol. 53, N. 3, pp. 1062-1068, Mar. 2005.
- [36] P-S. Kildal, *Foundations of Antennas – A Unified Approach*, Studentlitteratur, Lund, Sweden, 2000.
- [37] J. A. Stratton, *Electromagnetic Theory*, Wiley – IEEE Press, Piscataway, NJ, USA, 2007
- [38] W. H. Press, B. P. Flannery, S. A. Teukolsky and William T. Vetterling, *Numerical Recipes – The Art of Scientific Computing (FORTRAN Version)*, Cambridge University Press, Cambridge, United Kingdom, 1989.
- [39] A. Averbuch, R. R. Coifman, D. L. Donoho, M. Elad and M. Israeli, "Fast and Accurate Polar Fourier Transform", *Appl. Comput. Harmon. Anal.*, vol. 21, p.p.145–167, 2006.
- [40] S. Škokić, G. Carluccio, S. Maci, "New Wave-objects for Efficient Treatment of Complex Multi-reflector Systems", *Proc. 2nd European Conference on Antennas and Propagation (EuCAP 2007)*, Edinburgh, United Kingdom, 2007
- [41] A. Dutt and V. Rokhlin, "Fast Fourier Transforms for Nonequispaced Data", *SIAM J. Sci. Comput.*, vol. 14, p.p. 1368–1393, 1993.
- [42] A. Dutt and V. Rokhlin, "Fast Fourier transforms for Nonequispaced Data II", *Appl. Comput. Harmon. Anal.*, vol. 2, p.p. 85–100, 1995.

- [43] A. J. W. Duijndam and M. A. Schonewille, "Nonuniform Fast Fourier Transform", *Geophysics*, vol. 64, n.2, p.p. 539–551, 1999.
- [44] S. Maci, Z. Šipuš, A. Freni, A. Mazzinghi and S. Škokić, *Advanced Mathematics for Antenna Analysis* (European School of Antennas course book), European School of Antennas, *in preparation*
- [45] E. A. Siegman, *Lasers*, University Science Books, Sausalito, USA, 1986.
- [46] M. Born and E. Wolf, *Principles of Optics*, 7<sup>th</sup> ed., Cambridge University Press, Cambridge, United Kingdom, 1999.
- [47] S. B. Sørensen, course notes for the course "Beam Waveguides for Feeding Systems and Quasioptical Networks", TICRA, 2009.
- [48] J. Tuovinen, "Accuracy of a Gaussian Beam", *IEEE Trans. Antennas & Propagation*, Vol. 40, No. 4, pp. 391-398, Apr. 1992.
- [49] A. T. Friberg, T. Jaakkola and J. Tuovinen, "Electromagnetic Gaussian Beam Beyond the Paraxial Regime", *IEEE Trans. Antennas & Propagation*, Vol. 40, No. 8, pp. 984-989, Aug. 1992.
- [50] C. F. Gerald and P. O. Wheatley, *Applied Numerical Analysis*, 7<sup>th</sup> ed., Addison Wesley, Reading, USA, 2003.



## INTERNET REFERENCES

- [I-1] D. Gruber, "*The Mathematics of the 3D Rotation Matrix*", <http://www.fastgraph.com/makegames/3drotation>; accessed 05/11/2009
- [I-2] "*Angle Bisectors in Ellipse*", <http://www.cut-the-knot.org/Curriculum/Geometry/AngleBisectorsInEllipse.shtml#proof>; accessed 05/11/2009
- [I-3] "*Michael Elad Personal Page – Software (Pseudo-polar FFT Matlab Toolbox)*", <http://www.cs.technion.ac.il/~elad/software> ; accessed 05/11/2009
- [I-4] E. W. Weisstein, "*Radius of Curvature*", from MathWorld - A Wolfram Web Resource, <http://mathworld.wolfram.com/RadiusofCurvature.html>; accessed 05/11/2009

## LIST OF SYMBOLS

The symbols and conventions used in this thesis are listed below.

$x, y, z$	Cartesian coordinates, space domain
$\tilde{z}$	Cartesian $z$ -coordinate with complex displacement
$\rho, \varphi, z$	cylindrical coordinates, space domain
$r, \theta, \varphi$	spherical coordinates, space domain
$k_x, k_y, k_z$	Cartesian coordinates, spectral domain
$k_\rho, \alpha, k_z$	cylindrical coordinates, spectral domain
$\hat{x}, \hat{y}, \hat{z}$	unit vectors in rectangular coordinate system
$\hat{\rho}, \hat{\varphi}, \hat{z}$	unit vectors in cylindrical coordinate system
$\hat{r}, \hat{\theta}, \hat{\varphi}$	unit vectors in spherical coordinate system
$\hat{n}$	unit normal vector
$f, g   \tilde{F}, \tilde{G}$	general scalar functions in space and spectral domain, respectively
$\vec{f}, \vec{g}   \vec{F}, \vec{G}$	general vector functions in space and spectral domain, respectively
$\vec{E}, E_x, E_r$	electric field vector and components, space domain
$\vec{E}, \tilde{E}_{k_\rho}, \tilde{E}_\alpha$	electric field vector and components, spectral domain
$\vec{H}, H_x, H_r$	magnetic field vector and components, space domain
$\vec{H}, \tilde{H}_x, \tilde{H}_r$	magnetic field vector and components, spectral domain
$\vec{J}, \vec{J}^{eq}$	electric surface current (real or equivalent) vector, space domain
$\vec{J}, \vec{J}^{eq}$	electric surface current (real or equivalent) vector, spectral domain
$\vec{M}, \vec{M}^{eq}$	magnetic surface current (real or equivalent) vector, space domain
$\vec{M}, \vec{M}^{eq}$	magnetic surface current (real or equivalent) vector, spectral domain
$\vec{A}, A_x, A_r$	magnetic vector potential and components, space domain
$\vec{F}, F_x, F_r$	electric vector potential and components, space domain
$\varepsilon, \mu$	electric permittivity and magnetic permeability
$\eta$	characteristic impedance
$\omega$	angular frequency
$k$	wavenumber

## SAŽETAK

### **ANALIZA REFLEKTORSKIH ANTENSKIH SUSTAVA POMOĆU NOVIH KONUSNIH VALNIH OBJEKATA**

U radu se obrađuje metoda analiziranja reflektorskih antenskih sustava primjenom nove vrste valnih objekata. Razvojem prostornog spektra električnog polja na sumu eksponencijalnih funkcija s kompleksnim eksponentima (GPOF aproksimacija), radijacijski integral svodi se na sumu jednostavnijih integrala koje je moguće riješiti analitičkim putem, pri čemu svaki tako dobiveni integral označava jedan valni objekt koji rigorozno zadovoljava valnu jednadžbu. Veza valnih objekata s elektromagnetskim poljem uspostavlja se upotrebom vektorskih potencijala. U svrhu računanja refleksije od zakrivljenih metalnih površina, metoda je povezana s fizikalnom optikom u novu hibridnu metodu. Ovakva procedura je ponovljiva i omogućuje analiziranje niza reflektora bez povećavanja zahtjeva na računalne resurse. Za provjeru valjanosti opisane metode razvijena je programska podrška za analiziranje niza elipsoidnih reflektora. Dobiveni rezultati uspoređeni su s rezultatima dobivenim postojećim metodama ugrađenim u komercijalne elektromagnetske simulatore, kao i s egzaktnim rezultatima dobivenim izravno numeričkim integriranjem. Razvijena metoda jednako je točna kao metoda Fizikalne optike, a omogućuje znatno kraća vremena proračuna pri analizi sustava s više reflektora.

## **SUMMARY**

### **ANALYSIS OF REFLECTOR ANTENNA SYSTEMS BY MEANS OF NEW CONICAL WAVE OBJECTS**

This dissertation discusses a method of analysing reflector antenna systems by means of a new type of wave objects. By expanding the electric field spectrum in a sum of complex exponentials (GPOF expansion), the radiation integral reduces to a sum of simpler integrals which can be solved in closed form, whereby each of them represents one wave object that rigorously satisfies the wave equation. Vector electromagnetic fields are calculated from these wave objects via auxiliary vector potentials, while the reflection of the electromagnetic wave from curved metallic reflectors is treated with Physical Optics. The main advantage of this novel hybrid method is that it can be repeated without increasing the demands on computer resources, enabling fast analysis of a sequence of reflectors. To verify its validity, the method has been translated into a computer programme for analysing a sequence of ellipsoidal reflectors. The results are compared to those obtained with available commercial electromagnetic simulators and to reference results calculated via direct numerical integration. The developed method is shown to be as accurate as pure Physical Optics analysis, while performing much faster in case of multi-reflector systems.

**KEYWORDS / KLJUČNE RIJEČI****KEYWORDS:**

quasi-optical systems  
reflector antennas  
beam waveguides  
numerical methods  
physical optics  
wave objects  
complex conical beams  
GPOF approximation  
Gaussian beams

**KLJUČNE RIJEČI:**

kvazi-optički sustavi  
reflektorske antene  
snopovodi  
numeričke metode  
fizikalna optika  
valni objekti  
kompleksni konusni snopovi  
GPOF aproksimacija  
Gaussovi snopovi

## BIOGRAPHY

Siniša Škokić was born on 9th September 1978 in Zagreb, where he finished primary and secondary school and graduated from the Faculty of Electrical Engineering and Computing in 2001. During his studies he won the “Josip Lončar” award for exceptional success in studying (1997) and was a stipendiary of the City of Zagreb Scholarship (1999-2001). In 2000 he did a practice term in Neuchatel, Switzerland, with Xemics SA, where he participated in the design of high-frequency integrated circuits for Bluetooth transceivers.

He joined the Department of Wireless Communications in late 2001. In 2004, as a part of his masters degree studies, he went on a specialisation term of five months to the University of Siena, Italy, where he took part in the development of a mathematical model for analysing curved frequency selective radomes. He obtained his M.Sc. degree in November 2005, after which he went back to the University of Siena for another specialisation term related to his doctoral studies. The work involved the development of new mathematical models for analysing electrically large curved multireflector systems.

Siniša Škokić has authored and co-authored about 30 scientific papers and has received the URSI Young Scientist Award (2008) and the Best Poster Paper Award at the 3<sup>rd</sup> European Conference on Antennas and Propagation (2009). He speaks English, French and Italian.

## ŽIVOTOPIS

Siniša Škokić rođen je 9. rujna 1978. godine u Zagrebu, gdje je završio osnovnu i srednju školu te diplomirao 2001. godine na Fakultetu elektrotehnike i računarstva, smjer Radiokomunikacije i profesionalna elektronika. Za vrijeme studija dobio je priznanje “Josip Lončar” za izvanredan uspjeh u studiju (1997.) te bio stipendist grada Zagreba (1999-2001). 2000. godine bio je na stručnoj praksi u Neuchatel, Švicarska, pri firmi Xemics SA, gdje je sudjelovao u razvoju mikroelektroničkih visokofrekvencijskih sklopova za primopredajnike za komunikacijski protokol Bluetooth.

Na Zavodu za radiokomunikacije i mikrovalnu elektroniku Fakulteta elektrotehnike i računarstva zaposlio se kao znanstveni novak krajem 2001. godine. 2004. godine, u sklopu poslijediplomskog magistarskog studija, proveo je pet mjeseci na specijalizaciji pri Sveučilištu u Sieni, Italija, gdje je sudjelovao u razvoju matematičkog modela za analiziranje zakrivljenih frekvencijski selektivnih zaštitnih kupola. Magistrirao je u studenom 2005. godine, nakon čega 2006. godine ponovo odlazi na usavršavanje pri Sveučilištu u Sieni, u sklopu poslijediplomskog doktorskog studija. Tamo sudjeluje u razvoju novih matematičkih modela za analiziranje električki velikih zakrivljenih antenskih reflektorskih sustava.

Siniša Škokić autor je ili koautor oko 30 znanstvenih radova. Za svoj znanstveno-istraživački rad dobio je međunarodne nagrade URSI Young Scientist Award (2008.) i Best Poster Paper Award na konferenciji European Conference on Antennas and Propagation (2009.). Aktivno se služi engleskim, francuskim i talijanskim jezikom.